Acknowledgements

I would like to express my gratitude to a number of individuals I feel privileged to have worked with during my PhD. To all academic and student members of the Energy Storage CDT with whom every day has been a pleasure to work, with particular thanks to Sharon and Solomon Brown. I would also like to thank all members of the Green Nanomaterials research group who have shared interesting and novel scientific ideas along with friendship. In particular, I would like special thanks for Dr Mauro Chiacchia, Dr Joseph Manning, Eleni Routoula, Abi Balashanmugam and Max Yan.

For collaborative work concerning central facilities I would like to thank Professor Gregory Beaucage for arranging USAXS measurement and donating his time to teaching me data analysis. I would also thank Jan Ilavski and his team for data collection. With regards to XPDF, particular thanks is deserved for Dr Denis Cumming and Dr Sam Booth for their help at all stages from the funding application to data analysis. I would also like to acknowledge the great input of I-15 beamline scientist Dr Dean Keeble. With regards to XPS measurements I would like to thank Dr Mark Isaacs.

I have been privileged throughout my PhD to have been awarded additional funding from the Energy Storage CDT and the National Productivity Investment Fund for which I am truly grateful. For my placement at Queen Mary University I would like to thank Prof Maria-Magdalena Titirici and Sabina Nicolae for their great hosting and input to my work. For my placement with Exawatt all of their team deserve thanks with particular acknowledgements to Simon Price and Megan Wilson.

To my supervisor and mentor Professor Siddharth Patwardhan from who I have learnt a great deal and without whom this PhD would have been incomplete. Thank you.

I would thank everyone above for helping me on a personal level to complete and enjoy this work.

My deepest thanks go to my family, my mother and father, Martine and Nick, my brothers, Zack and Kyle, and to my grandparents who have forever provided their support.

The ability to complete these works as with all of the achievements in my life has, in large part, been due to the knowledge, skill and love passed onto me by my father Nick Entwistle. Although he will never see this work I know he would be proud.

Dedicated to Nick Entwistle

Table of Contents

List of Abbreviations

BJH	Barrett, Joyner, and Halenda
BET	Brunauer-Emmett-Teller
CVD	Chemical Vapour Deposition
C-PSD	Constant Potentiostatic Discharge
CE	Columbic efficiencies
CLD	Constant Load Discharge
dV/dQ	Differential voltage/Capacity
EIS	Electrochemical Impedance Spectroscopy
FEC	Fluoroethylene carbonate
GI-XRD	Grazing incidence – X-ray Diffraction
LIB	lithium-ion batteries
MgTR	Magnesiothermic Reduction
PSD	Potentiostatic Discharge
SEM	Scanning Electron Microscopy
SEI	Solid electrolyte interphase
TEM	Transmission electron microscopy
USAXS	Ultra Small angle X-ray Scattering
VC	Vinylene carbonate
S-PSD	Stepwise Potentiostatic Discharge
XRD	X-ray Diffraction
XPS	X-ray photoelectron spectroscopy
XPDF	X-ray Pair Distribution Function

List of Figures

List of Tables

List of Outputs

Papers

''A Review of Magnesiothermic Reduction of silica to porous silicon for lithium-ion battery applications and Beyond'' J. Entwistle, A. Rennie, S. Patwardhan, *J. Mater. Chem. A* **2018**, *6*, 18344.

''Mechanistic understanding of pore evolution enables high performance mesoporous silicon production for lithium-ion batteries'' J. Entwistle, G. Beaucage, S. Patwardhan. Under Review.

''Understanding the electrochemical reduction of silica for lithium-ion battery Applications'' J. Entwistle, S. Booth, D. Keeble, D. Cumming, S. Patwardhan. In preparation

Presentations

235th Annual meeting of the Electrochemical Society 2019

UK Energy Storage conference 2017 and 2019

STFC Early Career Researcher Conference 2017 and 2019

The Energy Storage and Applications CDT Annual conference 2018 and 2019

Workshops

Warwick Battery School 2016

Collaborations

Queen Mary University and partook in a 3-week knowledge transfer placement to carbon coat silica and silicon particles to enhance LIB performance.

Hosting a student from Imperial for LIB experiments based on thermal runaway.

EPSRC National Productivity Investment Fund, 2-month placement at Exawatt researching the commercial viability of the technologies contained within this thesis.

Supervised a number of lab based Masters research projects with students obtaining top marks.

Abstract

Silicon has been highlighted as a promising anode material in lithium-ion batteries due to its step change in capacity verses conventional graphite. The cycling of silicon anodes within a lithium-ion battery (LIB) leads to degradation and capacity fade due to the 280% volume change of silicon. Many avenues of silicon synthesis have been explored to produce nanostructures which can withstand this change in volume.

Magnesiothermic Reduction (MgTR) of silica to silicon shows significant promise over other syntheses in scalability, economic and environmental aspects for producing porous silicon nanostructures. The problem with MgTR is a lack of understanding regarding the pore evolution of porous silicon based on reduction parameters and precursor material, which in turn limits predictive design for desired applications. Here we show for the first time that the pore structure of porous silicon is strongly related to the interconnectivity of silicon crystallites. We show that the MgTR is a thermodynamically driven equilibria which determines the purity of the silicon product. Higher temperatures also cause sintering of silicon nanocrystallites. We show that it is the interconnectivity of these crystallites determine the pore size and distribution within porous silicon. These findings apply to a wide variety of porous silica precursors and we show this mechanism is true for the introduction of pores into nonporous quartz after MgTR. Further, we show that by exploiting this mechanism, mesoporous silicon can be produced which has excellent promise for LIB applications with a capacity of 2170 mAh/g after 100 cycles.

As a second section of the thesis, we focused on the use of silica directly in LIBs. The use of silica has potential advantages over other silicon based active materials, upon reduction with lithium silicon is produced and contained within a supporting structure of inactive material. However, there is no detailed understanding of how the lithium-silica reduction reaction progresses and the chemical nature of the products. Here we develop a new method to effectively monitor the rate of electrochemical reduction of silica and propose a mechanistic understanding of this process. In addition, and for the first time, we characterise the existence of elemental silicon in the reduced structures. Our proposed mechanism is based upon the initial insulating nature of the silica active material and how electronic conduction pathways are formed in the reduced material. We apply the principles of this mechanism to reduce

the length of the electrochemical reduction reaction to 13 hour compared with 400 hour reduction times reported in the literature.

The findings herein provide a significant step change and hence can be taken forward to design optimal materials for LIB applications. These results strongly support the potential for reduction in silicon costs for LIB in both economic and environmental terms as well as for a reverse engineering approach to design specific porous silicon and silica for desired applications.

Background

Rechargeable batteries play an important role in portable electronics and are increasingly being incorporated in electric transportation. Development of lithium-ion batteries (LIB) with higher energy density, improved safety and lower cost are highly desirable.

The cell of a battery stores electrical energy as chemical energy in two electrodes. The anode and cathode (reductant and oxidant) respectively are separated by an insulating separator and wetted by an ionically conducting electrolyte. When connected through an external circuit, electrons will flow from cathode to anode and lithium ions will travel across the separator to balance charge. Secondary (rechargeable) batteries can have this process reversed by applying an opposing bias across the electrodes reversing electron and ion transfer from anode-cathode. These processes can be visualised through the schematic in Figure 1. [1]

The LIB has the best performance of secondary batteries in regard to high specific and volumetric capacity, high power charging and discharging, and long cycle life. The most common anode material in the LIB is graphite, and cathode materials typically consist of layered metal oxides. The electrode active materials operate via an intercalation mechanism, where the lithium ions move into the interstitial sites between atoms. The ability of a material to reversibly store lithium-ions governs the amount of charge which a material can store. Therefore, a strive in research of new LIB active materials is focused on increasing the reversible lithium storage capacity.

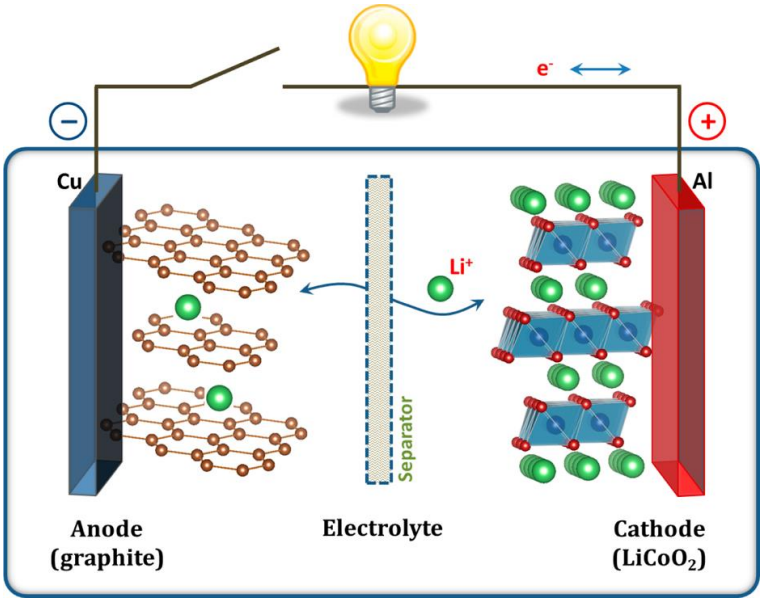

Figure 1. Schematic of a lithium-ion battery with graphite anode and lithium cobalt oxide cathode. Image taken from[1]

A significant research effort has been devoted to finding higher capacity electrode materials. For the anode, alloy type materials primarily silicon have received huge research investment due to the its charge storage capabilities which are an order of magnitude greater than commercial graphite materials. Silicon incorporation is the forefront of current commercial advances providing high energy density lithium-ion cells and the further development of silicon-based anodes will increase the cell capacity of future generations of LIBs.

The work presented in this thesis develops novel understanding and synthesis routes for two classes of silicon-based anode materials. The theme throughout is the development of economically and environmentally friendly synthesis routes, abiding to the principles of green chemistry.[2] We use the feedstock of silica (SiO_2) owing to its high natural abundance, wide variety of morphologies and well understood chemistry.

References

[1] J. B. Goodenough, K. Park, *J. Am. Chem. Soc.* **2013**, *135*, 1167.

[2] P. T. Anastas, J. Warner, *Green Chemistry: Theory and Practice*, Oxford Univeristy Press Inc, **2000**.

Chapter 1:

Introduction and Literature Review

1.1 Understanding Silicon Lithiation

In most commercial LIBs, active materials rely on intercalation mechanism where lithium atoms reside in the interstitial sites of the host lattice and the extraction/insertion of the lithium only results in small strains and minimal irreversible structural changes. Such active materials include graphite the commercial standard for negative electrodes (anodes), there is more variety of cathode materials based on metal oxides and phosphates, $LiCoO_2$ $LiMnO_2$ $LiFePO_4$ and $LiNi_xMn_yCo_zO_2$ (NMC). [1] Group iv elements such as Si, Ge and Sn can be utilised as negative electrode materials as they reversibly alloy with lithium, which involves the formation and destruction of chemical bonds. [1] As the atomic framework of the active material is no longer the constraint of the reaction, alloy materials can have much higher capacities and form multiple bonds to alloying lithium. The alloying process can cause significant strain on the materials by expansion in the alloy state. The large volumetric changed can lead to decay in capacity with cycling. The capacity and volume change of group iv elements along with their associated volume change with lithiation are compared to graphite in Table 1.1.

Table 1.1 Theoretical gravimetric capacities of Group IV elements and graphite and associated volume change upon lithiation. Values taken from[2][3][4]

Active Material	Theoretical capacity (mAh/g)	Volume change on lithiation (+%)
Graphite	372	10%
Silicon ($Li_{15}Si_4$)	3600	280%
Germanium ($Li_{4.4}Ge$)	1623	370%
Tin (Sn)	994	-

Within the constrained environment of a composite electrode volume expansion of silicon becomes an issue for three main reasons as depicted in Figure 1.1.[5] Firstly, considering Figure 1.1 (a), stresses within individual particles lead to fracturing and eventually pulverisation. Figure 1.1 (b), shows the impingement of expanding material in the electrode can lead to fragmentation on a larger scale, disconnecting sections of electrode. In each case, active material becomes electrically isolated and no longer contributes to the electrodes capacity. Figure 1.1 (c), illustrates the case when constant expansion and contraction leads to cracking of the Solid Electrolyte Interphase (SEI) layer, exposing fresh active material and causing further breakdown of electrolyte. Thickening of the SEI can increase the internal resistance of the cell and consumes lithium from the electrolyte.[5]

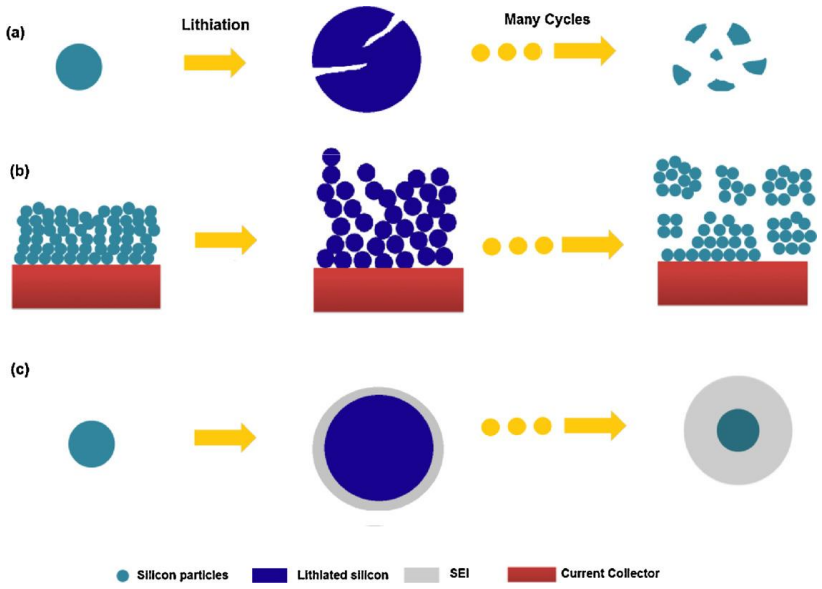

Figure 1.1 Electrode failure mechanisms for silicon active material: (a) Material cracking and pulverization. (b) electrode expansion and impingement leading to isolation. (c) Continual SEI formation.[5]

Another challenge is the relatively low lithium diffusion rates within silicon, 10^{-10}-10^{-11} cm^2/s, [6],[7] compared with the range 10^{-6}-10^{-11} cm^2/s reported for graphite electrodes.[8][9][10]

1.1.1 Electrochemical Lithiation of Silicon

Crystalline silicon is lithiated during the initial discharge of a LIB, this lithiation occurs via a two-phase mechanism between crystalline silicon and amorphous Li_xSi alloy which are separated by a short reaction front of a few nm. The amorphous Li_xSi phase is found to crystallise to $Li_{15}Si_4$ around and below 60mV vs Li/Li^+ and a number of studies have detailed how limiting cut off voltages and formation of $Li_{15}Si_4$ can effect cycle life [6],[7] (expanded on below Table 1.2). There is a large activation energy required to break Si-Si bonds within the crystalline silicon matrix therefore a high concentration of lithium-ions is required to weaken the Si-Si bonds, leading to favourable lithiation kinetics of the two-phased behaviour.[3] This results in a galvanostatic voltage profile with a flat voltage plateau around 0.1V vs Li/Li^+, shown in Figure 1.2. When the electrode potential falls below 50mV vs Li/Li+ the amorphous Li_xSi crystallises to form metastable $Li_{15}Si_4$ (Figure 1.3(a)). The dotted line Figure 1.2 shows a coulometric titration at 415 ºC, the stepped voltage profile is in accordance to the sequential formation of $Li_{12}Si_7$, Li_7Si_3, $Li_{13}Si_4$, $Li_{22}Si_5$, during ambient temperature electrochemical lithiation no such clear phase transitions are observed.[3] Literature consensus is that the $Li_{15}Si_4$ is the final phase formed upon electrochemical lithiation below 85 ºC. If held at 0V vs Li/Li+ for substantial time (>24 hours) X-ray Diffraction (XRD) has shown formation of higher lithiated states such as the thermodynamically stable $Li_{21}Si_5$.[11]

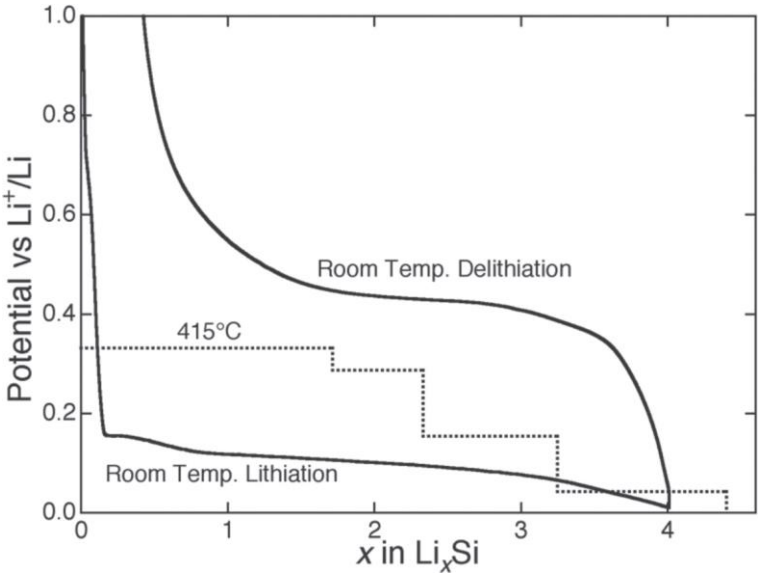

Figure 1.2. coulometric titration curve for a Li-Si system at 450 ºC (dotted line). Galvanostatic charge/discharge of a crystalline silicon powder electrode at room temperature (solid line).[3]

During the first delithiation another two phase system occurs in reverse eventually yielding amorphous Si. Large discharge capacities and low columbic efficiencies (CE) measured during the first lithiation can be attributed to: electrolyte degradation and irreversible lithium insertion into the solid electrolyte interphase (SEI).

After this first cycle behaviour, in the second cycle no two-phase region occurs and sloping voltage profiles are observed.[12] The changes to crystalline silicon through lithiation over the initial cycles were studied through in-situ XRD as summarised in Figure 1.3.[13] Figure 1.3 (a) demonstrates the voltage profiles during the first cycles of crystalline silicon, it shows the amorphisation of all crystalline silicon after lithiation, and the formation of crystalline $Li_{15}Si_4$ in the lithiated state. In-situ Transmission electron microscopy (TEM) has also been used to study these phase changes.[3] The sloping voltage profile on lithiation of amorphous Si (Figure 1.3(c)) evidences the difference in reaction between amorphous Si and crystalline Si (Figure 1.3(a)-(c)).

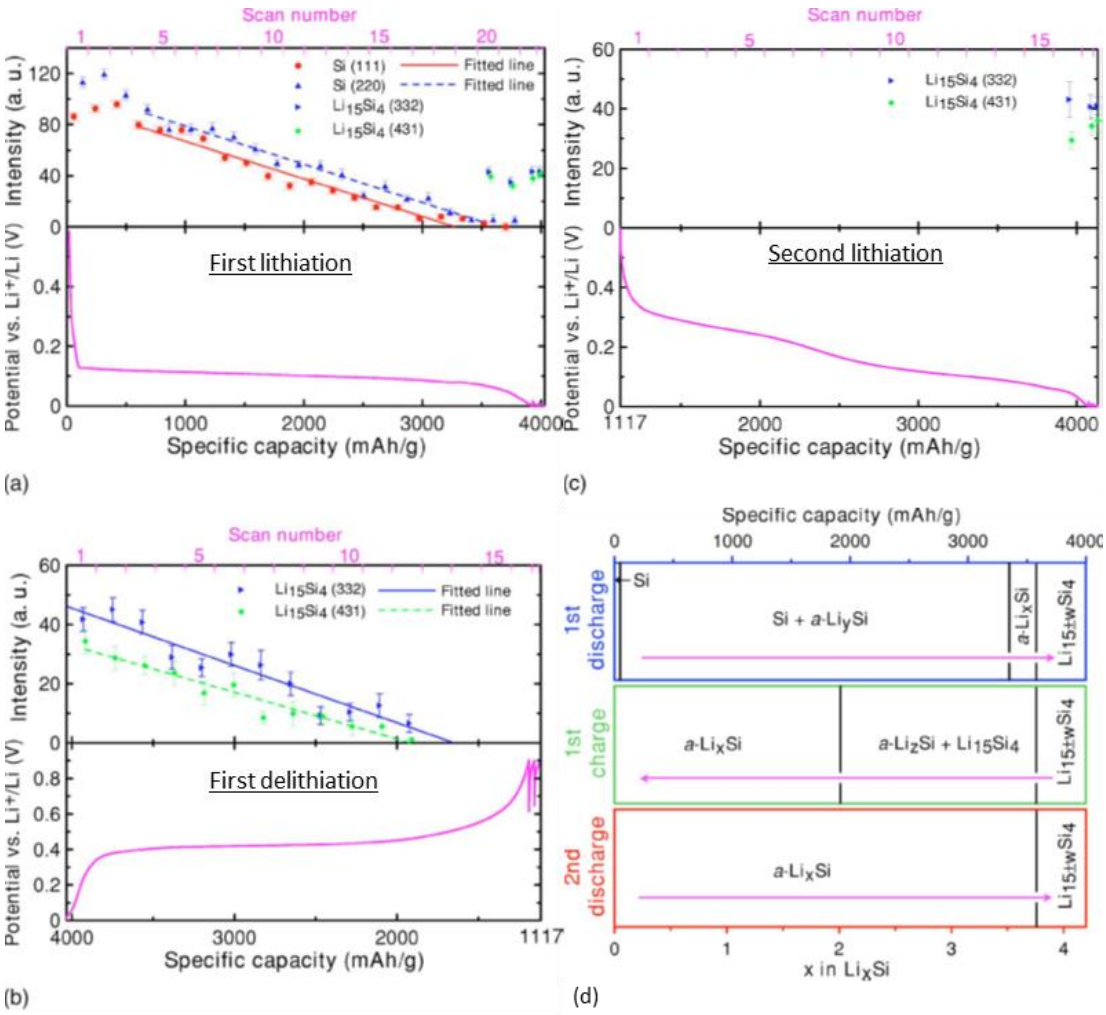

Figure 1.3. In-situ XRD during galvanostatic cycling. In(a-c) the line plots (top) show the intensity of Bragg peaks, (bottom) potential profile as a function of capacity during cycling at C/100. (a) during the first discharge, (b) during the first charge, and (c) during the second discharge. (d) Phase diagram summary as a function of specific capacity between 0.005-0.9V. Taken from [13]

A differential capacity voltage (dQ/dV) plot is straightforward to calculate from standard cell galvanostatic cycling data. They can show the appearance or disappearance of different phases or reactions and provide quantitative results of phase changes.[14] Upon first discharge crystalline Si conversion to amorphous a-LixSi (x~3.5) will dominate the dQ/dV plot with a cathodic peak around 100mV. dQ/dV plots can also be useful in determining SEI layer formation which occurs in the first cycle. After the first cycle, lithiation will occur into amorphous silicon the typical cathodic peaks for amorphous silicon lithiation start at 0.3 V (a-Si → a-$Li_{2.0}$Si), and a strong peak at 0.1 V (a-$Li_{2.0}$Si → a-$Li_{3.5}$Si) are all from the stepwise lithiation of silicon forming amorphous a-Li_xSi phases. As the discharge voltage approaches 50 mV and below the crystallisation of amorphous a-$Li_{3.75}$Si → c-$Li_{3.75}$Si can be observed, note some report lower potentials (30 mV) are needed for $Li_{3.75}$Si crystallisation in smaller

nanoparticle electrodes [15]. The first cycle charge will typically show an anodic peak at 0.43V indicating (c-$Li_{3.75}Si$ → a-$Li_{1.1}Si$), if the silicon is not fully converted to crystalline c-$Li_{3.75}Si$ on discharge then anodic peaks at 0.28V (a-$Li_{3.75}Si$ → a-$Li_{2.0}Si$) can be observed. The relative intensity of the 0.43 V and 0.28 V peaks can give a ratio of amorphous and crystalline Li_xSi phases at the end of lithiation. Peak shifts to lower voltage on the lithiation (cathoidic) curve and higher peak shifting on the delithiation (anodic) curves result with increased cell impedance causing polarisation during charging.[16] Shoulders and anodic peaks at 0.5 V (a-$Li_{2.0}Si$ → a-Si) and slightly above are also indicative of no crystallisation of c-$Li_{3.75}Si$ on discharge. [17],[15],[16] These phase transitions are summarised in Table 1.2.

The lithiation process finishes when the lithium-rich c-$Li_{3.75}Si$ is formed at the surface of the silicon electrode, similarly the delithiation finishes when the lithium-ions are extracted from the very outer surface layer. This arises as the potential of the cell is determined by the chemical potential difference of lithium-ions between the two electrodes. If the potential drops below the operational voltage window, then regardless of whether inner silicon has participated in lithiation/delithiation the process will stop. In general, this mechanism is responsible for the theoretical capacity not being reached, as at conventional charging rates the transfer of lithium-ions between the electrolyte and silicon interface and diffusion of lithium-ions inside the silicon are limiting factors. To improve silicon anode performance at more conventional (higher) current rates a large surface area for electrolyte access and thin silicon substructures for short lithium diffusion lengths are both desirable.

Table 1.2 summarising the potentials at which significant phase changes occur during the lithiation of silicon. [18][19]

Silicon Lithiation Process	Typical reduction voltage (V)
First cycle discharge	
c-Si →a-Li_xSi →c-$Li_{3.75}Si$	0.1 (<0.17*) can be dependent on crystallite size[14]
Subsequent Charges	
a-$Li_{3.5}Si$ →a-$Li_{2.0}Si$	0.28
c-$Li_{3.75}Si$ → a-$Li_{1.1}Si$	0.43
a-$Li_{2.0}Si$ → a-Si	0.50
Subsequent Discharges	
a-Si → a-$Li_{2.0}Si$	0.30
a-$Li_{2.0}Si$ → a-$Li_{3.5}Si$	0.10
a-$Li_{3.5}Si$ → c-$Li_{3.75}Si$	0.05

1.1.2 Volume expansion of Si

Crystalline and amorphous silicon undergo different mechanisms of lithiation, as introduced above. Crystalline Silicon is known to show anisotropic expansion upon lithiation, with large ~200% elongation along the <011> family of directions [20],[21],[5]. Volume change has been studied in amorphous silicon thin films with AFM and shown to be linear with Li content [22]. There is no observed anisotropic expansion event with amorphous Si as there is no crystallographic effects. X-ray data has shown the density of the $Li_{3.75}Si$ phase to be 1.179 g/cm3 meaning this fully lithiated phase under goes a volume expansion of 280%.[23]

There are in situ Transmission electron microscopy (TEM) observations for both crystalline and amorphous silicon indicating a critical size for nanoparticles, beyond which they could crack, 150 nm for crystalline silicon and 870 nm for amorphous.[24],[25] For porous crystalline silicon particles, the critical size can exceed 1500 nm as the pores of the material offer a buffer space for expansion. Additionally, porous structures usually consist of smaller domains which effects the extent of lithiation and shown to reduce lithiation stresses. [26] These TEM studies took place in a constraint free environment which is not the case for real electrodes.

As introduced above the volume expansion during lithiation of silicon has shown a strong linear trend. Obrovac et al.[27] show that this is the case for many lithium alloy type anode materials and that the amount of space occupied by a lithium atom is independent of the lithium content. They therefore suggesting a general Equation (1.1). Where υ_0 is the unlithiated molar volume (ml/mol), k is the molar volume (ml/mol) of lithium in the metal alloy and x is mole fraction of lithium in metal (Li_xSi). Using this equation leads to a theoretical capacity of lithiated $Li_{3.75}Si$ equal to 2240 mAh/ml. This value is in good accordance with the volumetric capacity calculated using density data obtained by XRD of 2190 mAh/ml.[13]

$$(x) = \upsilon_0 + kx \qquad \text{Equation (1.1)}$$

$$Si\ \upsilon_0 = 10.96\ ml/mol$$

$$Si\ k = 9.0\ ml/mol$$

1.1.3 Solid Electrolyte Interphase Formation

The organic electrolyte is typically unstable at the operating potential of the negative electrode during charging. This causes an irreversible decomposition of electrolyte at the anode surface which competes with the desired Faradic half-cell reaction. The decomposition products form a solid layer on the surface of the active anode material, referred to as the Solid electrolyte interphase (SEI). Typically, the SEI is electrically insulating, preventing further decomposition of electrolyte on the surface once formed, yet ionically conducting, allowing lithium ions to migrate and participate in Faradic reaction.

A stable SEI formation is critical for sustainable cycle life of lithium-ion batteries. The continuous SEI crack formation after the first charge-discharge cycle for silicon anodes exposes new surfaces to the electrolyte promoting SEI growth throughout cycling. The continuous SEI growth increases the internal impedance of the cell and consumes lithium from the electrolyte. The SEI formed in silicon anodes can be one of the dominant parameters influencing kinetics of lithiation/delithiation during repeated cycling.[28]

Residual water present in electrodes is known to catalytically react with PF_5 and lithium carbonate according to equations 1.2 and 1.3 below, propagating LiF salt formation.[29] It is therefore key to fully dry electrodes before cell preparation.

$$PF_5 + H_2O \rightarrow PF_3O + 2HF \qquad \text{Equation (1.3)}$$

$$Li_2CO_3 + 2HF \rightarrow CO_2 + 2LiF + H_2O \qquad \text{Equation (1.4)}$$

Carbonate electrolytes being the industrial standard for LIBs have received a high degree of attention in characterising SEI formation on silicon. Exploring carbonate additives has historically improved SEI formation in graphite, with a number of additives explored flouroethylene carbonate (FEC) and vinylene carbonate (VC) being adopted as standard electrolyte additives for improved SEI formation.[30] S. Zhang et al. recent review of electrolytes and additives for silicon anodes in LIB covers the range of routes being explored for more stable SEI formation.[30] FEC and VC both improve the stability of SEI in silicon anodes.[30],[31],[32] FEC incorporation 10-15 wt% in conventional organic electrolyte appears to give improved cycle life, higher specific capacity and lower SEI impedance when compared to VC.[15]

1.1.4 Binders in silicon anodes

Silicon has received considerable attention towards the importance of binder selection, primarily because choice of binder has been shown to significantly affect electrochemical performance. Polyvinylidene fluoride (PVDF) has conventionally been used as a binder for both composite cathodes and anodes. However, the more demanding requirements for silicon composite electrodes of expansion/contraction, low conductivity and unstable SEI formation quickly proved PVDF an inferior binder for this use. This can be attributed to a number of factors: PVDF can only interact with silicon particles via comparatively weak van der Waals forces. PVDF swells up to 20% in carbonate solvent, I, Luzinov and G, Yushin found that upon swelling PVDF has small resistance to plastic and elastic deformations, making unsuitable for volume change electrodes.[33]

As a replacement for PVDF the aqueous soluble Carboxymethly cellulose (CMC) has been explored with a significant literature presence. Historically CMC has been paired with the plasticiser styrene butadiene rubber (SBR) to increase elasticity and accommodate swelling in silicon anodes [34],[35]. However, purely CMC as a binder was discovered to give increased electrochemical performance compared to SBR-CMC combination and PVDF. It was shown that this purely CMC binder favours a more homogeneous distribution of carbon conductive additive and facilitates a more efficient networking process between the silicon and carbon particles. This was explained as due to CMCs extended conformation in solution and adsorption to Si and carbon particle surfaces, this enables the formation of bridges between particles. Upon drying this 3-D interconnected network can better withstand repeated expansion/contraction due to reversible hydrogen bonding between CMC carboxylic acid groups and particle surfaces displaying ‘self-healing’ like properties [36],[37]. The discovery of covalent linkage between binder carboxylic acid groups and silicon surface lead to studying the effect lowering the pH of slurry solution below the isoelectric point of silicon particles (3.5) and the pka of CMC (3.5) favouring esterification upon drying which greatly increased cycle life.[38],[39]

Until recently CMC was considered the state-of-the-art binder for silicon electrodes and a wide range of studies have investigated its various properties. For more information the reader is directed to D. Mazouzi et al, review paper [37]. With a better understanding of the role of binders in silicon anodes for lithium-ion batteries binders with similar characteristics to CMC were explored. [33],[40]

1.2 A Review of magnesiothermic reduction of silica to porous silicon for lithium-ion battery applications and beyond.

Much of the discussion and experimental data from this section can be found in the publication J. Entwistle, A. Rennie, S. Patwardhan, *J. Mater. Chem. A* **2018**, *6*, 18344'

1.2.1 The role of porous Silicon

Porous morphologies can potentially address the challenges of volumetric expansion and slow lithium diffusion. Porous silicon can expand into its own pore volume, thus limiting stresses on the material. Stress generation upon lithiation has been modelled for lithium insertion materials[41],[42] which in turn have been applied to models of lithiation in porous silicon structures.[41],[42],[21] A comparison of hollow and solid amorphous silicon nanospheres of the same silicon volume modelled by Yao et al showed the maximum tensile stresses experienced by a hollow sphere is significantly lower vs lithiation time, 83.5 vs 449.7 MPa respectively (Figure 1.4(A)).[44] M. Ge et al simulated the effect of pore size and porosity in the range of initial pore sizes 1-9nm, showing lower porosities lead to higher induced stress and smaller pore sizes result in higher maximum hoop stresses around the pore (Figure 1.4(B)).[43] X.Li et al have also show a linear decrease in porous particle volume change by increasing the void volume fraction for materials containing 10 and 25nm radius ordered pores. Figure 1.4(C) shows that increasing the void fraction to 60% should keep overall particle expansion within the narrower volumetric expansion range of 75 to 150%.[21]

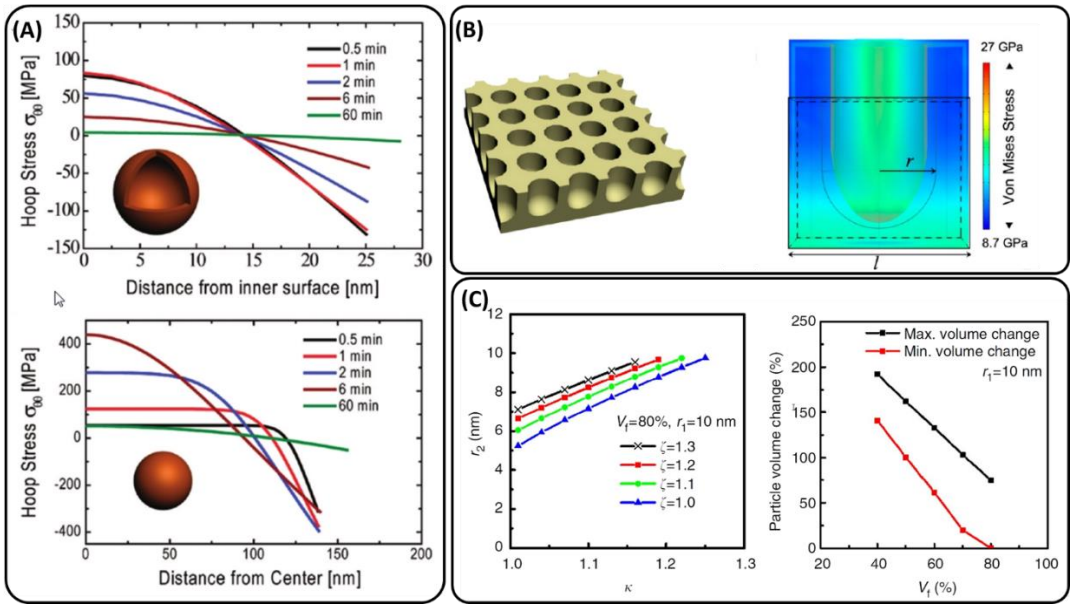

Figure 1.4. (A)Yao et al. stress evolution during lithiation in a hollow sphere vs a solid sphere with the same volume of silicon. Positive stress values are tensile stress, while negative are compressive. [44] **(B) Schematic of porous structure modeled by M. Ge et al with cross section analysis of stress generation under lithiation.**[43] **(C) X.Li et al expansion rates of mesoporous particle along radial direction (κ), axial direction (ζ) and pore radius after lithiation (r_2). Particle volume expansion versus void fraction (V_f).**[21] [18]

Porous silicon with high surface area can increase accessibility of electrolyte to silicon surfaces, shortening lithium diffusion lengths and increasing available capacity at higher rates. Porous structures with thin walls and silicon substructures can shorten the diffusion length of lithium within silicon. Polycrystalline porous structures with small silicon domains are hypothesised to have a higher resistance to fracture during lithiation similar to the observed strong size dependence of fracture of silicon nanoparticles [24]. In situ TEM observation has shown that the critical particle diameter for fracture in porous particles reaches 1520nm.[26] Additionally, in-situ TEM and dynamic simulation of lithiation behaviour of porous silicon particles found that the smaller domains of porous particles disfavour crystalline c-$Li_{15}Si_4$ phase upon full lithiation, providing a more favourable stress evolution on expansion (Figure 1.5).[26] Additionally, it was shown that these porous particles lithiated in an end-to-end fashion (Figure 1.5(e-h)), opposed to larger nanoparticles which lithiated in a surface-to-centre manner (Figure 1.5(a-d)).[26]

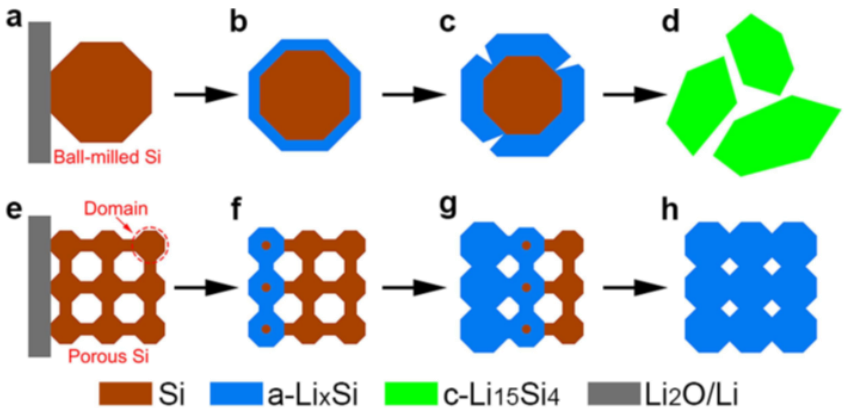

Figure 1.5 Schematic for the lithiation of ball-milled silicon and porous silicon nanoparticles. (a-d) Surface-to-center lithiation of ball milled silicon. (e-h) end-end lithiation manner of porous silicon particle.[26]

High surface area of porous silicon structures will however generate a larger SEI simply because of the increased electrode area in contact with electrolyte. This could be a significant drawback when coupled with the volume expansion of silicon and relative instability of the SEI.

1.2.1.1 Synthesis/Fabrication of Silicon

Worldwide annual production of silicon metal amounted to 8100 tons in 2015.[45] Industrial scale synthesis of metallurgical grade silicon is typically achieved by reduction of silica with carbon in electric arc furnaces at temperatures over 2000 ^{o}C.[46],[47] A common industrial method of refining metallurgical grade silicon is chemical vapour decomposition (CVD) Figure 1.6(b). CVD methods usually require reaction temperatures of 1100 ^{o}C in the presence of hydrogen gas. Producing the volatile silicon precursors needed also requires reaction with hydrochloric acid at 350 ^{o}C.[46] The other major refinement methods rely on crystallisation of molten silicon again requiring high temperatures >1414 ^{o}C to achieve molten silicon, Figure 4(a). The development of environmentally friendly, low cost and scalable production processes for high performance silicon anodes is essential.

There has been great progress developing silicon anodes with a wide range of nano structuring techniques being employed and extensively reviewed elsewhere.[3],[46],[49],[50] High capacities and good cyclability have been demonstrated using nanoscale silicon anode structuring.[3],[46],[50] Porous silicon structures have also been reviewed by Ge et al.[49] However, nanoscale engineering often requires a high degree of precision synthesis and can involve aggressive reaction conditions. Using energy intensive synthesis techniques will likely lead to high cost of materials and the inability to produce materials on an industrial scale.[51]

Magnesiothermic reduction can offer a facile method of bulk synthesis for porous silicon with varying degrees of structural control.[52] Figure 1.6 highlights the benefits of this single step reduction method from silica to silicon in comparison to existing technologies.[53] This review collates available literature concerning the influence of reaction conditions on the magnesiothermic reduction reaction as well as highlighting gaps in current understanding. The use of porous silicon produced through magnesiothermic reduction as an active material for anodes in LIBs is the focus of this review, but potential applications may be much further ranging with impact in fields such as photoluminescence,[54] solar power,[55] photocatalysis,[56] drug delivery[57][58] and catalysis support.[59]

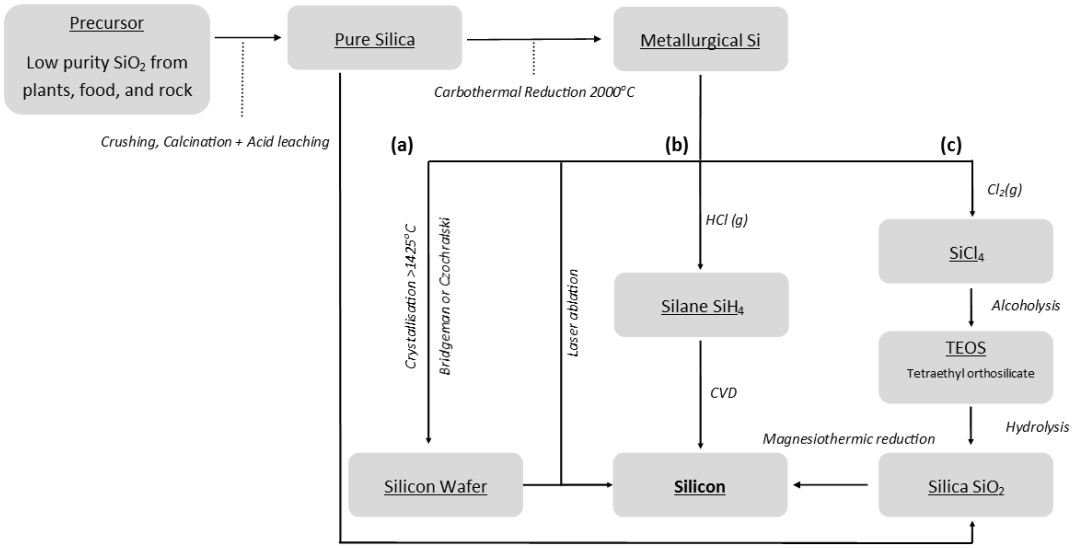

Figure 1.6. Flow chart of existing bulk silicon synthesis routes including magnesium reduction. [18]

1.2.2 Magnesiothermic Reduction

Magnesiothermic reduction of silica has the potential to produce porous silicon materials at lower temperatures than conventional silica reduction methods.[60] As the melting point of silicon is 1414 °C carbothermal reduction at 2000 °C is not suitable for maintaining silica template structure to give silicon pseudo morph analogues. Magnesiothermic reduction has been demonstrated to produce silicon structures from silica in the temperature range of 500-950 °C, permitting template assisted design on silicon structures. This method has shown the ability to preserve intricate features in the silicon produced as small as 15 nm.[61] The high diversity and robust understanding of silica chemistry allows for the possibility of creating a wide range of silica template structures with tailored geometries. This reduction entails the reaction of magnesium with silica resulting in an interwoven composite product of magnesia (MgO) and silicon (Equation (1.5)).

$$SiO_2 + 2Mg \rightarrow Si + 2MgO \qquad \text{Equation 1.5}$$

Magnesia is easily removed with HCl, leaving a silicon replica behind that possesses a higher surface area then the starting template. Figure 1.7 summarises the two step reduction-etching process. The interwoven nature of this morphology is crucial to allow the removal of magnesia in this way. The formation of the interwoven aggregate morphology of product Si and MgO is thought to relate to the stability of the reaction interface and flux of reactants across the product phases.[62]

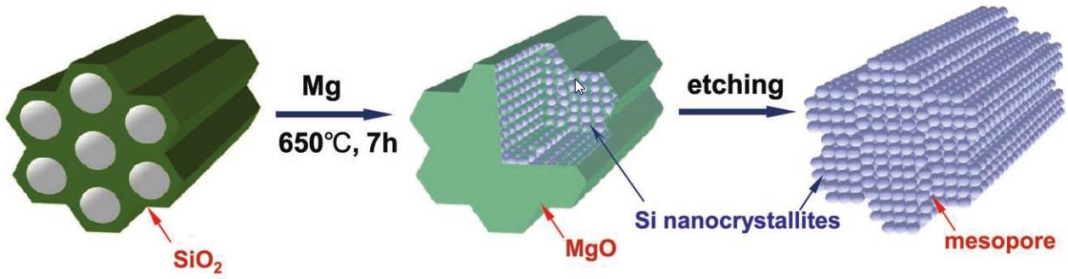

Figure 1.7. illustration of the Magnesiothermic reduction process to produce porous silicon from silica.[63]

The Gibbs energy of magnesiothermic reduction is negative for the entire temperature range 0-1000 ^{o}C this indicates that the reaction is exergonic. [64],[65] The enthalpy of Equation (1.5) is exothermic and has significant ramifications discussed below.[65] The melting point of magnesium is 650 ^{o}C, and the vapour pressure of Mg at 428 ^{o}C is 1Pa. This enables solid the magnesium and silica to be placed separately in the reaction vessel and the magnesium gas to either diffuse to reduce the silica and/or liquid magnesium to flow over the silica.[60],[66]

It is important to note the side reaction which can reduce the yield of silicon through the formation of magnesium silicide (Mg_2Si) (Equation (1.6)). A number of studies when placing the magnesium and silica separately and relying on the gas-solid type reaction, report the silica close to the source being reduced to Mg_2Si, a middle region forming Si, with further displaced sample showing no reduction and remaining as SiO_2.[60],[64],[66],[67] Mg_2Si formation reduces the yield of the reaction and affects product morphology upon removal which occurs simultaneously to MgO removal in the HCl wash. Mg_2Si is not thermodynamically stable in the presence of SiO_2 therefore its formation is due to kinetic limitations.[68] Silanes are produced by the reaction of magnesium silicide with acid. These react spontaneously with air.

$$Si(s) + 2Mg(g) \rightarrow Mg_2Si\ (s) \qquad \text{Equation 1.6}$$

Figure 6 displays key reaction variables with respect to the stages of reaction. Below we aim to summarise and evaluate critically the literature findings (Supporting Information Table S1 displays in detail the key parameters identified in the literature).

A number of challenges remain in the development of a controllable magnesiothermic reduction method for porous silicon production. Primarily the preservation of silica template morphology in the silicon analogue, which underpins the rationale of the method. Another challenge is control over the extent of reaction to fully reduce the silica avoiding the need for the undesirable process of HF etching, while simultaneously maintaining silicon yield by avoiding over reduction to form Mg_2Si.

In order to design the porous silicon product that is desirable for anode applications, the feedstock and the process parameters governing the magnesiothermic reduction process and their effects on the properties and performance of silicon should be understood. In Chapter 3 we investigate these key features and their effects on the product silicon.

As evident from the foregoing, a truly comparative literature review is difficult as most studies reduce just one specific silica material under a set reaction condition and report a limited number of variables. Magnesiothermic reduction reaction conditions are not all comparable from one study to another. As a result, the silicon product morphology can vary for the same silica templates between studies.

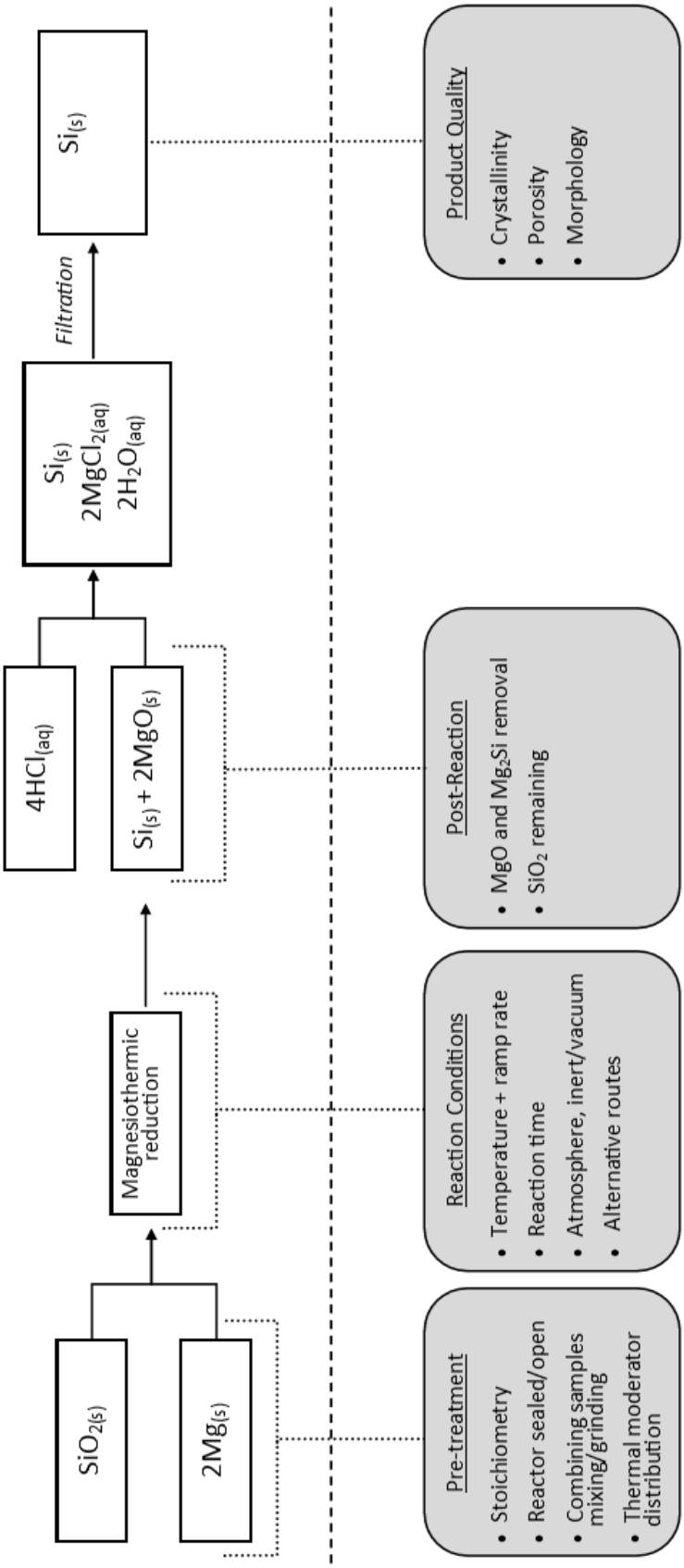

Figure 1.8. Scheme outlaying the magnesiothermic reduction and summary of key design factors for consideration. [18]

1.2.3 Reduction conditions

The key control parameters for the reduction reaction are; reaction time, temperature and temperature ramp rate, reactant proximity and morphology, and molar ratio of reactants. Conventionally the magnesiothermic reduction is carried out under a flowing 95% Argon or a nitrogen atmosphere, although some studies have performed the reduction under vacuum to promote a higher vapour pressure of magnesium.[69],[70],[71] Another source of magnesium gas can also be achieved from volitasation of Mg_2Si.[72],[73] All these parameters have significant effects on the silicon product. However, a comprehensive study on the effect of reaction conditions on the product properties is lacking from the literature. In the section below we aim to highlight key studies where quantitative conclusions can be drawn between reaction conditions and product silicon properties.

1.2.3.1. Ramp Rate

It has been shown the heating rate can strongly affect the silicon product morphology. This is due to the large negative enthalpies of the reduction reactions resulting in a large amount of heat being released in local areas. The faster ramp rate does not allow sufficient time for heat to dissipate through the sample, thus local temperature increases can accelerate nearby reactions. The high temperatures associated with fast ramping can cause fusion of silicon products and the loss of small pores. Additionally, the silicon formed can coat and fuse around MgO phases with two significant effects: it leaves some MgO in the final product that cannot be etched as it is fully coated by silicon and the MgO which can be etched, creating a macro porous silicon network in its place (typically 200-300 nm porous structure). Therefore, slower heating rates are typically employed. For lager batch sizes more heat energy is produced and heat transfer issues can be more pronounced.

Liu et al [66] studied the effect of temperature ramp rate up to 650 ^oC and in a closed type reactor of Mg powder and rice husk derived silica (Specific Surface Area, SSA 289 m^2/g, and Specific Pore Volume, SPV 0.45 cm^3/g). They compared the difference between 5oC/min and 40 ^oC/min heating rate on the morphology of the silicon produced from magnesiothermic reduction. The higher ramp rates of 40 ^oC/min produced mainly macroporous silicon particles with SSA of 54 m^2/g and negligible pores below 20nm. While the material produced at 5 ^oC/min gave partially interconnected mesoporous silicon nanoparticles with SSA 245 m^2/g. The 5 ^oC/min sample had significant porosity around 10nm width similar to the template, and pores in the 20-30 nm range which contributed to the increase pore volume to 0.74 cm^3/g.

Liu et al validated this study with Thermal Gravimetric Analysis (TGA) and Differential Thermal Analysis (DTA) showing a strongly exothermic reaction occurring at 400-450 ^{o}C. As no significant reaction occurs below 400 ^{o}C, quick ramping can be used to reach this point. Further decreasing heating rate below 5 ^{o}C/min does not decrease particle size or crystallinity of obtained particles. Upon scaling reaction volume up to 5 g, 1 ^{o}C/min heating rate was used.

Consistently the study of Shi et al[74] investigates the effect of heating rate on silica derived from rice husks at 5, 3 and 1 ^{o}C/min for a 4 g reaction volume where substantial effect on morphology was observed. The higher rates were observed fuse silicon particles together and remove micropores, in turn decreasing pore volume and surface area. Only the sample product at 1 ^{o}C/min was slow enough to prevent significant changes in the morphology. An XRD study on the heating rate effect also confirmed the formation of larger crystallite sizes for MgO and Si at faster ramping rates.[66],[74] Higher ramping rate also increase the presence of Mg_2Si as discussed in section 1.2.3.2.

Shi et al[74] also found that faster ramping rates and the associated heat accumulation lead to increased Mg_2SiO_4 formation, in this case the runaway kinetics of the faster ramping rates could have caused local mismatches at the SiO_2/Mg interface leading to more Mg_2SiO_4 formation, further discussed in section 1.2.3.4.

1.2.3.2. Temperature

The exothermic nature of the reaction means that true reaction temperature can be higher than the set experimental value. If the reaction temperature approaches the melting point of silica ≈1700 ^{o}C or silicon 1414 ^{o}C, then significant effects on morphology can be expected. The large quantity of heat released from the exothermic reaction can collapse the architectures of the silica precursors or silicon products causing agglomeration of the silicon domains into larger crystals.

$$SiO_2 + Mg_2Si \rightarrow 2Si + 2MgO \qquad \text{Equation 1.7}$$

Barati et al[71],[55] report that between 750 ^{o}C and 950 ^{o}C, temperature has little effect on Si yield. However, they reported that when Mg stoichiometric ratio is increased above 2:1 then higher temperatures yield more silicon. It is shown that at 750 ^{o}C significantly more Mg_2Si was produced than 950 ^{o}C (discussed below section 2.2.4). This affect is attributed to higher temperatures accelerating the kinetics of the solid state reduction of SiO_2 by Mg_2Si, as described in equation (1.7). This solid state

reduction is diffusion controlled so longer times and higher temperatures favour equation (1.7) and increase silicon yield.[55]

In addition, Xie et al[75] show that Mg_2SiO_4 formation can be reduced by increasing reaction temperature from 700 ^oC to 900 ^oC. Increasing reaction temperature increases Mg vapour pressure and hence concertation at SiO_2/Mg interface favouring MgO formation over Mg_2SiO_4.

Recent study has shown that the surface area and pore volume decrease as reaction temperature is increased between 500 ^oC and 800 ^oC an increase in average mesopore diameter is observed. This effected is determined to be from a higher degree of structural damage of the template at higher temperatures.[76]

1.2.3.3. Reaction Time

Reaction time for reduction varies between studies with durations reported from 30 minutes[69] up to 12 hours.[75],[77] The appropriate reaction time is dependent on many variables and should be deduced based on the effect towards product morphology and yield. For a particular experimental setup the silicon yield as a function of reaction time has been shown to plateau for longer times above 2 hours, indicating the reaction reaches completion. Sufficient time to reach completion should be determined for maximum silicon yield.[68]

A study into reaction temperature and time by Lui et al[64] was conducted on a nonporous silica of bundled nanowires. They report intuitively that higher temperatures lead to silicon at lower reaction times. Interestingly, by initiating the reaction at 600 ^oC then reducing to 400 ^oC crystalline silicon formed, whereas at 400 ^oC reaction temperature no silicon was observed even with ‘overnight’ reaction times. The onset of the reduction reaction has been reported between 400-540 ^oC (depending on silica source)[66],[55] explaining the need for this initiation temperature.

The study by H. Wu et al[70] found reaction times of 2 and 5 hours had little effect on morphology of product silicon and more so the state of magnesium, gaseous or liquid, during reaction. Promotion of the gaseous state of Mg is achieved by applying a vacuum to the reaction.[70] This could however further indicate the reaction reaching an equilibrium state in under 2 hours.

1.2.3.4. Molar ratios

Increasing the relative molar ratio of Mg:Si above the stoichiometric level of 2:1 decreases the silicon yield by increasing the formation of Mg_2Si. XRD quantitatively showed that an excess of magnesium of 5 wt% (2.1:1 Mg:SiO_2 stoichiometry) gave the maximum yield of silicon.[71],[55]

Magnesium silicate Mg_2SiO_4 has been detected in a number of XRD studies, Mg_2SiO_4 is not easily removed with HCl, therefore it will affect the silicon product properties. Insufficient Mg at the SiO_2/Mg reaction interface also favours Mg_2SiO_4 formation.[55] This is supported by Chen et al[78] where increasing the Mg molar ratio reduced the formation of Mg_2SiO_4 even at relatively low temperatures.

1.2.3.5. Mixing and Thermal Moderators

Although 'mixing' is a rather ambiguous term, homogenous distribution of reactants ensuring minimal diffusion lengths for reaction is advantageous for magnesium reaction with silica. In two studies using rice husk derived silica, operating at 650 ºC, the dispersion and mixing of reactants showed dramatic effects on Si yield.[66],[74] No remaining silica was observed with the yield of 64 %. This indicated a significant amount of Mg_2Si was formed when grinding was used to reduce sizes and mix the reactants. When the reactants were used without any mixing, overall yield was low at 4.2 wt% suggesting a significant portion of the SiO_2 remained un reacted. It is noted that the study with 'grinding' used 2 h reaction vs 7 h of non-grinding. Still resulting in higher yield. These results arise from the poor distribution of reactants highlighting the need for thorough mixing. Increasing the magnesium grain size from fine powder (-325 Mesh), chips (4-30 Mesh) and foil have shown to decrease the reduction rate, caused by improper mixing of the reactants.[76]

Mixing of the reactants in a ball milling process can provide enough kinetic energy to reach the reaction ignition point, and has been used to perform the magnesium reduction. This method has also been scaled up to a 5 litre scale in an attrition mill.[79] Care should therefore be taken if using milling to mix reactants pre reduction reaction. Ball milling reduction has also been applied to Aluminothermic reduction process which is discussed further below.[80]

The heat released during reaction requires lower ramping rates for larger batch sizes as there is more heat accumulation in these reactors.[66] Batchelor et al[81] demonstrated the production of mesoporous silicon from biosilica sources on a 30 g

reaction scale. The key to this larger batch size was the use of thermal moderator, sodium chloride (NaCl), which prevents silicon particles sintering together. Luo et also report the use of NaCl as a heat scavenger in the reduction reaction which showed the ability to better maintain diatom biosilica structure in the reduced form. Crystallite size was also reduced as a result of reducing reaction temperature.[67] More recently Miao et al. have shown that other salts such as KCl may provide better heat scavenging properties over the traditionally used NaCl.[82]

As reaction temperature begins to rise above the set temperature, NaCl melts at 801 ^{o}C, consuming the excess heat due to its high enthalpy of formation. Luo et al[74] ground Mg and SiO_2 together, reacting in a sealed vessel for a batch size of 1.9 g, typical of many reported synthesis routes. Without thermal mediators they reported true reaction temperatures above 1300 ^{o}C, and with their mediators the temperature was kept between 840-1100 ^{o}C. Greatly increasing the ratio of NaCl was unable to keep the reaction temperature below 801 ^{o}C as the method is limited by the degree of mixing between NaCl and silica. Others have shown more elaborate NaCl surface coating of silica to be beneficial.[76],[77] The addition of NaCl has also been reported to reduce the presence of Mg_2Si in the product silicon.[85]

1.2.3.6. Crystallite Size

The crystallite size (coherent scattering domain size) can be determined from XRD patterns using the Scherrer equation and or by TEM.[86] For LIB anode applications it is thought reduction in the crystallite size will reduce lithium diffusion lengths potentially increasing the charge/discharge rate capabilities. The strongest driver for increasing crystallite size is an increase in reduction temperature and then reaction time. Higher temperatures and longer reaction times provide more energy input resulting in sintering of silicon crystallites.[87]

Interestingly Xing et al[88] report smaller crystallite sizes (19.9 nm) when the silica template contained more porosity and higher surface area. This is attributed to the hindering of mass transport during heat treatment retarding the coarsening of the silicon crystallites. Silica feature size affects the crystallite size formation with smaller features leading to smaller silicon crystallites. A lower limit of ~13 nm has been suggested for crystallite size relating to the critical nucleation size for silicon under typical reduction conditions (675 ^{o}C 2 h).[61] However, for smaller template features the smallest crystallites sizes of 4 nm have been reported.[86]

Magnesia removal is attributed to the increase in pore volume upon HCl etching. Conclusions have been drawn from MgO crystallite size before etching and the introduction of pore volume in an attempt to correlate MgO crystallite size and pore diameter. However a direct correlation has not been found.[87],[88]

1.2.3.7. Non-conventional Reduction routes

The study by Liang, et al [89] demonstrates a novel 'Deep Reduction and Partial Oxidation' two-step pathway to produce mesoporous silicon structures, shown in Figure 1.9. The study relies on the deliberate production of Mg_2Si and MgO then partial oxidation described in (4-5).

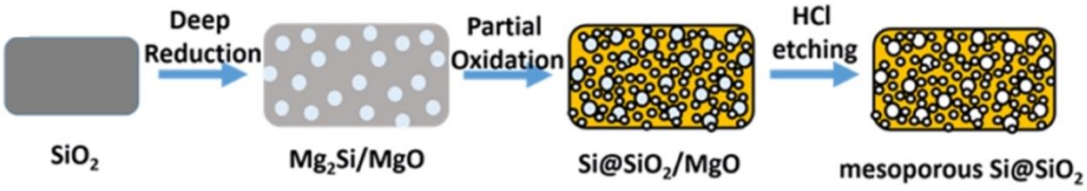

Figure 1.9. Schematic illustration of the deep reduction and partial oxidation process Reprinted with permission from.[89] Copyright (2016) American Chemical Society.

$$4Mg(g) + SiO_2 \rightarrow 2MgO + Mg_2Si \qquad \text{Equation (1.8)}$$

$$Mg_2Si + O_2 \rightarrow 2MgO + Si \qquad \text{Equation (1.9)}$$

They further optimised the oxidation time and temperature in ref [90]. Using commercial silicon they produced a 'nanoporous' high surface area product with a significant batch size (10 g of product) with a yield above 90 %. An excess of Mg to Si at 500 ^{o}C for 10 hours, propagated the Mg_2Si intermediate formation which in a second step was oxidised in air. Bulk silicon oxidation was not significant below 800 ^{o}C, but a surface SiO_2 layer was produced. This reduction method, with high yield and control on converting Mg_2Si, could have a great potential for silica reduction. The formation of surface oxide is partially credited with improved cycle life by potential of improving the quality of SEI layer formed. This is consistent with similar literature studies.[17],[84]

A twostep synthesis used by Choi et al[93] was demonstrated where first aluminothermic reduction (Equation(1.10)) at 900 ^{o}C, then subsequent magnesiothermic reduction at 700 ^{o}C of diatom silica produced porous silicon

(Equation (1.11)). The two steps involved in this synthesis each have lower Gibbs energies which avoided heat accumulation during reduction.[65] By controlling the stoichiometry in the magnesiothermic reduction, varying amounts of Al_2O_3 remained in the product. Retaining Al_2O_3 in the final product reportedly improved cycle life of the silicon materials aiding stable SEI formation and buffering volume expansion similar to that reported by J. Liang, et al[89] Since Al_2O_3 does not contribute to the capacity of the electrode, the specific capacity of the material was reduced.

$$3SiO_2 + 4Al \rightarrow 2Al_2O_3 + 3Si \qquad \text{Equation (1.10)}$$

$$Al_2O_3 + 3Mg \rightarrow 3MgO + 2Al \qquad \text{Equation (1.11)}$$

Expanding the field of metallothermic reduction, Lai et al [76] combined aluminothermic and magnesiothermic reduction into a one-step syntheses route. A eutectic mixture of 70 % Magnesium and 30% Aluminium is used as the reductant allowing for reduction to proceed at 450 ^{o}C. Of potential importance for Lithium-ion battery applications the silicon formed from this method is amorphous.[25]

1.2.4 Precursor Silica

A wide range of biological and synthetic silica sources are available and have been reduced via magnesiothermic reduction for LIBs. Both sources, as shown in Supporting information Table S1, have the ability to produce porous silicons with a variety of pore properties. It should be noted that biologically derived silica such as rice husk and bamboo silk requires the removal of organic components and commonly needs acid leaching of metal impurities. The synthetic silica sources can be equally time consuming as well as resource and energy intensive to produce (see Figure 4(c)). In the strive to produce battery materials in a more economical and environmentally friendly way, the choice of silica template is also significant.

Table S1 summaries key parameters of silica before and silicon after reduction where this data was available. In general, many of the reductions produce mesoporous silicon with a range of surface areas between 24-350 m^2/g and pore volumes 0.11-1.1 cm^3/g. Interestingly these mesoporous properties also appear in samples which initially were non-porous such as sand[85][94] and silica spheres[75][76][58]. In these cases the nature of the silicon-magnesia interwoven aggregate introduces porosity to the structure through the removal of the magnesia phase. The same effect is seen on non-porous starting silica/silicon used in the 'deep reduction partial oxidation' method.[90],[89] It appears that when overall template morphology is maintained, and if reaction temperatures can be controlled sufficiently below silicon melting point pores in the mesopore region and overall pore volumes will increase irrespective of the porosity of the precursors. This is somewhat expected as the magnesia phase occupies ~65% of the volume in the product structure and oxygen is being removed from the initial template.[72]

Rice husks have been reduced by magnesiothermic reduction in a number of studies.[66],[74],[88],[87],[95] Table S1 shows how initial rice husk precursors have similar SSA and pore volumes, however the purity of the silica varies. Where reported, pore volumes increase in all studies with surface areas remaining similar or lower than the starting silica, with the exception to reference [87] where surface area and pore volume are dramatically decreased from 234 m^2/g to 42 m^2/g and 0.43 cm^3/g to 0.31 cm^3/g. In this study the lower reaction temperature of 500 ^oC may contribute to these pore properties not following the trend. Note this is below the onset temperature reported at 540 ^oC by Larbi et al[55] who also reduced silica rice husk. This example highlights the lack of understanding in the evolution of magnesiothermic reduction reactions. Additionally, this shows how specific factors in each case can also contribute to

significant variation in product properties, these factors include furnace design, crucible design and packing and mixing of reactants.

Table S1 identifies a number of examples where the magnesiothermic reduction conditions have had a much greater effect on silicon morphology than the template used.[70],[96],[97] Kim et al[98] utilised a change of morphology to give their desired structure; when they reduced a vertically aligned mesoporous silica to give 10nm silicon nanoparticles dispersed on graphene sheets. Similarly, S. Zhu and L. Wu utilised magnesiothermic reduction to produce silicon nanoparticles on graphene sheets.[99],[100] Although not initially the function of this method it has proven to produce novel materials with good properties for lithium-ion battery applications and potentially beyond.

1.2.5 Summary

In this review it has been clearly shown how individual reaction parameters can affect the silicon product properties. In reality the interplay of reaction parameters with each other may add more complexity to the relationship between reaction conditions and product properties. However, the scientific understanding of the key parameters collated above should be able to provide valuable insight the importance of reaction conditions on product properties. Table 1.3 below summarises the key effects of ramp rate, temperature, time and molar ratio.

Table 1.3.Summary of reaction variables and reported effects on Magnesiothermic reduction reaction.

Experimental factor	Reported Range	Reaction consequence
Ramp Rate	1-40 ^{o}C/min	Magnesium reduction has severe heat accumulation raising temperature above silicon melting point has strong dependence on ramp rate and batch size. Severe heat accumulation associated with faster ramp rates and larger batch sizes has shown across studies to produce a macroporous silicon product. This product does not maintain silica template structure and typically has lower surface area and pore volume compared to silicon's produced at lower ramp rate Slower ramping rates mitigate heat accumulation and are increasingly necessary for larger batches Heat Scavengers such as NaCl have shown to be beneficial at limiting heat accumulation allowing faster ramp rates
Reaction temperature	500-900 ^{o}C	Heat accumulation may lead to true reaction temperatures higher than set conditions. The onset of reduction occurs between 400-540^{o}C Higher temps have been shown to decrease Mg_2Si and Mg_2SiO_4 formation increasing silicon yield Higher temperatures and longer reaction times are the drivers for increasing silicon crystallite size
Reduction time	0.5-12 hours	Silicon yield has been shown to plateau beyond reaction times of 2 hours Reduction time has scope for further optimisation as it has been indicated the reaction can be initiated at higher temperatures then greatly reduced until competition
Molar Ratio	1.5-3	If ratio of less than stoichiometric amount, 2:1 Mg:SiO_2 silica remains in product Slight excess Mg gives higher silicon yield Further increasing magnesium molar ration decreases Mg_2SiO_4 formation but increases in Mg_2Si formation

A wide variety of silica precursors have been studied through Magnesiothermic reduction. By reviewing the relevant literature, under circumstances where the heat accumulation has been mitigated the reduction of silica will introduce mesopores into the silicon product and increase overall pore volume. This is observed for precursors which initially have micropores, mesopores and even for non-porous precursors. A strong indication that heat accumulation in the reaction has approached or exceeded the melting point of silicon is a typical macroporous product with spherical pores around 200 nm.[70],[66] These two affects can be described by the nature of the interwoven aggregate silicon/magnesia product phase. At lower temperatures smaller magnesia phases (in the mesopore size range 2-50 nm) are formed interwoven with silicon, with elevated temperatures causing the aggregation of magnesia crystallites into larger grains (in the macropore range ~200 nm).

1.2.6 Anode Performances

The studies using rice husks as a silica source presented in Table 1.4 are examples of how varying magnesiothermic reduction conditions (Supporting information Table S1) can greatly affect SSA and pore volumes of the silicon product. In general the lower surface areas and pore volumes result in lower capacities and poorer capacity retention. [66],[87],[88] The example of rice husk reduction from Lui et al[66] shows the benefits of porous silicon, with high stable capacity of 1750 mAh/g and reasonable capacity retention over 300 cycles. Although factors such as electrode composite and electrolyte additives also likely played a key role in performance parameters. Interestingly the best performing rice husk derived silicon electrode were formed using Polyvinylidene fluoride (PVDF) binder; which has previously been shown to be inferior for silicon [33],[101]. The high porosity of these samples is likely to limit the overall particle expansion, as discussed in section 1.2, negating the need for the more flexible binders.

SBA-15 is a silica with mesopores, a biphasic system of ordered hexagonal arrays of pores.[102] A number of studies have used a magnesiothermic reduction method with SBA-15 to achieve ordered mesoporous silicon for anodes [63],[78],[89]. The SBA-15 used is either produced in house [63] or purchased from different suppliers [78],[89],[57] introducing some discrepancies between studies. The best performing SBA-15 silicon analogue is reported by Jai et al[63] especially when considering the fast charging rates shown in Figure 1.10(c). The lower surface area and larger pore diameters could perhaps be responsible for this success, as it favours less SEI formation and larger pores experience smaller stresses on expansion. This material performs well at 1500 mAh/g for 100 cycles with 94.4% capacity retention when using a carbon coating (Figure 1.10 (b)). In this case the porous silicon is coated with a 4nm layer of amorphous carbon via chemical vapour deposition filling some pores and decreasing surface area. With the carbon coating negating the negative effects of increased silicon surface area causing excessive SEI formation, it can be seen that this mesoporous material has very attractive properties for LIB applications. A number of studies demonstrate the attractive properties of combining carbon coating and porous silicon in this manner.[75],[103],[104],[105],[106]

Table 1.4. Various mesoporous silicon materials with SSA, pore size distribution and pore volume data when available. Performance parameters of silicon as an anode material. For further detail see Supporting information Table S1. [18]

Silica Source	Silicon Properties BET Surface area, Pore volume	Anode Performance
Rice Husks [66]	245 m^2/g Mesoporosity 0.74 cm^3/g	1750mAh/g @2.1 A/g 300cycles 86% capacity retention
Rice Husks [88]	150 m^2/g Mesoporous 0.60 cm^3/g	1600mAh/g @1.0 A/g 100cycles 76% capacity retention
Rice Husks [87]	42 m^2/g Mesoporous 0.31 cm^3/g	1400mAh/g @0.08 A/g 50 cycles 65% capacity retention
SBA-15[63]	74 m^2/g Mesoporous 28nmAPD 0.56 cm^3/g	2727 mAh/g @4.2 A/g 100cycles 53% capacity retention
SBA-15[89]	103 m^2/g Mesoporous Majority 4-16 nm	≈1300 mAh/g @0.36 A/g 100 cycles 77% capacity retention
Diatom[89]	74 m^2/g Mesoporous ≈ 30 nm Average pore diameter (APD)	≈1400mAh/g 0.36 A/g 100 cycles 71%capacity retention
Sand[89]	23.9 m^2/g Mesoporous ≈30 nm APD	≈1782mAh/g @0.36 A/g 100 cycles 82% capacity retention
Aerogel [89]	239 m^2/g Mesoporous 4 nm pores	1782 mAh/g @0.36 A/g 100 cycles 82% capacity retention

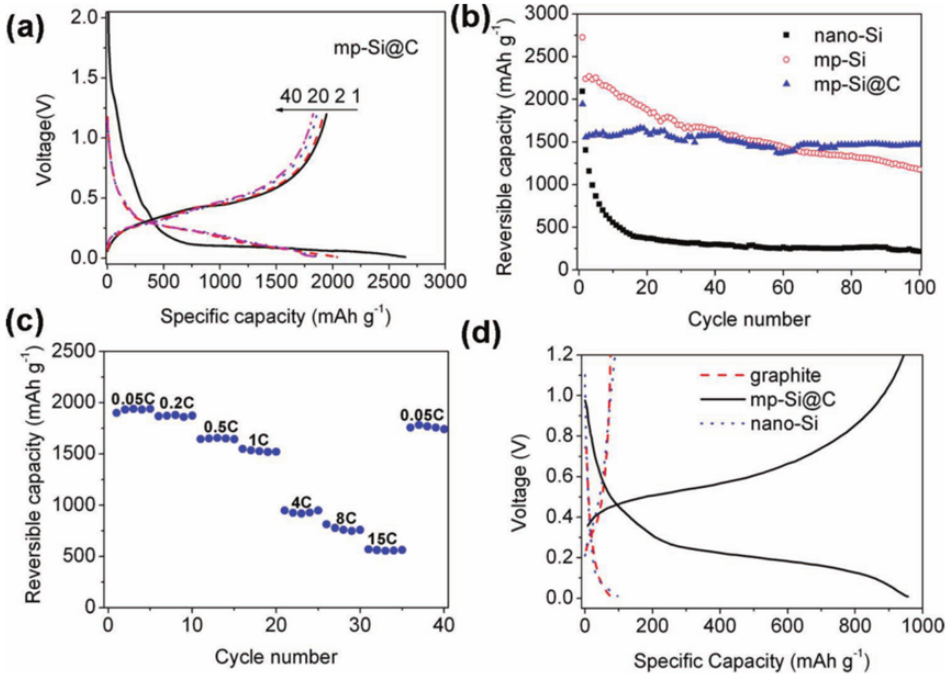

Figure 1.10 (a) voltage profile of mesoporous silicon particles with carbon coating (mp-Si@C). (b) cycling performance of mesoporous silicon (mp-Si), mp-Si@C and silicon nanoparticles (nano-Si). (c) Reversible capacities of mp-Si@C cycled at different current rates. (d) voltage profiles of mp-Si, nano-Si and graphite. [63][18]

The study of Liang et al[89] using 'deep reduction and partial oxidation' is an example for the comparison of the effects of various porous silicon structures on anode performance. The properties and performance of the four materials are summarised in Table 1.4. The two best performing materials are the reduced aerogel and sand. These two materials have the highest and lowest surface area of the four materials and the smallest and largest of the pore diameters respectively. This stands as an important example showing SSA and pore properties are not the only key parameters determining porous silicon's success as an anode material. Liang et al[89] report that the morphology of the SBA-15 and Diatom, which is an aggregation of isolated particles, adversely influence cycle life. The route created a 3nm passivation layer of silica over the surface of the porous silicon. The aggregation of particles is therefore not beneficial as ion and electronic conduction is hindered through silica layers. Post cycling TEM study of the Diatom, SBA-15 and sand silicon appears somewhat different to that studied by Shen et al[26] and Liu et al[66]. Further indicating that upon cycling these samples, with passivated silica layers, perform differently.

1.2.7 Challenges and Opportunities

It is clear that surface area and porosity do not completely govern the success of silicon for LIB anodes. For this reason, it is imperative that researchers publish detailed characterisations of material properties such as surface areas, pore volumes, pore size distributions, crystalline properties and particle morphology.

The evolution of pore structure in porous silicon during lithiation has not been studied in great detail. With the ability to see which pore structures are beneficial to improved performance, an in-situ or ex-situ method of evaluating pore structure vs cycle life would significantly improve understanding in this area. Such insight would give researchers the information necessary to use the versatile magnesiothermic reduction to provide these porous material properties on a bulk scale.

Cycling parameters and other testing variables such as electrolyte additives[15] and binders[101],[37] are well known to improve capacity and cycle life of silicon anodes. Testing criteria for the fabrication of electrodes and cells should be reported in detail. Equally as these variables have shown significant improvements in non-porous materials their effect on porous materials is still to be quantified.

Like for like comparison between reports may never be possible due to experimental inconsistencies. However, for better comparison in future, researchers should strive to publish porous silicon performance vs a silicon standard material.

1.3 Conclusion

Silicon has outstanding features as an anode material in LIBs, primarily it's high specific and volumetric energy density. The major drawback is hinged upon the large volume change associated with lithiation causing the reversible cycling capacity to be poor. The properties of porous silicon have been shown to be advantageous in increasing the capacity and extending cycling life. If performed effectively magnesiothermic reduction offers a relatively facile bulk synthesis route to porous silicon materials with morphological control over the silicon product.

Synthesis via magnesiothermic reduction has been shown to offer the possibility of using templated silicon analogues from the vast catalogue of synthetic and natural sources. This method provides an instrument to study the varying effect of porous silicon morphology on anode performance. The reduction is a highly exothermic reaction and efforts must be taken to avoid excessive rises in reaction temperature. A number of studies have shown slower ramping rates and thermal moderators can overcome excessive heat accumulation. Additionally, two step synthesis with lower enthalpies have been shown not only to avoid template destruction but provide oxide layers linked to improved cycling performance. The exothermic nature of the reaction means the true reaction temperature can be well above the set conditions, and reported in excess of 1300 ^{o}C. It can therefore be difficult to strictly control and study the effect of temperature on the reaction. The reports of initiating the reaction at higher temperatures then lowering the reaction temperature is interesting from both a control and efficiency aspect.

The magnesiothermic reduction template assisted method leads to a mainly mesoporous silicon product with a similar shape to the initial template, although mesopores can be introduced into samples even if the templating structure is non porous. To better understand the processes occurring under magnesiothermic reduction conditions studies should report in detail all the reaction criteria recommended above. Additionally, complete characterisation of both the reactant and product structures is needed to see how reaction conditions may affect different templates.

Key to assessing the effectiveness of porous silicon as an anode is understanding the evolution of porous structure during lithiation. Methods such as TEM have started to reveal these behaviours.[26],[89],[66],[107] More analysis of porous silicon would be a valuable addition to understand how pore structure evolves under cycling.

The high surface areas and pore volumes along with the nanocrystallite properties of magnesiothermically reduced silicon are advantageous for a number of additional applications. Fields such as photoluminescence,[54] solar power,[55] photocatalysis,[56] drug delivery,[57] and catalysis support.[59] Understanding the magnesiothermic reduction mechanism of producing porous silicon is crucial for the expansion of this technique. A clear design pathway should be identifiable form feed stock silica and to desired silicon properties.

1.4 References

[1] J. B. Goodenough, K. Park, *J. Am. Chem. Soc.* **2013**, *135*, 1167.

[2] M. Yoshio, R. Brodd, A. Kozawa, *Lithium-Ion Batteries*, Springer, **2009**.

[3] M. T. McDowell, S. W. Lee, W. D. Nix, Y. Cui, *Adv. Mater.* **2013**, *25*, 4966.

[4] R. Dash, S. Pannala, *Sci. Rep.* **2016**, *6*, 27449.

[5] H. Wu, Y. Cui, *Nano Today* **2012**, *7*, 414.

[6] R. Ruffo, S. S. Hong, C. K. Chan, R. A. Huggins, Y. Cui, *J. Phys. Chem. C* **2009**, *113*, 11390.

[7] N. Dimov, K. Fukuda, T. Umeno, S. Kugino, M. Yoshio, *J. Power Sources* **2003**, *114*, 88.

[8] K. Persson, V. A. Sethuraman, L. J. Hardwick, Y. Hinuma, *Phys. Chem. Lett.* **2010**, 1176.

[9] P. Yu, B. N. Popov, J. A. Ritter, R. E. White, *J. Electrochem. Soc.* **1999**, *146*, 8.

[10] M. D. Levi, D. Aurbach, *J. Electroanal. Chem.* **1997**, *421*, 79.

[11] J. Y. Kwon, J. H. Ryu, S. M. Oh, *Electrochim. Acta* **2010**, *55*, 8051.

[12] D. Ma, Z. Cao, A. Hu, *Nano-Micro Lett.* **2014**, *6*, 347.

[13] J. Li, J. R. Dahn, *J. Electrochem. Soc.* **2007**, *154*, A156.

[14] M. N. Obrovac, L. J. Krause, *J. Electrochem. Soc.* **2007**, *154*, A103.

[15] C. C. Nguyen, B. L. Lucht, *J. Electrochem. Soc.* **2014**, *161*, 1933.

[16] T. Yoon, C. C. Nguyen, D. M. Seo, B. L. Lucht, *J. Electrochem. Soc.* **2015**, *162*, A2325.

[17] K. Ogata, E. Salager, C. J. Kerr, A. E. Fraser, C. Ducati, A. J. Morris, S. Hofmann, C. P. Grey, *Nat. Commun.* **2014**, *5*, 3217.

[18] J. Entwistle, A. Rennie, S. Patwardhan, *J. Mater. Chem. A* **2018**, *6*, 18344.

[19] M. J. Loveridge, M. J. Lain, I. D. Johnson, A. Roberts, S. D. Beattie, R. Dashwood, *Nat. Publ. Gr.* **2016**, 1.

[20] M. K. Y. Chan, C. Wolverton, J. P. Greeley, *J. Am. Chem. Soc.* **2012**, *134*, 14362.

[21] X. Li, M. Gu, S. Hu, R. Kennard, P. Yan, X. Chen, C. Wang, M. J. Sailor, J. Zhang, J. Liu, *Nat. Commun.* **2014**, *5*, 1.

[22] L. Y. Beaulieu, S. D. Beattie, T. D. Hatchard, J. R. Dahn, *J. Electrochem. Soc.* **2003**, *150*, A419.

[23] M. N. Obrovac, L. Christensen, *Electrochem. Solid-State Lett.* **2004**, 93.

[24] X. H. Liu, L. Zhong, S. Huang, S. X. Mao, T. Zhu, J. Y. Huang, *ACS Nano* **2012**, *6*, 1522.

[25] M. T. McDowell, S. W. Lee, J. T. Harris, B. A. Korgel, C. Wang, W. D. Nix, Y. Cui, *Nano Lett.* **2013**, *13*, 758.

[26] C. Shen, M. Ge, L. Luo, X. Fang, Y. Liu, A. Zhang, J. Rong, C. Wang, C. Zhou, *Sci. Rep.* **2016**, *6*, DOI 10.1038/srep31334.

[27] M. N. Obrovac, L. Christensen, D. B. Le, J. R. Dahn, *J. Electrochem. Soc.* **2007**, *154*, A849.

[28] N. S. Choi, K. H. Yew, K. Y. Lee, M. Sung, H. Kim, S. S. Kim, *J. Power Sources* **2006**, *161*, 1254.

[29] A. L. Michan, M. Leskes, C. P. Grey, *Chem. Mater.* **2016**, *28*, 385.

[30] S. Zhang, M. He, C. C. Su, Z. Zhang, *Curr. Opin. Chem. Eng.* **2016**, *13*, 24.

[31] L. Chen, K. Wang, X. Xie, J. Xie, *J. Power Sources* **2007**, *174*, 538.

[32] M. Sina, J. Alvarado, H. Shobukawa, C. Alexander, V. Manichev, L. Feldman, T. Gustafsson, K. J. Stevenson, Y. S. Meng, *Adv. Mater. Interfaces* **2016**, *3*, 1.

[33] A. Magasinski, B. Zdyrko, I. Kovalenko, B. Hertzberg, R. Burtovyy, C. F. Huebner, T. F. Fuller, I. Luzinov, G. Yushin, *ACS Appl. Mater. Interfaces* **2010**, *2*, 3004.

[34] H. Buqa, M. Holzapfel, F. Krumeich, C. Veit, P. Novák, *J. Power Sources* **2006**, *161*, 617.

[35] W.-R. Liu, M.-H. Yang, H.-C. Wu, S. M. Chiao, N.-L. Wu, *Electrochem. Solid-State Lett.* **2005**, *8*, A100.

[36] B. Lestriez, S. Bahri, I. Sandu, L. Roué, D. Guyomard, *Electrochem. commun.* **2007**, *9*, 2801.

[37] D. Mazouzi, Z. Karkar, C. R. Hernandez, P. J. Manero, D. Guyomard, L. Roué, B. Lestriez, *J. Power Sources* **2015**, *280*, 533.

[38] N. Ding, J. Xu, Y. Yao, G. Wegner, I. Lieberwirth, C. Chen, *J. Power Sources* **2009**, *192*, 644.

[39] D. Mazouzi, B. Lestriez, L. Roué, D. Guyomard, *Electrochem. Solid-State Lett.* **2009**, *12*, A215.

[40] Y. Bie, J. Yang, Y. Nuli, J. Wang, *RSC Adv.* **2016**, *6*, 97084.

[41] J. Christensen, J. Newman, *J. Solid State Electrochem.* **2006**, *10*, 293.

[42] X. Zhang, W. Shyy, A. Marie Sastry, *J. Electrochem. Soc.* **2007**, *154*, S21.

[43] M. Ge, J. Rong, X. Fang, C. Zhou, *Nano Lett.* **2012**, *12*, 2318.

[44] Y. Yao, M. T. McDowell, I. Ryu, H. Wu, N. Liu, L. Hu, W. D. Nix, Y. Cui, *Nano Lett.* **2011**, *11*, 2949.

[45] N. Lebedeva, F. Di Persio, L. Boon-Brett, *Eur. Comm.* **2016**.

[46] J. O. Odden, G. Halvorsen, H. Rong, *Silicon Chem. Sol. Ind. IX* **2008**, 1.

[47] B. G. Gribov, K. V Zinov, *Inorg. Mater.* **2003**, *39*, 653.

[48] J. R. Szczech, S. Jin, *Energy Environ. Sci.* **2011**, *4*, 56.

[49] M. Ge, X. Fang, J. Rong, Chongwu Zhou, *Nanotechnology* **2013**, *24*.

[50] X. Su, Q. Wu, J. Li, X. Xiao, A. Lott, W. Lu, B. W. Sheldon, J. Wu, *Adv. Energy Mater.* **2014**, *4*, DOI 10.1002/aenm.201300882.

[51] D. Larcher, J.-M. Tarascon, *Nat. Chem.* **2015**, *7*, 19.

[52] G. Zhu, W. Luo, L. Wang, W. Jiang, J. Yang, *J. Mater. Chem. A* **2019**, *7*, 24715.

[53] P. T. Anastas, J. Warner, *Green Chemistry: Theory and Practice*, Oxford Univeristy Press Inc, **2000**.

[54] L. T. Canham, *Appl. Phys. Lett.* **1990**, *57*, 1046.

[55] K. K. Larbi, M. Barati, a McLean, *Can. Metall. Q.* **2011**, *50*, 341.

[56] F. Dai, J. Zai, R. Yi, M. L. Gordin, H. Sohn, S. Chen, D. Wang, *Nat. Commun.* **2014**, *5*, 1.

[57] M. Guo, X. Zou, H. Ren, F. Muhammad, C. Huang, S. Qiu, G. Zhu, *Microporous Mesoporous Mater.* **2011**, *142*, 194.

[58] Y. Lai, J. R. Thompson, M. Dasog, *Chem. - A Eur. J.* **2018**, *24*, 7913.

[59] J. Llorca, A. Casanovas, T. Trifonov, A. Rodríguez, R. Alcubilla, *J. Catal.* **2008**, *255*, 228.

[60] Z. Bao, M. R. Weatherspoon, S. Shian, Y. Cai, P. D. Graham, S. M. Allan, G. Ahmad, M. B. Dickerson, B. C. Church, Z. Kang, H. W. Abernathy, C. J. Summers, M. Liu, K. H. Sandhage, *Nature* **2007**, *446*, 172.

[61] E. K. Richman, C. B. Kang, T. Brezesinski, S. H. Tolbert, *Nano Lett.* **2008**, *8*, 3075.

[62] R. A. Rapp, A. Ezis, G. J. Yurek, *Metall. Trans.* **1973**, *4*, 1283.

[63] H. Jia, P. Gao, J. Yang, J. Wang, Y. Nuli, Z. Yang, *Adv. Energy Mater.* **2011**, *1*, 1036.

[64] X. Liu, Y. Gao, R. Jin, H. Luo, P. Peng, Y. Liu, *Nano Energy* **2014**, *4*, 31.

[65] S. Haouli, S. Boudebane, I. J. Slipper, S. Lemboub, P. Gębara, S. Mezrag, *Phosphorus, Sulfur Silicon Relat. Elem.* **2018**, *193*, 280.

[66] N. Liu, K. Huo, M. T. McDowell, J. Zhao, Y. Cui, *Sci. Rep.* **2013**, *3*, 1.

[67] W. Luo, X. Wang, C. Meyers, N. Wannenmacher, W. Sirisaksoontorn, M. M. Lerner, X. Ji, *Sci. Rep.* **2013**, *3*, 2222.

[68] M. Barati, S. Sarder, A. McLean, R. Roy, *J. Non. Cryst. Solids* **2011**, *357*, 18.

[69] D. Cho, M. Kim, J. Hwang, J. H. Park, Y. L. Joo, Y. Jeong, *Nanoscale Res. Lett.* **2015**, *10*, 424.

[70] H. Wu, N. Du, X. Shi, D. Yang, *J. Power Sources* **2016**, *331*, 76.

[71] Y. Zhang, J. Huang, *J. Mater. Chem.* **2011**, *21*, 7161.

[72] S. C. Davis, Stress and Microstructural Evolution During Shape Preserving Silica Magnesiothermic Reduction, Georgia Institute of Technology, **2013**.

[73] R. F. Shepherd, P. Panda, Z. Bao, K. H. Sandhage, T. A. Hatton, J. A. Lewis, P. S. Doyle, *Adv. Mater.* **2008**, *20*, 4734.

[74] L. Shi, W. Wang, A. Wang, K. Yuan, Y. Yang, *J. Alloys Compd.* **2016**, *661*, 27.

[75] J. Xie, G. Wang, Y. Huo, S. Zhang, G. Cao, X. Zhao, *Electrochim. Acta* **2014**, *135*, 94.

[76] Y. Lai, J. R. Thompson, M. Dasog, *Chem. - A Eur. J.* **2018**, *24*, 7913.

[77] K. Chen, Z. Bao, A. Du, X. Zhu, G. Wu, J. Shen, B. Zhou, *Microporous Mesoporous Mater.* **2012**, *149*, 16.

[78] W. Chen, Z. L. Fan, A. Dhanabalan, C. H. Chen, C. L. Wang, *J. Electrochem. Soc.* **2011**, *158*, A1055.

[79] W. C. Cho, H. J. Kim, H. I. Lee, M. W. Seo, H. W. Ra, S. J. Yoon, T. Y. Mun, Y. K. Kim, J. H. Kim, B. H. Kim, J. W. Kook, C. Y. Yoo, J. G. Lee, J. W. Choi, *Nano Lett.* **2016**, *16*, 7261.

[80] D. L. Fang, Y. C. Zhao, S. S. Wang, T. S. Hu, C. H. Zheng, *Electrochim. Acta* **2020**, *330*, 135346.

[81] L. Batchelor, A. Loni, L. T. Canham, M. Hasan, J. L. Coffer, *Silicon* **2012**, *4*, 259.

[82] R. Miao, S. Kang, W. Liao, Y. Wang, J. Liu, G. Zhong, H. Wu, J. Zhang, *Ionics (Kiel).* **2020**, *26*, 1249.

[83] W. Wang, Z. Favors, R. Ionescu, R. Ye, H. H. Bay, M. Ozkan, C. S. Ozkan, *Sci. Rep.* **2015**, *2*, 2.

[84] C. Li, C. Liu, W. Wang, Z. Mutlu, J. Bell, K. Ahmed, R. Ye, M. Ozkan, C. S. Ozkan, *Sci. Rep.* **2017**, 1.

[85] Z. Favors, W. Wang, H. H. Bay, Z. Mutlu, K. Ahmed, C. Liu, M. Ozkan, C. S. Ozkan, *Sci. Rep.* **2014**, *4*, 5623.

[86] M. Dasog, Z. Yang, J. G. C. Veinot, *CrystEngComm* **2012**, *14*, 7576.

[87] S. Liu, B. Liu, Y. Yao, P. Dong, S. Zhao, *J. Wuhan Univ. Technol. Sci. Ed.*

2016, *31*, 965.

[88] A. Xing, S. Tian, H. Tang, D. Losic, Z. Bao, *RSC Adv.* **2013**, *3*, 10145.

[89] J. Liang, X. Li, Z. Hou, W. Zhang, Y. Zhu, Y. Qian, *ACS Nano* **2016**, *10*, 2295.

[90] J. Liang, X. Li, Z. Hou, C. Guo, Y. Zhu, Y. Qian, *Chem. Commun.* **2015**, *51*, 7230.

[91] S. Sim, P. Oh, S. Park, J. Cho, *Adv. Mater.* **2013**, *25*, 4498.

[92] F. Lepoivre, D. Larcher, J. Tarascon, *J. Electrochem. Soc.* **2016**, *163*, 2791.

[93] S. Choi, T. Bok, J. Ryu, J. I. Lee, J. Cho, S. Park, *Nano Energy* **2015**, *12*, 161.

[94] A. Darghouth, S. Aouida, B. Bessais, *Silicon* **2020**, DOI 10.1007/s12633-020-00433-1.

[95] D. Soo, M. Ryou, Y. Joo, S. Bin, J. Wook, **2013**, *110*, 12229.

[96] C. Wang, J. Ren, H. Chen, Y. Zhang, K. Ostrikov, W. Zhang, Y. Li, *Mater. Chem. Phys.* **2015**, *173*, 89.

[97] Y. Yu, L. Gu, C. B. Zhu, S. Tsukimoto, P. A. van Aken, J. Maier, *Adv. Mater.* **2010**, *22*, 2247.

[98] K. H. Kim, D. J. Lee, K. M. Cho, S. J. Kim, J.-K. Park, H.-T. Jung, *Sci. Rep.* **2015**, *5*, 9014.

[99] S. Zhu, C. Zhu, Q. Meng, Z. Guo, Z. Yu, T. Lu, Y. Li, D. Zhang, W. M. Lau, *RSC Adv.* **2013**, 6141.

[100] L. Wu, J. Yang, J. Tang, Y. Ren, Y. Nie, X. Zhou, *Electrochim. Acta* **2016**, *190*, 628.

[101] I. Kovalenko, B. Zdyrko, A. Magasinski, B. Hertzberg, Z. Milicev, R. Burtovyy, I. Luzinov, G. Yushin, *Science (80-.).* **2011**, *334*, 75.

[102] D. Zhao, J. Feng, Q. Huo, N. Melosh, G. Fredrickson, B. Chmelka, G. Stucky, *Science (80-.).* **1998**, *279*, 548.

[103] H.-C. Tao, L.-Z. Fan, X. Qu, *Electrochim. Acta* **2012**, *71*, 194.

[104] M. S. Wang, L. Z. Fan, M. Huang, J. Li, X. Qu, *J. Power Sources* **2012**, *219*, 29.

[105] H. Kim, B. Han, J. Choo, J. Cho, *Angew. Chemie - Int. Ed.* **2008**, *47*, 10151.

[106] L. Shen, X. Guo, X. Fang, Z. Wang, L. Chen, *J. Power Sources* **2012**, *213*, 229.

[107] D. Qiu, G. Bu, B. Zhao, Z. Lin, *J. Solid State Electrochem.* **2015**, *19*, 935.

Chapter 2:

Experimental Procedures and Techniques

2.1. Magnesiothermic Reduction

2.1.1 Introduction

The magnesiothermic reduction process has been reviewed in detail in Chapter 1. As is stated magnesiothermic reduction can be performed with the magnesium and silica mixed together i.e. in direct contact or with the two reactants separated. This is due to the low vapour pressure and melting point of magnesium, which means magnesium can be mobile during the reduction reaction. In this study all magnesiothermic reductions were performed with reactants mixed together as powders, this allows for better contact between reactants and higher reaction yields.

2.1.2 Procedure

In an argon glove box (MBraun), magnesium powder -325 mesh (Sigma Aldrich) was weighed into a pestle, the chosen silica powder was weighed into the pestle with a desired stochiometric ratio with Magnesium. The two powders were ground thoroughly and evenly together. The reactants were transferred to the reactor (Figure 2.1) and evenly distributed within before transferring the reactor to a tube furnace (Carbolite). The tube furnace was purged with argon at a flow rate suitable to replace the atmosphere in the furnace 5 times (typically 30 minutes). Under Argon the furnace was ramped at 5 ^{o}C/min to 400 ^{o}C then 1 ^{o}C/min to the desired temperature for a set time. Once cooled overnight in argon the powder was extracted from the furnace. Carefully the sample was added to 1M HCl (Sigma Aldrich). NB this step can produce sparking dependant on the amount of Mg_2Si produced in the reaction. The solution was left mixing with a stirrer bar for 48 hours with an aluminium foil cover to prevent evaporation and dust contamination. The remaining silicon powder was filtered through a Buckner funnel with a 450 nm cellulose filter paper and washed with deionised water. The silicon was dried and stored in a 120 ^{o}C vacuum oven.

N.B. Preparation of the reactants was achieved by mortar and pestle grinding of stoichiometric amounts of silica and magnesium powders. Thorough mixing in this way achieved a homogenous distribution of magnesium and BIS. The respective sizes of the magnesium and BIS particles are, <44 μm mesh and 300nm respectively. The smaller silica particles are therefore aggregated and spread evenly between the larger magnesium particles. The low vapour pressure and melting point of magnesium allow the magnesium to become mobile during the reduction and react with BIS particles that are not in direct contact.[1]

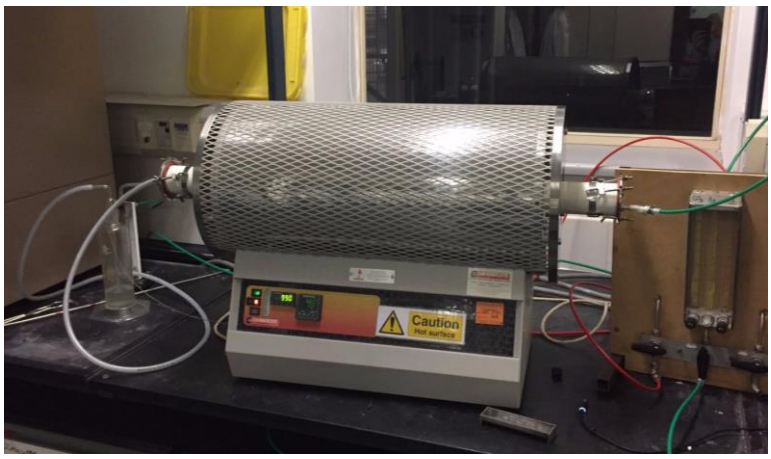

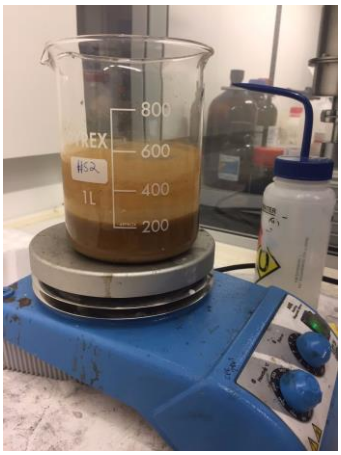

Figure 2.1. (top) steel through/ half pipe reactor used for MgTR. (Middle) Carbolite tube furnace with flowing Argon atmosphere, used for all MgTR in this study. (bottom right) Washing process of Silicon plus reduction products in 1 M HCl.

2.2. Cell assembly and testing

2.2.1 Introduction

Academic researchers need to be able to produce electrodes for lithium-ion batteries that are comparable to those used in industry.[2] Electrodes must adhere well to the current collector and prevent particle detachment during cycling. To achieve this active materials and conductive additives must be mixed homogeneously with a polymeric binder to form and ink/slurry. These inks are then spread onto current collecting foil from which electrodes can be cut. Once sufficiently dry these electrodes can be incorporated into coin cell cases to make full or half cells for electrochemical testing. Figure 2.2 shows a simplified schematic representation of these steps at a lab scale.

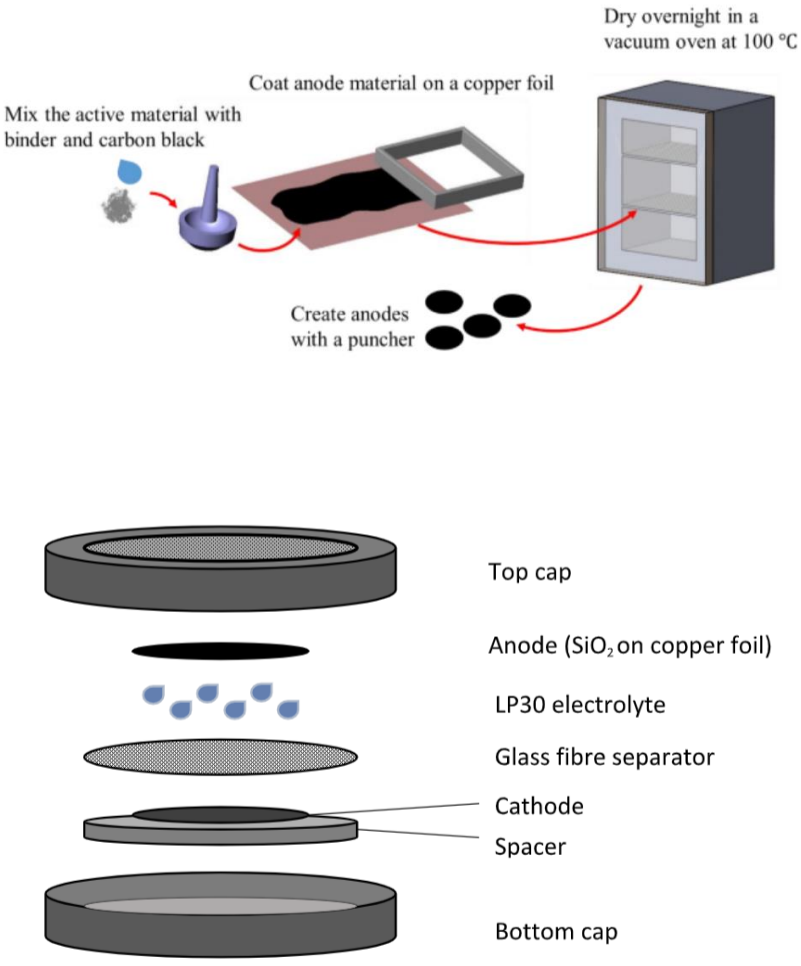

Figure 2.2(above) Simplified schematic of electrode material mixing, coating, drying and cutting steps. (below) individual components of a coin cell assembly before crimping. [3]

2.2.2 Procedure

A 2.5 w% solution of carboxymethyl cellulose (Sigma) binder and deionised water was prepared. The desired solid amount of binder 20 wt% in electrode was added to a Thinky mixer 10ml pot. The conductive additive C-65 (MTI) 20 wt% of electrode was added to the Thinky. The mixer was sealed and mixed at 1500 rpm for 5 minutes. The silicon was added to the mixer and mixed together for a further 10 minutes to give a viscous ink. The ink was transferred to a 10 ml Perspex ball mill vial and milled in a Spex M8000 Mill with a stainless-steel baring for 10 minutes. This ink was then applied to a carbon coated copper foil (MTI) using a vacuum table (MTI)and doctor blade with thickness 300 µm. The coating was air dried for 1-2 hours then placed in an 80 ^{o}C vacuum for a minimum of 6 hours. Once dry 12 mm diameter electrodes are punched from the foil, weighed, and used for cell preparation. Electrochemical experiments were performed using MIT2016-type coin cells with a Whatman glass fibre separator and lithium foil (Sigma Aldrich) as the counter electrode. The electrolyte was 1M $LiPF_6$ in a 1:1 solution of ethylene carbonate (EC) and dimethyl carbonate (DMC) (Sigma Aldrich) with added 5w% fluoroethylene carbonate (FEC) (VWR). The composition of working electrodes was: 60 wt% silicon active material, 20 wt% conductive additive C-65 , 20 wt% carboxymethyl cellulose. The commercial silicon nano-particle size was <100nm from IOLiTech. The cells where assembled in an Argon filled glove box (MBraun) with oxygen and water contents less than 0.1ppm.

The electrochemical performances were tested on a Maccor 4000M Battery and Cell test system in a 25^{o}C temperature chamber. The cut off voltage was 0.01V versus Li/Li^{+} for discharge (lithium insertion) and 1.2 V versus Li/Li^{+} for charging (Li extraction). The specific capacity was calculated on the basis of active material mass. The charging rate was calculated from the fraction of active material in the electrode and based on silicon theoretical capacity at 25 ^{o}C of 3600 mAh/g. Electrochemical data presented in this thesis are data collected from an experiment on a single cell.

2.3. Silica Synthesis

2.3.1 Introduction

Biomineralisation is the process where biological organisms produce minerals. The function of such biominerals spans commonly identifiable applications such as bones (calcium phosphates) and shells (calcium carbonates) to less well known but spectacular applications such as sensory magnetic iron oxide nanoparticles.[4],[5] Additives play an important role in mineralisation. Additive control of synthesis already produces materials for a wide range of applications in the chemical, pharmaceutical and food industries.[6]

Silica is produced by biological organisms through biomineralisation of silicic acid (Figure 2.3) naturally silica is produced on a scale orders of magnitude larger than man made silica production, all at mild reaction conditions. Biomimetic and bioinspired in vitro synthesis routes to silica offer mild reaction conditions and control to produce an important industrial material. This approach centres around the identification of silica-depositing proteins and other biomolecules in organisms such as diatoms and sponges which naturally produce silica structures. A series of biomolecules; proteins (silaffins and cingulins) and poly peptides, polysaccharides and polypropyl amines are proposed to be crucial for silica deposition in vivo.[7],[8]

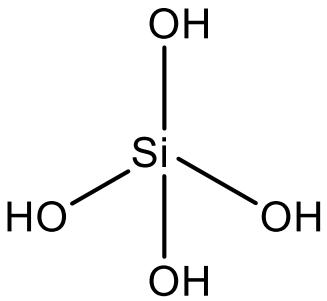

Figure 2.3. Orthosilicic acid. weakly acidic pKA = 9.8

Orthosilicic acid (Figure 2.3) is weak acid however the small number of ionized molecules at neutral pH will readily condense to form small oligomers. These oligomers are the initial seeds for the formation of stable particles. As the concentration of Orthosilicic silicic acid molecules decreases below the solubility limit smaller particles and oligomers dissolve and redeposit onto larger particles in the process known as Oswald ripening. As silica particles start growing, they will remain isolated due to repulsion as at pH-7 as they carry a negative surface charge. Manipulation of the growth process using other charged species can cause

aggregation though charge neutralisation and bridging of individual particles as shown in Figure 2.4.

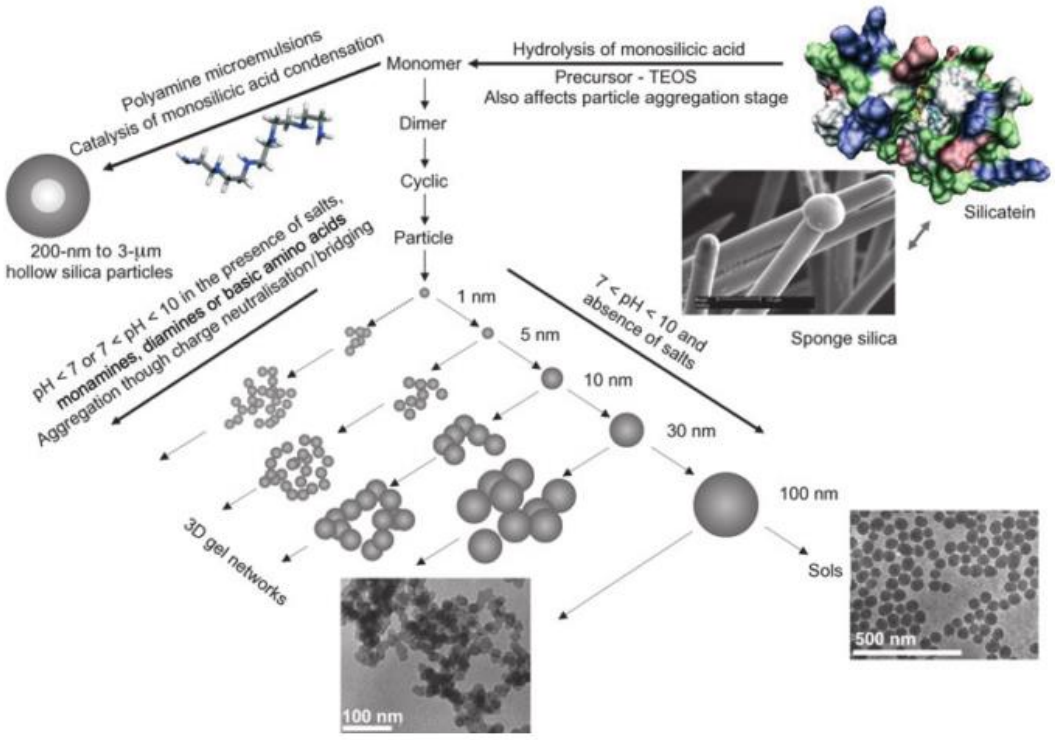

Figure 2.4. The pathways to silica formation from orthosilicic acid through oligomers to particle and aggregate structures.[9]

Due to the prevalence of amine functionality in proteins responsible for biosilicifaction in nature, the possibility of using cheaper synthetic analogues to produce silica products has been explored. Polyamines have been shown to rapidly precipitate nanosized silica particles in-vitro.[10],[11],[12] Varying the degree of polymerisation and extent of methylation effects the activity of the polyamines and subsequently the silica material produced.[13]

Using cheap synthetic analogues of biological additives (such as pentaethylene hexamine 'PEHA') porous silica materials can be produced in water, at room temperature, referred to now as 'Bioinspired silica' (BIS). Additional benefits of green silica are scalable synthesis and tailorable properties by varying additive used.

Procedure

Sodium metasilicate (Sigma Aldrich) 31.8210 g (0.15 moles) was dissolved into 4650 ml of deionised water, inside of a 5000 ml Radley's lab reactor. The solution is brought up to a mixing speed of 450 rpm (identified as the critical mixing speed). Pentaethylene hexamine (PEHA) (Sigma Aldrich) 5.8093 g (0.025 moles) was

transferred to the 4650 ml solution. A pH probe was used to measure the pH of the reaction mixture in-situ. Hydrochloric acid 1M (HCl) (Sigma Aldrich) 350 ml (87.5 moles) was quickly added to the reaction mixture. The pH was monitored. Using a micro pipette addition HCl is added so the pH comes to rest at 7.00±0.05 within 2 minutes. The solution was allowed to react for 5 minutes. The product solution was collected from the bottom of the reactor. Vacuum filtration was used to removed unreacted species and separate out the silica. A minimum of 2 washes with deionised water was performed. Oven drying at 120 ^{o}C for 24 h followed by drying under vacuum at 120 ^{o}C for 24 h, completely dried the silica. The silica was calcined at 550 ^{o}C under air for 5 hours to remove all organic additives. The resulting calcined silica was ball milled for 5 minutes to give a fine homogeneous powder ready for Magnesiothermic Reduction or Electrode fabrication.

2.3.2 Commercial Silica

Other silica sources were sourced from commercially available materials. Precipitated silica refers to Perkasil KS4080PD (Grace), Silica Gel refers to ‘mesoporous silica gel 13nm’ (Sigma), porous silica refers to microporous Syloid AL-1FP (Grace), Quarts was obtained as ‘quartz white sand >99.995%’ (Sigma).

2.3.3 Stöber silica

Glassware must be cleaned with HCl, then ethanol, then DI water. This was to remove particulate matter which can provide any nucleation point for silica growth. TEOS (15.5ml,) is added to absolute ethanol 99.99% (203.0 ml) and DI water (27.8 ml) to make up a 0.07 mol solution of silicic acid. An aqueous solution of 34 wt% ammonium hydroxide (NH_4OH) catalyses the condensation reaction of silicic acid to form silica particles. The more NH_4OH to larger the particles will be. NH_4OH solution was added (3.8 ml) which forms 200 nm Stöber particles. The vessel was closed and placed in a sonic bath at 25 ^{o}C for 2 hours. The solid particles were then extracted from the solution via centrifugation and calcined at 550 ^{o}C for 5 hours.

2.4. Electrochemical Reduction

2.4.1 Introduction

All electrochemical reduction reactions of silica with lithium were performed in lithium-silica half cells. These half cells were made using 2016 coin cells. Using coin cells made sure that each test had the same electrode area, compression, electrolyte volume and resistance. Cells consisted of a negative lithium metal electrode disk 10 mm diameter, and a positive silica based working electrode 12 mm diameter. The two electrodes were separated by a Whatman glass fibre separator. The cell electrolyte was 1M $LiPF_6$ in a 1:1 solution of ethylene carbonate (EC) and dimethyl carbonate (DMC) (Sigma Aldrich) with added 5w% fluoroethylene carbonate (FEC) (VWR).

2.4.2 Procedure

The electrochemical performances were tested on a Maccor 4000M Battery and Cell test system in a temperature chamber. The cut off voltage was 0.01 V versus Li/Li^+ for discharge (lithium insertion) and 1 V versus Li/Li^+ for charging (Li extraction). The specific capacity was calculated on the basis of active material mass. The charging rate was calculated from the fraction of active material in the electrode and based on theoretical of 680 mAh/g.

Potentiostatic discharge (PSD) procedure for the electrochemical reduction of BIS was as follows. Electrode was cycled galvanostatically for 5 cycles at C/10. Upon 5^{th} discharge to 0.01V the cell was subject to a potentiostatic step for 20 hours, holding the cell at 0.002 V. This galvanostatic cycling followed by potentiostatic step was repeated for 20 cycles. The voltage profile for the first galvanostatic cycling steps is shown in Figure 2.5 followed by the PSD step for 20 hours, after this treatment step the clear activation of the material can be seen for the voltage profile in the following 5 cycles.

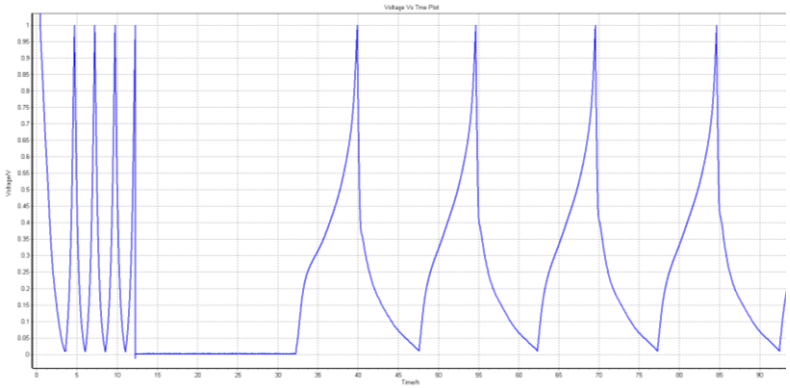

Figure 2.5. Typical Voltage profile vs Time for the first stepwise PSD of silica electrode.

Short circuit reduction procedure was not performed by electrochemical testing equipment. Upon construction the silica half cells were stored at the desired reduction temperature for 8 hours of rest and equilibration. After 8 hours a crocodile clip was used to electronically connect the positive and negative electrodes (Figure 2.6). The cell was stored in an insulating plastic bag and placed in a temperature chamber for the desired time period. Upon the desired short circuit step the cell was removed, allowed to rest for 8 hours and then tested galvanostatically as described above.

Figure 2.6. Photo of the short circuiting method of lithium-silica coin half cells.

Constant load discharge (CLD) was an equivalent experiment to short circuit reduction but using a Maccor 4000M Battery and Cell test system so voltage profile could be monitored. Cells were cycled 5 times galvanostatically then subject to a constant load discharge of 0.8 Ω for the desired time duration. Cells could

subsequently be cycled for capacity evaluation. This procedure was performed in a temperature controlled environment.

2.5. Characterisation Techniques

2.5.1 X-ray Diffraction

2.5.1.1 Theory[14][15]

The wavelength of X-rays is in the same order of magnitude as the distances between planes of atoms in crystalline materials. Electrons within atoms coherently scatter light. As X-rays are reflected off crystal planes within a lattice they can be detected. As the incident angle of the incoming X-rays is varied, the distance parallel waves are travel before being scattered off crystal planes is changed. If the extra distance travelled is an integer value of the x-ray wavelength, then constructive interference will increase the intensity of this reflection. The distance (d) between parallel planes of atoms in a crystal unit cell can therefore be related to the wavelength of incoming x rays and their incident angle, this relation is named Bragg's law Equation 2.1.

$$Bragg's\ Law$$

$$n\lambda = 2dsin\theta \qquad \text{Equation 2.1}$$

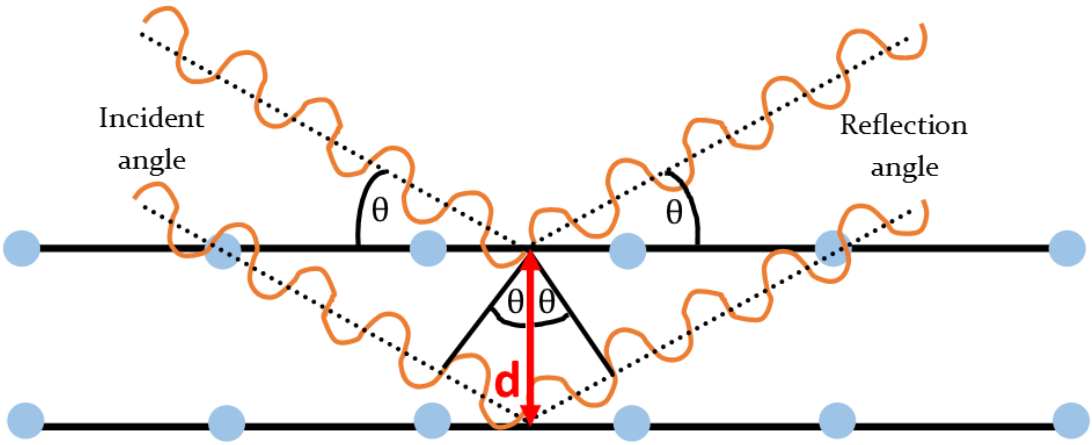

Figure 2.7. Schematic representing constructive interference of X-rays satisfying the Bragg conditions whilst scattering off crystal plans.

Consequently, a family of crystal planes produces a diffraction pattern which can be conveniently plotted as Diffractogram of peak intensity vs Bragg angle (incidence angle) in 2θ degrees. The intensity of a given peak is related to the reflecting atoms electron density and position within the plane. Resulting diffractograms can be used to match phases of known crystalline materials in a fingerprinting manner to identify phases present in a sample. Properties such as unit cell parameters, crystal structure and crystallite size (coherent scattering domain size) can also be determined.

Diffraction data presented in this thesis was collected from a single powder diffraction of each sample.

2.5.1.2 Scherrer Analysis

For very small crystals where the number of unit cells in a given direction is relatively low a peak will appear broader, with smaller crystals leading to broader patterns. The peak breadth can therefore be expressed in terms of crystallite size; hence a measurement of peak breadth gives a simple method for determining crystallite sizes in the size range up to 100 nm. The extent of crystallite broadening can be given by the Scherrer Equation 2.2.

$$B = \frac{0.9\lambda}{t\,cos\theta} \qquad \text{Equation 2.2}$$

t= diameter of crystal particle

0.9=Shape factor of sphere

λ = wavelength of source

θ =Bragg angle (radians)

B=broadening of diffraction line measured (radians)

A key parameter in determining crystallite size is to distinguish the instrumental broadening from the measured broadening. This is possible by running a standard sample with crystallite size >1000nm which will give sharp peaks close to the angle of measured peaks with no broadening from particle size. Broadening (B) is not simply given by the difference of the measured broadening and the instrument broadening due to the assumption that the diffraction line has the shape of an error curve (with Gaussian shape). Broadening is determined with equation 2.3

$$B^2 = B_m^2 - B_s^2 \qquad \text{Equation 2.3}$$

B=Broadening of diffraction line measured (radians)

$B_s = Broadening\ from\ the\ standard\ (radians)$

$B_m = Measured\ Boradening\ of\ sample\ (radians)$

For further derivation see Supplementary Chapter 9 Section 1.2

2.5.1.3 Grazing Incidence XRD

GI-XRD is a method were the incident angle of incoming X-rays to a sample is set to very small angles so that diffraction can be made surface sensitive. The penetration of X-rays can such be limited so the study of surface layers can be performed.

2.5.1.4 Procedure

XRD patterns were collected using a STOE STADI IP diffractometer in transmission mode unless stated otherwise. Cu $k_{\alpha 1}$ radiation wavelength 1.5406Å was selected for diffraction collection and patterns were collected by an image plate detector. A total of 5 patterns were collected over the 2θ range of 10-80^{o} for 5 minutes each. Diffraction patterns were combined before analysis. Scherrer analysis was performed in WinXPow software using integral breadths vs a polycrystalline silicon standard. [15][17]

Grazing incidence XRD was performed on a Panalytical X'Pert 3 in reflection-transmission configuration. Cu $k_{\alpha 1}$ radiation wavelength 1.5406Å was selected for diffraction measurement between 20-76.5 ^{o} with a step size of 0.1 ^{o}.

2.5.2 Electrochemical Impedance Spectroscopy

2.5.2.1 Theory

Impedance can be described as the opposition to the flow of electrons during the application of alternating current (AC) to a complex system. A complex electrical system in a passive component comprises of both an energy dissipater (resistor) and energy storage elements (inductors/capacitators). Materials containing composite phases or heterogeneities commonly show a dielectric response between the impedance (admittance) and the frequency of the applied AC field. Almost all physical-chemical systems contain energy dissipation and storage properties, impedance spectroscopy examines them.

$$E = IZ \qquad \text{Equation 2.4}$$

Impedance extends ohms' law to an alternating circuit where resistance is noted as Z (impedance) (Equation 2.4). The measurement of impedance is made by applying an oscillating voltage (E) and measuring the current response. The equation for the oscillating voltage (2.5) includes the terms for $|E|$ for voltage amplitude and ω for angular frequency (ω=2πf). The current response to an alternating voltage signal can be shifted in phase (θ) from the form the applied signal. This shift is related to the reactance of the circuit, the effect of inductive and capacitive elements which cause lagging and leading phases respectively. The impedance with respect to time can is expressed in equation (2.6).[24]

$$E = |E|\sin(\omega t) \qquad \text{Equation 2.5}$$

$$Z = \frac{E_{(t)}}{I_{(t)}} = \frac{|E|\sin(\omega t)}{|I|\sin(\omega t+\theta)} = |Z|\frac{\sin(\omega t)}{\sin(\omega t+\theta)} \qquad \text{Equation 2.6}$$

Eulers formula can be used to rewrite the above equation 2.6 using complex numbers (Equation 2.7). (j=$\sqrt{-1}$). The ratio of the oscillating voltage to an oscillating current is the impedance with the magnitude of $|Z|$ and a phase angle of θ.

$$Z = |Z|e^{j\theta} = \frac{|E|e^{j\omega t}}{|I|e^{j\omega t+\theta}}$$

$$E = IZ = I|Z|e^{j\theta} \quad \text{Equation 2.7}$$

The complex impedance can be split into the real and imaginary components (Equation 2.8), this is commonly done to provide a Cartesian plane representation. Z' and Z'' are the resistive and the reactive (capacitive + inductive) components of impedance respectively.[24]

$$Z = Z' + iZ'' \quad \text{Equation 2.8}$$

The graphical representation of any Z with respect to its Z' and Z'' is termed an Argand diagram. The Nyquist plot which is commonly used to represent impedance data is a series of points, where each point is at a different frequency (Figure 2.8). Characteristic shapes can appear within Nyquist plots and can be interpreted to varying degrees visually.[24]

The Nyquist plot contains no information of the frequency at which a data point is acquired, however high frequencies are plotted from left to right to lower frequencies. Semicircles are common in Nyquist plots and are usually associated with charge transfer processes.[25]

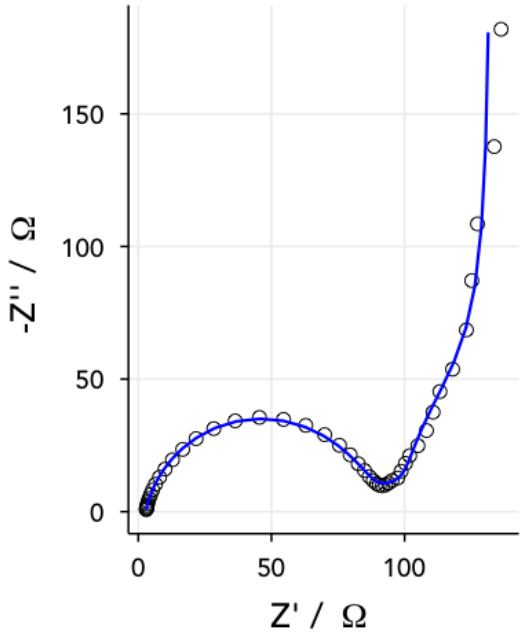

Figure 2.8. Nyquist plot.

2.5.2.2 Resistance-Capacitance-Inductance

It is helpful to define the key passive components of electrical circuits, resistors, capacitors and inductors. These passive components cannot electronically control the flow of electrons.

- Resistance is a measure of how well a component resists the flow of electric current in a circuit.
- Capacitance is the ability of a device to store a store energy as electrical charge.
- Inductance is the ability of a component to store energy as a magnetic field.

2.5.2.3 Equivalent Circuit models

Charge transfer processes, as shown above are common in EIS and give semi-circular patterns. In a charge transfer two parallel processes are occurring, firstly the transfer of charge across a medium, secondly the build-up of the double layer capacitance. A charge transfer process can therefore be represented by a parallel electrical circuit of a resistor and capacitor, (Figure 2.9). In parallel the reciprocals of the impedances are additive, so the equation 2.9 can be written and simplified.

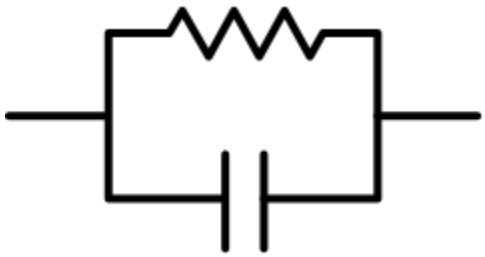

Figure 2.9. Resistor and capacitor in parallel.

$$\frac{1}{Z} = \frac{1}{R} + j\omega C \qquad \text{Equation 2.9}$$

$$Z = \frac{R}{1+j\omega \mathrm{RC}} \qquad \text{Equation 2.10}$$

Equation 2.9 can be used to visualise the semi-circular pattern of a charge transfer: at high frequency ω tends to infinity i.e. the denominator tends to infinity and impedance to zero (circuit behaves like a capacitor). At low frequency ω tends to 0 the denominator tends to 1 so Z=R (circuit behaves like a resistor).

Electrochemical processes often do not behave as idea circuit components. Constant phase elements (CPE) are commonly used to describe capacitance as it appears in real electrochemical systems where non uniform surfaces and distribution of reaction sites effects behaviour. The mathematic definition is presented in equation 2.11, where p is the constant chase $(-90 \times p)^{o}$ and p is a number between 0-1, the case for p=0 is an ideal resistor and p=1 describes an ideal capacitor.

$$Z_{CPE} = \frac{1}{Q_0 (j\omega)^p} \qquad \text{Equation 2.11}$$

One physical explanation for CPE behaviour is electrode roughness caused by fractal surfaces and inherent porosity.[24] [26]

2.5.2.4 Procedure

The electrochemical impedance spectroscopy (EIS) was performed by a Solartron Modulab XM MTS. The procedure for EIS measurements was an analysis of frequency response between 0.01-100’000 Hz. Prior to impedance measurement cells were held at OCV for 3 hours to allow for sufficient voltage stabilisation before frequency response analysis. Fitting of Nyquist plots was performed in ZView.

2.5.3 BET and BJH Theory of Nitrogen Absorption

2.5.3.1 Theory

The absorption of gasses onto solid samples is described with isotherms, the amount of adsorbent as a function of its pressure at a constant temperature. Normalisation of the amount of adsorbent is done with respect to the samples mass to allow for comparison between samples. Nitrogen is the most common adsorbate used to analyse surfaces primarily due to its inert nature which leads to physisorption onto surfaces. Surface analysis requires the complete absorption and desorption of the adsorbate onto the surface therefore absorption analysis must take place at the boiling point of liquid nitrogen (77 K), such that at a partial pressure of 1 all pores contain liquid nitrogen. The importance of complete adsorption (liquid N_2) onto surfaces is explained below in 'stages' of pore filling.

2.5.3.2 Classification of isotherms[18]

- The types of isotherm can be broken into specific classifications as defined by IUPAC, displayed in Figure 2.10.
- Type I isotherm seen in microporous solids with small external surface areas. (a) are given by micropores with narrow micropore <1nm and (b) found with pores up to 2 nm.
- Type II are given by the physisorption of gasses on nonporous or macroporous absorbents, monolayers and subsequent multilayer absorption. A sharp knee at point B corresponds to complete monolayer coverage where more gradual curvature indicated an overlap between monolayer coverage and multilayer adsorption.
- Type III no knee therefor no identifiable monolayer formation. If interaction between adsorbate and adsorbent the adsorbate molecules will cluster around the most favourable sites on the surface of a non-porous / macroporous solid.
- Type IV are seen in mesoporous material, discussed further below. Type a hysteresis occurs when pore width exceeds critical r_c. for small mesopores and/or cylindrical and conical shape type IV b is observed.
- Type V may form in similar circumstances to III when adsorbate and adsorbent interaction is weak and the clustering step is followed by micro/mesopore filling.
- Type VI stepwise layer by layer absorption on a uniform nonporous surface. The step high represents the capacity of each layer.

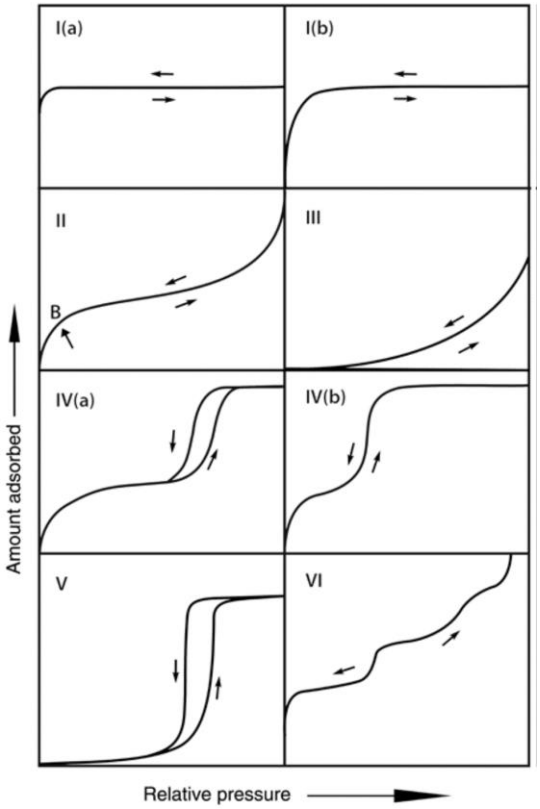

Figure 2.10. Types of Isotherm as classified by IUPAC[18]

2.5.3.2 The stages of pore filling

A pore is deemed filled when it contains liquid nitrogen. Due to capillary action it is more favourable for nitrogen gas to condense within the pores of a material than exist as a gas. The propensity of the gas to condense within pores is related to the relative pressure of the gas and the diameter of the pore.

The stages of pore filling are defined 1-4 in Figure 2.11: Stage 1. Continuous micropore volume filling at low relative pressures. Stage 2 BET multilayer absorption, multiple layers of adsorbate build up on the surface of the substrate. This region is used to determine BET surface area (discussed below).

Stage 3 mesopore filling. At a critical radii r_c, N_2 will condense in the pore leading to a large uptake of N_2 at a given partial pressure, filling the mesopore. The P/P_o this occurs at depends on the radius of pore and number of multilayers needed before condensation. The critical radium for nitrogen is known and it is therefore possible to use the condensation at P/P_o to determine the size of pores within a sample. With regard to calculating thickness of the absorbed film at the critical radius, (and hence the pore size) the numerical integration method of Barrett, Joyner, and Hallenda (BJH). This method is considered the most popular method for determining mesopore

size, volume and distribution.[19] NB BJH can underestimate mesopore sizes by 25% when under 10nm, this should be taken into account. [20]

At Stage 4 a plateau arises as macro surfaces build more multilayers after all pores are filled. If stage 4 doesn't plateau it can indicate pores are filling until very end of the absorption process (macropores), and/or interconnected particles.

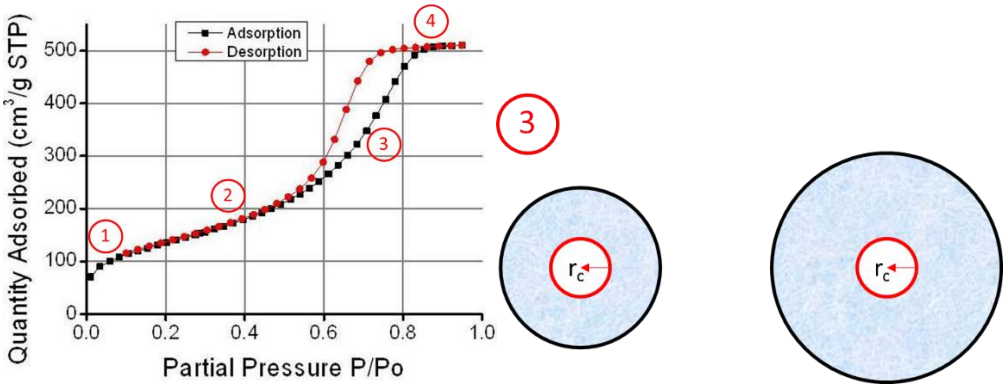

Figure 2.11. Typical Type iv isotherm of mesoporous material. Position 3 has been highlighted to demonstrate how the critical radium (r_c) is reached at different partial pressures dependant on pore size.

2.5.3.3 Assessment of Surface Area[18,21]

The most widely used method for assessment of surface area is the Brunaur-Emmett-Teller (BET) method. The resulting BET equation is shown in Equation 2.12 where the terms are as follows. p is the equilibrium pressure, $p_o$is the saturation pressure, v_m is the monolayer adsorbed gas quantity, v is the adsorbed gas quantity and c is the BET constant. It is necessary to transform the physisorption isotherm data into a 'BET plot' (to derive a value of monolayer capacity of the sample. The surface area is then calculated from the monolayer capacity and the molecular cross-sectional area of the adsorbent (0.162 nm^2 for liquid nitrogen).

$$\frac{1}{v[\left(\frac{p_o}{p}\right)-1]} = \frac{c-1}{v_m}\left(\frac{p}{p_o}\right) + \frac{1}{v_m c} \qquad \text{Equation 2.12}$$

N.B The C parameter in BET theory is exponentially related to the energy of the interactions of absorbent molecules and the surface. A value of >80 for C indicates the knee is well defined at the point of monolayer completion. If C <50 the monolayer coverage cannot be identified as a single point on the isotherm as there is an overlap of monolayer and multilayer adsorption. If C < 2 BET is not applicable

2.5.3.4 Procedure

Samples for N_2 absorption/desorption were degassed at 120^{o}C under vacuum for minimum 12 hours before measurement. Analysis gas was N_2 with free space being measured with Ar using a Micromeritics 3Flex. The sample analysis ran from relative pressures of 0.01 to 0.998. Isotherms were fitted with the BET model for surface area and BJH on the desorption branch for mesopores volume using Micromeritics software. [18–23] N_2 isotherm data presented in this thesis was collected from an experiment on a single powder sample.

2.5.4 Ultra Small Angle X-ray Scattering (USAXS)

2.5.4.1 Theory

USAXS and SAXS are scattering techniques where differences in sample density can be quantified. In this way particle size distributions, particle size and shape, pore sizes and characteristics can be determined. The advantage of USAXS over XRD is that amorphous samples can be characterised.

USAXS and SAXS measures X-ray intensities scattered elastically from a sample at very small angles (<5 degrees). With decreasing scattering angle, increasingly larger structural features are being probed. USAXS is particularly suited for the structural investigation of partially ordered materials which have features from ~1 nm-10 um.

The analysis of USAXS and SAXS data is reliant on mathematical models which describe the behaviour of scattering X-rays off sample features. In these works, a unified exponential/power-law approach has been used to fit USXAS data. Developed by Beaucage, this approach describes scattering from complex systems that contain multiple levels of related structural features.[27]

A general breakdown of USAXS data fitting it provided below of the IRENA package of IGOR Pro for data fitting with the unified fit model.[27]

1. Data is imported to the Unified modeling input panel and plotted as Intensity vs Q on a log-log scale plot.
2. With unified fit you must begin your model with the finest particles of your system moving to the largest.
3. The range for level 1 particles should be identified form a Q^4 vs Q plot. These datapoints are highlighted for the fitting.
4. The Guinier area for level 1 is fitted first by setting the G and Rg components to variable. Once fit is good these parameters are fixed and the power slope is fitted.
5. The data cursors should be moved to the power law slope area, selecting the relevant data points.
6. The level 1 particles due to their small size are assumed to have smooth surfaces and hence fitted with a power law of exactly 4. Therefore P is fixed and B is allowed to be variable to achieve good fit.
7. A flat background subtraction at the highest q is made by moving the data point cursors to the flat data points at highest q.

8. Finally selecting the fit with background option and sleeving all data points withing level 1 allowing G, Rg and B to be variable a complete fit of level 1 can be performed. Residual errors are plotted for the standard error between the fitted line and the real data. In all data fits these should be minimized.
9. Level 1 should have achieved a good fit.
10. Moving onto level 2 with the 'number of levels' option the same process from points 3-8 are iterated. In the case of the system studied in this work the larger level two aggregates did not have smooth surfaces so the P in power law slope can be variable. In addition, a further background subtraction is not needed.

    Tip: an initial increase in G and Rg by 2 orders of magnitude brings the initial start point of the fit closer to the normal range of level two particles and reduced fitting time.
11. With a good fit for the data points in the level 2 region the whole range of the data from highest q to the lowest q in level to can be fitted. To do this use the data cursors and select the relevant data and use the fit button.
12. The low Q power law slope requires prior knowledge of the material. Often it represents large powders and particle agglomerates of level 2. Within this system it was assumed that this region denoted as level 3 was particle agglomerates.
13. Select the data for the level 3 power law data. There is no Guinier area for this region therefore G is set to 0. This data is then fitted with the power law variables B and P.

    Note: it is common for aggregates to have fractal surfaces.
14. Finally all data points can now be selected and using the unified fit tool can be fitted. The normalized residuals should be reasonably small by this step <5 (-5). See Figure 2. 12
15. To analyze the results select the 'analyze results' option this will present the results as a text file for all 3 levels of the system. Alternatively select results to graph as shown below.

This Figure 2. 12 represents a good fit of representative data from reduced silicon samples used in this study. See the unified fit calculated intensity overlaid on the experimental results.

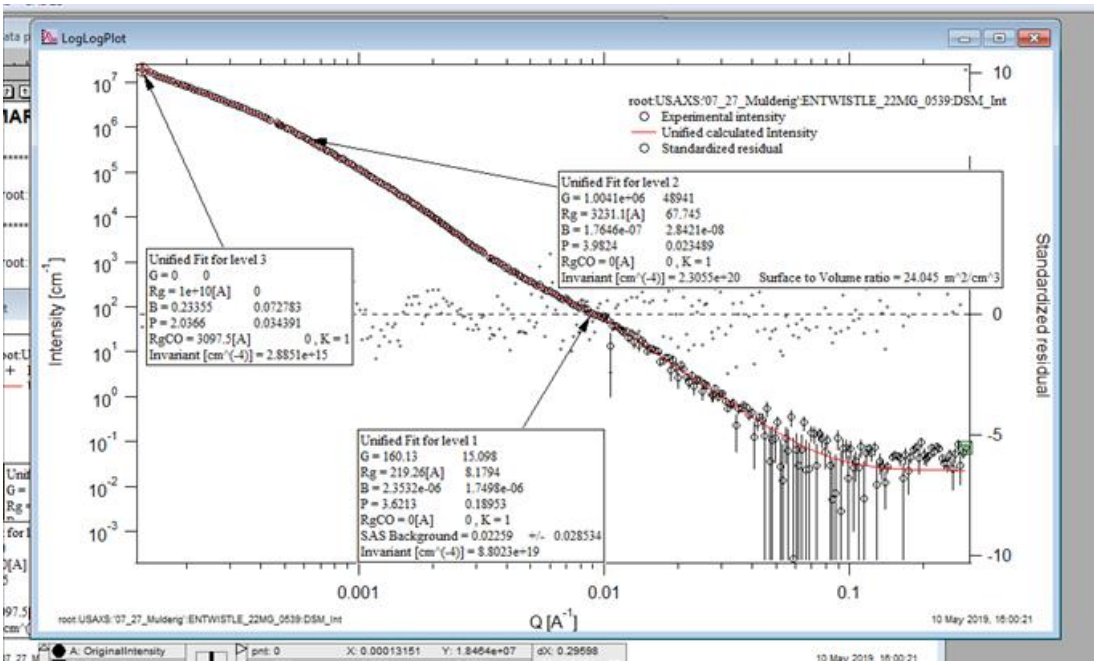

Figure 2. 12. Example data set of unified fit applied to porous silicon powder reduced by MgTR. Includes background subtraction and fitted Guinier areas and power slopes of 3 distinct levels.

Again I would thank Jan Ilavsky for his useful video tutorials and direct further information to his page. https://www.youtube.com/watch?v=Sy5f5Im1Lz4

2.5.4.2 Procedure

USAXS studies were carried out at beamline 9 ID-C at the Advanced Photon Source, a U.S. Department of Energy (DOE) Office of Science User Facility by Argonne National Laboratory. This instrument is operated and maintained by Jan Ilavsky and his team.[28][29] Data reduction was performed using NIKA and IRENA packages in IGOR Pro.[30][31] Sauter Mean diameter was taken as level 1 particle size and the radius of gyration (R_g) as an indication of level 2 particle size.

2.5.5 X-ray Pair Distribution Function (XPDF)

2.5.5.1 Theory[32][33]

XPDF or 'total scattering' is an analytical technique that can provide structural information from disordered (amorphous) materials. This technique measures the Bragg scattering and underlying diffuse scattering, this diffuse scattering is used to determine structural information of the disordered phases. The atomic structure can be quantitatively determined from this diffuse scattering; this structure is described by the atomic pair distribution function.

The reduction of X-ray data from the diffractograms produces the so called structure function, following a Fourier transform the radial pair distribution function is calculated.[33] This pair distribution function describes the probability of finding two atoms separated by a certain distance within the material. Each unique atom is placed at the origin and larger and larger concentric circles are drawn radiating from the origin. A histogram for the probability of an atom being located at a given radius is the produced. This process is visualised in Figure 2.13. [33]

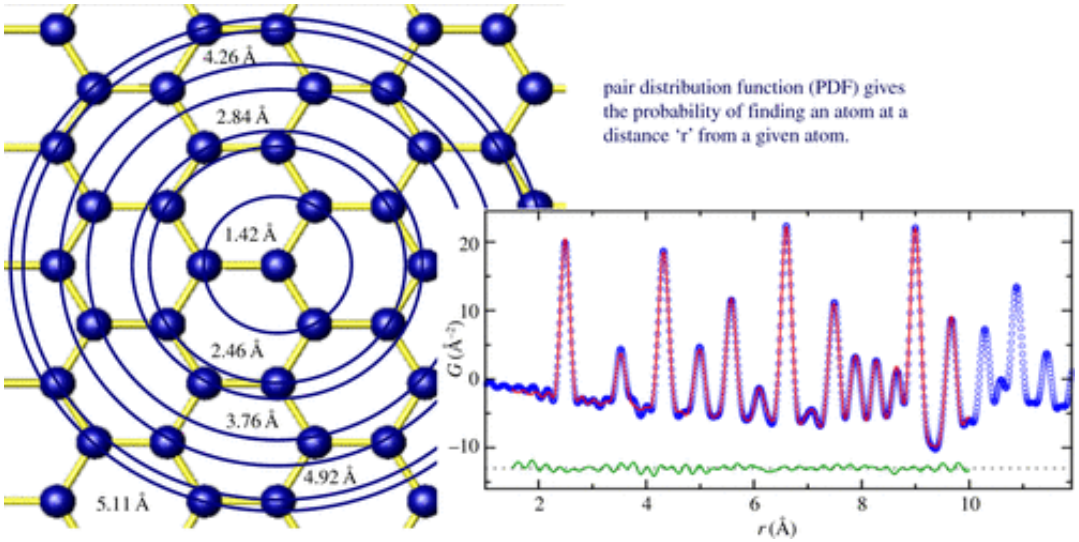

Figure 2.13. A schematic of the short range structure within a material and resulting PDF.[33]

2.5.5.2 Procedure

XPDF data were collected on the I15-1 beamline at the Diamond Light Source, UK using an X-ray wavelength λ=0.161669 Å (76.69 keV). Electrode material samples were compacted into borosilicate glass capillaries of 1.17 mm (inner) diameter. Data from the samples, empty instrument, and empty capillary were collected, and integrated to 1D using DAWN.[34] Corrections for background, multiple scattering, container scattering, and attenuation were made using the GudrunX software.[35] XPDF data presented in this thesis are data collected from a single experiment.

2.5.6 X-ray Photo Electron Spectroscopy (XPS)

2.5.6.1 Theory[33]

XPS can be used to measure the elemental composition of a materials surface (<20 nm). Further information can be quantified such as the chemical and electronic states of the elements. To allow for precise measurement of emitted electrons XPS must be performed in an ultra-high vacuum as the electron detectors are some distance (up to 1m) from the sample. Figure 2.14 schematically represents of X-rays irradiate a surface and how emitted electrons are subsequently detected.

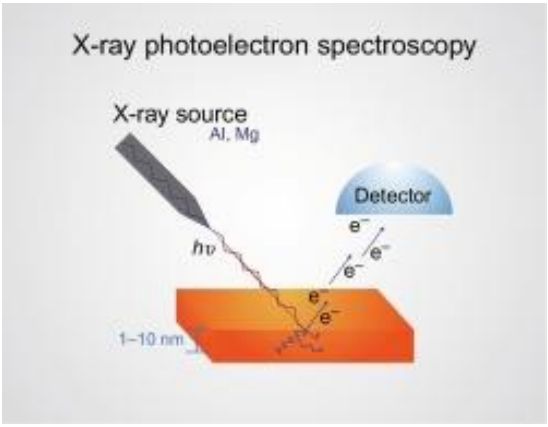

Figure 2.14. Schematic of how XPS measurements at performed. [33]

The XPS technique works by irradiating a material with a beam of X-rays and measuring the kinetic energy of electrons that escape. As the emitted electrons kinetic energy can be measured, the binding energy of that particular electron can be determine. Data from an XPS spectrum is presented as an intensity vs the binding energy of the electrons. The characteristic peaks give information of the orbitals from which electrons have been emitted.

2.5.6.1 Procedure

XPS measurements were performed at the Harwell campus by Mark Issacs. The measurement was made in a front-loaded N_2 filled glovebox at 300 K. The measurement was performed on a Kratos Axis Supra instrument at < 10^{-8} Torr pressure. The area for analysis was 300 x 700 um. X-ray power was 225W with X-ray energies of 1486.7 eV. Spectra were run with 100ms dwell times and a step size of 0.1eV. Data analysis was performed in CASAXPS software.

2.5.7 Raman Spectroscopy

2.5.7.1 Theory[36]

Raman Spectroscopy is based on the interaction of light with the chemical bonds of a sample. Raman relies on the inelastic scattering of photons, the wavelengths of emitted Raman scattered photons vary in energy dependant on the rotational and vibrational energy levels of a system. These rovibrational emissions can provide a structural fingerprint for the identification of molecules.

2.5.7.1 Procedure

Raman spectroscopy was performed with a Renishaw invia microscope using a green argon laser (wavelength 514.5 nm). Powder samples were prepared by compression between two glass slides. Spectra were collected on a CCD detector between 0 and 3500 (cm^{-1}). XPS data presented in this thesis are data collected from a single experiment.

2.5.8 Silicon Purity Determination

2.5.8.1 Theory

The determination of purity in samples containing Silicon and Silica is possible by thermogravimetric analysis. During a heating step to 1000 ^{o}C (with a long dwell time) all silicon within a species will be oxidised to form silica (Equation 2.13), while the silica component will remain chemically unchanged. By measuring the weight change of the sample it is possible to determine the mass of oxygen added to the sample weight, from this a molar amount of oxygen can be determined. By using the initial sample mass and the molar amount of oxygen gained a simple stoichiometric calculation can be performed to determine the weight % of silicon in the initial sample.

$$Si_{(S)} + O_{2(g)} \rightarrow SiO_{2(s)} \qquad \text{Equation 2.13}$$

In the development of this technique a number of important experimental factors were established. Firstly, it was found that minimum reduction times of 24 hours were needed to completely oxidise silicon within a sample. The complete removal of crystalline silicon was determined by XRD, in addition, excessive heating times (72 hours) were used to determine no significant mass gain occurred beyond 24 hours. The complete removal of moisture from samples before and after weighing was found to be a significant source of error. Therefore, samples must be thoroughly dried in a vacuum oven before measurement. In all measurements a minimum of triplicates of each sample were measured. In addition, a balance sensitive to 10 µg must be used for improved accuracy.

2.5.8.2 Procedure

Silicon content was determined by thermo-gravimetric analysis performed in Air in a muffle furnace (MTI). The full oxidation of silicon to silica in air was achieved under heating to 1000^{o}C for 24 hours. Full oxidation of silicon results in 114% weight gain, any deviation from this value allows evaluation of the initial silica concentration. To determine silicon concentration a minimum of 3 samples were oxidised (typically 3-5), the mean average result is plotted with appropriate errors bars representing 1 standard deviation between measurements.

2.5.9 Scanning Electron Microscopy (SEM)

2.5.9.1 Theory[37]

SEM is a type of microscopy where a focused beam of electrons is scanned over a surface to produce an image. Electrons are emitted from an electron gun and focused using magnetic lenses (as displayed in Figure 2. 15). As the focused electron beam is rastered across a surface the position of the beam is combined with the intensity of the backscattered electrons to produce an image. Conventionally SEM is performed under high vacuum to reduce scattering of the electron beam and backscattered electrons.

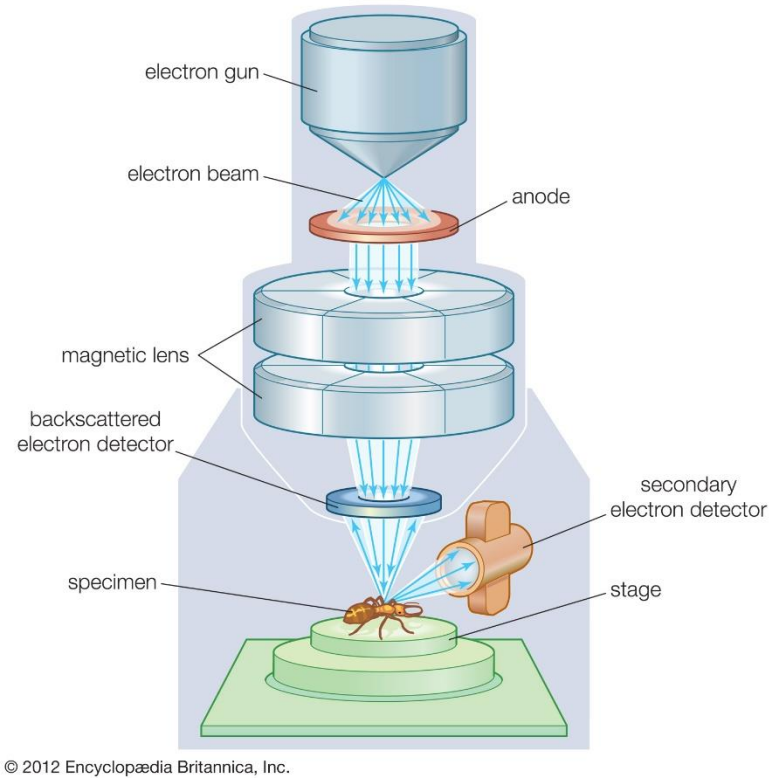

Figure 2. 15. Schematic illustration of an SEM set up.[38]

2.5.9.1 Procedure

SEM images were taken on a FEI Inspect F50 scanning electron microscope. Samples were dispersed into dilute solutions of ethanol with sonication, then pipetted onto the carbon tabs and allowed to dry before analysis. Images were taken with 5-20kV accelerating voltage with SE detector, typical spot sizes of 3 were used.

2.6 References

[1] J. Entwistle, A. Rennie, S. Patwardhan, *J. Mater. Chem. A* **2018**, *6*, 18344.

[2] T. Marks, S. Trussler, A. J. Smith, D. Xiong, J. R. Dahn, *J. Electrochem. Soc.* **2011**, *158*, A51.

[3] F. Ayub, D. Cumming, *Investigation of Porous Silicon Anodes to Increase the Capacity of Lithium-Ion Batteries*, **2019**.

[4] S. Staniland, *Nat Nano* **2014**, *9*, 163.

[5] I. Kolinko, A. Lohsze, S. Borg, O. Raschdorf, C. Jogler, Q. Tu, M. Posfai, E. Tompa, J. M. Plitzko, A. Brachmann, G. Wanner, R. Muller, Y. Zhang, D. Schuler, *Nat Nano* **2014**, *9*, 193.

[6] R.-Q. Song, H. Cölfen, *CrystEngComm* **2011**, *13*, 1249.

[7] N. Kröger, R. Deutzmann, C. Bergsdorf, M. Sumper, *Proc. Natl. Acad. Sci. U. S. A.* **2000**, *97*, 14133.

[8] N. Kroger, *Science (80-.).* **2002**, *298*, 584.

[9] D. J. Belton, O. Deschaume, C. C. Perry, *FEBS J.* **2012**, *279*, 1710.

[10] S. V Patwardhan, *Chem. Commun. (Camb).* **2011**, *47*, 7567.

[11] D. J. Belton, S. V. Patwardhan, C. C. Perry, *J. Mater. Chem.* **2005**, *15*, 4629.

[12] F. Noll, M. Sumper, N. Hampp, *Nano Lett.* **2002**, *2*, 91.

[13] D. J. Belton, S. V Patwardhan, V. V Annenkov, E. N. Danilovtseva, C. C. Perry, *Proc. Natl. Acad. Sci. U. S. A.* **2008**, *105*, 5963.

[14] B. Warren, *X-Ray Diffraction*, Dover Publications Inc, **1990**.

[15] B. D. Cullity, *Elements of X-Ray Diffraction*, Adison-Wesley Publision Company, Inc, **1978**.

[16] B. D. Cullity, *Elements of X-Ray Diffraction Second Edition*, Addison-Wesley Publishing INC, **1978**.

[17] B. Warren, *X-Ray Diffraction*, Dover Publishing, **1990**.

[18] M. Thommes, K. Kaneko, A. V Neimark, J. P. Olivier, F. Rodriguez-reinoso, J. Rouquerol, K. S. W. Sing, **2015**, *87*, 1051.

[19] E. Barrett, L. Joyner, P. Halenda, *J. Am. Chem. Soc* **1951**, *73*, 373.

[20] M. T. S. Lowell, Joan E. Shields, MArtin A. Thomas, *Characterisation of Porous Solids and Powders: Surface Area, Pore Size and Density.*, Springer, **2004**.

[21] S. Brunauer, P. H. Emmett, E. Teller, *J. Am. Chem. Soc.* **1938**, *60*, 309.

[22] M. Thommes, K. A. Cychosz, **2014**, 233.

[23] J. Groen, L. Peffer, J. Pérez-Ramírez, *Microporous Mesoporous Mater.* **2003**, *60*, 1.

[24] ZView, in *Oper. Man.*, Scribner Associates, Inc, **2016**.

[25] M. Lacy, “Electrochemical Impedance spectroscopy,” can be found under http://lacey.se/science/eis/fitting-with-real-data/, **2019**.

[26] W. H. Molder, J. H. Sluyters, *J. Electroanal. Chem. Interfacial Electrochem.* **1990**, *285*, 103.

[27] G. Beaucage, *J. Appl. Crystallogr.* **1995**, *8898*, 717.

[28] J. Ilavsky, F. Zhang, A. J. Allen, L. E. Levine, P. R. Jemian, G. G. Long, *Metall. Mater. Trans. A* **2012**, *44A*, 68.

[29] J. Ilavsky, F. Zhang, R. N. Andrews, I. Kuzmenko, P. R. Jemian, L. E. Levine, A. J. Allen, *J. Appl. Crystallogr.* **2018**, *51*, 867.

[30] J. Ilavsky, P. R. Jemian, *J. Appl. Crystallogr.* **2009**, 347.

[31] J. Ilavsky, *J. Appl. Crystallogr.* **2012**, *45*, 324.

[32] E. Takeshi, S. J. L. Billinge, *Pergamon Mater. Ser.* **2012**, *16*, 55.

[33] S. J. L. Billinge, *Philos. Trans. R. Soc. A Math. Phys. Eng. Sci.* **2019**, *377*, DOI 10.1098/rsta.018.0413.

[34] M. W. Gerring, M. L. Hart, O. V Magdysyuk, S. Michalik, A. Smith, C. C. Tang, N. J. Terrill, M. T. Wharmby, H. Wilhelm, **2017**, 959.

[35] A. K. S. and E. R. Barney, *J. Appl. Crystallogr.* **2011**, *44*, 714.

[36] J. Brown, *Molecular Spectroscopy (Oxford Primer)*, Oxford Science Publications, **1998**.

[37] L. Reimer, *Scanning Electron Microscopy: Physics of Image Formation and Microanalysis*, Springer Science, **1998**.

[38] S. Bradbury, D. Joy, B. Ford, *Encycl. Br.* **2019**.

Chapter 3:

A Mechanistic Understanding of Magnesiothermic Reduction of Silica

Much of the discussion and experimental data from this section can be found in the publication J. E. Entwistle, G. Beaucage, S. Patwardhan, J. Mater. Chem. A 2020

3.1 Introduction

Porous silicon morphologies can address both volumetric expansion and slow lithium diffusion rates of silicon. Stress generation upon lithiation has been modelled for lithium insertion materials[1],[2] which in turn have been applied to models of lithiation in porous silicon structures.[3],[4],[5] The maximum stresses experienced in porous silicon during lithiation is lower than solid silicon.[4] Additionally it has been shown that higher void fractions lead to lower induced stresses and larger pores have lower hoop stresses than smaller pores.[3] Ultimately porous silicon can expand into its own pore volume, thereby limiting stresses on the material. The innate high surface area of porous silicon increases accessibility of electrolyte to silicon surfaces, shortening lithium diffusion lengths and aiding higher rate capabilities.

Porous silicon can be produced via a number of synthetic routes, such as electroless and electrochemical etching, chemical vapour deposition and ball milling, to name a few.[6],[7] However, to make an impact on a commercial scale, any synthesis route needs to be scalable, economical and desirably environmentally friendly. MagnesioThermic Reduction (MgTR) has previously been highlighted not only for scalability and potential low cost, but it can offer additional advantages, such as relatively low reaction temperatures, benign reactants and products, and a wide variety of silicon product properties.[8]

MgTR is a two-step synthesis route where a silica template is reduced by magnesium according to Equation (3.1), secondly magnesium oxide is removed from the products with hydrochloric acid. This process is schematically shown in Figure 3.1 (top) The first reduction step is typically performed in the temperature range of 550 – 950 ^{o}C under an argon atmosphere. Due to the reduction temperature being lower than the melting point of silica and silicon, the correct conditions can produce silicon analogues of silica templates.

$$SiO_2 + 2Mg \rightarrow Si + 2MgO \qquad \text{Equation (3.1)}$$

$$Si + 2Mg \rightarrow Mg_2Si \qquad \text{Equation (3.2)}$$

The porosity of silicon produced through MgTR is a key parameter in the justification for studying these materials for LIB applications as discussed above. However complete characterisation of pore properties in silica precursors and silicon products is often lacking. It has been highlighted in literature that magnesiothermic reduction conditions can have a much greater effect on the silicon properties than the silica template used.[8] Understanding of MgTR conditions and their effect on the pore properties of silicon is critical to the utilisation of these materials in LIBs.

It is known that pore properties of the silica template are not the only factor governing pore properties in the silicon analogue. This is to be expected, as the silicon analogue generally adopts the morphology of the templating silica, however, oxygen atoms are being removed from the host, thus inevitably causing structural changes. Additionally, the product phases of magnesium oxide and silicon are interwoven with each other, this morphology is crucial to allow the complete removal of magnesia during the HCl washing.[9]

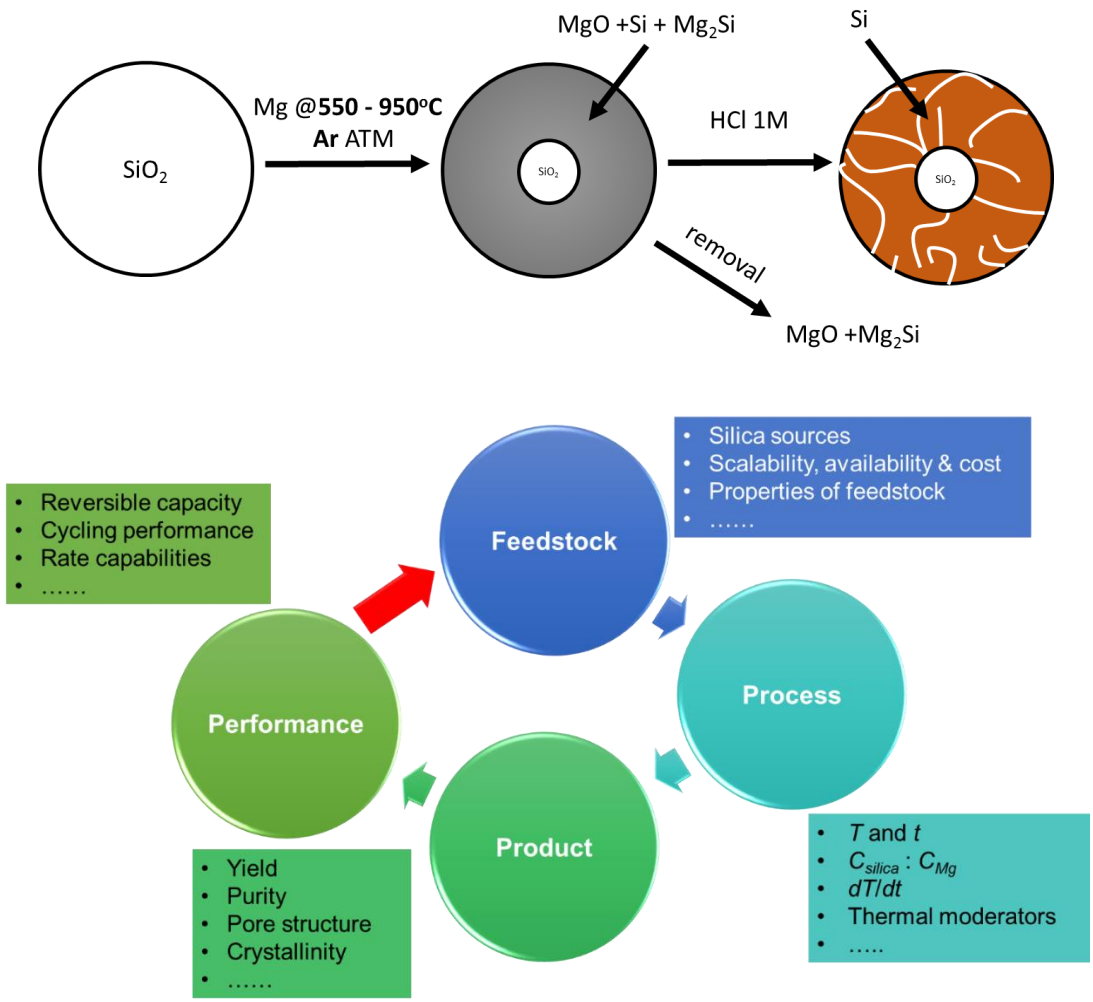

Figure 3.1. (Top) A schematic representation of the Magnesiothermic reduction reaction. (Bottom) A schematic showing the interconnectivity between the feedstock, the reduction process, the resultant silicon produced and its performance in LIB. The red arrow shows desired reverse engineering required to select feedstock and process for a given performance. T and t are temperature and duration of MgTR. C_{silica} : C_{Mg} is the stoichiometric ration of precursors and dT/dt is the heating rate.[10]

As well as pore properties, the purity of the silicon formed is critical for LIB applications. Often MgTR does not fully reduce the silica to silicon. Typically, the remaining silica has been selectively removed with toxic HF to optimise battery performance, more often than not the yield of the reduction is not stated in these cases.[8] The use of HF will add economic and environmental burden to any future development of MgTR. Recent studies have shown that small amounts of silica after reduction may be beneficial bringing into question the need for HF.[11]

Despite the scattered investigations, currently a detailed understanding of the evolution of pore properties during the MgTR reaction is lacking. For example studies may report reaction times above 2 hours have no effect on increasing the silicon yield,

[12][13] but the specific effect on pore properties and surface area evolution have not been studied.[8] Likewise a variety of molar ratios have been studied however the effect of stoichiometric ratio on the pore properties and surface area of porous silicon has not been investigated.[8] The effects of feedstock (silica) properties and the MgTR process on the properties and the performance of porous silica produced are unknown (see the red arrow in, Figure 3.1 (bottom)). This stops a predictive design of a method to produce mesoporous silicon structures for lithium-ion battery anodes. In this study, we aim to address this gap in our knowledge by systematically investigating the effect of reaction conditions (time, temperature and stoichiometry) and the silica precursors on product pore properties and purity. The anode performance of silicon thus produced will be assessed in order to understand the interconnections between feedstock, MgTR process, product and performance as shown in Figure 3.1 (bottom). Specifically, herein we systematically study the MgTR reaction conditions and for the first time provide an in-depth analysis of how key reaction parameters affect the pore properties of the MgTR products, which in turn affect the electrochemical performance. A key expected outcome is the understanding of pore evolution in silicon, which can help design MgTR process for desired product attributes.

3.2 Experimental

This section details specific experimental procedures needed for understanding this work. The general experimental section concerning experiments not specified here can be read in Experimental Chapter 2.

USAXS studies were carried out at beamline 9 ID-C at the Advanced Photon Source, a U.S. Department of Energy (DOE) Office of Science User Facility by Argonne National Laboratory. This instrument is operated and maintained by Jan Ilavsky and his team.[14][15] Data reduction and interpretation was performed by myself using NIKA and IRENA packages in IGOR Pro.[16][17] Sauter Mean diameter was taken as level 1 particle size and the radius of gyration (R_g) as an indication of level 2 particle size.

Aside from BIS, which was synthesised in house according to experimental (chapter 2), other silica sources were sourced from commercially available materials. Precipitated silica refers to Perkasil KS4080PD (Grace), Silica Gel refers to ‘mesoporous silica gel 13nm’ (Sigma), porous silica refers to microporous Syloid AL-1FP (Grace), Quarts was obtained as ‘quartz white sand >99.995%’ (Sigma).

3.3 Reduction of BIS Parametric Study

3.3.1 Bioinspired Silica

The silica used for this study is produced in house via a well-established bioinspired synthesis route.[18] The choice of silica precursor will have an important effect on the economic and environmental impact for development of this technique at an industrial scale. Bioinspired silica is synthesised in water and at room temperature in minutes, it has shown promising scalability and economic feasibility.[19][20] Additionally the properties of the silica can be modified by changing the catalytic additive and by post/pre-treatment of supernatant.[19] A variety of other naturally occurring and synthetic silica is also studied. The bioinspired silica produced in this study (from now on referred to as BIS, see Experimental section for details) is fully characterised in Figure 3.2 and summarised in Table 3.1. The BIS is comprised of secondary particles with an average diameter of ~330nm, it has been shown previously these secondary particles are comprised of smaller primary particles of smaller diameter.[21] The BIS has micro and small mesoporosity which arises from the interstitial space between these primary particles.[22]

Table 3. 1. Materials properties of BIS. PV= Pore volume

	BET SSA (m^2/g)	BJH PV (cm^3/g)	USAXS Particle Size	
			Level1 (nm)	level 2 (nm)
Bioinspired PEHA	301	0.16	26	370

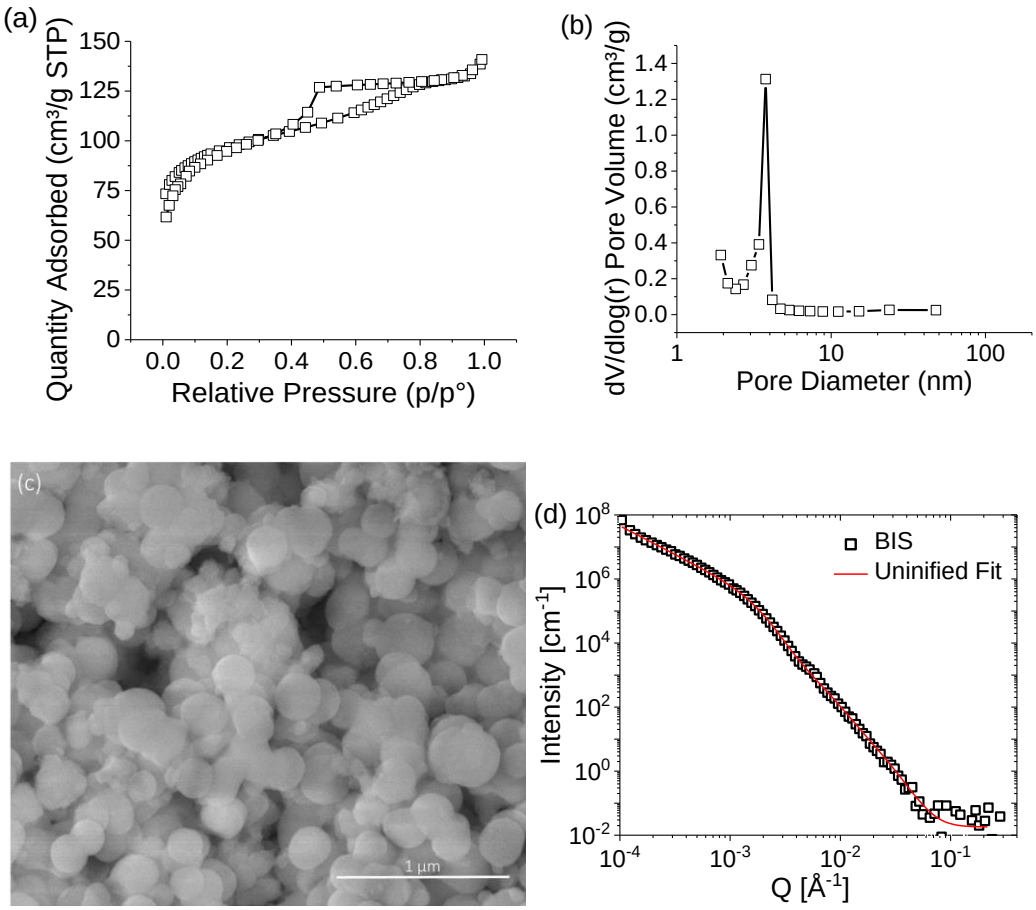

Figure 3.2. Characterisation of BIS, (a) N_2 absorption Isotherm, (b) BJH pore size distribution, (c) SEM image, (d)USAXS data obtained for BIS along with unified fit. [10]

3.3.2 Reduction of BIS

Before systematically studying MgTR process by exploring the effects of the reaction time, temperature and the stoichiometry of the reactants, we present results from a typical MgTR experiment. Figure 3.3 presents the characterisation of typical BIS porous silicon after MgTR. Figure 3.3(a) shows a Type IV isotherm indicative of a mesoporous material. Desorption branch fitting with the Barrett-Joyner-Hallenda (BJH) model provides the pore size distribution (Figure 3.3(b)), confirming mesopores with average pore size of 13 nm. The formation of crystalline silicon from MgTR was observed using XRD Figure 3.3(c)), which also confirmed that magnesia and magnesium silicide are present after the reduction and shows that both species are completely removed during the acid washing. It has been shown previously that potential side reactions may also lead to the formation of magnesium silicates, however, no magnesium silicates were observed throughout this study. We note that this is the first report of mesoporous silicon production using BIS and it has it has technological advantages due to scalable, economical and sustainable nature of BIS.[23] Although this is the first MgTR of BIS the pore volume 0.48 cm^3/g, SSA 221 m^2/g and pore size distributions are very similar to other silica precursors which have been studied. Specifically, the properties of this sample in Figure 3.3 are similar to the silica precursors of Nanorods[24], SBA-16[25] and rice husks [26] (reader directed to SI Table S1. This was a promising indicator that like these other materials silicon derived from BIS will be a promising candidate for anode applications.

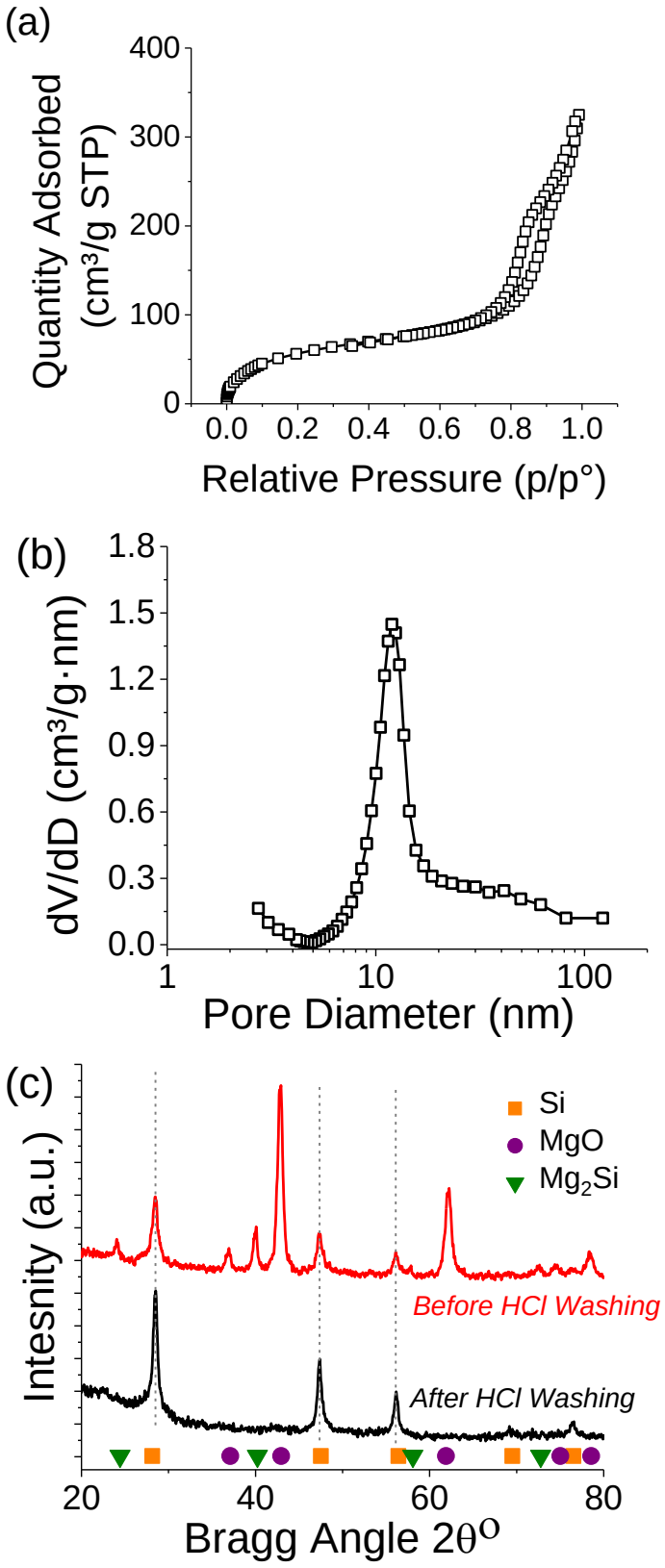

Figure 3.3. (a) N_2 absorption isotherm, (b) BJH pore size distribution of porous silicon product of BIS reduced for 6 hours at 650 °C with a stoichiometric ratio of 2.5:1 ($Mg:SiO_2$). (c) XRD of reaction products before and after HCl washing. [10]

3.3.3 Study of reduction time

The effect of reduction time was investigated, as discussed above within the literature reduction times from 30 minutes[27] up to 12 hours.[28],[29] are reported and the total reduction time is dependant on the samples being reduced. For this reason a range of 1 hour to 10 hours was studied to encompass almost the whole range of potential reduction times required.

Figure 3.4 shows that 1-hour reaction time had produced mesoporous silicon and average pore diameters around 10 nm. For longer reduction times, the porosity (pore sizes, pore volumes, specific surface areas) and the silicon crystallite sizes (obtained from Scherrer analysis of the diffractograms) did not change between 1-10 hours (Figure 3.4 and Table 3.2). Consistent with previous studies it was found that reaction time between 1 and 10 hours did not affect the silicon yield with all products comprising of 57-65% silicon. We determine that reduction times longer than 1 hour do not affect the silicon/silica composites produced, in terms of purity, pore properties and crystallite size.

Table 3.2 Summary of Figure 3.4 for the kinetic study of, 2.5:1 Mg:SiO_2 stoichiometry reacted between 1 and 10 hours at 650 ºC. APD=Average Pore Diameter. Scherrer analysis was calculated from diffraction patterns in Figure 3.4(d).

Reaction Time (h)	BET SSA (m^2/g)	BJH PV (cm^3/g)	APD (nm)	wt% Si	Si_{Cry} Size (nm)
1	232	0.50	10	65	12
3	181	0.46	13	57	11
6	221	0.48	13	57	10
10	186	0.49	14	60	12

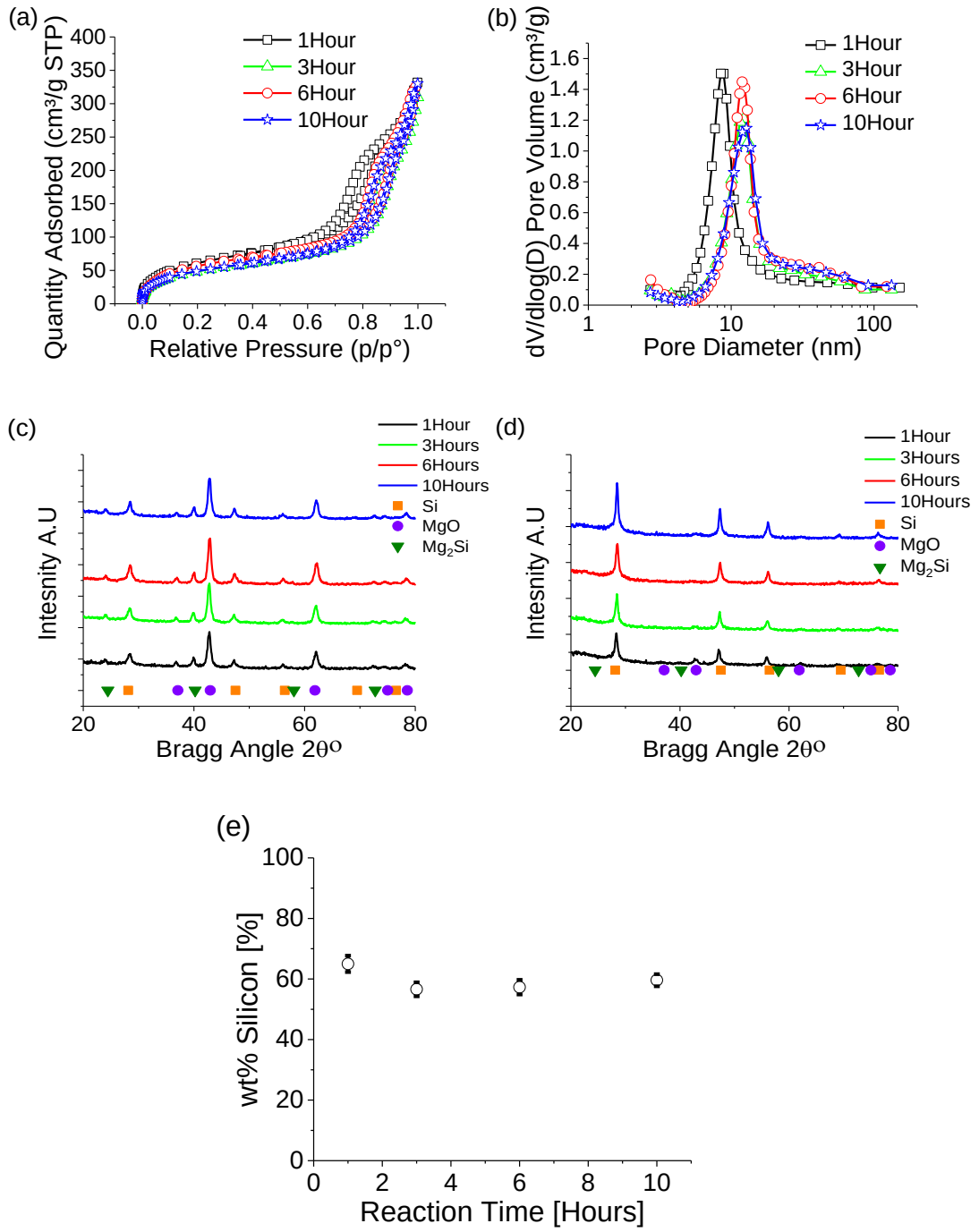

Figure 3.4. Characterisation of silicon produced during kinetic study of, 2.5:1 Mg:SiO_2 stoichiometry reacted between 1 and 10 hours at 650 ºC. (a) N_2 absorption Isotherm, (b) BJH pore size distribution, (c) XRD of reaction products before washing with HCl, (d) XRD of reduction products after washing with HCl, (e) purity of silicon samples.[10]

3.3.4 Study of reduction temperature

As the MgTR temperature is a key parameter, controlling the reaction pore evolution, it was investigated next. The onset of reduction reaction is known to take between 400 and 540 ^{o}C depending on the silica source used.[26],[30] Therefore a lower limit of 550 ^{o}C was selected for this study into reduction temperature. We show below that above 950 ^{o}C product nano structural properties are lost so this was the upper temperature investigated. [31],[30] The reduction temperature had an important effect on all aspects of product silicon morphology as presented in Table 3.3 and Figure 3.5. Table 3.3 shows a decrease in surface area from 400 to 65 m^2/g over the temperature range. The overall pore volume remained unchanged between 550 ^{o}C and 750 ^{o}C at 0.50 cm^3/g, which decreased to 0.35 and 0.10 cm^3/g respectively for reaction temperature of 850 and 950 ^{o}C. The trend in surface area is related to the pore sizes. Smaller pores contribute a higher surface area for the same overall pore volume. Therefore, the increase in pore diameter and decrease in pore volume lead to the lower surface areas observed for the samples reduced at higher temperatures. This evolution of porosity with MgTR temperature is of great importance and it is discussed in detail below (Figure 3.5(e)). The purity of silicon product linearly increased from 29-87 wt% from 550 – 850^{o}C (Figure 3.5 (e)) and then between 850-950 ^{o}C it begins to plateau. A clear correlation was observed between the reduction temperature and the increase in pore diameters of silicon from 4 nm at 550 ^{o}C to 34 nm at 850 ^{o}C (Figure 3.5 (b)).

$$SiO_2 + Mg_2Si \rightarrow 2Si + 2MgO \qquad \text{Equation (3.3)}$$

The yield of pure silicon increased with the temperature. At high temperatures (>850 ^{o}C), any magnesium silicide formed, gets converted to silicon via Equation (3.3). This can be seen in Figure 3.5 (c) where the relative intensity ratio of the Mg_2Si peak gets reduced at higher temperature, and is consistent with the literature.[30] Temperatures <850 ^{o}C are not sufficient enough to fully convert the silicide and hence they can be observed in the XRD results (before acid etching). After acid etching it can be seen that all crystalline components are removed apart from silicon, Figure 3.5 (d).

The average crystallite size increased from 5 nm to 48 nm across the temperature range (Table 3.3), mainly due to sintering[1] at higher temperatures. Although this produced purer silicon at higher temperatures, sintering resulted in the loss of

porosity. This suggests that MgTR temperature between 750 and 850 ^{o}C can provide an optimum between high porosity and high purity. [1]

Table 3.3. Summary of Figure 3.5 for the thermodynamic study of, 2.5:1 Mg:SiO_2 stoichiometry reacted 6 hours at temperatures between 550 and 950 ^{o}C. USAXS data presented in Figure S 3.2. [10]

Reaction Temp (^{o}C)	BET SSA (m^2/g)	BJH PV (cm^3/g)	APD (nm)	wt% Si	Si_{Cry} Size (nm)	USAXS Particle Size	
						Level 1 (nm)	Level 2 (nm)
550	402	0.48	4	29.0	5	25	413
650	230	0.48	12	57.3	10	40	208
750	185	0.54	13	66.0	13	17	333
850	110	0.35	34	87.0	21	24	323
950	65	0.10	-	89.3	48	71	645

[1] Sintering herein: Describes the heating of one or more silicon crystallites which leads to the fusing to form larger crystallites.

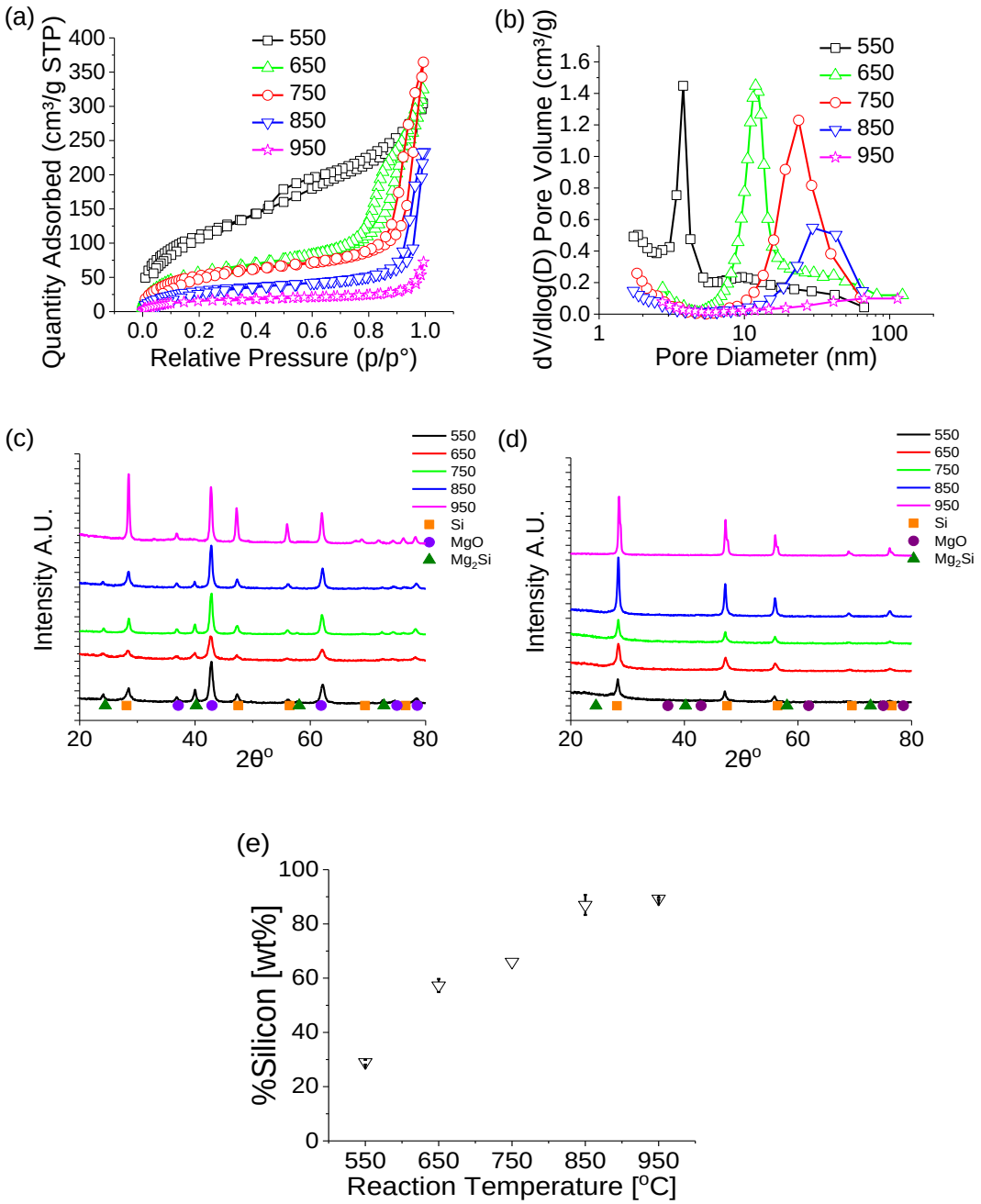

Figure 3.5. Characterisation of silicon produced during thermodynamic study of 2.5:1 Mg:SiO_2 stoichiometry reacted for 6 hours between temperatures of 550-950 °C. (a) N_2 absorption Isotherm, (b) BJH pore size distribution, (c) XRD of reaction products before washing with HCl, (d) XRD of reduction products after washing with HCl, (e) purity of silicon sample. [10]

3.3.5 Study of reduction stoichiometry

The MgTR of silica has a stoichiometric ratio of 2:1 Mg:SiO_2 if the reaction progresses without any side reactions (see Equation (3.1)). However, side reaction and the formation of magnesium silicide usually decreases the silicon yield and perhaps affects the porosity. We desired to study the effect of Mg:SiO_2 much more deeply than has previously been reported. Previous studies have neglected to systematically investigate the stoichiometry and the effect on reduction yield and product properties is not understood.[31] Bariati et al[30][32] have shown that a slight molar excess 2.05:1 Mg:SiO_2 therefore the range in this study was selected to investigate stoichiometry around this ratio. In order to study this effect, the Mg:SiO_2 ratio was varied from 1.5 to 3.5 and the results are shown in Figure 3.6 and Table 3.4. Increasing the stoichiometric ratio from 1.5 – 2.5:1 increased the pore sizes from 4 nm to 13nm, but maintained the size distribution profile. Increasing the stoichiometric ratio to 3:1 resulted in a bimodal distribution of mesopores. The pores cantered around 13 nm decreased with a increase in larger mesopores (>10 nm). Increasing the stoichiometric ratio further to 3.5:1 resulted in even broader distribution of pores between 10-100 nm. Throughout this broadening of mesopore size distribution, pore volumes and surface areas did not show any dramatic changes unlike those seen when the MgTR temperature was varied Figure 3.6 (c). Figure 3.6(d) shows clearly that all crystalline components were removed after the acid etching. The yield of the silicon formed increased between 1.5 and 2.25:1 stoichiometry from 24 to 69 wt%. Increasing the stoichiometry further decreased the yield of the silicon back to 23 wt% for the 3.5:1 ratio (Figure 3.6 (e)). As excess magnesium is available (>2.25:1), the side reactions of the formation of magnesium silicide reduces the yield of silicon (Figure 3.6 (e)).

Table 3. 4. Summary of Figure 3.6 for the stoichiometric study of, Mg:SiO_2 stoichiometry between 1.5-3.5:1 Mg:SiO_2 reacted 6 hours at 650 ºC

Stoichiometric Ratio (Mg:SiO_2)	BET SSA (m^2/g)	BJH PV (cm^3/g)	APD (nm)	wt% Si	Si_{Cry} Size (nm)
1.5:1	340	0.50	4	24	11
2.0:1	315	0.55	6	68	6
2.25:1	217	0.56	12	69	10
2.5:1	230	0.48	13	57	10
3.0:1	206	0.43	12*	48	9

3.5:1	271	0.57	28*	23	15

*Bimodal distribution so representative of pore size distribution, see Figure 3.6(b)

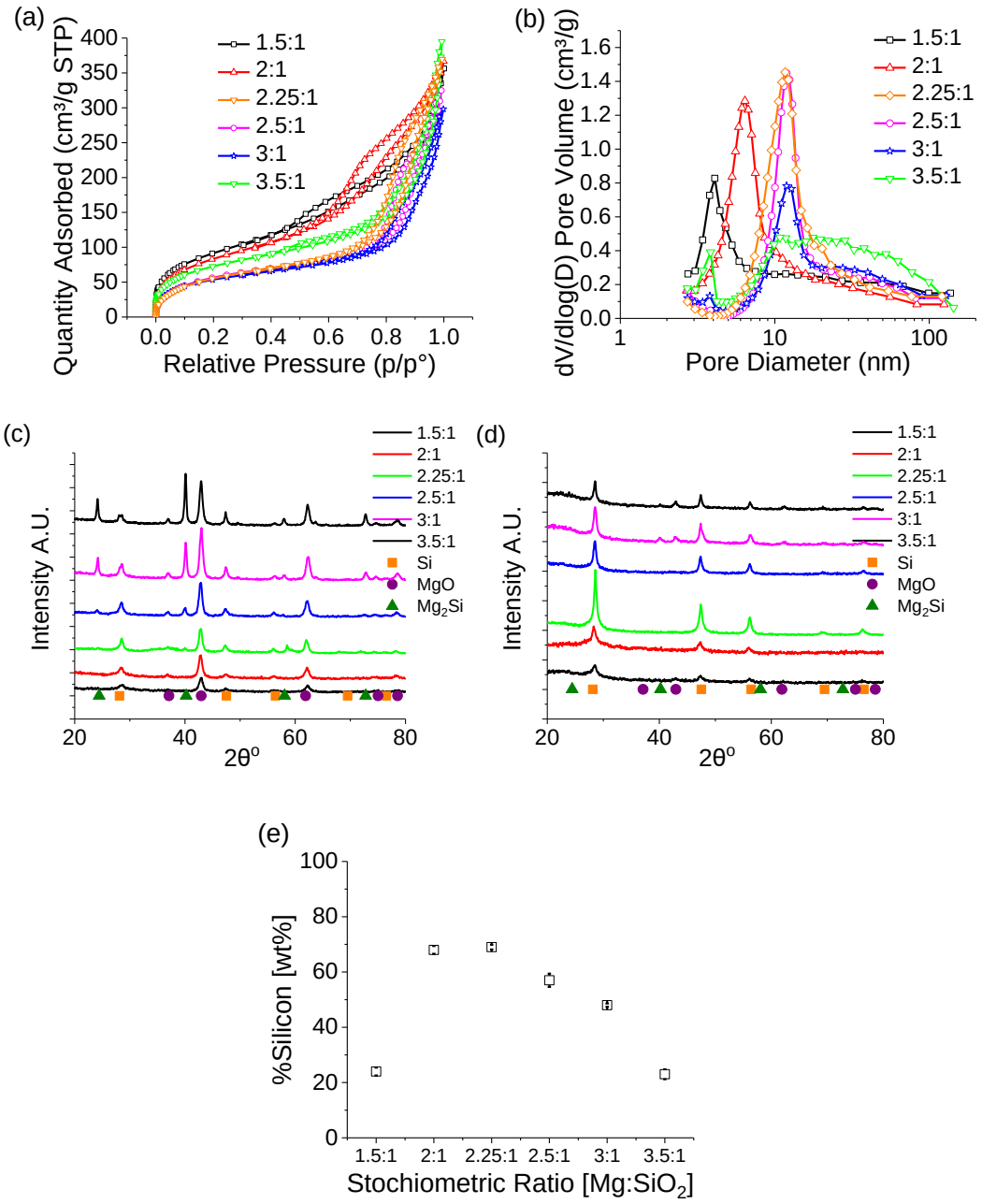

Figure 3.6. Characterisation of silicon produced during stoichiometric study for stoichiometries between 1.5-3.5:1 Mg:SiO_2 reacted for 6 hours at 650 ºC. (a) N_2 absorption Isotherms, (b) BJH pore size distributions, (c) XRD of reaction products before washing with HCL, (d) XRD of reduction products after washing with HCl, (e) purity of silicon samples. [10]

3.3.6 Summary

In summary the temperature affects the purity and silicon crystal sizes via sintering, which in turn affects the porosity. Stoichiometry of the reduction also has an effect on the formation magnesium silicide by-product, which affects the purity and the pore network of silicon formed. Figure 3.7 summarises the two key parameters of reduction temperature and stoichiometry and their effects on product properties. It is clear that the reaction chemistry and the processing conditions affect the properties of silicon, where the porosity and purity are interlinked with the crystallite size and the by-products formed.

In the next section, we aim reveal these interdependencies by providing a mechanistic understanding.

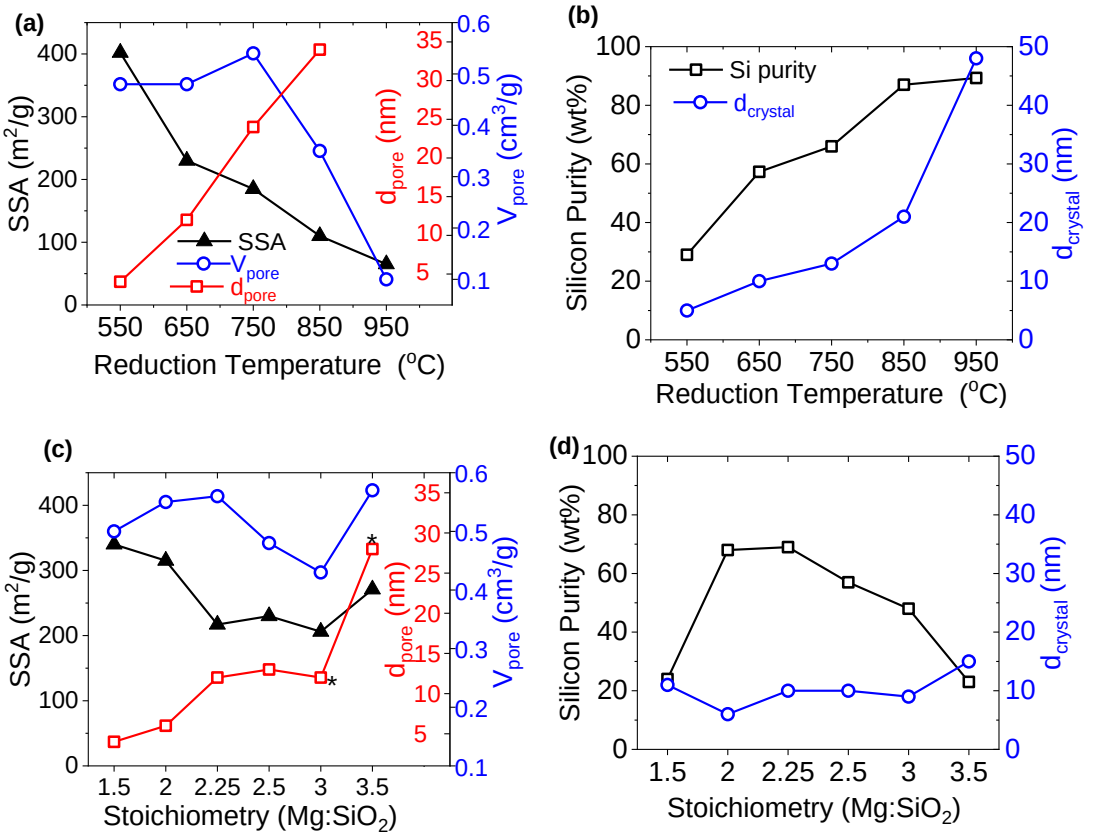

Figure 3.7. Effect of reduction temperature performed at a 2.5:1 Mg:SiO_2 stoichiometry (a, b) and feedstock stoichiometry at reduction temperature of 650 °C (c, d). On (a, c) BET specific surface area (SSA), BJH pore volume (V_{pore}) and average pore diameter (d_{pore}) and (b, d) silicon purity and crystallite size. * Represents bimodal distribution of pore diameters for samples reduced at 3:1 and 3.5:1 Mg:SiO_2 (see Figure 3.6 (b) for pore size distribution).

3.4 Understanding Magnesiothermic reduction

Our results show that the two key factors affecting the porosity, the purity and the morphology of silicon produced from MgTR are the silicon crystal size and the amount of magnesium silicide (Mg_2Si) by-produced produced. We propose a mechanistic view that connects the MgTR process conditions to the physicochemical properties of silicon via the silicon crystal sizes and Mg_2Si formation (see Figure 3.8). Below we explain this mechanism by discussing the roles of both the silicon crystal size and Mg_2Si in porous silicon formation.

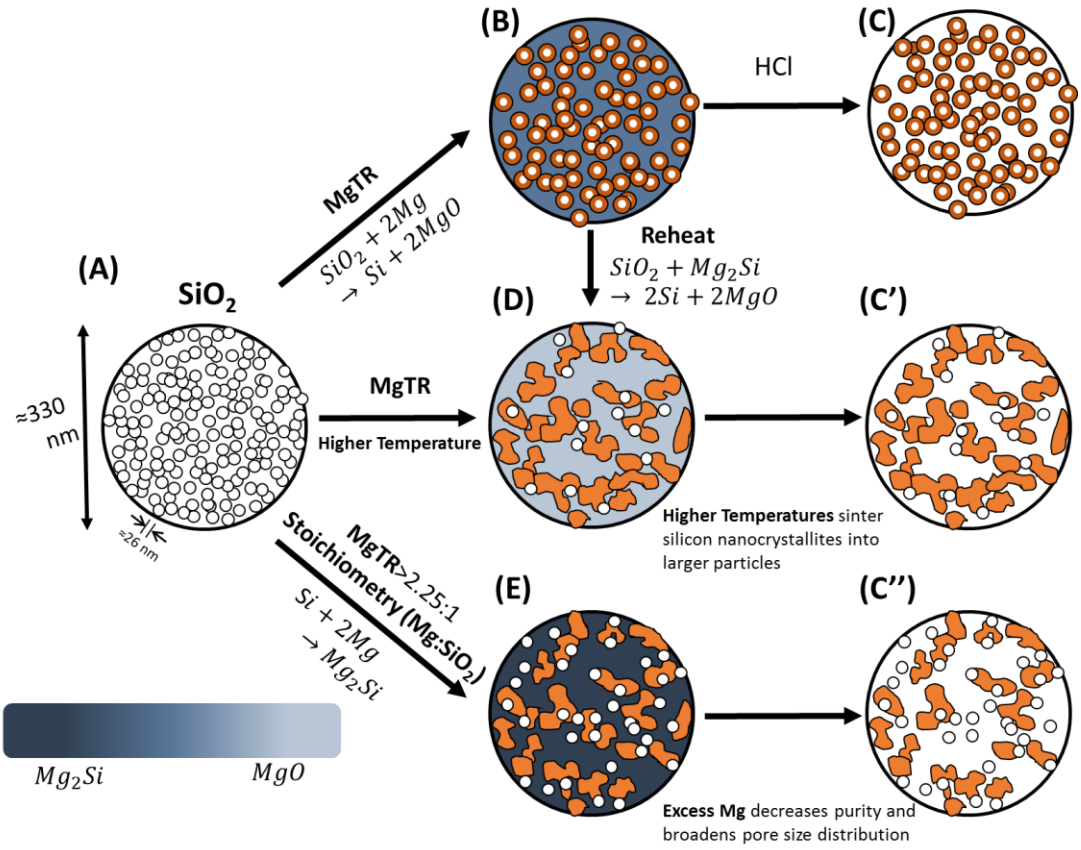

Figure 3.8. A schematic showing the formation and evolution of silicon crystals (C, C' and C'') from precursor BIS silica and the effect of temperature and stoichiometry on pore evolution. White particles with black outlines show primary silica particles. The dark black outline indicates a secondary particle. Orange colour denotes pure silicon nanocrystals. Other products (MgO, Mg_2Si and their mixture) are shown in shades of blue corresponding to the colour bar shown in the bottom left – darkest blue represents pure Mg_2Si and the lightest MgO (any colour in between represents a mixture of these two products).

3.4.1 The role of Si crystal size in controlling porosity

Characterisation of BIS using SEM and USAXS reveal that it is a hierarchically structured material with primary particles of ~26 nm, which aggregate to form secondary particles ~330 nm (Figure 3.2 (a-d) and Table 3.1). These features are depicted in Figure 3.8 (A). As observed from the results above, the same starting materials (BIS in this case, Figure 3.8 (A)) produces widely varying porous silicon as shown in Figures 3.5-7. We propose that this transformation of primary silica particles within the secondary particles occurs from the surface to the core (see the core-shell particles shown in Figure 3.8B)). The temperature of MgTR controls the extent of this conversion, while the removal of oxygen (via MgO) from silica creates mesoporosity (Figure 3.8 (C)). Higher temperatures of MgTR (>750 ^{o}C) induce sintering of silicon nanocrystals (Figure 3.8 (D)), while also increasing the purity of silicon. The sintering leads to large crystals and concomitant reduction in porosity (Figure 3.8 (C')). This is a key finding, especially because it can enable monitoring/controlling MgTR by measuring silicon crystallite size as a suitable measure of product quality. This mechanism is explained below by focusing on the morphology and the crystallite sizes.

For MgTR temperatures up to 750 ^{o}C, the spherical morphology of the BIS secondary particles appears to be maintained throughout the reduction (Figure 3.9 and Figure S 3.1), while also showing 'speckles' on these particles. These speckles are likely to correspond to the silicon crystallites and as the MgTR temperature is increased, more silica is reduced to silicon, thereby increasing these features. The sample produced at 750 ^{o}C shows that the parent ~330 nm spherical particles with constituent smaller crystallites (Figure 3.9 (c-d)). This observation is supported by the Scherrer analysis, which shows the silicon crystallites sizes systematically increase from 5 nm to 48 nm (Figure 3.9(f)) as the MgTR temperature is increased. When these particles are large enough (>10 nm), they are also visible via SEM (e.g. for MgTR temperature ≥750 ^{o}C). USAXS results also show that the primary particles between 17-71 nm are present (Figure 3.9(f)). which represent the primary silica particles from BIS as well as the silicon crystals. As USAXS cannot discriminate between silicon crystals and silica primary particles, the measurement covers both components. As samples reduced at 550 and 650 ^{o}C contain 40-70% of unreacted silica, USAXS measurements are overshadowed by the combination of silicon crystallites and silica particles, hiding the silicon crystals. For sample produced at 850 ^{o}C, although the silicon crystallites are clearly visible by SEM (21 nm, see Figure 3.9 and Figure S3.1), the parent particles

of ~330 nm begin to disappear (Figure S 3.1(d)). This is caused by higher conversion of silica to silicon and of sintering of silicon crystals. As this sintering continues at 950 ^{o}C, the parent particles disappear almost completely and all we can see is the 48 nm silicon crystals and fused (much larger) particles (Figure S3.1 (e)), leading to a loss of porosity. These results explain the observed trends with porosity, purity and silicon crystal sizes in the temperature study above shown in Figure 3.5 (b and e).

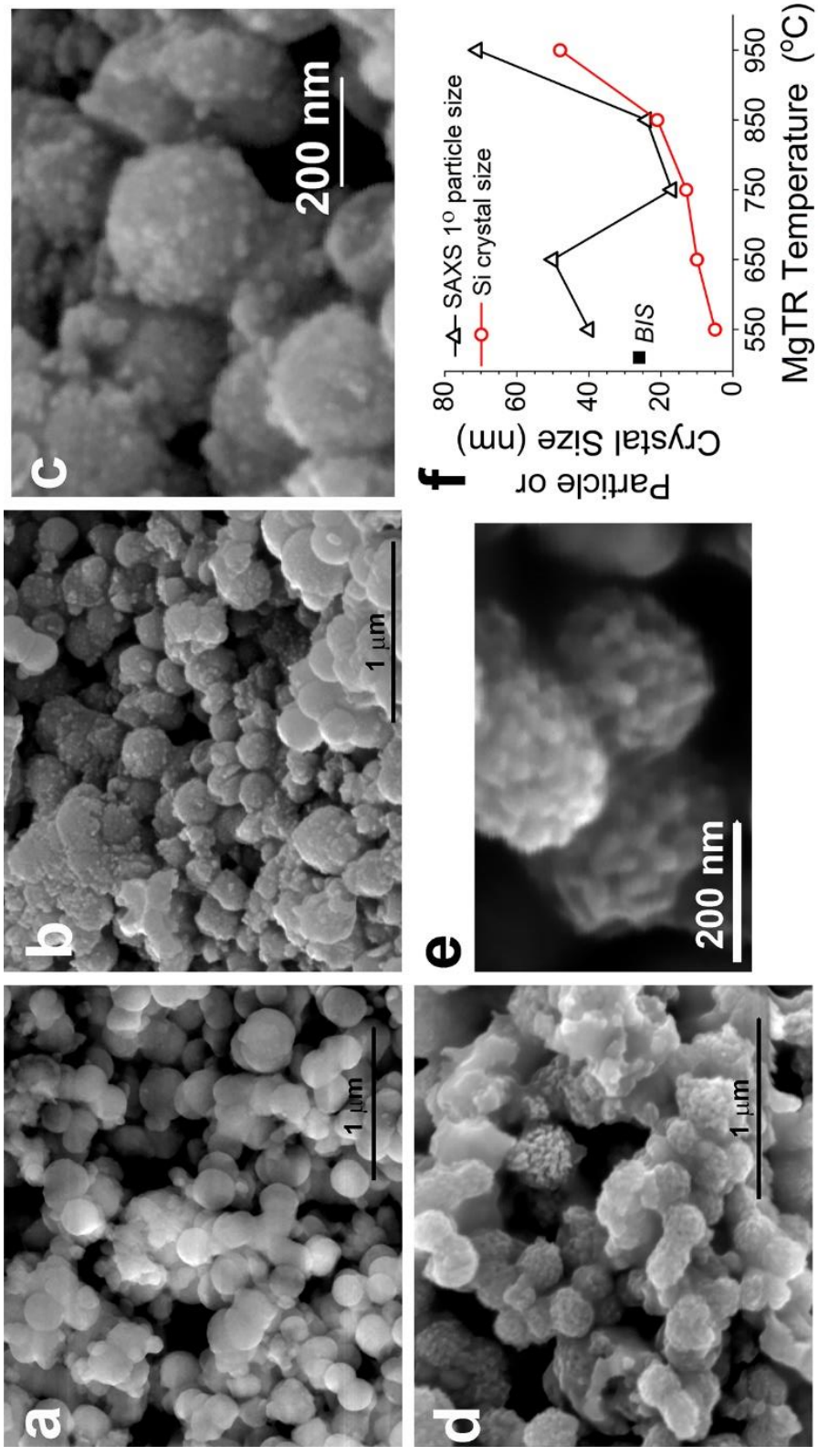

Figure 3.9. SEM images of (a) unreacted feedstock BIS, and porous silicon reduced at temperatures (b-c) 550 °C and (d-e) 750 °C. (f) A comparison of primary particle size obtained from USAXS and crystallite size obtained from XRD for mesoporous silicon samples reduced between 550-950 °C. See Figure S 3.1 and Table 3.3 for full details. [10]

3.4.2 The effect of Mg_2Si on pore evolution

The stoichiometry ($Mg:SiO_2$) also controls the process by affecting the production of Mg_2Si by-product (Equation (3.2)). The purity of silicon can be maximised by using an optimum stoichiometry thereby minimising the formation of Mg_2Si, as discussed above. However, as Mg_2Si is removed by etching (acid washing), it also affects the porosity as seen in Figure 3.6 where broader pore size distributions are observed at higher $Mg:SiO_2$ ratios. In order to test the role of Mg_2Si in the entire process additional experiments were performed as follows. $Mg:SiO_2$ ratios were explored at MgTR temperatures of 650 and 850 ^oC. As was shown above in section 3.3.4 at higher reduction temperatures the purity of the samples is increased and the relative ratio of Mg_2Si is reduced due to the solid-state reaction in equation 3.3.

$$SiO_2 + Mg_2Si \rightarrow 2Si + 2MgO \qquad \text{Equation (3.3)}$$

As reported above in Figure 3.7 (and replotted in Figure 3.10(a)), for MgTR at 650 ^oC, the higher $Mg:SiO_2$ stoichiometry leads to loss in purity from the side reaction producing Mg_2Si by-product. This was further confirmed by the analysis of relative intensities of Mg_2Si and silicon peaks (Figure 3.10(b)). However, for the same stoichiometries at 850 ^oC, the purity changes only slightly. This aligns with the slight increase in the relative intensities of the Mg_2Si and silicon peaks. These results strongly support that the conversion of Mg_2Si (Equation (3.3)) is responsible for increasing silicon yield at higher temperature and that a temperature >650 ^oC drives this conversion.

As the $Mg: SiO_2$ ratio was increased for MgTR at 850 ^oC, an increased amount of Mg_2Si was formed, which converted to silicon. This leads to large increases in the silicon crystal size (from 10 nm at 2:1 to 30 nm at 3:1, see Figure 3.10(c) as well as a broadening of pore size distribution (Figure 3.10(d)). The broadening of pore sizes at higher ratios of magnesium is consistent with the findings at 650 ^oC (Figure 3.6). These observations are consistent with the mechanism proposed in Figure 3.8 (see the conversion of A to D to C' and A to E to C'').

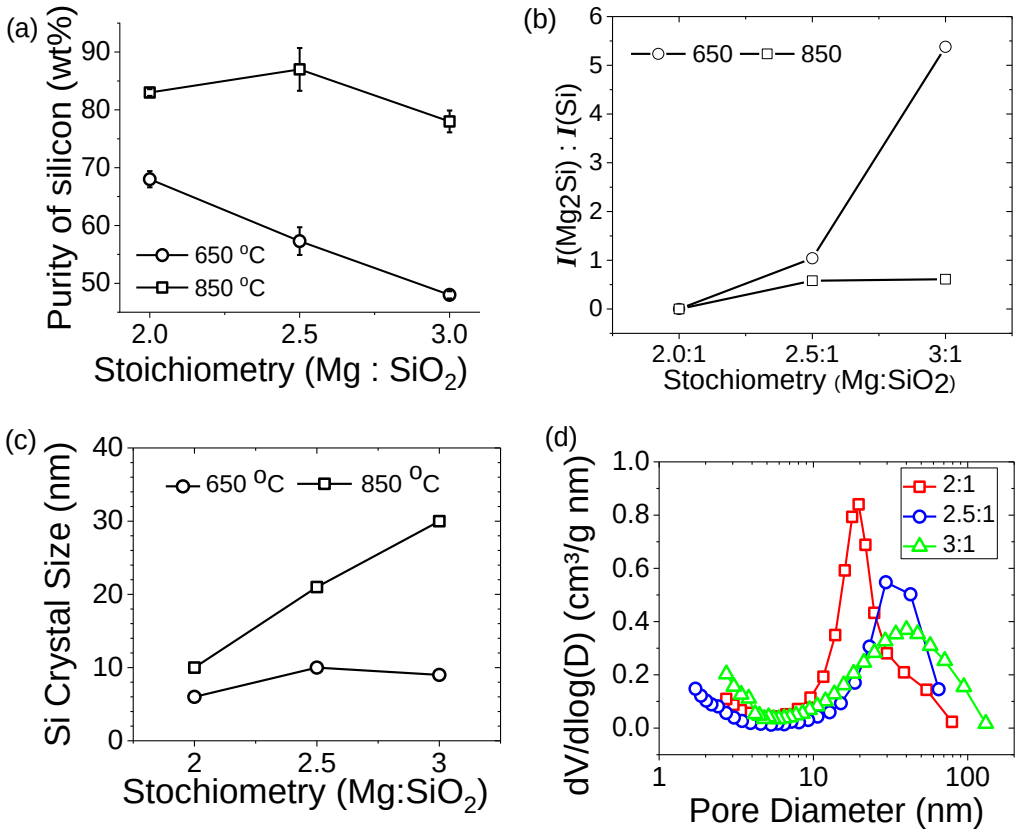

Figure 3.10. Silicon produced at stoichiometric ratios 2,2.5,3:1 for reduction temperatures of 650 and 850 °C (a) purity of product (wt%). (b) ratio of Mg_2Si to Si peaks in pre acid washing XRD (c) crystallite size (d) BJH pore size distribution. Full data set provided in Figure S 3.1 and Figure S 3.3. [10]

In order to further verify this mechanism, two additional samples were produced as follows. Firstly, a sample called *650-E-850* was prepared by performing MgTR at 650 °C for 6 hours and then cooling it to room temperature. The sample was then etched with acid to obtain porous silicon; this silicon was then heated to 850 °C for 6 hours and cooled to room temperature for analysis. Secondly, *650-850* was prepared similar to *650-E-850*, but without any acid etching (Figure 3.8 pathway B to D). The results of this experiment are presented in Figure 3.11 and summarised in Table 3.5.

Table 3.5. The effect of removal (or not) of Mg_2Si intermediate. A stoichiometry of 2.5:1 and reduction time of 6 hours in each step was used. 'E' denotes etching via acid washing. Full results are shown in Figure 3.11.

Sample	BET SSA (m^2/g)	BJH PV (cm^3/g)	APD (nm)	wt% Si	Si_{Cry} Size (nm)
650	230	0.48	12	57	10
850	110	0.35	34	87	21
650-E-850	155	0.42	14	59	11
650-850	107	0.24	38	79	25

The *650-E-850* sample appeared to be identical to the sample reduced at 650^{o}C (see no change in the purity, silicon crystal size, pore volume or the pore size distribution in Figure 3.11 and Table 3.5), while very different to the sample prepared at 850 ^{o}C. This clearly suggests that once the Mg_2Si was removed, there was no further change in the sample, even upon heating to higher temperature. This observation, along with the increase in silicon yield for the *650-850* sample compared to the 650 sample, means that at high MgTR temperatures, the predominant reaction occurring is the reaction Equation 3.3 (the conversion of silicide to silicon). Further, the *650-850* sample appears to be similar to the sample prepared directly at 850 ^{o}C. Noting that *650-850* sample was reduced for 6 hours at each temperatures (12 hours in total), while the sample prepared directly at 850^{o}C was reduced only for six hour, it further supports that the purity of the silicon produced via MgTR is thermodynamically and not kinetically limited.

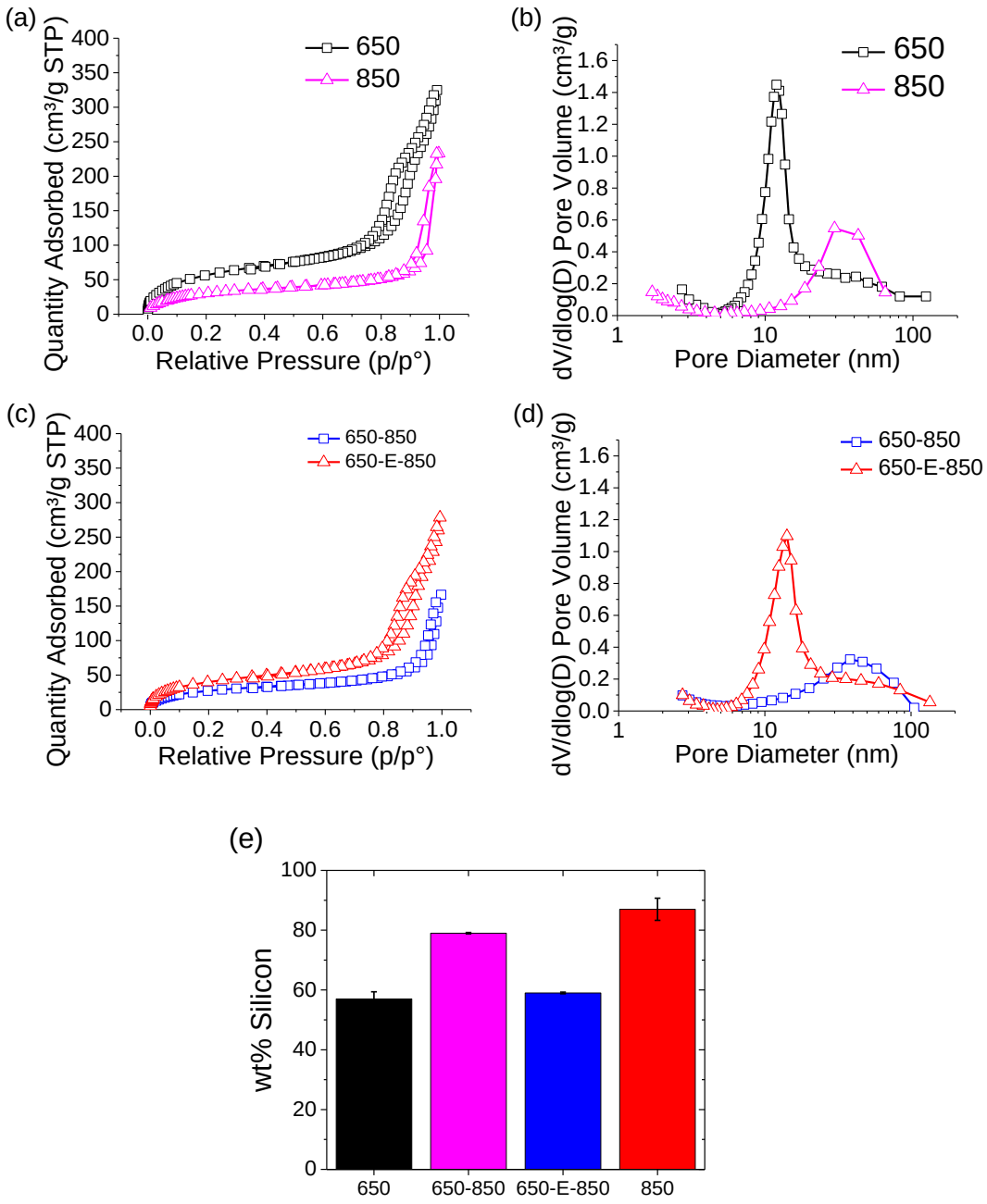

Figure 3.11. Characterisation of samples used to understand the thermodynamic evolution of the MgTR reaction, samples include silicon reduced at 650 and 850ºC, Silicon reduced at 650 ºC washed in HCl acid then heated to 850 ºC under argon (650-E-850), and silicon reduced at 650 ºC allowed to cool then reheated to 850ºC (650-850). (a)(c) N_2 absorption Isotherms, (b)(d) BJH pore size distributions, (e) purity of silicon samples. [10]

In summary, in this section, it has been shown how the silicon crystal size and the formation/conversion of Mg_2Si control the critical quality attributes of silicon produced (Figure 3.8), such as the purity and the porosity (surface area, pore volume and pore size distribution). It was also shown how these features relate to the MgTR conditions; by exploiting this knowledge, it was possible to produce porous silicon with widely varying properties from a single feedstock (BIS in this case). In order to further validate the utility of this mechanism, below, we present the results from using a range of silica feedstocks for producing silicon via MgTR.

3.5 Application to other precursors

The mechanism proposed in Figure 3.8 suggests that the arrangement of the primary silicon nanocrystallites and their formation are the critical factors determining the pore properties of the product. It has been shown that this is the case for one type of silica (BIS), to test this mechanism this section studies reduction of alternative silica precursors, in particular silica precursors which initially do not have a hierarchical structure or are not porous. The following three commercial grade silicas (precipitated silica, silica gel and porous silica) and quartz were selected. The porous properties of these silica precursors are fully characterised in Figure 3.12. In the above literature review it was highlighted that characterisation of silica precursors is often lacking, and this characterisation of these properties is crucial to understand the formation of porous silicon via MgTR. Note that these silicas are not known to exhibit hierarchical structures that are seen for BIS and that quartz did not contain any porosity (Figure 3.12). These silica precursors with varying initial porosities were reduced at 650 and 850 ^{o}C to study the effect of silica precursor properties on the silicon purity porosity.

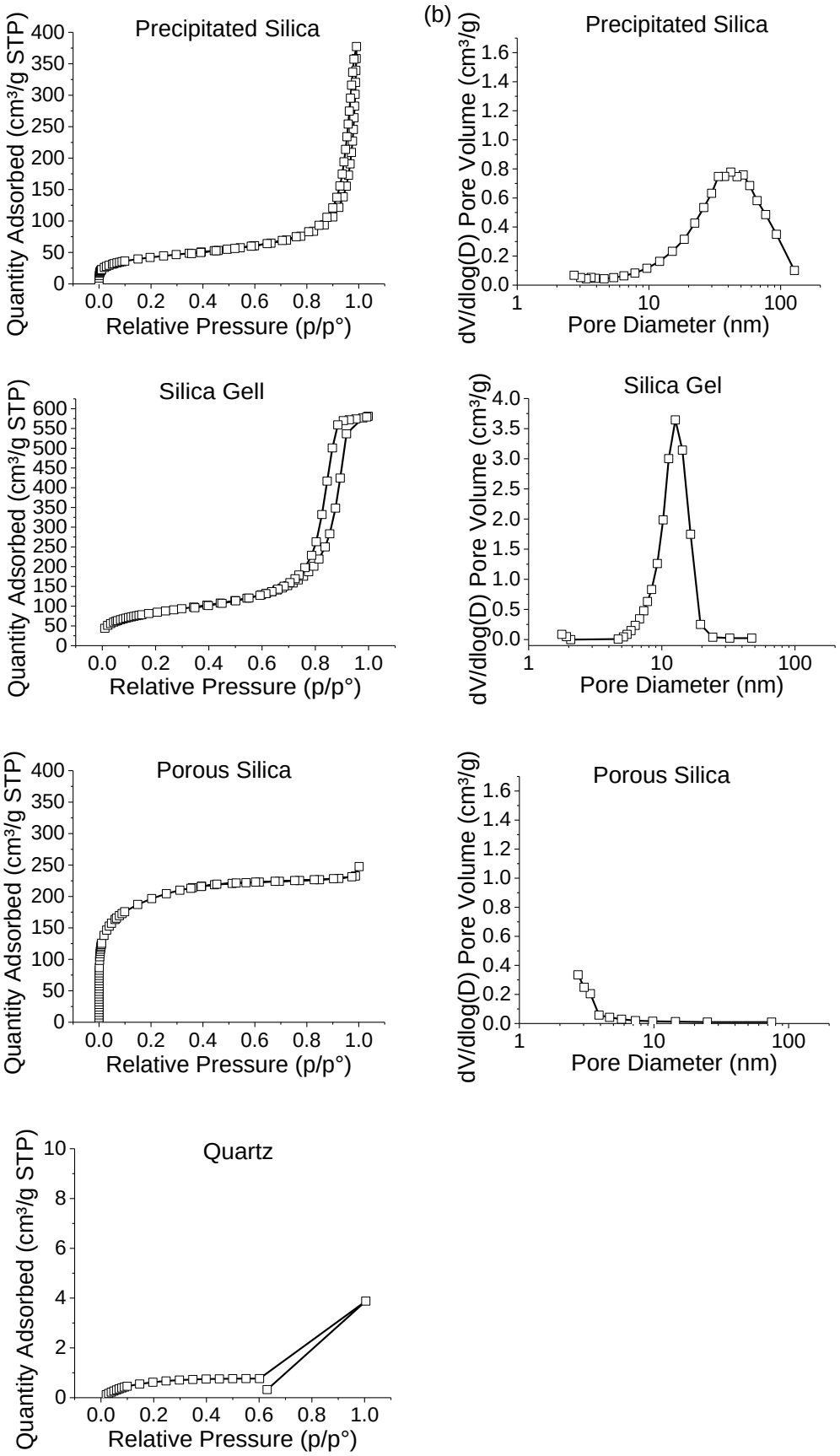

Figure 3.12. N_2 absorption Isotherms and BJH pore size distributions of silica sources[10]

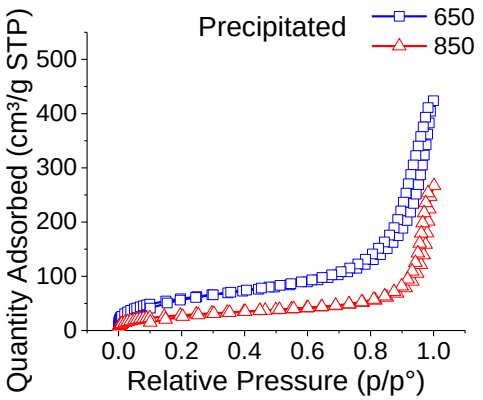
Precipitated
650
850
Quantity Adsorbed (cm³/g STP)
Relative Pressure (p/p°)
0
100
200
300
400
500
0.0
0.2
0.4
0.6
0.8
1.0

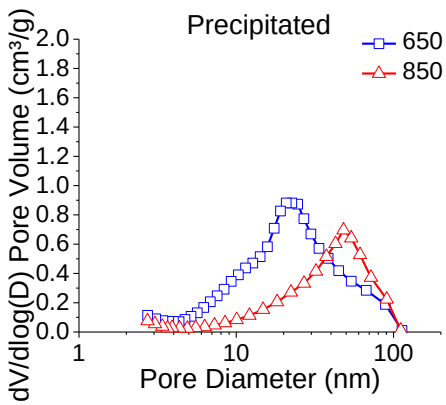
Precipitated
650
850
dV/dlog(D) Pore Volume (cm³/g)
Pore Diameter (nm)
0.0
0.2
0.4
0.6
0.8
1.0
1.2
1.4
1.6
1.8
2.0
1
10
100

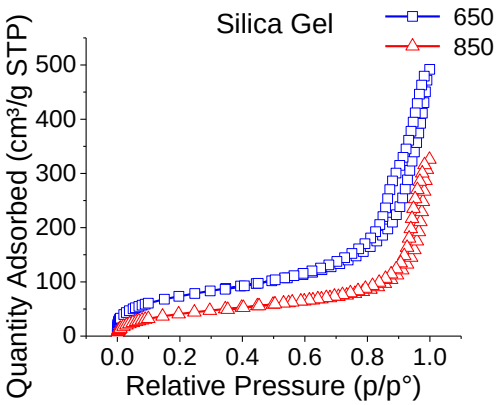
Silica Gel
650
850
Quantity Adsorbed (cm³/g STP)
Relative Pressure (p/p°)
0
100
200
300
400
500
0.0
0.2
0.4
0.6
0.8
1.0

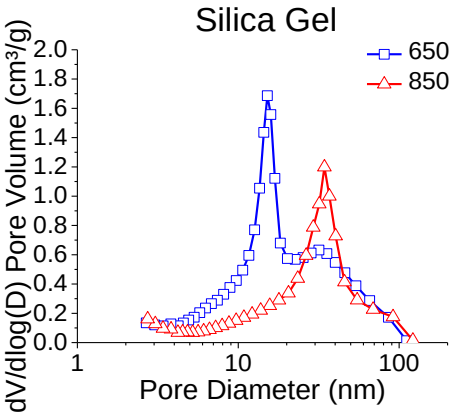
Silica Gel
650
850
dV/dlog(D) Pore Volume (cm³/g)
Pore Diameter (nm)
0.0
0.2
0.4
0.6
0.8
1.0
1.2
1.4
1.6
1.8
2.0
1
10
100

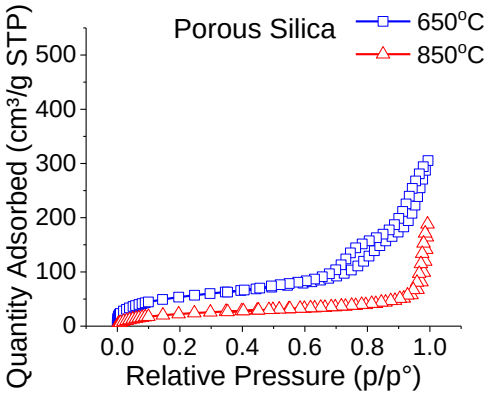
Porous Silica
650°C
850°C
Quantity Adsorbed (cm³/g STP)
Relative Pressure (p/p°)
0
100
200
300
400
500
0.0
0.2
0.4
0.6
0.8
1.0

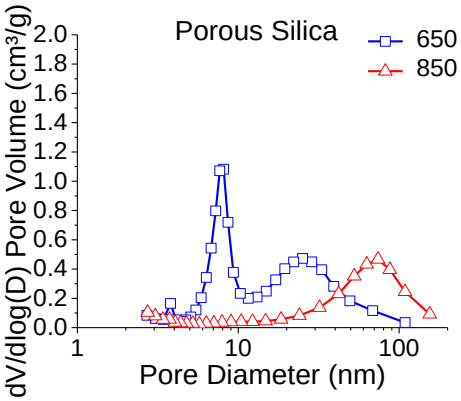
Porous Silica
650
850
dV/dlog(D) Pore Volume (cm³/g)
Pore Diameter (nm)
0.0
0.2
0.4
0.6
0.8
1.0
1.2
1.4
1.6
1.8
2.0
1
10
100

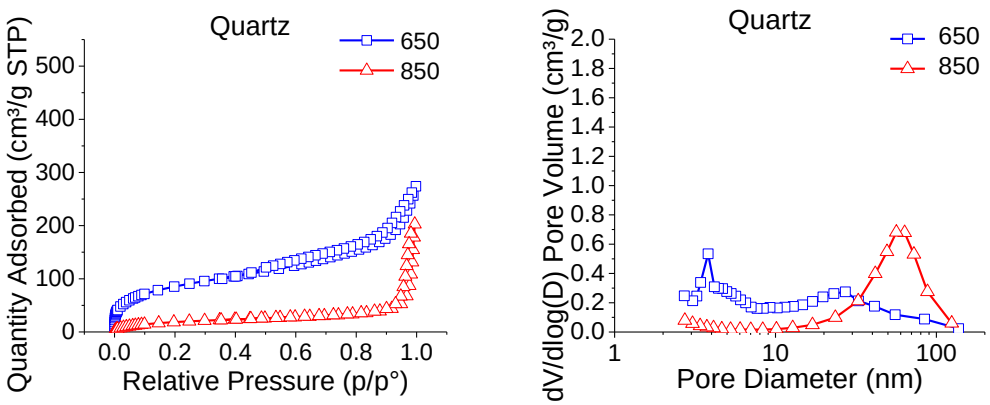

Figure 3.13. N_2 absorption Isotherms and BJH pore size distributions of silicon reduced from variety of silica sources at 650 and 850 ºC. [10]

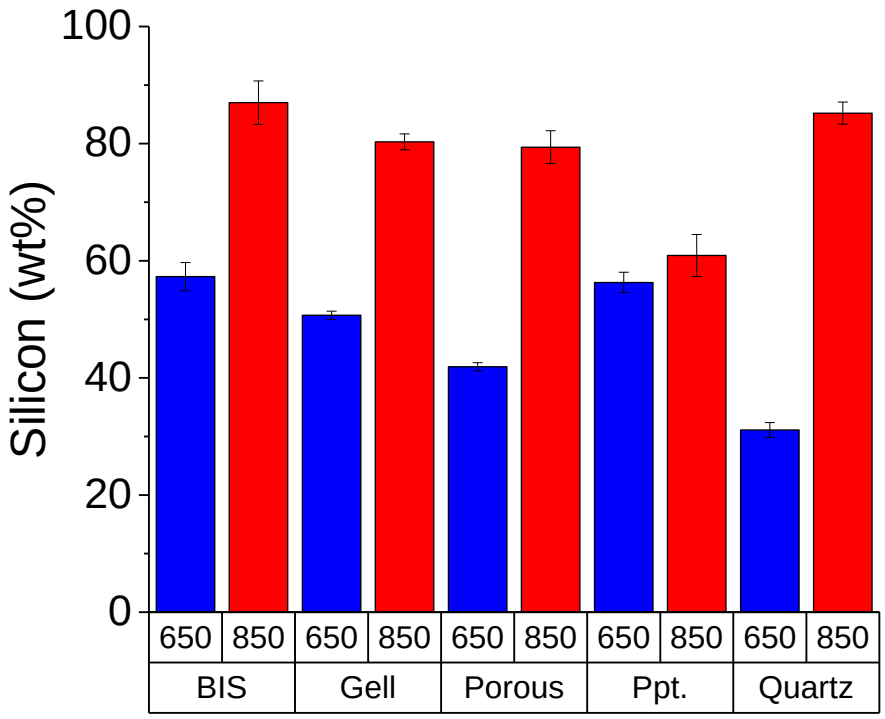

Figure 3.14. Purity of silicon reduced from silica sources at 650 and 850 ºC[10]

Table 3.6 BET SSA, BJH pore volume, purity and crystallite size of silicon reduced at 650 and 850 ºC for different silica precursors. [10]

Precursor	Reduction Temperature (ºC)	BET SSA (m^2/g)	BJH PV (cm^3/g)	wt% Si	Si_{Cry} Size (nm)
Ppt. silica		156	0.56		
Ppt. silica	650	220	0.63	56.3	9
Ppt. silica	850	108	0.40	60.9	19
Silica Gel		264	0.89		
Silica Gel	650	275	0.73	50.7	6
Silica Gel	850	158	0.48	80.3	13
BIS		301	0.16		
BIS	650	216	0.48	57.3	10
BIS	850	110	0.35	87.0	21
Porous SiO_2		725	0.09		
Porous SiO_2	650	205	0.45	41.9	22
Porous SiO_2	850	90	0.27	79.4	28
Quartz	Non-porous				
Quartz	650	310	0.36	31.1	17
Quartz	850	76	0.30	85.2	26

As shown in Figure 3.13 and Table 3.6 without exception, each precursor produced mesoporous silicon, irrespective of the porosity (or not) of the precursors. These results have been observed before, specifically for the reduction of Quartz [11] [33] and mesoporous silica (SBA-15)[34][11][32], however the nature of how new pores have formed within these materials has not been investigated. This clearly highlights that the porosity of the feedstock silica does not control the porosity of silicon produced upon MgTR. The silicon crystal sizes, the porosity and purity of silicon produced from these different silicas were examined, the trends observed with respect to the MgTR temperature were in full agreement with those reported for BIS above and the mechanism proposed in Figure 3.8. For example, the silicon crystal sizes were always larger for MgTR performed at 850 ºC compared to 650 ºC.

Of particular interest is the reduction of the non-porous and crystalline quartz precursor. Although quartz[33],[11] and other non-porous precursors[35] have been reduced to silicon via MgTR before, by thorough characterisation, we are able to demonstrate a relation between the silicon nanocrystals and the porous nature of the

reduction products. In the case of non-porous quartz, the pores in the product can only be produced as a result of the MgTR, the formation of silicon nanocrystallites and the removal of magnesium oxide from around these crystallites. This introduction of mesoporosity (and some macroporosity) in a non-porous quartz sample supports the pore formation mechanism proposed in Figure 3.8. In this quartz-derived structure, all pores are a result of silicon nanocrystals forming during the MgTR process and corresponding loss of oxygen atoms via MgO. We discover that, independent of the pore structure of the precursor silica used, mesoporosity can be induced in the product silicon during MgTR reaction, which is strongly related to the silicon crystallite size. The pore structure is dependent on the interconnectivity of nanocrystallites within silicon particles once magnesia and magnesium silicide are removed.

The mesoporous precipitated silica is also of interest, as the yield for this sample did not increase much between 650 and 850 ^{o}C as the other precursors, just +6%. However, the crystallite size did increase from 8 to 19 nm respectively, as expected from sintering of crystallites at higher temperatures. Due to the increase in crystallite size the pore size distribution increased form a centre at 22 to 50 nm. This finding fits with our presented hypothesis of the relation between crystallite size and pore size distribution in this sample where despite only a small increase in purity, the pore size changed due to the increasing silicon crystal size.

These experiments reinforce the key findings from the above study on BIS and crucially that they apply to a wide variety of porous and non-porous silica sources: Firstly, the overall purity of the silicon product, governed by the extent of the MgTR reaction, is increased by increasing reduction temperature. Secondly, performing MgTR at higher temperature causes sintering and increase in silicon nanocrystal size. Finally, and linked with the findings above, the introduction of silicon nanocrystallites leads to porosity within the product and the size of these mesopores is strongly related to the silicon crystallite size as well as Mg_2Si formation. The introduction of mesopores into reduced quartz exemplifies that initial porosity within the template silica structure is not necessary to produce a porous silicon product. Instead this sample shows that the silicon nanocrystallites produced form a porous structure, and the size and distribution of these crystallites determines the pore properties formed.

3.6 Conclusions

Magnesiothermic reduction is a hard-templating synthesis method which can be used to produce porous silicon from silica templates. The use of HF and poor characterisation of silicon products has led to little understanding of how the MgTR process produces porous silicon.[8]

It has been shown here that although the macrostructure of the silica templates can be maintained through MgTR, the pore structure of the porous silicon is determined by the arrangement of free space between the silicon nanocrystallites formed. The maximum temperature of the reduction is the driving factor of nanocrystallite sintering, as these nanocrystllites sinter the average pore sizes increases. The stoichiometry of the reactants is also a key factor determining the purity of the porous silicon formed. The side reaction (Equation (3.2)) reduces the purity of samples via the formation of Mg_2Si, which is removed during acid washing. The formation and removal of Mg_2Si is shown to broaden pore size distribution in the silicon product. We show that the reduction reaction reaches a thermodynamic equilibrium after 1 hour of reaction and that by increasing the temperature the purity of the samples can be increased. This purity increase is driven by the solid-state reduction of silica with magnesium silicide (Equation (3.3)). The effect of larger silicon crystallites formed leads to larger pores between crystallites and at higher temperatures >850 ^{o}C the degradation of the BIS secondary particle structure.

Herein the formation of mesoporous silicon from previously non-porous quartz silica was characterised. This sample consolidates our theory that the formation of mesopores are between silicon nanocrystallites formed. The reduction of a variety of silica precursors showed an increase in silicon purity and sintering of nanocrystallite sizes at higher reduction temperatures, in turn this leads to an increase in pore size across the study.

With the detailed reaction design pathway for MgTR we have outlined, particularly the porous nature of these samples, future work can be more systematically applied to produce silicon products with targeted porous properties. This ability is exactly what has been missing from previous literature studies. Furthermore, the easily obtained crystallite size can be used to provide a quality control indicator as to the porous nature of the product.

The anode performance of mesoporous silicon's produced in this study will be evaluated in Chapter 4.

3.7 References

[1] J. Christensen, J. Newman, *J. Solid State Electrochem.* **2006**, *10*, 293.

[2] X. Zhang, W. Shyy, A. Marie Sastry, *J. Electrochem. Soc.* **2007**, *154*, S21.

[3] M. Ge, J. Rong, X. Fang, C. Zhou, *Nano Lett.* **2012**, *12*, 2318.

[4] Y. Yao, M. T. McDowell, I. Ryu, H. Wu, N. Liu, L. Hu, W. D. Nix, Y. Cui, *Nano Lett.* **2011**, *11*, 2949.

[5] X. Li, M. Gu, S. Hu, R. Kennard, P. Yan, X. Chen, C. Wang, M. J. Sailor, J. Zhang, J. Liu, *Nat. Commun.* **2014**, *5*, 1.

[6] M. Ge, X. Fang, J. Rong, Chongwu Zhou, *Nanotechnology* **2013**, *24*.

[7] M. Ge, Y. Lu, P. Ercius, J. Rong, X. Fang, M. Mecklenburg, C. Zhou, *Nano Lett.* **2014**, *14*, 261.

[8] J. Entwistle, A. Rennie, S. Patwardhan, *J. Mater. Chem. A* **2018**, *6*, 18344.

[9] R. A. Rapp, A. Ezis, G. J. Yurek, *Metall. Trans.* **1973**, *4*, 1283.

[10] J. E. Entwistle, G. Beaucage, *J. Mater. Chem. A* **2020**, DOI 10.1039/c9ta13633a.

[11] J. Liang, X. Li, Z. Hou, W. Zhang, Y. Zhu, Y. Qian, *ACS Nano* **2016**, *10*, 2295.

[12] M. Barati, S. Sarder, A. McLean, R. Roy, *J. Non. Cryst. Solids* **2011**, *357*, 18.

[13] H. Wu, N. Du, X. Shi, D. Yang, *J. Power Sources* **2016**, *331*, 76.

[14] J. Ilavsky, F. Zhang, A. J. Allen, L. E. Levine, P. R. Jemian, G. G. Long, *Metall. Mater. Trans. A* **2012**, *44A*, 68.

[15] J. Ilavsky, F. Zhang, R. N. Andrews, I. Kuzmenko, P. R. Jemian, L. E. Levine, A. J. Allen, *J. Appl. Crystallogr.* **2018**, *51*, 867.

[16] J. Ilavsky, P. R. Jemian, *J. Appl. Crystallogr.* **2009**, 347.

[17] J. Ilavsky, *J. Appl. Crystallogr.* **2012**, *45*, 324.

[18] J. R. H. Manning, E. Routoula, S. V Patwardhan, *JoVE* **2018**, e57730.

[19] S. V Patwardhan, *Chem. Commun. (Camb).* **2011**, *47*, 7567.

[20] C. Drummond, R. McCann, S. V. Patwardhan, *Chem. Eng. J.* **2014**, *244*, 483.

[21] S. V Patwardhan, V. P. Taori, M. Hassan, N. R. Agashe, J. E. Franklin, G. Beaucage, J. E. Mark, S. J. Clarson, *Eur. Polym. J.* **2006**, *42*, 167.

[22] J. R. H. Manning, T. W. S. Yip, A. Centi, M. Jorge, S. V. Patwardhan, *ChemSusChem* **2017**, *10*, 1683.

[23] S. V Patwardhan, J. R. H. Manning, *Curr. Opin. Green Sustain. Chem.* **2018**, *12*, 110.

[24] Y. Zhou, X. Jiang, L. Chen, J. Yue, H. Xu, J. Yang, Y. Qian, *Electrochim. Acta* **2014**, *127*, 252.

[25] M. Guo, X. Zou, H. Ren, F. Muhammad, C. Huang, S. Qiu, G. Zhu, *Microporous Mesoporous Mater.* **2011**, *142*, 194.

[26] N. Liu, K. Huo, M. T. McDowell, J. Zhao, Y. Cui, *Sci. Rep.* **2013**, *3*, 1.

[27] D. Cho, M. Kim, J. Hwang, J. H. Park, Y. L. Joo, Y. Jeong, *Nanoscale Res. Lett.* **2015**, *10*, 424.

[28] J. Xie, G. Wang, Y. Huo, S. Zhang, G. Cao, X. Zhao, *Electrochim. Acta* **2014**, *135*, 94.

[29] K. Chen, Z. Bao, A. Du, X. Zhu, G. Wu, J. Shen, B. Zhou, *Microporous Mesoporous Mater.* **2012**, *149*, 16.

[30] K. K. Larbi, M. Barati, a McLean, *Can. Metall. Q.* **2011**, *50*, 341.

[31] Y. Zhang, J. Huang, *J. Mater. Chem.* **2011**, *21*, 7161.

[32] W. Chen, Z. L. Fan, A. Dhanabalan, C. H. Chen, C. L. Wang, *J. Electrochem. Soc.* **2011**, *158*, A1055.

[33] Z. Favors, W. Wang, H. H. Bay, Z. Mutlu, K. Ahmed, C. Liu, M. Ozkan, C. S. Ozkan, *Sci. Rep.* **2014**, *4*, 5623.

[34] H. Jia, P. Gao, J. Yang, J. Wang, Y. Nuli, Z. Yang, *Adv. Energy Mater.* **2011**, *1*, 1036.

[35] C. Li, C. Liu, W. Wang, Z. Mutlu, J. Bell, K. Ahmed, R. Ye, M. Ozkan, C. S. Ozkan, *Sci. Rep.* **2017**, 1.

Chapter 4:

Electrochemical Testing and Scale-up

4.1 Introduction

Porous silicon morphologies can address both volumetric expansion and slow lithium diffusion rates of silicon. it has been shown that higher void fractions lead to lower induced stresses and larger pores have lower hoop stresses than smaller pores.[1] Porous silicon can expand into its own pore volume, thereby limiting stresses on the material. For this reason, a number of porous silicon has been produced and its electrochemical performance will be tested in this chapter.

In Chapter 3 detailed characterisation of silicon produced from MgTR is detailed. The mesopore properties, silicon purities and crystallinities are all produced. The above has presented a detailed understanding of the nature of porous silicon structures produced from the MgTR and below the anode performance of these porous silicon is assessed.

The importance of inventing scalable synthesis methods for porous silicon is reviewed in Chapter 1. For silicon material to make a positive impact into the LIB market by increasing cell capacity, it must be economically feasible. Many synthesis routes to porous silicon require intricate chemical reactions, large energy inputs and specific reaction vessels. MgTR is promising due to its ability to provide a bulk synthesis route to mesoporous silicon. However, the exothermic nature of the MgTR is known to cause issues when scaling this synthesis to larger scales.[2] Therefore, the scalability of MgTR for the reduction of BIS is explored.

4.2 Experimental

A 2.5w% solution of carboxymethyl cellulose (Sigma) binder and deionised water was prepared. The desired solid amount of binder 20 wt% in electrode was added to a thinky mixer 10ml pot. The conductive additive C-65 (MTI) 20 wt% of electrode was added to the thinky. The mixer was sealed and mixed at 1500 rpm for 5 minutes. The silicon was added to the mixer and mixed together for a further 10 minutes to give a viscous ink. The ink was transferred to a 10ml Perspex ball mill vial and milled in a Spex M8000 Mill with a stainless steel baring for 10 minutes. This ink was then applied to a carbon coated copper foil (MTI) using a vacuum table (MTI)and doctor blade with thickness 300 µm. The coating was air dried for 1-2 hours then placed in an 80 ^{o}C vacuum for a minimum of 6 hours. Once dry 12 mm diameter electrodes are punched from the foil, weighed, and used for cell preparation. Electrochemical experiments were performed using MIT2016-type coin cells with a Whatman glass fibre separator and lithium foil (Sigma Aldrich) as the counter electrode. The electrolyte was 1M $LiPF_6$ in a 1:1 solution of ethylene carbonate (EC) and dimethyl carbonate (DMC) (Sigma Aldrich) with added 5w% fluoroethylene carbonate (FEC) (VWR). The composition of working electrodes was: 60 wt% silicon active material, 20 wt% conductive additive C-65 , 20 wt% carboxymethyl cellulose. The commercial silicon nano-particle size was <100nm from IOLiTech. The cells where assembled in an Argon filled glove box (MBraun) with oxygen and water contents less than 0.1ppm.

The electrochemical performances were tested on a Maccor 4000M Battery and Cell test system in a 25^{o}C temperature chamber. The cut off voltage was 0.01V versus Li/Li^{+} for discharge (lithium insertion) and 1.2 V versus Li/Li^{+} for charging (Li extraction). The specific capacity was calculated on the basis of active material mass. The charging rate was calculated from the fraction of active material in the electrode and based on silicon theoretical capacity at 25 ^{o}C of 3600 mAh/g.

Scale up of Mg reduction

All previously presented MgTR results were at a total reactant mass of 1g, reactant mass refers to the total mass of Mg and SiO_2 placed in the reactor. In this work total ‘reactant mass’ and ‘batch size’ are used interchangeably. NaCl was introduced as a thermal moderator in the mortar and pestle grinding stage of reactants. NaCl was introduced at predetermined mass ratios proportional to the total reactant mass, such that a 5:1 NaCl:(reactant) ratio for a batch size of 1 gram contained 1 gram of Mg + SiO_2 and 5 of NaCl. The grinding of the reactants together was the same as for other

MgTR reactions, however, it was observed that the presence of coarse NaCl crystals physically changed the consistency of the reactants during this step. Giving the powder a ‘harder’ texture and increased flow properties.

All other equipment and subsequent stages were identical to the MgTR experimental procedure described above.

4.3 Anode performance of porous silicon

One striking feature of many reports on MgTR is the use of hydrofluoric acid (HF) in the selective removal of silica from the porous silicon produced. The use of HF adds a second synthesis step, a step with particular environmental and economical drawbacks if MgTR is ever to be commercialised. We therefore choose to present the anode performance of porous silicon produced from MgTR without the use of HF.

Silicon produced at temperatures ranging from 550-950 ^{o}C have a wide range of purity and pore properties. The capacity of these porous silicon samples is displayed in Figure 4.1(a). The low purity of 29 wt% Si produced at 550 ^{o}C had an initial capacity of 830 mAh/g; after 100 cycles only 16% of this initial capacity is lost. Although this capacity is the lowest of the study, the capacity is still more than twice the theoretical capacity of graphite and retention over 100 cycles is excellent (compare this with the -325mesh silicon, which showed 94% capacity fade to 150 mAh/g after 35 cycles (Figure S4.1). The initial capacities of the 650 and 750 ^{o}C are 1770 and 2080 mAh/g respectively. After 100 cycles the capacity of both samples faded 39% and 59% respectively. The 850 ^{o}C reduced sample shows the highest initial capacity of 3270 mAh/g, and also shows good capacity retention of 2170 mAh/g after 100 cycles. The 950 ^{o}C sample has a high initial capacity of 2990 mAh/g due to its high purity of 89 wt%Si but shows a rapid capacity fade after 100 cycles of 75% reaching a final capacity recorded for the 550 ^{o}C reduced sample. Without exception this silicon shows greatly increased stability than commercially available -325mesh silicon particles (Figure S4.1).

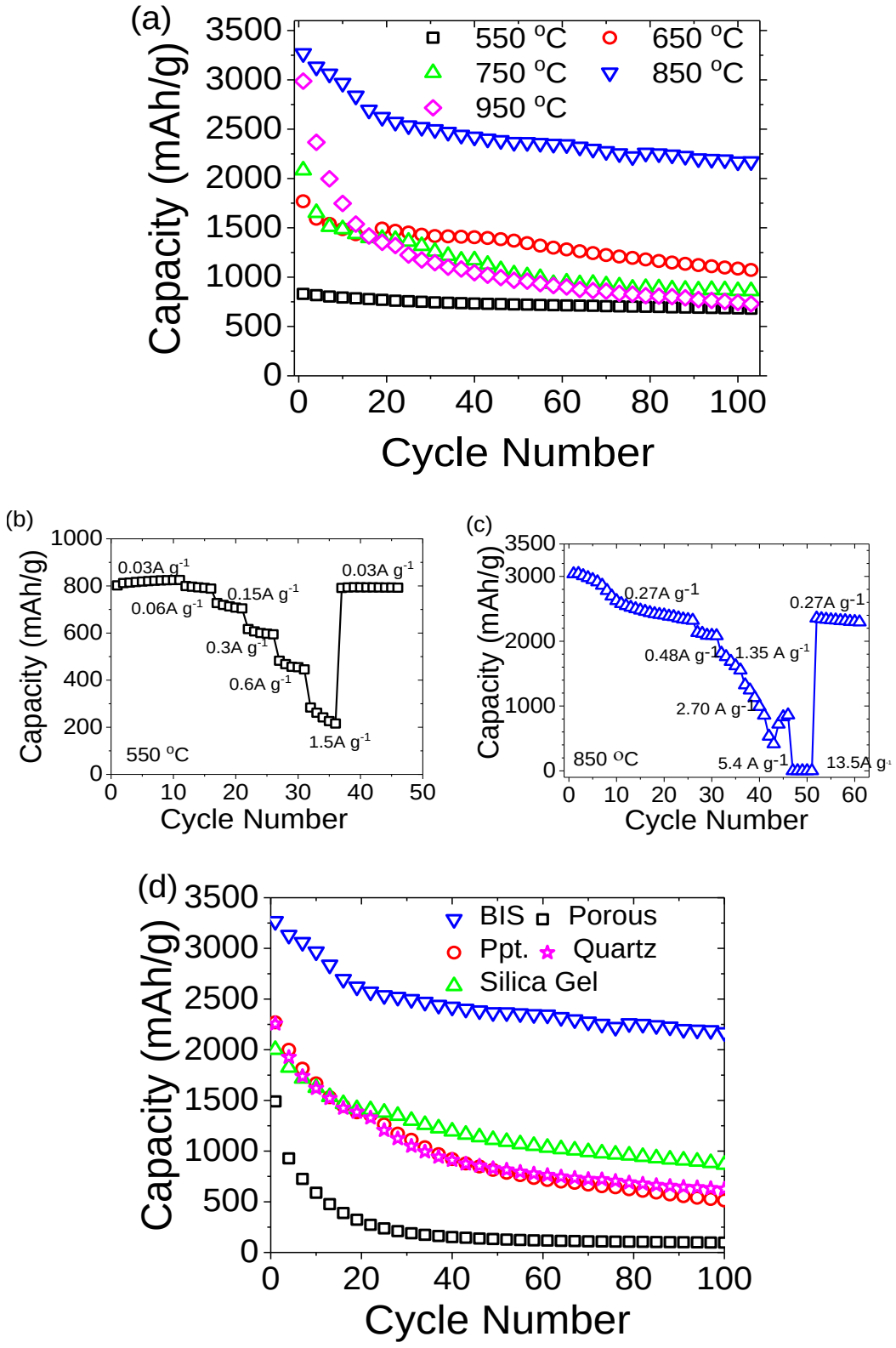

Figure 4.1 Discharge capacity of porous silicon/silica composites reduced between 550-950 °C from (a) BIS and The rate capabilities of porous silicon reduced at (b) 550 °C and (c) 850 °C. (d) other silica precursors reduced at 850 °C. For full materials properties of these samples see Table 3.3 and Table 3.6 [3]

For the 550 °C sample, the good capacity retention is attributed to the inactive silica component. This silica can act as a scaffold to buffer the volume expansion of silicon between cycles. As the wt% of silicon in the samples increases, the initial capacity increases, however the stability is affected by removing more silica. It is hypothesised that as the amount of silica in the sample decreases, the scaffolding effect is reduced, and the silica present hinders the capacity retention. A notworthy improvement on the initial capacity and cycling of the sample produced at 850 °C is attributed to a combination of a step change in both its purity (from 66% for 750 °C to 87%) and nanocrystal size (from 13 nm at 750 °C to 21 nm), while retaining mesoporosity. The larger diameter mesopores experience smaller hoop stresses around the surface of a pore as it expands.[1] The larger mesopores of the 850 °C sample are therefore better suited to buffer the stresses of Si volume expansion upon cycling. These properties suggest an optimum in terms of electrochemical performance. The initial fading of the capacity in first 20 cycles is from the destruction of 13% silica present.

The porous nature of the composites also plays an important role in the capacity and cyclability of these materials. This is clearly shown in the difference between the 850 and 950 °C reduced samples. Both samples have similar purities of 87 and 89 wt% silicon respectively, the 850 °C sample contains mesopores and small macro pores whilst the 950 °C sample does not (Figure 3.2 (b)). The non-porous silicon has a rapid and catastrophic capacity fade in the first 10 cycles.

The rate capabilities were tested for the 550 and 850 °C reduced samples (Figure 4.1(b-c)). The C-rates were calculated based on the active silicon content of the material therefore are expressed in A g^{-1} to allow easy comparison. Previous studies have shown an upper limit for commercial graphite electrodes of 4C above which substantial electrode breakdown occurs (for graphite 4C = 1.48 A g^{-1}).[4] The 550 °C silicon had excellent rate performance and provided 215 mAh/g of capacity at the upper limit used for conventional electrodes, the electrode shows excellent ability to return to its initial capacity when charging rate is reduced (Figure 4.1((b)). Due to the higher silicon content in the 850 °C sample, higher charging rates were attempted. This electrode showed poor ability to handle rates >0.48 A g^{-1} and maintain high capacity. After subjecting the 850 °C electrode to extreme charging rates, the electrode is still able to return to its original high and stable capacity showing the materials robustness.

The electrochemical performance of porous silicon produced from the alternative silica precursors was also assessed and presented in Figure 4.1((d) (for samples

reduced at 650 ^{o}C see Figure S4.2). The higher purity of the silicon produced at 850 ^{o}C resulted in higher capacity of electrodes for silicon obtained for all feedstocks used herein. However, the initial capacities and the stability over 100 cycles for the BIS silicon were much higher when compared to other silicon samples produced. This is interesting because silicon samples produced from silicas other than BIS did contain high purities (~80%) and mesoporosity (Figure 3.13) the primary difference between these silica and the BIS being the secondary hierarchical particle structure. The hierarchical structure of the BIS template and hence silicon analogues as described in detail above is responsible for the better electrochemical performance of BIS. The small <370nm size of the secondary particles coupled with their porous network allows for shorter lithium diffusion pathways during cycling and an access to higher capacity's.

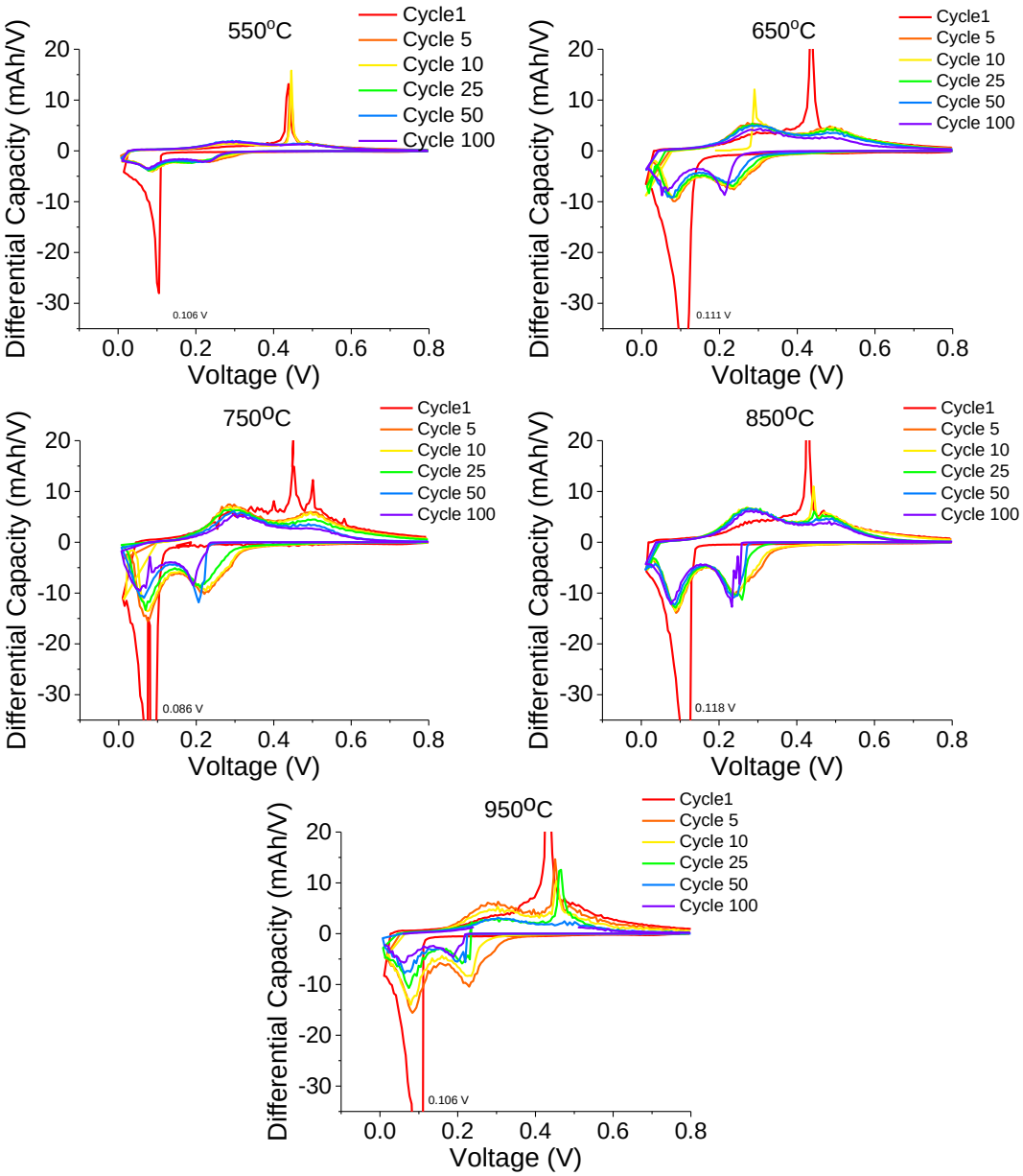

Figure 4.2. Differential capacity plots of the 1st, 5th, 10th, 25th, 50th and 100th cycles for silicon reduced between 550-950 °C

In order to further probe the electrochemical process, in particular lithiation and delithiation of silicon during cycling, differential capacity plots are presented Figure 4.1. The differential capacity plots show similar characteristics across the sample range. The disappearance of the sharp cathodic peak at 0.43 V in the first 10 cycles corresponds to the delithiation of the silicon of the highest lithiated state (c-$Li_{3.75}Si \rightarrow$ a-$Li_{1.1}$ Si) the disappearance of this peak during cycling suggests an increase in electrode resistance as cycles progress.[5],[6] These high surface area, porous silicon samples inherently lead to a larger formation of solid electrolyte interphase (SEI), this is reflected in the low initial columbic efficiencies (CE), (see Figure 4.3(a)). The low CE in the initial cycles of the electrodes indicate a large amount of SEI formation. In

addition, the unstable CE over protracted cycles (Figure 4.3 (b)) is indicative of continual SEI formation or isolation of active material in the electrode. The 750 and 950 ^{o}C reduced samples have volatile CE across the 100 cycles further highlighting the instability of these active materials and indicating the breakdown from expansion and contraction which exposes virgin silicon surfaces. The other samples have much more stable trends towards high CE at 100 cycles (99.5%) suggesting minor damage to the SEI and/or a thickening of the layer. The differential capacity plots (Figure 4.2) show shifting of anodic peaks to lower voltages between 50 and 100 cycles and cathodic peaks vis-versa, this is consistent with an increase in internal resistance of the cells caused by a thickening of the SEI. The voltage profiles (Figure S4.3 show the voltage plateau ~100 mV during the first lithiation of crystalline silicon, thereafter each cycle shows the typical hysteresis of voltage profile during charge-discharge.[7]

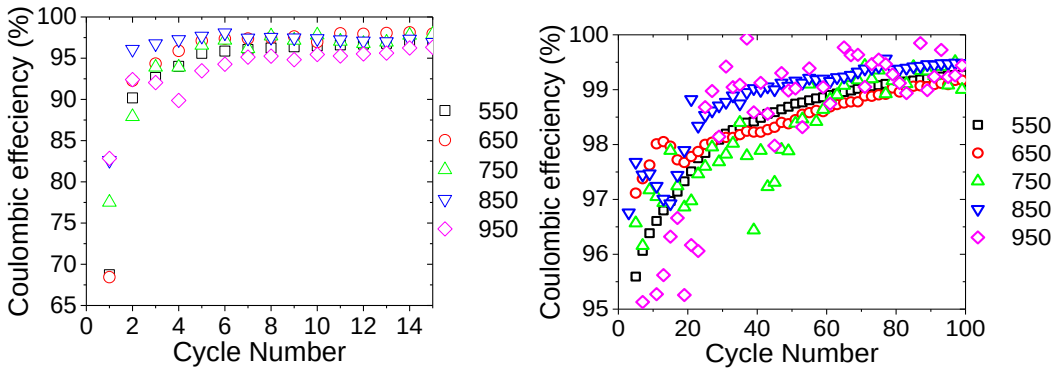

Figure 4.3. Columbic efficiencies (a) during the first 10 cycles, (b) for 100 cycles of silicon's reduced at 550-950 ^{o}C[3]

For the application of silicon in LIB anodes, nano-structuring of the active material is often accompanied by other tools for improving capacity fade. Examples of this are tailored binders, carbon coating of silicon and/or carbon silicon composite formation, electrolyte additives for more stable SEI formation. In this study results present the raw porous active material with carboxymethylcellulose binder and cycled with 10wt% fluoroethylene carbonate electrolyte additive, both of which have been shown to increase cyclability in silicon electrodes.[8],[6] Based on the capacity and capacity fade highlighted above, two varieties of porous sample are of interest. Low purity samples such as that reduced at 550 ^{o}C and high purity, such as 850 ^{o}C sample. It is envisaged that future work on electrode/electrolyte formulation and carbon coating will only increase the cyclability and initial CE of these materials.

These results demonstrate the complex nature of using porous silicon produced via MgTR as an anode material. Our results suggest that silica removal from the silicon

product is not necessary and that it can be beneficial for the stability of silicon produced. The interplay of purity and pore properties in these samples is crucial. Purity most importantly affects the capacity reached, high purities reach higher capacities. Higher purities require porous structure to buffer silicon volume expansion upon cycling, larger mesopores are better able to mitigate the stresses of volume change.

4.4 Scale up of Magnesiothermic Reduction

4.4.1 Scale up of BIS MgTR

As previously stated all MgTR reactions presented in this work were performed at a 1 g reactant mass, this typically yielded ~0.25g of silicon product. MgTR is touted for its economic and environmental advantages over synthesis routes for silicon in LIB applications.[2] It also has the proposed advantage of being a bulk synthesis route, this has potential benefits for the scalability of this synthesis route over the surface based syntheses of competitive technologies.[2] As described in Chapter 1, the large exothermic nature of the MgTR reaction can lead to self-heating. This is a known problem for larger batch sizes and can lead to temperatures exceeding the melting point of silicon (1414 ^{o}C) and loss of silicon microstructure. For this reason, the scale up of MgTR will not be straight forward. The work below describes initial experiments performed to increase the batch size of MgTR of BIS above 1 gram.

Experiments were performed to determine to optimum batch size in MgTR. Figure 4.4 presents the results for MgTR batch sizes of 1, 2 and 3 grams. N.B. for these reactions an optimised 2.5:1 Mg:SiO_2 ratio was used, which is equivalent to a 24:25 mass ratio of reactants. In addition, slow ramping rates of 1 ^{o}C/min were used to prevent localised hotspots.

The pore properties were greatly affected by the batch size in this study. When increasing the batch size above 1 g an almost complete loss of mesoporosity of observed along with reduced SSA and pore volume (See Table 4.1). From the Scherrer analysis of data in Figure 4.4 (d), the silicon crystals displayed no nano-crystallites for 2 g and 3 g batch sizes with crystal sizes being outside of Scherrer analysis range (>100 nm). From SEM analysis (Figure 4.5) there was also a clear change in the product morphology was observed when going from 1 to 2 g. The initial hierarchical structure of the BIS template was destroyed and replaced with macroscale melted particles (Figure 4.5 (below)), most likely fused together due to the formation of hotspots at larger batch sizes.

It is apparent that for reducing BIS in batch sizes above 1 g, self-heating occurs. The increasing of silicon crystallite sizes to macroscale suggests the reduction temperature exceeded the melting point of silicon (1414 ^{o}C). The SEM images also suggest a complete change in morphology occurred from melting, and the porosity characterisation supported this view.

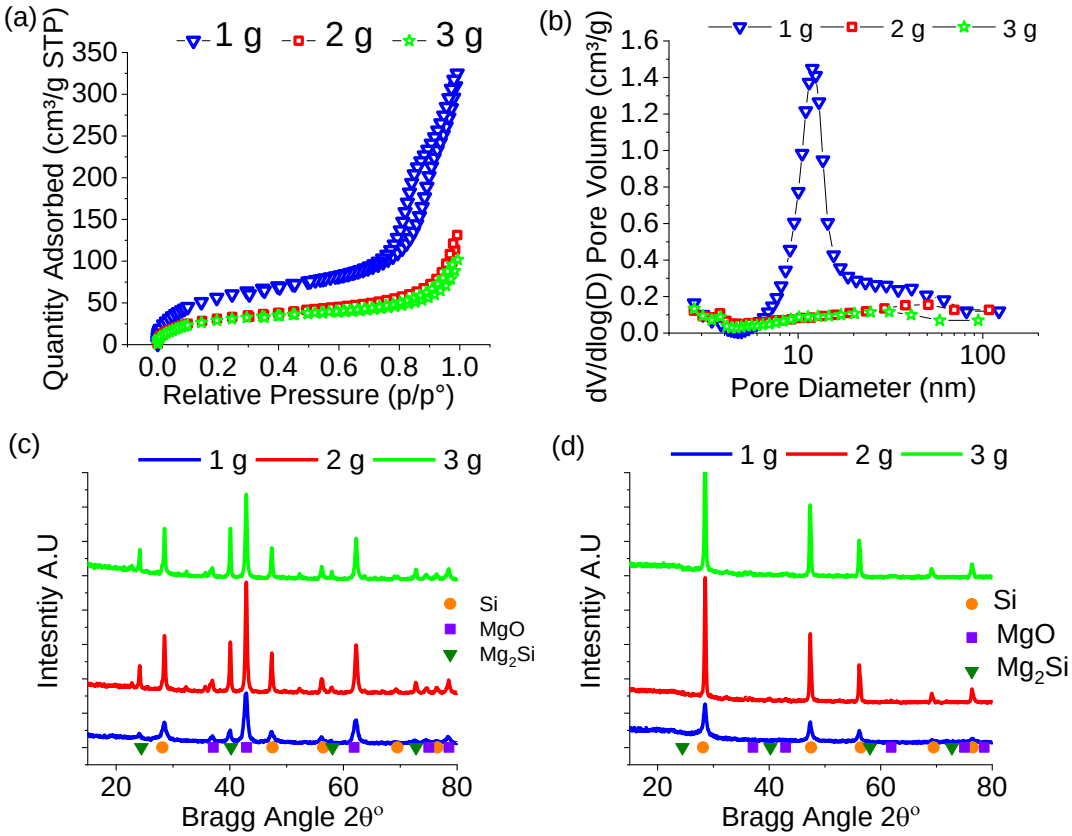

Figure 4.4. Characterisation of silicon produced during scale up study of 1 – 3 g, 2.5:1 Mg:SiO_2 stoichiometry reacted for 6 hours at 650 ºC. (a) N_2 absorption Isotherm, (b) BJH pore size distribution, (c) XRD of reaction products before washing with HCl, (d) XRD of reduction products after washing with HCl.

Table 4.1. Summary of Figure 4.4 for the scale up study of 1 – 3 gram, 2.5:1 Mg:SiO2 stoichiometry reacted for 6 hours at 650 ºC.

Batch Size (g) Mg+SiO_2	SSA (m^2/g)	BJH PV (cm^3/g)	wt% Si	Si_{Cry} Size (nm)
1	230	0.48	57	10
2	112	0.18	50	>100
3	116	0.14	50	>100

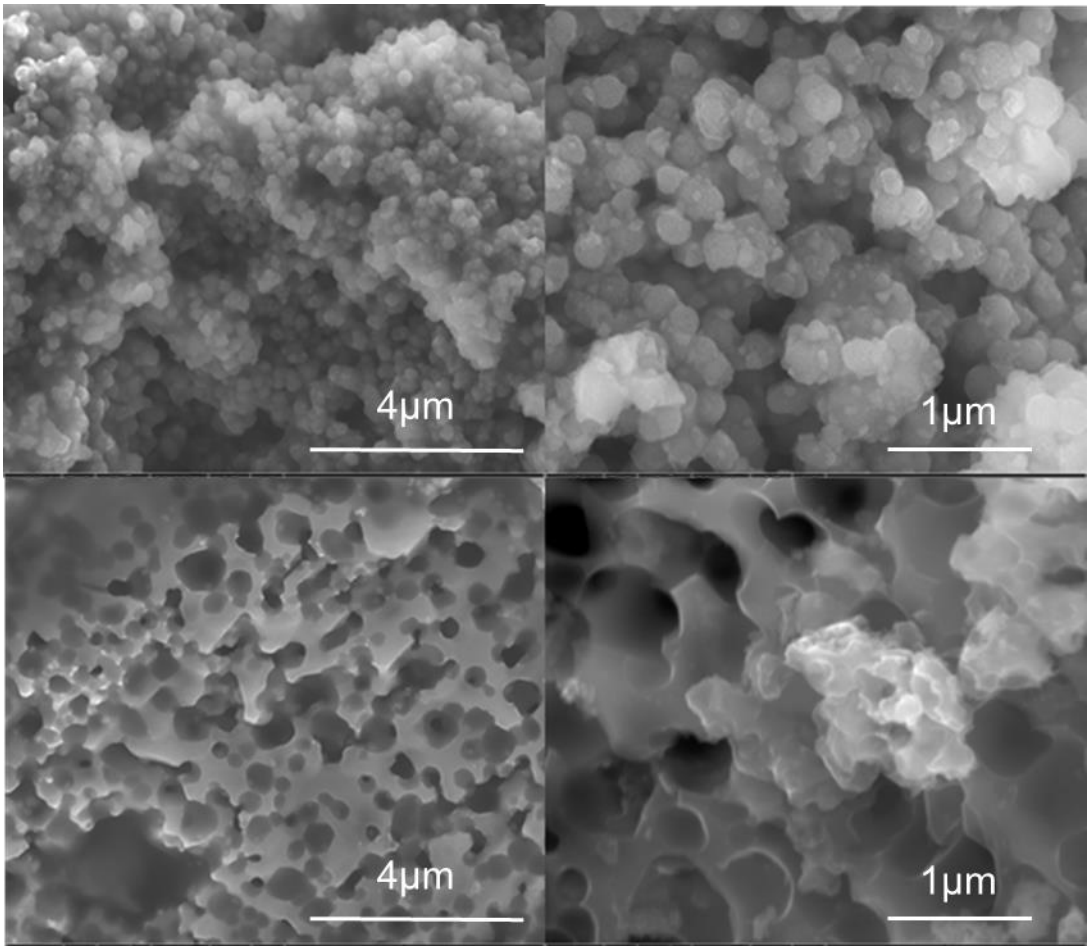

Figure 4.5. (Above) spherical morphology of a typical 1-gram batch size reduction of BIS. (Below) the melted 'sponge like' structure from a 2-gram batch size reduction of BIS.

4.4.2 Sodium chloride as thermal moderator

The heat released during MgTR can lead to reactants heating excessively and react uncontrollably. This issue has been overcome by using slow heating rates and smaller batch sizes.[9] Unreactive thermal moderators such as sodium chloride can be used to limit the effects of self-heating in MgTR. Sodium chloride (NaCl) melts at 801 ^{o}C, therefore NaCl is commonly used during MgTR as the large endothermic latent heat energy can moderate the MgTR temperature.[10]

The above experiment for the scale up of BIS reduction to 3 g was repeated in the presence of NaCl thermal moderator, the results are presented in Figure 4.6. All samples display identical N_2 isotherms and hence pore size distributions (Figure 4.6 (a-b) the surface areas and pore volumes are also very similar (Table 4.2). The pre-etch XRD Figure 4.6 (c) was dominated by the strong diffraction signals from NaCl present and hence details of MgTR products (MgO, Si, Mg_2Si) cannot be identified. However, after acid etching, it was clear that NaCl was removed along with other by-products to leave crystalline silicon (Figure 4.6(d)). Further Scherrer analysis confirms almost identical nanocrystallite sizes of 11-12 nm for each reduction.

The results presented in Figure 4.6 support the view that NaCl acts as a thermal moderator in the MgTR to provide a nanocrystalline mesoporous silicon product. In addition, the purity of silicon product in the presence of NaCl (62-71 wt%) was greater than the equivalent purities when NaCl is not used (50-75 wt%) (Table 4.1 and Table 4.2). A potential reason behind this increase in purity is believed to be related to the pestle and mortar mixing of the Mg, SiO_2 and NaCl. The course nature of NaCl crystals is believed to increase the homogeneity of the grinding step. The increased homogeneity of Mg and SiO_2 may lead to less isolated SiO_2 and hence increase the overall purity in the reduced sample. This also implies that a systematic future study of the effects of milling the precursors on the purity and properties of the silicon produced is warranted.

Sodium chloride is a successful thermal moderator for the MgTR of BIS allowing scale up of the reduction reaction to 3g. A large amount of NaCl 5:1 (NaCl:(Mg+SiO_2)) was used in this study. Although NaCl is a cheap commodity, it is desirable to optimise the level of NaCl used. Additionally, it is important to understand the effect of NaCl ratio with reactants and its effect on silicon product properties.

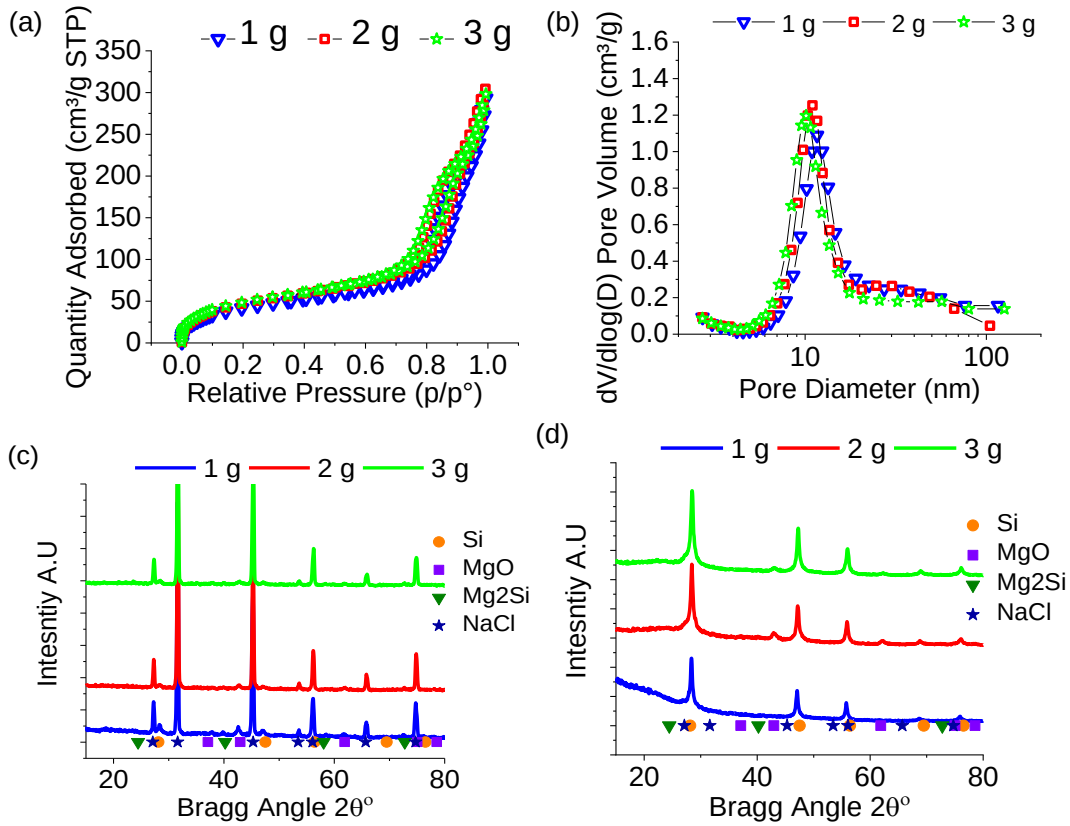

Figure 4.6. Characterisation of silicon produced during scale up study of 1 – 3 g, 2.5:1 Mg:SiO_2 stoichiometry reacted for 6 hours at 650 °C, thermal moderator NaCl 5:1 ratio. (a) N_2 absorption Isotherm, (b) BJH pore size distribution, (c) XRD of reaction products before washing with HCl, (d) XRD of reduction products after washing with HCl,

Table 4.2. Summary of Figure 4.6 for the scale up study of 1 – 3 gram, 2.5:1 Mg:SiO2 stoichiometry reacted for 6 hours at 650 °C, thermal moderator NaCl 5:1 ratio.

Batch Size (g) Mg+SiO_2	SSA (m^2/g)	BJH PV (cm^3/g)	wt% Si	Si_{Cry} Size (nm)
1	162	0.43	65	12
2	182	0.46	71	12
3	184	0.45	62	11

4.4.3 Sodium chloride ratio

The ratio of NaCl to reactant material ($Mg+SiO_2$) was studied between 1:1 and 5:1 for a batch size of 3 g, results presented in Figure 4.7. Overall there was little difference in reducing the NaCl ratio from 5:1 to 2:1: All samples had similar mesopore distributions around 12 nm and nanocrystallite size of 11 or 12 nm. However, the purity of these samples did vary between 56 - 73 wt % with no clear correlation, it is likely that the grinding step was affecting product purity, which will be discussed further below. For the reduction reaction performed with 1:1 NaCl:reactant ratio, there was an increase in the crystallite size to 28 nm (Figure 4.7(c)) and subsequent increase in pore size distribution, coupled with a reduction in pore volume. It is therefore concluded that reducing the NaCl ratio below 2:1 will inhibit the thermal moderation of the reduction reaction, the crystallite size to rise and mesopore size to broaden.

The lithium-ion battery performance of silicon produced in this study is presented in Figure 4.7(d). The silicon reduced at NaCl ratios of 2:1-5:1 showed similar cyclability with initial capacities between 1250-1900 mAh/g based upon silicon purity. These capacities reduced steadily with the 3:1 and 4:1 ratio having the most capacity fade. The 1:1 ratio sample has the highest initial capacity of 2250 mAh/g and shows better capacity retention over 80 cycles than the other samples. This is likely caused by the larger pores and wide pore size distribution in this sample. As previously presented by M. Ge et al[1], larger pores have lower hoop stresses around their diameter which limits the fracturing due to expansion.

These capacities and cycling stabilities are not dissimilar to silicon reduced at 650 ^oC without NaCl moderator (Figure 4.1(a)). The increased capacity and cycling stability of the 1:1 sample is likely to be related to the increase in pore size distribution which is known to decrease the stresses of volume expansion in silicon.

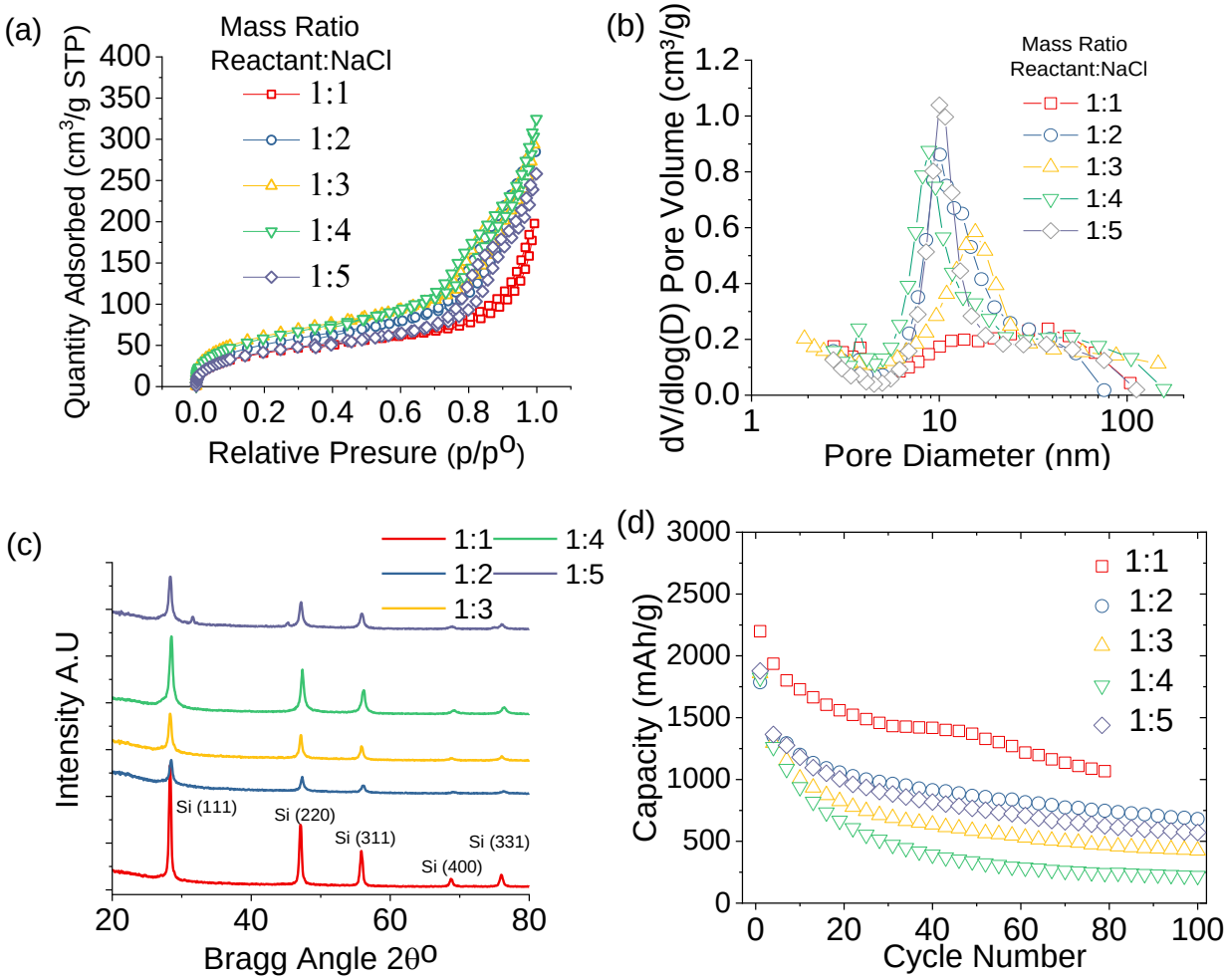

Figure 4.7. Characterisation of silicon produced during scale up study of 3 gram, 2.5:1 Mg:SiO_2 stoichiometry reacted for 6 hours at 650 °C, thermal moderator NaCl ratio varied from 1-5:1. (a) N_2 absorption Isotherm, (b) BJH pore size distribution, (c) XRD of reaction products before washing with HCl, (d) capacity and cycle life as anode in lithium half-cell.

Table 4.3. Summary of Figure 4.7 for the NaCl ratio study, 2.5:1 Mg:SiO_2 stoichiometry reacted for 6 hours a 650 °C, thermal moderator NaCl ratio varied from 1-5:1.

(SiO_2+Mg):NaCl Ratio	Reduction Temperature (°C)	SSA (m^2/g)	BJH PV (cm^3/g)	wt% Si	Si_{Cry} Size (nm)
1:1	650	157	0.28	69	28
1:2	650	197	0.43	73	11
1:3	650	231	0.43	56	12
1:4	650	225	0.49	66	11
1:5	650	162	0.39	63	11

4.4.4 Effect of Reduction Temperature in presence of Sodium Chloride

In Chapter 3 it was shown that the upper temperature of MgTR effects the pore properties, and hence the battery performance of product silicon. The effect of MgTR temperature in conjunction with NaCl ratio is not known in the literature, above we have showed the importance of reduction temperature on driving product purity and porosity and therefore this was further explored. Figure 4.8 presents the results from MgTR with NaCl thermal moderator in a 5:1 ratio with reactants at a batch size of 3 g. As can be seen in Figure 4.8 (a) and (b), the pore properties of the silicon product were still driven by the upper MgTR temperature. This is consistent with the proposed mechanism for pore formation driven by an increase in silicon crystallite size (Table 4.4). Crystallite size was calculated from Scherrer analysis of silicon diffractograms presented in Figure 4.8(c).

The primary difference between the MgTR with NaCl thermal moderator and when no NaCl is used (Chapter 3 Fig 3.5) is that porosity is lost between 750 – 850 ^{o}C. Whereas when no NaCl is used 850 ^{o}C samples still contain large mesopore volume. This can be explained by considering the melting point of NaCl (801 ^{o}C): at reduction temperatures higher than 801 ^{o}C, molten NaCl will exist during the MgTR. After this phase transition, NaCl will not moderate the self-heating of the reaction. It is likely that molten NaCl can play some role in silicon formation, although this has not been studied in the literature.

A reduction reaction was performed at 790 ^{o}C to avoid NaCl melting and create a sample with high purity containing mesopores. This experime nt was partially successful in producing high purity (82 wt%) and mesoporous silicon, although the pore volume was low (0.12 cm^3/g, Figure 4.8 (b)). Further work is required if a thermal moderator is needed and the desired reduction temperature is close to or more than 801^{o}C.

The performance of these silicon samples was evaluated as lithium-ion anode active materials, Figure 4.8(d). As expected, the high purity but low porosity sample reduced at 850 ^{o}C showed rapid capacity fade (97 % after 100 cycles) due to lack of pore structure to absorb expansion stresses. The other mesoporous silicon reduced at 650, 750 and 790 ^{o}C all displayed similar capacity fade profiles: this suggests that their porous structure is not ideal for containing the stresses of volume expansion during cycling. This result was surprising and further experiment is needed to

differentiate why these samples performed poorly compared to samples reduced with no NaCl present.

Above in Figure 4.1(a) low purity silicon reduced at 550 ^{o}C showed excellent capacity retention (830 mAh/g initial capacity with 18% capacity fade over 100 cycles). In this study the addition of NaCl to a 550 ^{o}C reduction has increased the purity from 29 to 51 wt% with respect to the same parameters without NaCl moderator. As above this observation is likely related to enhanced mixing when using NaCl. In addition, the crystallite size and hence pore properties of this sample have remained similar as to when no NaCl was used. It was therefore expected that this sample may display the same stable capacity over cycling but would have a higher initial capacity due to the increase in purity.

The high and stable capacity of this sample is displayed in Figure 4.8(d), the initial capacity of 1300 mAh/g with 19 % capacity fade over 100 cycles. When compared to previous promising results obtained at 550 ^{o}C (830 mAh/g initial capacity with 18% capacity fade over 100 cycles), the increased purity as a result of NaCl addition has increased the capacity of the material but not compromised the stable cycling characteristic.

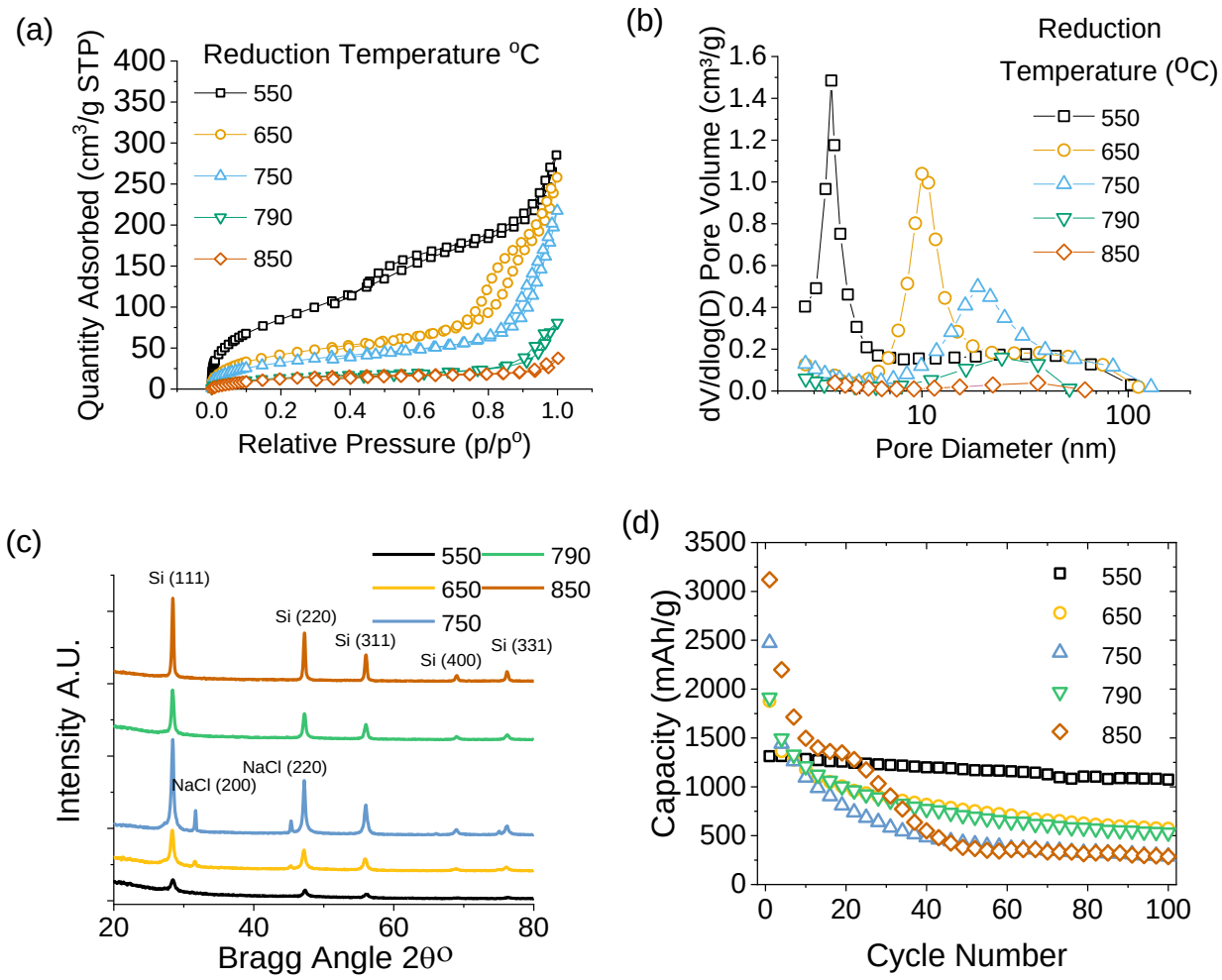

Figure 4.8. Characterisation of silicon produced during scale up study of 3 gram, 2.5:1 Mg:SiO_2 stoichiometry reacted for 6 hours between 550 – 850 °C, thermal moderator NaCl ratio 5:1. (a) N_2 absorption Isotherm, (b) BJH pore size distribution, (c) XRD of reaction products before washing with HCl, (d) capacity and cycle life as anode in lithium half-cell.

Table 4.4. Summary of Figure 4.8 for the NaCl ratio 5:1, 2.5:1 Mg:SiO_2 stoichiometry reacted for 6 hours temperatures between 550 – 850 °C.

(SiO_2+Mg):NaCl Ratio	Reduction Temperature (°C)	SSA (m^2/g)	BJH PV (cm^3/g)	wt% Si	Si_{Cry} Size (nm)
1:5	550	326	0.41	51	8
1:5	650	162	0.39	63	12
1:5	750	125	0.32	73	16
1:5	790	53	0.12	82	20
1:5	850	54	0.04	96	60

4.4.5 Summary

The self-heating of MgTR is known to destroy templating structures. When scaling the synthesis of MgTR of BIS above 1 g of total reactant mass, the self-heating effect leads to loss of nano-crystallinity and porous structure. It has previously been reported that the addition of NaCl can act as a thermal moderator of the MgTR. In the presence of NaCl at ratios of 2-5:1, porous silicon structure could be produced at a 3 gram reactant mass scale. Below 2:1 ratio the NaCl was less able to moderate the self-heating effect. Owed to the low melting point of NaCl (801 ^{o}C), it was unable to act as a successful thermal moderator above 800 ^{o}C.

The addition of NaCl in the grinding step of reactants is hypothesised to have led to an increase in yield for all reductions performed relative to their respective experiment without NaCl.

The battery performance of the silicon reduced in the presence of NaCl was reduced in terms of capacity and cyclability relative to the silicon produced with same conditions in the absence of NaCl. However, the 3 g reaction batch reduced at 550 ^{o}C with NaCl present showed excellent cyclability and a 500 mAh/g increase in initial capacity over it's respective counterpart reduced without NaCl. This is a promising example of how future work may best be guided to provide scalable silicon synthesis with high anode capacity and stable cycle life and potentially even lower reaction temperatures of 550 ^{o}C.

4.5 Conclusions

The anode performance of these porous silicon materials demonstrates the multifaceted nature of using porous silicon produced via MgTR as an anode material. The interplay of purity and pore properties in these samples is crucial. Higher purity, high capacity samples require porous structure to buffer silicon volume expansion upon cycling otherwise suffer from rapid capacity fade. All samples produced from MgTR showed improved cyclability compared to commercial -325 mesh silicon particles.

The cycling results of note are for the BIS reduced at 550 and 850 ^{o}C: The low purity sample reduced at 550 ^{o}C has a capacity of 830 mAh/g this should be considered verses the commercial standard of graphite with a theoretical capacity of 375 mAh/g. This sample displays excellent stability over 100 cycles due the hypothesised scaffolding nature of the remaining silica. If future work can focus on understanding the scaffolding nature of the remaining silica then purities maybe increased yet suitable silica scaffolding could be tailored. The high purity porous sample reduced at 850 ^{o}C shows high capacity and good retention over 100 cycles. For this material it is believed that future work involving electrode processing optimisation such as binder, conductive carbon and electrolyte additives will further increase it's stability.

The scale up of MgTR is crucial for the future development of this technique in any industrial application. The self-heating of MgTR is well known and hinders the production of silicon in large batch sizes. The use of NaCl as a thermal moderator has been employed in many literature studies. However, the exact role of NaCl has not been investigated. This work has shown that NaCl is crucial for scaling up the batch size during the MgTR of BIS. Preliminary investigations into the amount of NaCl needed in the reactor suggest a mass ratio of >2:1 (NaCl:reactant) is needed to prevent self-heating from modifying the silicon product.

The effect of reduction temperature was also studied in conjunction with NaCl present. The same increase in crystallite size and hence pore size distribution was observed when reduction temperature is increased. However, the use of NaCl as a thermal moderator is limited by its melting point (801 ^{o}C), above which it can no longer effectively moderate self-heating.

A promising finding was that the introduction of NaCl increased the purity of MgTR silicon relative to when no NaCl is present. This effect is thought to be related to the enhanced mixing during reactant preparation which is achieved with NaCl present, however this hypothesis needs further work. The increased purity caused by NaCl addition allowed for a 51 wt% silicon sample to be produced at 550 ^{o}C, an increase of 22 wt% relative to no NaCl present. The anode performance of this silicon was excellent achieving 1300 mAh/g with 19% capacity fade over 100 cycles. The stable cyclability and high capacity of this material make for a promising prospect for future investigation, especially so due to the lower reduction temperature which will provide further environmental and economical benefits.

With the detailed reaction design pathway for MgTR outlined in chapter 3, particularly the porous nature of these samples, future work can be more systematically applied to produce silicon products with targeted properties. If future work can focus on the promising performance of the silicon samples reduced at low temperature and further scale up this synthesis procedure then MgTR will become much closer to commercial viability.

4.6 References

[1] M. Ge, J. Rong, X. Fang, C. Zhou, *Nano Lett.* **2012**, *12*, 2318.

[2] J. Entwistle, A. Rennie, S. Patwardhan, *J. Mater. Chem. A* **2018**, *6*, 18344.

[3] J. E. Entwistle, G. Beaucage, *J. Mater. Chem. A* **2020**, DOI 10.1039/c9ta13633a.

[4] L. Somervile, J. Bareno, S. Trask, P. Jennings, A. Mcgordon, C. Lyness, I. Bloom, **2016**, *335*, 189.

[5] K. Ogata, E. Salager, C. J. Kerr, A. E. Fraser, C. Ducati, A. J. Morris, S. Hofmann, C. P. Grey, *Nat. Commun.* **2014**, *5*, 3217.

[6] C. C. Nguyen, B. L. Lucht, *J. Electrochem. Soc.* **2014**, *161*, 1933.

[7] M. T. McDowell, S. W. Lee, W. D. Nix, Y. Cui, *Adv. Mater.* **2013**, *25*, 4966.

[8] D. Mazouzi, Z. Karkar, C. R. Hernandez, P. J. Manero, D. Guyomard, L. Roué, B. Lestriez, *J. Power Sources* **2015**, *280*, 533.

[9] N. Liu, K. Huo, M. T. McDowell, J. Zhao, Y. Cui, *Sci. Rep.* **2013**, *3*, 1.

[10] W. Luo, X. Wang, C. Meyers, N. Wannenmacher, W. Sirisaksoontorn, M. M. Lerner, X. Ji, *Sci. Rep.* **2013**, *3*, 2222.

Chapter 5: Electrochemical Reduction of Silica

5.1 Introduction

It has long been believed that silica is electronically inactive towards lithium due to its low lithium-ion diffusivity, and has been overlooked for battery applications due to its electronically insulating nature.[1] However, it has recently been shown that silica can react with lithium and that this reaction is at least partially reversible.[2] This discovery has opened a field of investigation into utilising silica as an active material in lithium-ion battery applications. Owing to its high natural abundance, low price and well explored chemistry, silica is a promising candidate.[3] As some silicon chemistries currently in use today for LIBs contain varying amounts of silica within their structure, whether as an impurity or a passivating layer, the understanding of silica behaviour within a LIB may have ramifications for these materials beyond their use as active materials.

Lepoivre et al recently studied the electrochemical reduction of silica particles (size ~200nm). They showed that an initial pre-treatment step was required before the silica would react reversibly, this step involved a prolonged potentiostatic discharge (PSD).[2] Potentiostatic discharge involved holding silica/lithium half cells at 0.02 mV for long periods, which allows the electrochemical reduction of silica to occur. PSD was shown to increase capacity with longer discharge times: 60 hours of PSD creating an electrode with 200 mAh/g capacity and 250 hours PSD creating an electrode with 400 mAh/g (Figure 5.1). This capacity is in the range of current graphite based commercial active materials, yet silica is readily manufactured, and has high natural abundance. The ability to incorporate silica particles into conventional composite electrodes opens a wide range of materials for study.

Since the PSD treatment represents an additional processing step before silica electrodes can be incorporated into LIBs it is desirable to assess new silica materials based upon the rate at which they react during PSD and the upper capacity they can

achieve. The work herein this chapter concerns the invention of a stepwise PSD treatment where the kinetics of capacity increase within silica electrodes could be studied. This new stepwise PSD allows for quantitative measurement of both these parameters.

Stöber silica previously explored by Lepoivre et al was assed with the new stepwise PSD in order to provide a clear comparison. Various other silica sources were investigated with many proving to be electrochemically inactive. However, when BIS is explored and is shown to have important performance benefits over Stöber silica, reaching upper capacities of >600 mAh/g.

The development of the stepwise PSD for evaluating new silica materials leads to a further invention of stepwise short circuiting of silica to enable the electrochemical reduction reaction. Short circuiting of silica/lithium half-cells is a simple method which removed the need for potentiostats required for PSD, therefore representing an advantage with regards to processing costs. Additional advantages of faster reaction kinetics and higher capacities are also presented.

5.2 Literature Review of Silica (SiO_2) active material

5.3.1 Silica active material

Silica can be directly used as an anode active material. However due to the insulating nature of silica and its low lithium-ion conductivity, small particle sizes are needed to enhance the electrochemical activity. Early work has focused on silica nanoparticles between 7-400nm.[4][5] Initial investigations into silica nanoparticles have produced capacities of up to 1100 mAh/g. However long-term cycling has revealed unstable capacity and initial columbic efficiencies can be as low as 33% (conventional commercial anodes require >90% initial columbic efficiency to prevent loss of lithium inventory). Table 5.1 shows literature values for capacity and general stability of silica anode materials. The initial columbic efficiencies were extremely low as can be seen. It has been postulated that, at low potentials, silica is reduced by lithium to form unknown species and theoretically silicon (although comprehensive proof of this is lacking). The silicon formed is responsible for the reversible capacity of the active material in subsequent cycles. The nature of the irreversibly formed species will be discussed in detail within Chapter 7. The most commonly postulated reaction equations responsible for silica reduction are reactions (5.1) and (5.2)[6][7][8][9][10][2][11], while the reaction (5.3) is responsible to the reversible lithiation capacity within these reduced materials. Note that the exact nature of the species postulated by reaction 5.1 and 5.2 are unknown and will be discussed further in Chapter 6. It is the formation of these irreversible species which cause the low columbic efficiency in the first cycles.

$$SiO_2 + 2Li \rightarrow Si + 2Li_2O \qquad \text{Equation (5.1)}$$

$$2SiO_2 + 4Li \rightarrow Si + Li_4SiO_4 \qquad \text{Equation (5.2)}$$

$$Si + 3.75Li \leftrightarrow Li_{3.75}Si \qquad \text{Equation (5.3)}$$

Table 5.1. Material parameters and electrochemical performances for silica active material in literature. NA=Not available.

Material Description	Initial CE (%)	Initial capacity (mAh/g)	Number of cycles	Final capacity (mAh/g)	Ref
150-200nm Stöber silica particles, 250h potentiostatic treatment	NA	400	200	400	[2]
Silica nanotubes 200nm diameter, synthesized through hard templating	43	1100	100	~1250	[12]
7nm silica particles	~33	300	1	300	[4]
Amorphous silica gel produced from rice husk	~33	400	50	350	[11]

The electrochemical reduction of silica during the first cycle was studied by Lepoivre et al.[2] They show that the extent of the reduction reaction of silica can be driven forward by a prolonged potentiostatic discharge, Figure 5.1. They reported capacities of 400 mAh/g after 250 hours of potentiostatic discharge. Through stoichiometric calculation, they speculated that this capacity was equivalent to a shell of reduced material about 40-50nm thick around the 200nm particles, however no characterisation of this proposed mechanism or products was provided. Another investigation using larger, 500 nm particles reported a smaller capacity, which was stoichiometrically equivalent to 45 nm thick shell. From Table 5.2 it can be seen that the size of silica particles studied throughout the literature is small, between 7 – 500 nm.

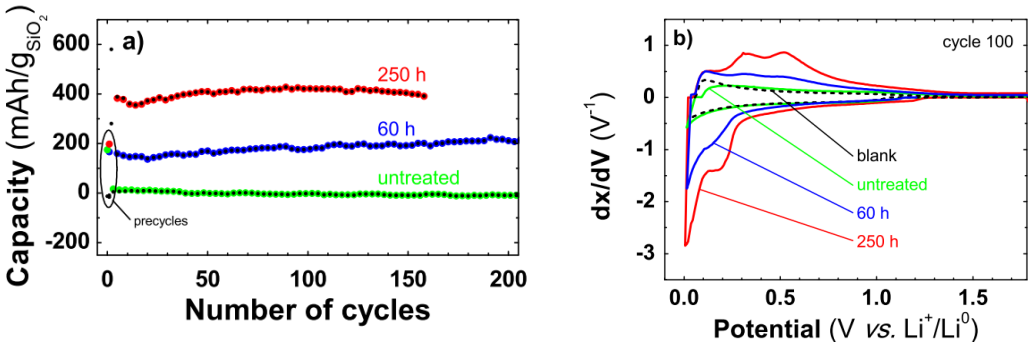

Figure 5.1. (a) Capacity retention and (b) differential capacity plot of 200nm Stöber silica nanoparticles held at 2 mV PSD for 60 and 250 hours. Reproduced from Lepoivre et al.[2]

Often very low charge rates such as 50 mA/g are used for cycling.[13] Under such conditions, electrodes remain at low potentials for extended periods, in which time the silica reduction can occur.[13] When utilising pure silica in a composite electrode, besides the initial columbic efficiency little information is presented about the duration and complexity of the first cycle. More information about the charging regimes such as the duration of this first cycle would be useful. The very low columbic efficiencies reported indicate substantial irreversible reactions during the first cycle, which reinforces the current hypothesis that lithiated species are formed during lithiation.

5.3.2 Carbon-Silica composites

Conductive carbon is added to composite electrodes to improve electronic conduction pathways.[14] With silicon-carbon composites, higher capacities have been achieved compared with the direct use of silica (Table 5.2) Given the importance of conductive carbon, carbon-silica composites where the carbon and silica are interconnected in a close manner are of specific interest. Studies from table 5.1 have all used conductive carbon additive during electrode fabrication; 10-30 wt% conductive carbon additive is common. Note that this is much larger than commercial anodes where ≤5 wt% conductive carbon is used.[15]

Table 5.2. Material properties and electrochemical performances for silica-carbon composite active materials in literature

Carbon (wt%)	***Material Description***	***Initial CE (%)***	***Initial capacity (mAh/g)***	***Number of cycles***	***Final capacity (mAh/g)***	***Ref***
76	Silica particles (<100nm) in hard carbon composite, synthesised via hydrothermal synthesis	~60	630	15	630	[6]
50	7nm silica particles in carbonised sucrose composite.	NA	620	50	580	[13]
7.5	Amorphous silica carbon composite from sol-gel route plus mechanical milling and post heat treatment.	~60	500	100	600	[16]
41	10-50nm silica particles in carbon matrix synthesised from carbonised rice husk.	52	400	80	450	[17]
-	Carbon coated silica diatoms.	~50	600	95	500	[8]
26	(50nm) Mesoporous silica around a (100nm) carbon core particle with (6nm) carbon coating to produce layered C-SiO_2-C material.	56.5	1055	150	1055	[7]
46	Mesoporous silica confined within ‘nitrogen doped	42	1250	100	700	[18]

	carbon framework', complex synthesis					
36.5	Hollow silica shells 350nm embedded within mesoporous carbon matrix.	74	780	150	900	[19]
6	Mesoporous silica spheres with carbon coating. Synthesised from polymer templating	66	600	180	580	[20]

~ denotes value calculated from data available. NA = information not available/reported. Within all the studies reported in Table 5.2 additional conductive carbon has been incorporated in electrode formulation, (Apart from[8]).

Combining silica and carbon into one material has beneficial effects: Firstly, the high electronic conductivity of carbon enhances both the rate capabilities and the reduction process of silica by allowing the electrons access to reduction sites. Secondly the requirement of small nanoparticle silica, as described above, leads to high specific surface area for electrodes. This high surface area leads to low columbic efficiencies during the first cycle due to more SEI formation. Embedding these small silica particles within a carbon matrix reduces the surface area in contact with electrolyte, reducing the amount of SEI formation. Thirdly carbon materials with graphitic and hard carbon phases are commonly used as active materials for lithium-ion anodes and can reversibly intercalate and de-intercalate lithium stably over many cycles. Therefore, the carbon materials can also provide capacity.

Table 5.2 summarises the material characteristics and performances of carbon-silica composite materials reported in the literature. As one can see, the capacity of silica-carbon composites presented in Table 5.2 tends to be higher than pure silica alone (Table 5.1) Some reports [19] quantified the capacity arising from pure carbon within the composite (in one case 200 mAh/g)[19], which revealed the contribution from silica within their composite to be roughly 580 mAh/g of capacity. This is higher than the average capacity reported for pure silica in Table 5.1. However, it is not clearly understood why carbon-silica composites lead to an increased capacity from the reduction of silica.

As well as higher capacity of carbon-silica composites, the average columbic efficiencies were also higher (40-74 %). Low columbic efficiency is inherent to the nature of the reduction reaction and its irreversible products. However, the higher average columbic efficiencies for carbon-silica composites supports the hypothesis

of more stable SEI formation within these materials. The highest capacities yet reported for silica and carbon-silica based active materials were around 1100-1200 mAh/g.[7][12][18] Due to the lack of in depth characterisation of the reduction products in the literature, it is not possible from literature sources to conclude why these materials achieve a step change in capcity upon carbon doping. This is further discussed in Chapter 7.

A detailed study into the nature of electrochemical reduction of silica within the first cycles of silica anode materials is lacking within the literature. Such a study will provide key information around the rate and extent of silica reduction at low potentials and enable the use of silica as an active material. In view of this challenge, this chapter focuses on the following key aims:

1. A new stepwise Potentiostatic Discharge (S-PSD) is developed to study the extent of the electrochemical reduction of silica with respect to time. This method shows how the capacity of a silica electrode increases with respect to the total reduction time at low potentials. Using this method an optimum reduction time can be determined.
2. Bioinspired Silica (BIS) is reduced with PSD and shown to have advantages over previously explored Stöber silica. BIS can be produced in an environmentally friendly and scalable synthesis method (as discussed in Chapter 2) which holds great promise for a future battery material. In addition, we show the oligomers used in BIS can be advantageously turned into a carbon coating within BIS.
3. Finally, a short-circuit reduction method is introduced, this method can be performed at temperatures up to 50 ^{o}C where high capacities for BIS can be reached with much shorter reduction times. The use of silica anodes in full-cells will require a pretreatment step. This short-circuit method provides dual benefits of decreasing the total reduction time, and removing the need for potentiostats (needed for PSD).

5.3 Experimental

5.3.1 Cell Preparation

Electrochemical experiments were performed using MIT2016-type coin cells with a Whatman glass fibre separator and lithium foil (from Sigma Aldrich) as the counter electrode. The electrolyte was 1M $LiPF_6$ in a 1:1 solution of ethylene carbonate (EC) and dimethyl carbonate (DMC) from Sigma Aldrich with added 5w% fluoroethylene carbonste (FEC). The composition of working electrodes was: 60w% PEHA-BIS active material, 20w% conductive additive C-65, 20w% binder carboxymethyl cellulose. The electrochemical performances were tested on a Maccor 4000M Battery and Cell test system in a 25^{o}C temperature chamber. The cut off voltage was 0.01 V versus Li/Li^{+} for discharge (lithium insertion) and 1 V versus Li/Li^{+} for charging (Li extraction). Cells where charged under a constant-current constant-voltage (CCCV) regime: galvanostically at 0.1C, unless specifically stated otherwise, and held at 0.01V until current fell below 0.05C upon discharge. The specific capacity was calculated based on active material mass. The charging rate was calculated from the fraction of active material in the electrode and based on a theoretical capacity of 680 mAh/g for silica.

5.3.2 Potentiostatic discharge (PSD)

The PSD was performed on a MACCOR 4000M Battery and Cell test system. Cells were discharged galvanostatically at 0.1C to 0.01V. The cell was then subjected to 0.002 V potentiostatic discharge for 20 hours. Following this, 5 CCCV cycles were performed according to the above criteria. This procedure was looped in accordance to the desired experiment, typically 20 loops, therefore 400 hours total time at 0.002 V and 100 cycles.

5.3.3 Short Circuit Reduction

Short circuit reduction involved the application of a crocodile clip (RS-components) across the positive and negative electrodes of the 2016 coin cell providing a path for current flow. The short circuit was applied to freshly made cells, unless stated otherwise. The short-circuited cells were stored in a sealed glass vial and placed within a temperature-controlled oven. The duration of short circuiting and temperature of the oven were varied as specified.

5.3.4 Carbon Coating of BIS

The carbon coating experiments were undertaken at Queen Mary University under the supervision of Professor Magdalena Titirici. We would like to acknowledge their valuable input and the funding the from Energy Storage CDT for the funding.

BIS was prepared and calcined as described in experimental Chapter 2. The impregnation with carbon containing precursor Glucose (Glu) (Sigma Aldrich) or mesophase pitch (MPP) was performed in their respective solvents, deionised water and tetrahydrofuran (THF). The impregnation solutions were made up to contain 5 wt % precursor and 95 wt% solvent. The 5 wt% solutions were dosed onto 0.5 g of BIS such that 0.5 g of carbon precursor was transferred. The mixture of dissolved carbon precursor and BIS were mixed with a spatula until BIS power was completely wetted, then transferred to an 80 ^{o}C vacuum oven. Samples were dried under vacuum for 24 hours. The dry powder samples were transferred to a tube furnace (Carbolite) which was purged under Argon. The furnace was ramped at 10 ^{o}C/min to 900 ^{o}C and held there for 4 hours. Once cool the samples were removed and stored in an 80 ^{o}C vacuum oven. All subsequent electrode and cell preparation stages were identical to the standard experimental procedure, Chapter 2.

5.4 Results and Discussion

5.4.1 Stepwise potentiostatic reduction

Previously Lepoivre et al[2] reported reduction times of 60 and 250 hours and that higher capacities were reached at 250 h. However, the extent and the rate of reduction are unknown. The necessity of electrochemical reduction of silica is an added processing step for this active material. The long 250 h reaction times reported by Lepoivre et al will increase production time and hence it is likely to inhibit the commercialisation of these materials. It is therefore important to understand the kinetics of the reaction to optimise this process, with the aim of reduction the duration of the electrochemical reduction step. An experiment was designed to study the kinetics of electrochemical reduction of silica, where the capacity increase of silica electrodes at 20-hour intervals of PSD. The increase of capacity was measured by 5 galvanostatic cycles in-between every 20 hours of PSD.

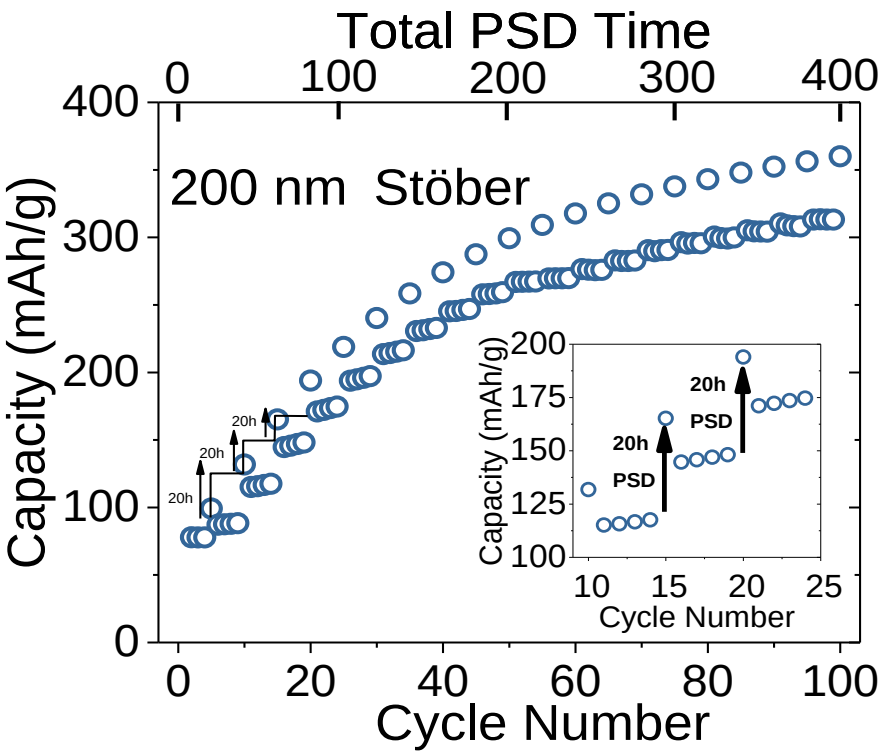

Figure 5.2. Capacity of Stöber silica during 20 hour PSD steps at 2 mV. Insert is a magnification of cycles 10-25 showing the increase in capacity after a 20 hour PSD step.

Figure 5.2 presents the results of stepwise PSD on 200 nm Stöber silica particles. One can now envisage the progress of the electrochemical reduction at a resolution of 20 hours. Capacity increase within each step is related to the extent of the

electrochemical reduction, as more silica is reduced (liberating more silicon), the capacity of the electrode increases. The capacity in increased rapidly up to 250 mAh/g after 200 hours of PSD (50 cycle, Figure 5.2). After this point the capacity increased slowly with each subsequent PSD step to a final capacity of 315 mAh/g after 400 h total PSD. Fitting of the capacity profile with a simple exponent provides a perfect fit with R^2=0.9997. Using this model to determine the equilibrium capacity (at infinite PSD time) was 379 mAh/g

The capacity reported by Lepoivre et al[2] is 400 mAh/g with 250 hours of PSD. After 400 hours of stepwise PSD, the capacity in Figure 5.2 is 22% lower than those reported by Lepoivre et al.[2] As lepoivre et al, did not provide detailed characterisation of their Stöber silica it is not possible to provide a direct comparison with our results in Figure 5.2. However, our results confirm that Stöber silica can be electrochemically reduced by PSD. We also show that the extent of the reduction reaction can be studied by using a stepwise PSD method.

5.4.2 Bioinspired Silica as Anode Material

Previous work of reduction of silica has focused on non-porous silica materials. The reduction of silica within the electrode occurs at the interface between the silica particle and lithium containing electrolyte. Increased surface area in contact with electrolyte may increase the rate of lithium reduction. For this reason, porous silica may provide better performance characteristics during electrochemical reduction. Indeed, in the case for carbon-silica systems, when non-porous particles were used, the initial capacities were between 400-600 mAh/g (see Table 5.2). However when mesoporous silica was used instead, the capacities obtained were typically >1000 mAh/g[7][18]. In this section the novel results of using porous silica directly as an anode active material are explored.

Based on the above hypothesis a number of porous silica were investigated. Of these silicas, only BIS was shown to be active during PSD (discussed in future work). BIS has a number of competitive advantages over commercial silica: An economic feasibility study of the biologically inspired precipitation of silica showed that the green synthesis route may prove economically competitive to Stöber silica and mesoporous silicas.[21] The bio-inspired method also provides the ability to produce a diverse range of porous silica.[22]

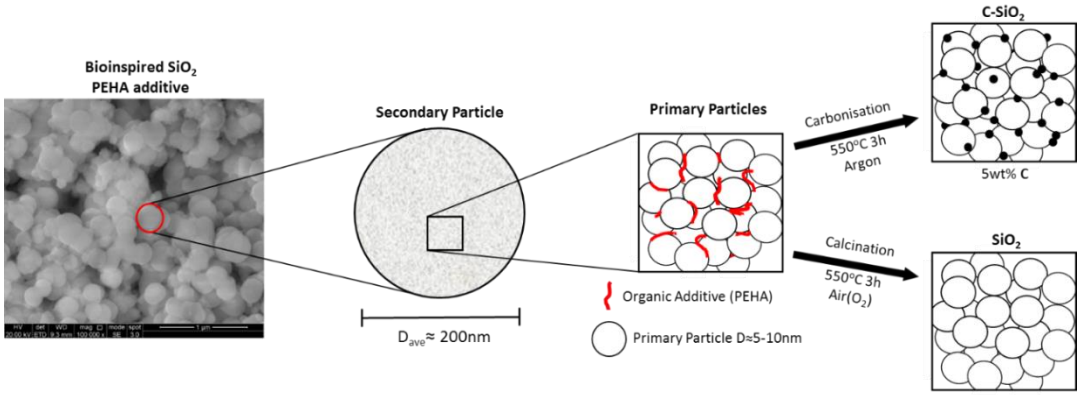

Figure 5.3. Schematic of bioinspired silica particle structure and theoretical representation of carbon coating and calcination to produce final product.

In addition to porous properties bio-inspired synthesis provides another important attribute which can potentially address the low electronic conductivity of silica. Post synthesis, bio-inspired silica contains an organic additive used for the precipitation, which is entrapped on the surface and within the silica structure. Figure 5.3 presents a schematic of how the organic additive may be either calcined and completely removed by heating in air or can be carbonised into soot particles by heating under

an inert atmosphere. Carbon coating of bioinspired silica in this way may improve the electronic conductivity of silica further highlighting the potential for BIS in this application. BIS can provide the combination of increased silica porosity and a carbon coating by a facile two step synthesis. The ability to electrochemically reduce BIS is studied in detail below.

5.4.2.1 Characterisation of bio-inspired silica anode material

BIS was synthesised with the amine additive pentaethylene hexamine (PEHA). After synthesis and drying PEHA additive is contained between the primary particles of the silica structure and on the surface (Figure 5.3). Calcination oxidises the PEHA allowing it to leave the silica as a gas, in turn this combustion leaves voids in the silica structure creating micropores and small mesopores. Calcination causes a mass loss of 20 wt% due to the removal of PEHA from the silica. Figure 5.4 presents the nitrogen absorption isotherms and Table 5.3 summarises the BET surface areas and mesopore volumes.

The carbonisation causes the formation of carbon containing soot particles from the incomplete combustion of the PEHA additive. Gravimetric analysis confirmed the amount of carbon remaining within the particles was 5 wt% (See Table S5.1). The adsorption isotherm (Figure 5.4) shows the presence of micropores and some macropores. The calcined BIS has the highest SSA and pore volume as expected. The SSA and pore volume of the carbonised material lies between the calcined and uncalcined-sample.

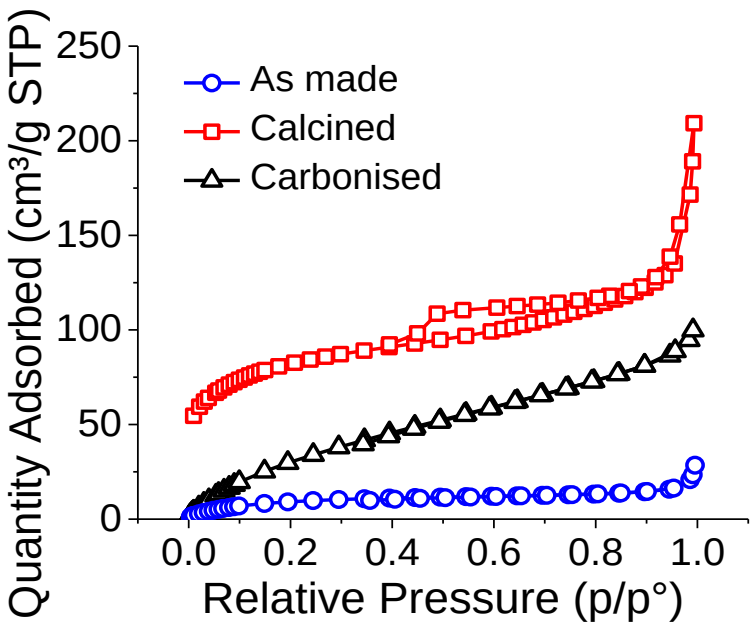

Figure 5.4. N_2 isotherms of PEHA silica before calcination, after calcination and after carbonisation.

Table 5.3. BET surface area and BJH pore volume of PEHA bioinspired silica.

	BET Surface Area (m^2/g)	*BJH pore volume (cm^3/g)*
Uncalcined	35.5	0.01
Calcined	301	0.16
Carbonised	147	0.12

The pore properties of BIS are determined by the interconnectivity of the primary particle, as previously established (Chapter 2). SEM images were used to determine that no difference in secondary particle morphology was caused by the calcination and carbonisation processes (Figure 5.5). It was therefore concluded that the lower surface area and pore volume of the carbonised BIS was caused by carbon particles in between primary silica particles - carbonisation had the desired effect of providing a carbon network on the surface and within the BIS pore network.

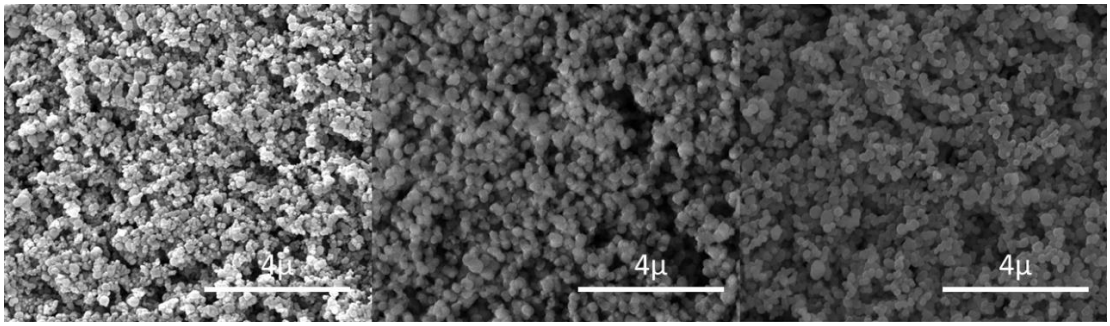

Figure 5.5 SEM images of (left) Fresh PEHA-BIS after drying (middle) calcined PEHA-BIS and (right) Carbonised PEHA-BIS.

5.4.2.2 Potentiostatic Discharge (PSD) Electrochemical Reduction of BIS

To investigate the promise of BIS as an anode material the previously invented stepwise PSD was employed. Figure 5.6 shows the capacity evolution of calcined and carbonised PEHA-BIS. Carbonised PEHA (C-SiO_2) capacity increased quicker and reached a capacity of 600 mAh/g after 400 hours of PSD (100 cycle). The calcined silica gained little capacity in the first 60 hours of PSD (15 cycles) but then increases to 370 mAh/g by 400 hours of total PSD. The C-SiO_2 reached a higher capacity quicker as electronic conduction over the surface of silica primary particles is likely to be quicker and more uniform, thus providing more electronic reduction sites. Electrochemical impedance spectroscopy (EIS) was used to find the contact resistance and the charge transfer resistance before the first 20 hour PSD (Figure S5.1). These measurements can provide information on how well the electrode conducts electricity and as such a measure of if the carbon coating had the desired effect. The values of contact resistance and charge transfer resistance were found to be lower in the C-SiO_2 electrode by 8.5% and 16.0% respectively compared to the calcined silica electrode. It is clear that the increased conductivity of the carbon conducting layer on the silica increased the electronic accessibility of the reduction sites thus increasing the reduction rate.

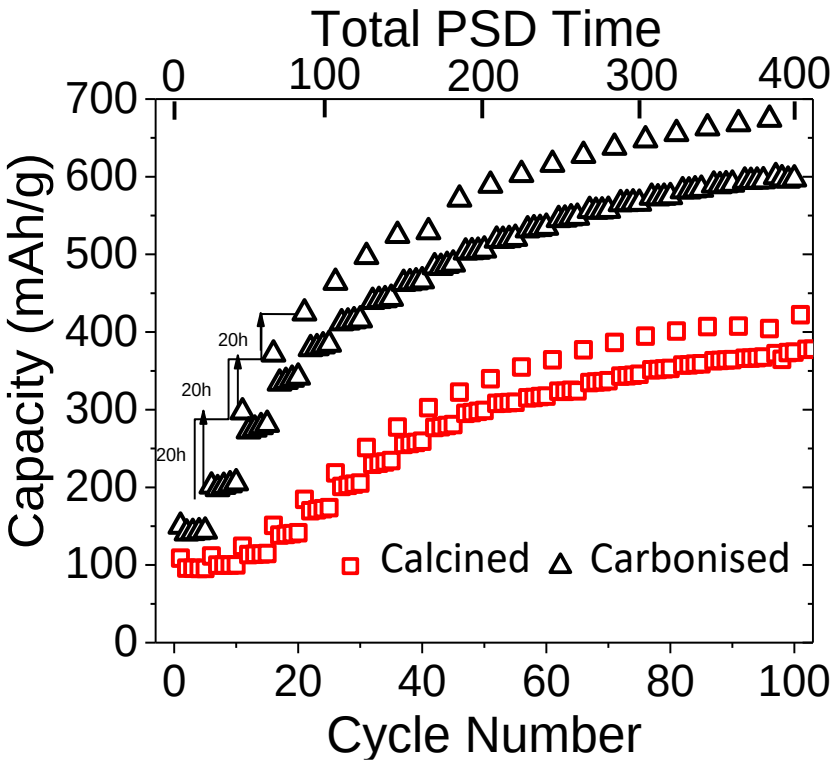

Figure 5.6. Capacity vs cycle life of PEHA-Silica (red) calcined, (black) carbonised (5 wt% carbon).

The first cycle of each step is consistently higher than the subsequent 4. Additionally, from the 2nd cycle to the 5th cycle, there is small increase in capacity. It was found that the increased capacity in the first cycle after a PSD step is due to a limited amount of lithium storage in the electrode, which is deposited on the anode during the low voltage PSD step. The voltage profile during the first cycle after PSD is flat at 0 V for a period before beginning to rise, as would be expected during lithium metal extraction from the surface of the electrode.

Initial capacities of 90 mAh/g were observed in Figure 5.6 even without any reduction of silica. This is attributed to the 20 wt% C-65 (carbon) as shown in Figure S5.2 to have capacity of 241 mAh/g (based on electrode mass of 1.4 mg). Figure 5.7 shows the capacity of the PEHA silica electrodes over 100 cycles without the use of the PSD treatment. Capacity increases were small for the both electrodes (15 mAh/g increase for calcined and 40 mAh/g for carbonised electrodes at 100 cycles). This highlights the requirement for electrochemical reduction of silica to increase electrode capacity. These small capacity increases observed are an order of magnitude smaller than the increase presented in Figure 5.6 by PSD treatment. The increase in capacities seen in Figure 5.7 is credited to the low current rate used in the cycling and hence the time which the electrode is at low voltages. During the galvanostatic cycling, silica can be

reduced when the cell potential allows and hence as cycles progress, the capacity increased. The reduction of silica in this manner may have ramifications to many other fields where silica materials are used in LIBs.

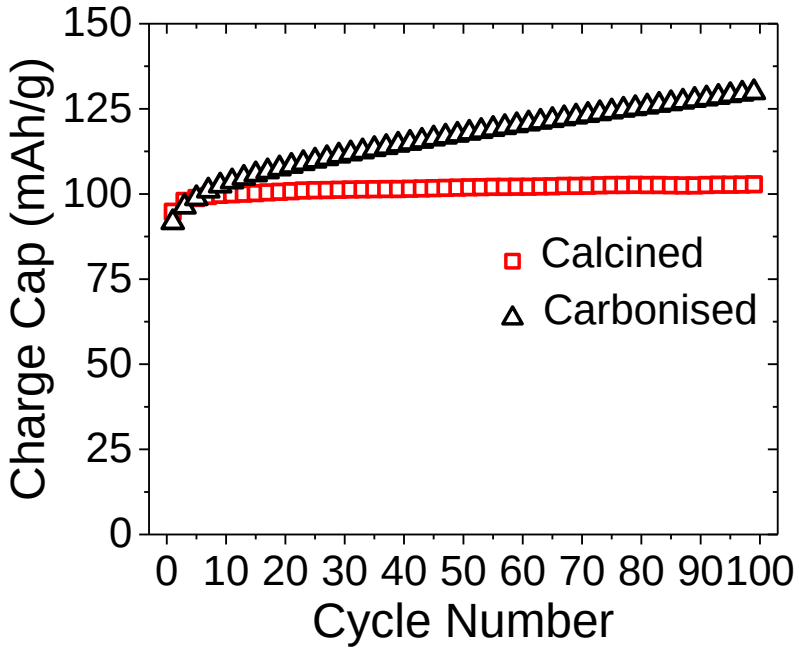

Figure 5.7. Capacity of calcined and carbonised silica electrodes over 100 galvanostatic cycles at C/10.

Figure 5.6 showed it was possible to achieve capacities of >600 mAh/g using PSD for the carbonised PEHA silica. This is 50% larger than the reported capacities of Lepoivre et al.[2] After the PSD shown in Figure 5.6 both electrodes where galvanostatically cycled for 100 cycles to determine the stability their capacity (see Figure 5.8). The results show that the capacities of 625 mAh/g and 410 mAh/g obtained at the end of 400 h PSD (cycle number 100) showed as little as +2.4% and 0% loss for the carbonised and calcined electrodes respectively after a subsequent 100 cycles. This high capacity and stable cycle life show great potential for the use of BIS as an anode material.

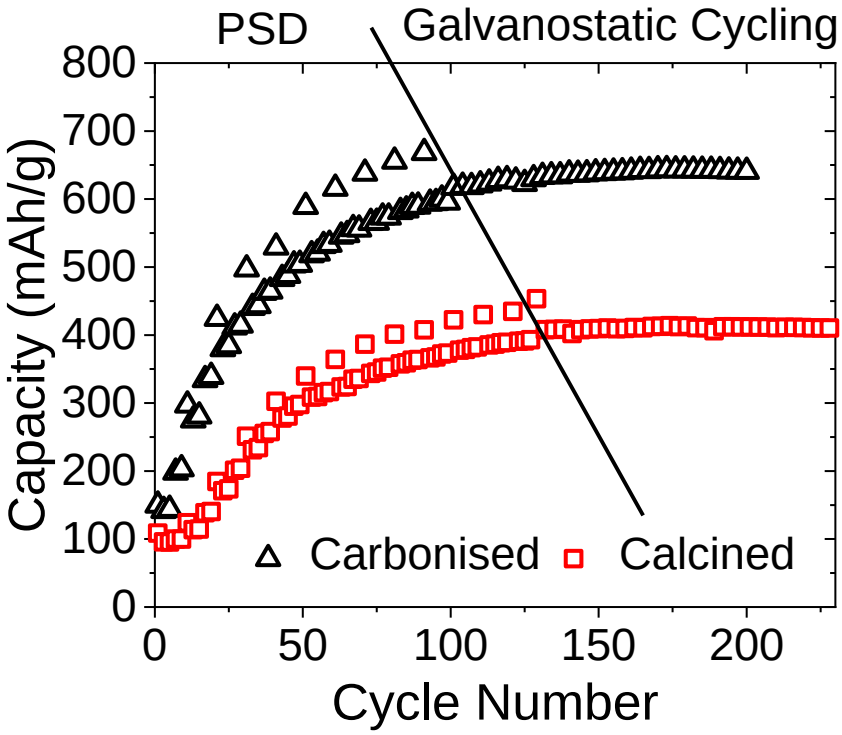

Figure 5.8. Capacity vs cycle life of carbonised and calcined PEHA silica electrodes throughout 400 hour total PSD with 5 galvanostatic cycles every 20 hours, total PSD equivalent of 100 cycles. Subsequently subjected to 100 cycles galvanostatic cycles.

To reach the high capacities achieved in Figure 5.8 the stepwise PSD and 5 galvanostatic cycles each step was a protracted process (~21 days). Therefore, optimisation of the PSD steps was subsequently studied to reduce the overall reduction time required to reach maximum capacity for both materials. Figure 5.9 shows capacities of the calcined and carbonised BIS electrodes with 400 hour PSD and no cycling every 20 hours. After 400 hours of constant PSD, capacities observed were 500 and 350 mAh/g respectively for carbonised and calcined electrode. These are 17 % and 5% lower than when PSD was combined with cycling. Upon subsequent 100 cycles, the capacities of both electrodes increased to 635 and 435 mAh/g respectively. Two noteworthy effects are concluded from this finding: Firstly 400 hours of PSD did not increase capacity to the same extent as 400 hours PSD with 5 cycles every 20 hours. Secondly, after 400 hours of PSD the reduction of silica has not reached completion as capacity continued to rise. Both of the above points were investigated further as it is desirable to optimise the quickest path to the largest and most stable capacity.

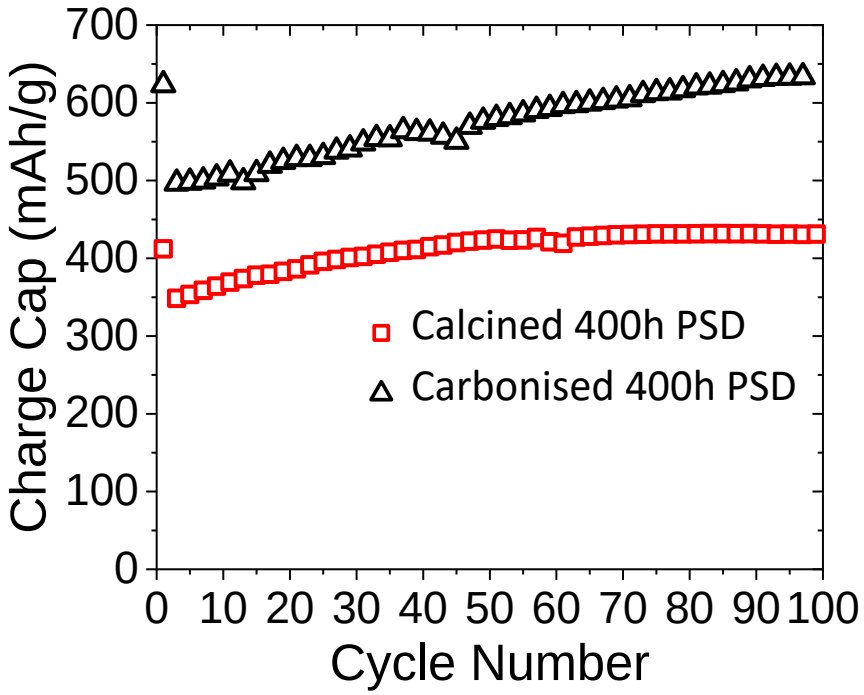

Figure 5.9. Capacity of carbonised and calcined electrodes subjected to 400 hours of PSD

5.4.2.3 Stepwise Potentiostatic Discharge (S-PSD) vs Constant PSD (C-PSD)

Extended cycling was performed after 400 hours PSD to determine when the capacity would stabilise. The results of 400 galvanostatic cycles are presented in Figure s5.3, note a faster C-rate of C/2 was used in this investigation due to time constraints. At faster C-rates the maximum capacity of the electrode will be reduced (due to voltage drop across the electrode). The trend in capacity stabilisation can be studied. The maximum capacity of the carbonised silica electrode was measured as 620 mAh/g after 400 hours of PSD and 170 cycles. The capacity of the calcined sample reached a maximum of 460 mAh/g after 400 hours of PSD and 115 cycles. Interestingly, the maximum capacities obtained match well with the capacities from Figure 5.6, suggesting a ceiling for maximum capacity of these materials. After reaching their maximum capacities, both electrodes were relatively stable for 10-30 cycles, then a gradual decrease in capacity was observed to 400 cycles. The final capacity of the electrodes were 570 mAh/g and 400 mAh/g for the carbonised and calcined electrode respectively. The capacity fade of the electrodes maybe related to the half-cell arrangement used for testing, extended cycling in half cells has shown capacity fade

due to passivation and degradation of the lithium electrode. Loss of capacity via this mechanism should not be concluded to be loss of intercalation capacity.[23]

To investigate this further, electrodes which underwent both treatments were cycled for 100 cycles as follows. Figure 5.9 shows the capacity results of 400 hours straight PSD and Figure 5.8 shows 100 cycles after 400 hour stepwise PSD. Their differential capacity plots are shown in Figure 5.10.

Differential capacity plots of electrodes in the 1st and 100th cycle after PSD are presented in Figure 5.10. The 1st cycle of C-PSD had one broad anodic peak between 0.1-0.7 V, while their cathodic profile slopes from 0.3 to 0 V. The first cycle for S-PSD had an anodic profile with two distinct peaks visible at 0.32 and 0.47 V. The cathodic profile of S-PSD is also different with a new peak at 0.19 V sloping profile down to a second peak at 0.05 V. In the 100th cycle (red) the S-PSD shows the same profile as its first cycle. The differential capacity profile of the C-PSD clearly changes across the 100 cycles such that it matches that of the S-PSD with anodic peaks at 0.32 and 0.47 V, cathodic peak at 0.19 V and 0.05V. The result of Figure 5.10 on carbonised BIS was repeated on calcined BIS and showed the exact same behaviour (Figure S5.4).

The differential capacity (dV/dQ) profiles are distinctive of silicon lithiation and delithiation (See Chapter 1, Table 1.2). Firstly, the profiles observed in Figure 5.10 provide strong evidence that silicon was produced as a direct product of lithium reduction of silica, and that this silicon can reversibly alloy and de-alloy with lithium. Secondly the well documented lithium phase transitions at specific voltages can be used to infer which lithiated states of silicon were formed in each case.[24] Lithiation of amorphous silicon will produce typical cathodic peaks around 0.25V corresponding to (a-Si → a-$Li_{2.0}$Si), a strong cathodic peak at 0.1 V will follow corresponding to the (a-$Li_{2.0}$Si → a-$Li_{3.5}$Si) phase transition, the final lithiation and crystallisation of (a-$Li_{3.75}$Si → c-$Li_{3.75}$Si) occurs at <0.1 V (note literature consensus is that smaller silicon particles/crystallites require lower voltages to for the $Li_{3.75}$Si phase formation).[25] Delithiation will produce anodic peaks at 0.28 and 0.5 corresponding to the delithiation of (a-$Li_{3.5}$Si → a-$Li_{2.0}$Si) and (a-$Li_{2.0}$Si → a-Si) respectively. If the c-$Li_{3.75}$Si phase is formed on lithiation this will show a sharp distinctive anodic peak at 0.43 V corresponding to the reaction (c-$Li_{3.75}$Si → a-$Li_{1.1}$Si).

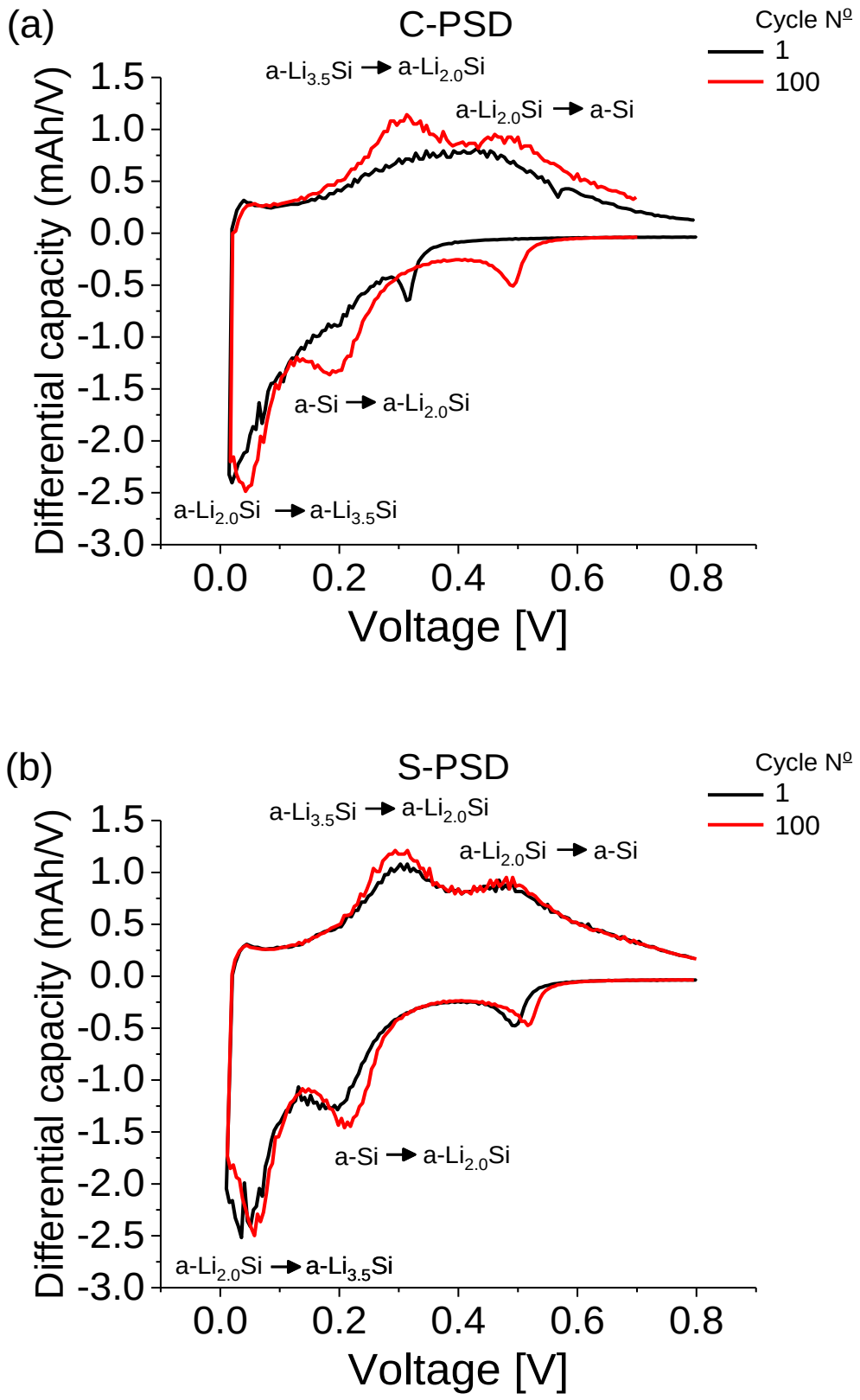

Figure 5.10. Differential capacity plots of C-SiO_2, comparison of (a) 400 hours C-PSD and (b) 400 hour S-PSD (5 galvanostatic cycles every 20 hours).

Understanding the lithiation and delithiation phase transitions can explain the lower capacity achieved when just 400 hours of PSD is used compared to stepwise PSD and cycling. The sloping cathodic profile during the 1st lithiation after PSD Figure 5.10(a, black) had no distinct peaks near the expected phase transitions. This indicates that for this current rate incomplete lithiation is occurring and that the a-Si → a-$Li_{2.0}$Si and a-$Li_{2.0}$Si → a-$Li_{3.5}$Si phase transitions are occurring in parallel with each other. Upon delithiation a similar effect seems to be occurring: no clear peaks were seen where expected. This suggests that the a-$Li_{2.0}$Si and a-$Li_{3.5}$Si states formed were small in number and hence underneath the broad delithiation peak of Li_xSi states, or the conductivity pathways were too slow for a-$Li_{2.0}$Si and a-$Li_{3.5}$Si states to delithiate at the appropriate voltages. No sharp peak at 0.43 V was observed, indicating that the highest lithiated state c-$Li_{3.75}$Si did not form, but this is not uncommon for silicon materials.

Figure 5.10 (b) presents the results from the stepwise PSD, where the electrode had experienced 100 cycles during the 400 h PSD, in this case the dV/dQ profiles resemble more strongly the typical features of silicon within the first cycle (Chapter 1, Table 1.2). The cycling of the electrode during PSD changes the reduced materials structure such that it can better respond to the galvanostatic cycling and the lithiation of silicon progressed via the established pathways. This is ultimately responsible for the higher capacities achieved by the stepwise S-PSD than just doing the C-PSD in just one step.

It is hypothesised that the repeated volume expansion and contraction of silicon during cycling increases the capacity of the electrode. Little is known about the order and/or composition of the silicon phases within the structure of the active material. However, alloying and de-alloying of silicon inherently involves volume expansion. The ideal species, hypothetical lithium silicates and lithium oxide provide a structural scaffolding network around the silicon species leading to the observed stable capacity of this material. However, for the silicon to reach maximum capacity, cycling as well as PSD are required. The repeated expansion and contraction will cause stress on the reduced material thus breaking some of this scaffolding structure. It is hypothesised that this stress changes the scaffold structure and improves the silicon conductivity pathways. This allows better conduction of electrons and lithium ions to silicon within the active material.

Based on the above observations that stepwise cycling during PSD leads to a higher capacity than constant PSD, 625 mAh/g vs 500 mAh/g respectively, a mechanism

has been proposed. Based upon the differential capacity plots of stepwise vs constant PSD it was shown that the established pathways for silicon lithiation and delithiation do not occur sequentially if the electrode is subjected to C-PSD.

5.4.2.4 Rate capability of BIS electrode

The rate capabilities of calcined and carbonised BIS were tested between 0.1 and 5.0C. The C-rate was determined by a theoretical capacity of 680 mAh/g hence 0.1C corresponds to 0.068 A/g of active material and 5.0C corresponds to 3.4 A/g. Figure 5.11 presents the rate capabilities of electrodes treated to 400h C-PSD. Both electrodes show excellent rate capabilities even at the extreme C-rate of 3.4 A/g where the carbonised and calcined electrode can still provide 180 and 145 mAh/g capacities respectfully.

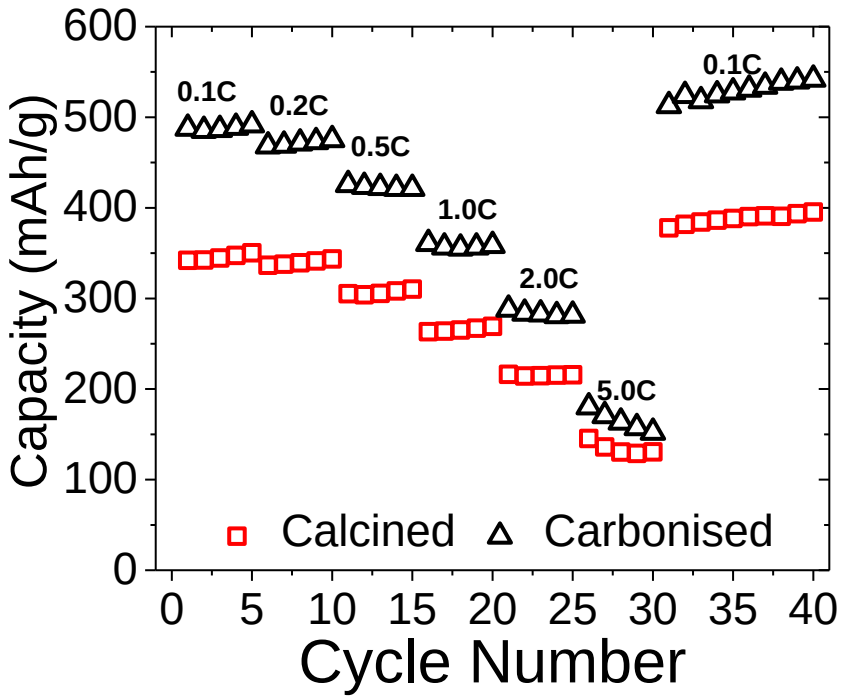

Figure 5.11. Rate capability of calcined and carbonised PEHA-silica electrodes.

Previous studies have shown an upper limit for energy density commercial graphite electrodes of 4C, above which substantial electrode breakdown occurs (4C=1.484 A g^{-1}).[26] For our BIS electrode material, a similar C-rate of ~2.0C, can still provide 290 mAh/g of capacity. After subjecting the electrode to the C-rate test, the electrodes showed excellent abilities to return to their original capacity at 0.1C. This indicates the stability of the reduced material and the robustness of the electrode fabrication.

5.4.3 Short Circuit Electrochemical Reduction

Above it was shown that a stepwise PSD can be used to investigate the kinetics of electrochemical reduction of silica. The use of BIS as an anode material was investigated in detail and shows promise as a future active material due to its high capacity and stable cycle life. The use of PSD is reliant on the use of a potentiostatic device to control cell voltage. Therefore, the future processing step of activating silica electrodes will be reliant on using such a device, thereby increasing the CAPEX and complexity of the electrode fabrication. According to the standard redox potentials of Lithium and silica the reduction reaction is spontaneous with a potential of -2.13V i.e. a galvanic cell (Table 5. 4, Equation 5.5). Therefore the reduction reaction should occur during the PSD at 2 mV. If an electronic pathway between the two electrodes is established, then due to the spontaneity of the reaction the reduction reaction should proceed without the need for the application of an external bias (voltage). This reaction is here termed 'external short circuiting' and describes the connection of the positive (silica) electrode and the negative (lithium) electrode via a low resistance external circuit.

Table 5. 4. Standard redox potentials for silica and lithium.

Half Reaction	Potential (V)
$SiO_2(s) + 4H^+ + 4e^- \leftrightarrow Si(s) + 2H_2O$	-0.91
$Li^+ + e^- \leftrightarrow Li\ (s)$	-3.04

$$SiO_2 + 2Li \rightarrow Si + 2Li_2O \qquad \text{Equation (5.1)}$$

$$E^o\text{cell} = E^o\text{red} + E^o\text{ox} \qquad \text{Equation (5.4)}$$

$$E^o\text{cell} = 3.04 - 0.91 = \underline{2.13V} \qquad \text{Equation (5.5)}$$

A series of silica-lithium half cells where externally short circuited in a 25 ^oC temperature chamber and left for 5 and 10 days before being subjected to 100 galvanostatic cycles at C/10 to study the effect of short circuiting on the electrochemical reduction of silica. Figure 5.12 shows the resulting reversible capacity.

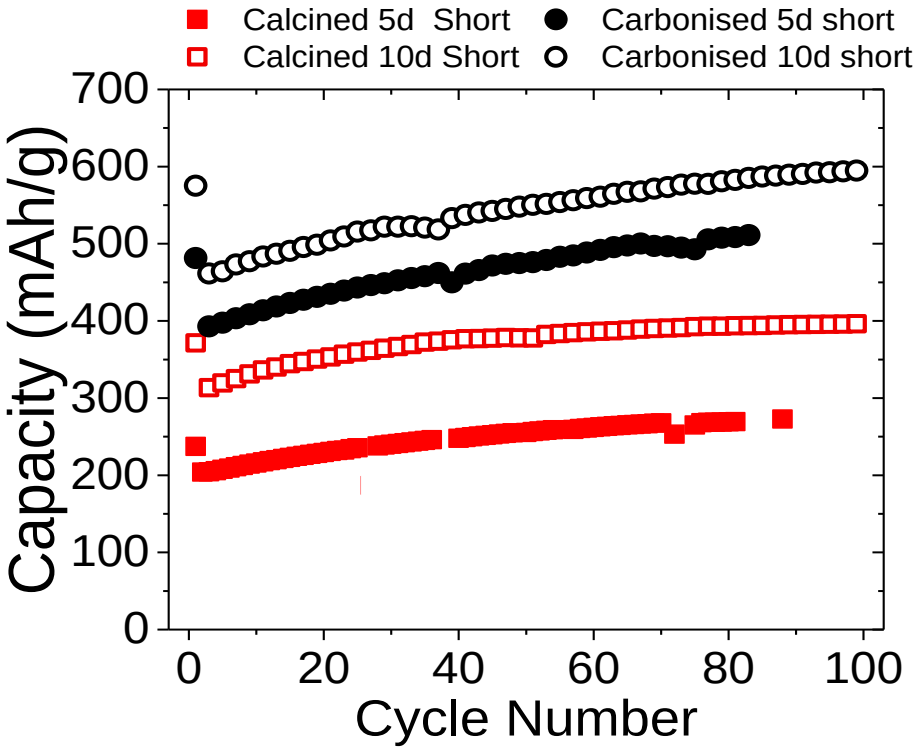

Figure 5.12. Externally short circuited calcined and carbonised BIS cells at 25 ^{o}C for 5 and 10 days. Resulting capacity upon galvanostatic cycling for 100 cycles.

5.4.3.1 Kinetics of short Circuit reduction

All electrodes show an increase in capacity capered with untreated silica electrodes, validating that the reduction reaction is spontaneously proceeding when an external short circuit is applied. The calcined silica electrodes reached capacities of 200 and 310 mAh/g after 5 and 10 days of short circuit respectively. The carbonised electrodes reached higher capacities of 395 and 460 mAh/g after 5 and 10 days respectively. After 100 cycles, capacities of all four electrodes increased further. This is because as discussed above, the dV/dQ plots evolve over the 100 cycles to produce a more typical silicon profile after cycling and this further confirms cycling is crucial to achieve higher capacity.

Capacity increase observed from the external short circuit matches well with the capacity increase measured for PSD times of 120 h (5days) and 240 hours (10 days) for both the calcined and carbonised electrodes, (cross reference with Figure 5.6).

The discovery of short circuiting to increase silica electrode capacity may have implications for any industrial scale fabrication of this electrode material. Due to the ease of performance and the removal of any energy input requirement.

The rate of the reduction reaction and hence the capacity achieved by the silica electrodes was still improved by carbonisation on the silica surface. As discussed above, it is clear that the improved electronic conduction pathways provided by carbon coating increased the rate of reduction. A limiting factor for governing the rate of reaction is lithium-ion availability at the reaction site. As the reduction reaction progresses from the surface of the silica, lithium-ions will be required to move into the solid particles. The asymptotic behaviour observed for the extent of reduction reaction during PSD, Figure 5.6 suggests that as the silica is increasingly reduced it becomes harder for virgin material to react. This may be related to the electronic conductivity and/or the lithium ion conductivity within the product species that form and will be explored in further detail in Chapter 6 below.

As stated above the electrochemical reduction of silica active materials will require an added fabrication step before the silica electrodes can be incorporated into a full cell. It is therefore important to understand and optimise this process step to provide high capacity and a stable cycle life. Reducing the reaction time of this reduction step will be crucial for the commercialisation of this process.

Here an experiment was proposed to increase the rate of the electrochemical reduction. The diffusion of ions within a solid is known to increase in rate as temperature increases. With the discovery of the external short circuit reduction method, these cells could be placed in a temperature-controlled chamber. Hence, the cells were short circuited at 50 ^{o}C (instead of 25 ^{o}C) for 5 days then cycled galvanostatically for 100 cycles. Figure 5.13 shows the cycling results for the calcined and carbonised electrodes. Both electrodes reached a capacity >490 mAh/g in the second cycle and both rose almost identically to a capacity of 600 mAh/g after 100 cycles. Over the 100 cycles, the differential capacity profiles evolve as described above with a more prominent silicon profile emerging after cycling.

Both electrodes have reached capacities higher than their equivalents at 25 ^{o}C for 5 and 10 days of short circuit (cross reference with Figure 5.12). This shows that the rate of the reduction reaction is occurring faster at higher temperature. Equally both the calcined and carbonised electrodes reached the same capacity in the same amount of time, which suggests that at 50^{o}C, the electronic conductivity of the electrodes may no longer be a limiting factor for the rate of reduction. It is expected that higher temperatures still would increase the rate of electrochemical reduction. However, the cell cases used in this study were unable to hold at temperatures higher than 50 ^{o}C for prolonged periods.

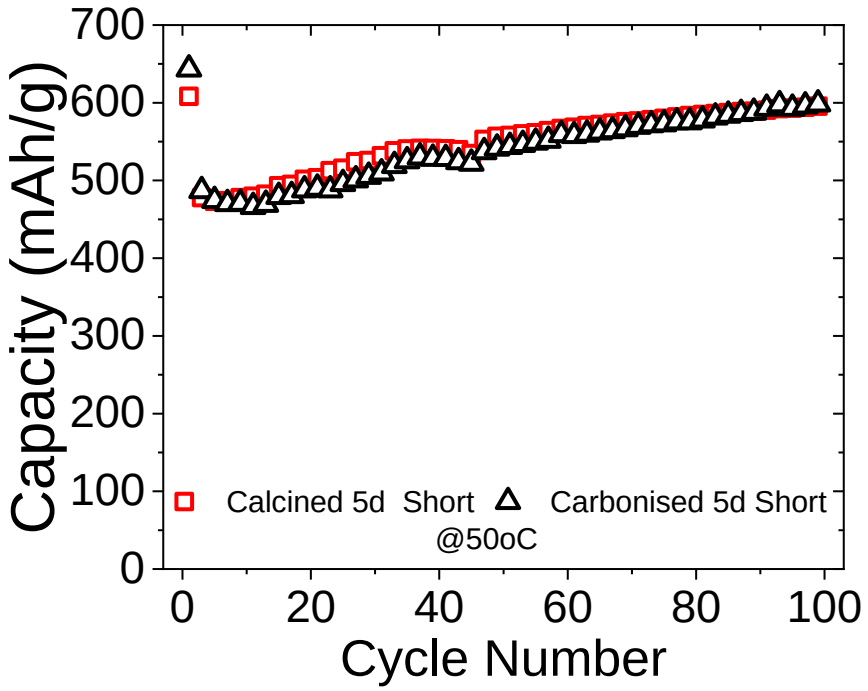

Figure 5.13. Capacity of externally short circuited PEHA-BIS half cells at 50 ^{o}C for 5 days.

A further investigation was performed to study the evolution of capacity during short circuiting between 0.25-5 days for a calcined silica electrode to better determine the optimal time for short cuircuiting. Figure 5.14 presents the capacity for 10 galvanostatic cycles of cells reduced for times between 0.25 and 5 days. An increase to 200 mAh/g can be observed after 0.25 h and the capacity continued to rise quickly up to 2 days of short circuit where 500 mAh/g is reached. Between 2 and 5 days, no large change in initial capacity was observed. Figure 5.14 shows the difference for the same individual cell which was short circuited then cycled, short circuited then cycled, repeated up to 5 days (blue). Higher capacities were observed compared with individually cycled cells for each data set (Figure 5.14 red). This is explained as above where the expansion and contraction of the reduced electrode structure during cycling changes the electrode structure and allows complete lithiation of silicon. Comparison of the dV/dQ curves is consistent with this, with the shorted then cycled cell showing a more defined silicon profile (Figure S5.5).

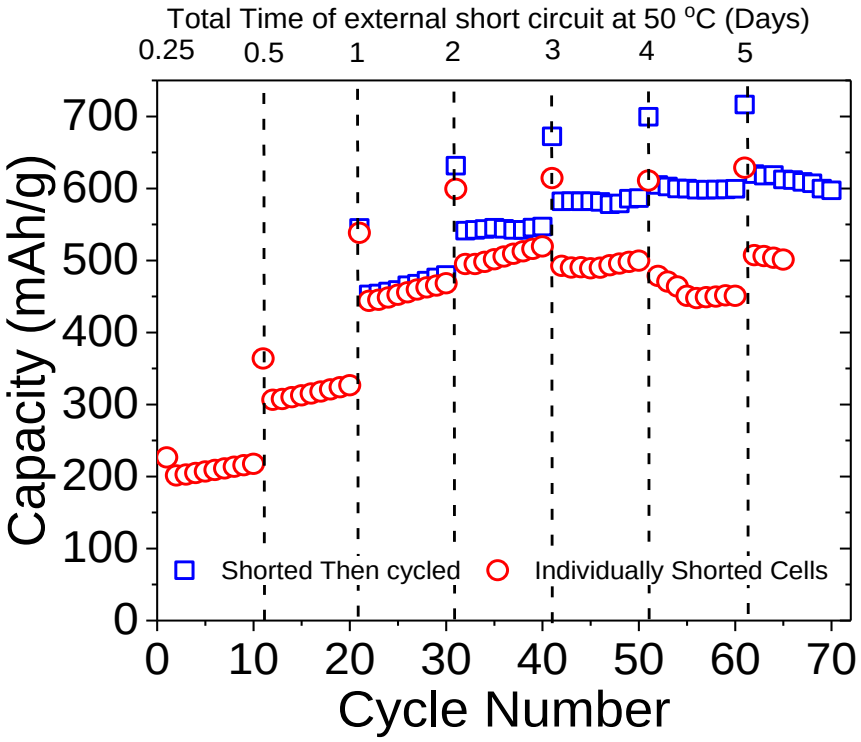

Figure 5.14. Capacity of externally short circuited, calcined BIS-silica electrode, short circuited at 50 °C. (red) cells short circuited for the total indicated time. (blue) individual cell short circuited, cycled then short circuited further up to a total of 5 days.

With short circuiting at 50 °C and with cycling, Figure 5.14 has shown that it is possible to achieve stable capacities of 600 mAh/g in just 4 days of treatment. As well as being able to produce capacities of >430 mAh/g with just 1 day of short circuit treatment. This result should be compared with literature where 250 hours (>10 days) of PSD was required to produce 400 mAh/g in 200 nm Stöber silica particles.[2] The short circuit results presented in Figure 5.14 were performed on calcined BIS. Previously the highest capacity achieved through S-PSD on this material was 410 mAh/g. This is a further advantage of this short circuit method.

5.4.4 Carbon coating of BIS

The ability to carbon coat BIS in a one-step carbonisation has been presented in section 5.4.2. The effect of carbon coating on PEHA-BIS electrodes has been to reduce electrical resistance and lead to higher capacities quicker under stepwise PSD in comparison to calcined silica. The carbon in the carbonised BIS makes up 5 wt% of the material mass. A brief study of carbonisation time of 1, 3 and 5 hours was performed, however in all cases the carbonised PEHA-silica consistently contained 5 wt% carbon.

The ability to increase the coating layer of carbon on PEHA-silica may potentially increase the rate of reduction reaction during PSD. Additionally, it was shown in that the addition of carbon can increase the rate capabilities of the reduced electrode material. This further highlights the benefits of carbon coating.

Previous literature regarding silica as an active material relied on silica carbon composites with carbon contents of up to 76% (Table 5.2).[6] It is believed that the increased conductivity of these electrodes can increase the rate of electrochemical reduction reaction with silica (although robust characterisation of silica reduction process and products is lacking). In some cases, the carbon not only acts as an electronic conductor but the carbon itself has reversible capacity with lithium.[19]

The following results are based on impregnation of BIS with two carbon precursors and the subsequent carbonisation. The two precursors were chosen for their low cost, wide availability and controllable nature of carbon structure formed upon carbonisation. Glucose (Glu) is the first carbon source, it is water soluble, low cost, and upon carbonisation forms amorphous carbon with low amounts of graphitic phases. Mesophase pitch (MPP) is a high molecular weight petrochemical with low cost, it is soluble in tetrahydrofuran (THF) and upon carbonisation forms amorphous carbon with large amounts of graphitic phases compared to glucose.[27][28] Graphitic phases can reversibly intercalate lithium ions and their presence would hypothetically increase the materials reversible capacity.

Briefly, the experiment involved impregnation of calcined BIS with the Glu or MPP precursor in the respective liquid solvent, evaporation of the solvent left the precursor on the surface of the BIS which was subsequently carbonised at 900 ^{o}C in an inert atmosphere. The carbon content of the two BIS-Carbon composited was determined gravimetric analysis, presented in Table 5.5, the carbon content was 9.7 and 9.3 wt%

for the Glu and MPP composited respectively. This carbon content is higher than from the direct carbonisation of PEHA-BIS as reported above.

The Raman spectra presented in Figure 5.15 (a-b) confirm the presence of carbon on the BIS. The Raman results show two peaks labelled D and G. The G peak corresponds to vibrations of sp2 bonded carbon atoms whereas the D peak is due to vibrations of sp3 carbon sites. By comparing the ratios of these peaks one can determine the presence of graphitic (sp2) carbon phases. The D/G ratio has no change between the Glu and MPP precursor used. The propensity of naphthalene species within MPP is reportedly responsible for the formation of larger amounts of graphitic phases upon carbonisation when compared to non-aromatic precursors.[27][28] However, within this experiment, this effect has not been observed. It is likely that the low carbonisation temperatures used in this study (900 °C) led to a low amount of graphitic phases and temperatures above 1400 °C are required.[27][28]

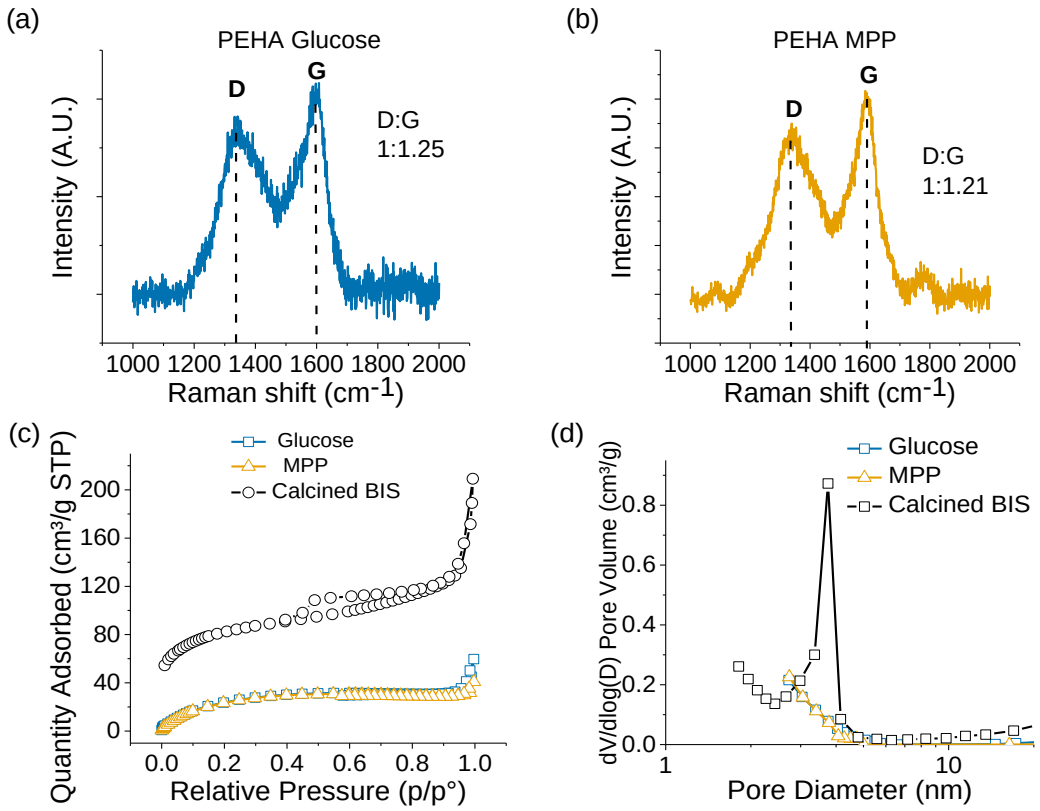

Figure 5.15. Raman spectra of carbon D and G bands (a) Glucose carbonised BIS, (b) MPP carbonised BIS. (c) N_2 absorption isotherm, (d) BJH pore size distributions.

Nitrogen adsorption isotherms collected showed type II nature with some hysteresis at high relative pressures (>0.9). This behaviour is indicative of micropore filling and then large meso/macropores and filling between particles. When analysing the pore properties (Figure 5.5(d)) the disappearance of mesopores centred at 4nm is

observed upon carbonisation along with a decrease in pore volume (Table 5.5). The disappearance of mesopores is attributed to a filling with carbonised material. The impregnation of precursor into the BIS pores was therefore successful.

Table 5.5. BET surface area, BJH pore volume and carbon wt% of glucose and MPP impregnated PEHA silica after carbonisation.

	BET Surface area(m^2/g)	BJH PV (cm^3/g)	Carbon content (wt%)
Calcined BIS	301	0.16	0
Glu Carbonised BIS	107	0.08	9.7
MPP Carbonised BIS	107	0.05	9.3

The kinetics of electrochemical reduction were assessed for these carbon coated materials and are presented in Figure 5.16 by subjecting to stepwise PSD. Both carbon coated materials show much quicker increases in capacity compared with C-BIS (Cross reference with Figure 5.6 and the C-BIS plotted alongside) with MPP-BIS reaching 350 mAh/g and Glu-BIS reaching 475 mAh/g after just 20 hours of PSD at 25 ^{o}C. The MPP-BIS increases to a stable capacity of 650 mAh/g by 120 h of PSD. In contrast the Glu-BIS increases to 575 mAh/g after just 40 hours but then rapidly falls in capacity with subsequent PSD steps. This contrast in behaviour between these two carbon coated silica is surprising, especially as they show similar properties with regards to carbon content, porosity and polymorphicity of carbon. The results of Figure 5.16 are promising as they show the promise of carbon coating for reducing the time required under PSD to reach high capacity. This may have important ramifications for the commercialisation of this technique.

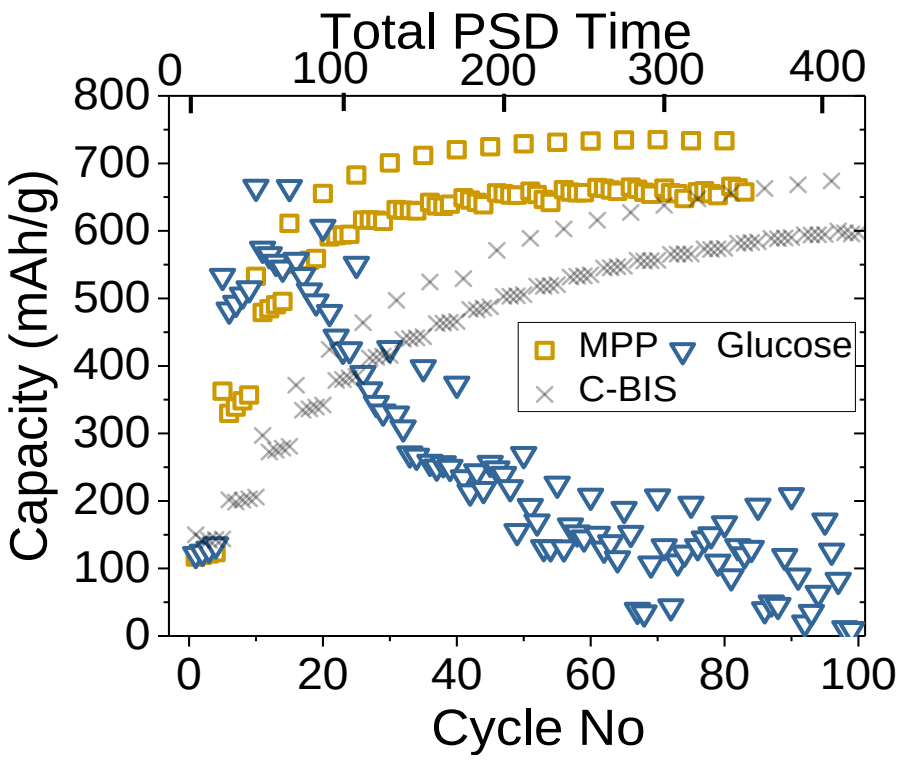

Figure 5.16. Capacity of MPP and glucose impregnated PEHA silica electrodes during 20h stepwise PSD at 25 °C. Can be compared with the Carbonised BIS reported above in Figure 5.6, replotted here.

The impregnation and carbonisation of BIS successfully filled BIS pores with carbonised material. The carbon content of the C-BIS was increased up to 9.7 wt% which is a doubling in carbon content compared with the direct carbonisation of PEHA-BIS. The incorporation of carbon into the BIS reduced the carbonised SSA and pore volume. Raman spectroscopy showed that both precursors gave relatively the same degree of graphitisation. MPP has been reported to form graphitic phases upon carbonisation,[27] however, the temperatures used herein were lower than the 1400 °C used in literature. This low carbonisation temperature is responsible for the lack of graphic phases in the MPP carbonised sample. The electrochemical performance of these carbonised materials is promising. The quick rise in capacity suggests much faster reduction kinetics compared with C-BIS, especially when considering these results are at 25 °C. However, the stability of the MPP-BIS compared with the contrasting instability of the Glu-BIS cannot be explained by these results and will require further investigation.

5.4 Conclusion

A new family of active materials for lithium-ion batteries has been introduce based on using silica. To use silica as an active material it must first be electrochemically reduced to liberate silicon, which can reversibly react with lithium. In this chapter a new stepwise PSD has been proposed to study the extent of electrochemical reduction of silica by lithium in silica-lithium half-cells. We validated this new method by reproducing the results from literature by reducing 200 nm Stöber silica particles to get a capacity of 315 mAh/g.

Porous silica morphologies were next explored based upon the hypothesis of having an increased surface area for faster electrochemical reduction to proceed. The commercial porous silicas used did not show any electrochemical activity to PSD, which is believed to be related to the surface properties of these silica and should be investigated in detail in the future work. A new silica-based anode material based on BIS was shown to have the ability to provide raw silica or carbonised silica surfaces due to the nature of its synthesis. Both the calcined and carbonised BIS showed promise as anode materials after undergoing PSD, where capacities of 635 and 400 mAh/g were achieved for the carbonised and calcined BIS respectively.

Further investigation into the S-PSD process proved that S-PSD has advantages over one C-PSD process. It was shown that higher and more stable capacities were reached when S-PSD was used over one C-PSD. This was related to the galvanostatic cycling involved in the S- PSD which it is hypothesised alters the silicon structure within the active material.

The electrochemical reduction of silica occurs spontaneously and hence it was demonstrated that a short circuit can be used to reduce a silica electrode vs lithium. The electrochemical reduction of silica was found to progress more quickly under short circuiting than PSD at 25 ^{o}C. Due to the lower level of control needed during a short circuit the experiment could be performed at higher temperatures. We have shown that the reduction reaction occurred more quickly at 50 ^{o}C and capacities of 600 mAh/g can be achieved after 4 days. The kinetics of the short circuiting have been presented and an asymptotic profile was observed like that from the PSD treatemnt.

For the electrochemical reduction of silica the benefits of carbon coating are known from literature (Table 5.2) and have been reinforced in this work. Direct carbonisation

of BIS has the advantage of the carbon precursor already being impregnated into the BIS structure. However, attempts to increase the amount of carbon above 5 wt% where not successful. Therefore, an independent carbonisation step was investigated to study the effect of increased carbon content on BIS. Carbon precursors of glucose and mesophase pitch were successfully impregnated into BIS and carbon content was increased to 9.7 wt%. The results during PSD at 25 ^{o}C confirmed the advantage of increasing carbon content as the electrochemical reduction progressed much faster within these samples. The mesophase pitch sample reached a stable capacity of 650 mAh/g but the glucose impregnated BIS had very unstable cyclability and a large capacity loss. These results are promising for reducing the total time needed during PSD. This carbon coating technique could be used in conjunction with the methods evolved in these works such as short circuit at 50 ^{o}C to reduce the electrochemical reduction time further.

Consistently for PSD and short circuiting, it was shown that when the reduction reaction was accompanied by cycling, then higher capacities could be achieved. This phenomenon has been attributed to materials stresses upon expansion and contraction during the active silicon cycling. The differential capacity profiles suggest that with cycling, the silicon structure can evolve, thus allowing more lithiation and higher capacities as cycling progresses.

With the new tools presented in this work, it is now possible to study and optimise the kinetics of electrochemical reduction of silica. Going forward these methods can be used on new silica materials to assess their applicability as anode materials. Table 5.6 should be used to reiterate how these works have studied the extent of the electrochemical reduction process, while previous studies neglect the reactions occurring in the first cycle. The capacities obtained by BIS are promising especially if compared to all literature in this field (Table 5.1-2). With a deeper understanding of the electrochemical reduction process it may be possible to achieve the higher capacities (Table 5.6) reported in literature with BIS and other silica precursors.

Further work is needed to determine the commercialisation aspects of the electrochemical reduction synthesis step which is needed for silica active materials. An initial investigation should be directed at larger scale and reusable cells, unlike coin cells, and the use of more economically and environmentally friendly electrolytes as opposed to the lithium carbonates used in this study.

Table 5.6. A comparison of literature with this work. Reporting the reduction conditions for silica active materials and their resulting capacity as a LIB anode. For a full list of literature see Table 5.1-2.

Material Type	Reduction conditions	Capacity (mAh/g)	Ref
200 nm Stöber silica	250 h of PSD	400	[2]
Mesoporous silica confined within carbon framework	No information just galvanostatic cycling with very low initial columbic efficiency (42%)	1250	[18]
200nm Silica nanotubes	No information just galvanostatic cycling with very low initial columbic efficiency (42%), also unstable capacity which rises to 1250 mAh/g over 100 cycles	1100	[12]
200 nm Stöber silica	400 hours PSD	315	
BIS	400 hours PSD	625	
BIS	5 days (240 hours) short circuit	600	
BIS-MPP	120 hours PSD	650	

5.5 References

[1] Z. Liu, Q. Yu, Y. Zhao, R. He, M. Xu, S. Feng, S. Li, L. Zhou, L. Mai, *Chem Soc Rev* **2019**, *48*, 285.

[2] F. Lepoivre, D. Larcher, J. Tarascon, *J. Electrochem. Soc.* **2016**, *163*, 2791.

[3] M. Pagliaro, *Silica-Based Materials for Advanced Chemical Applications*, RSC Publishing, **2009**.

[4] B. B. Gao, S. Sinha, L. Fleming, O. Zhou, *Adv. Mater.* **2001**, 816.

[5] J. Tu, Y. Yuan, P. Zhan, H. Jiao, X. Wang, H. Zhu, S. Jiao, *J. Phys. Chem. C* **2014**, DOI 10.1021/jp5011023.

[6] B. Guo, J. Shu, Z. Wang, H. Yang, L. Shi, Y. Liu, L. Chen, *Electrochem. commun.* **2008**, *10*, 1876.

[7] D. Huang, S. Li, *J. Mater. Chem. A* **2015**, 22739.

[8] A. Lisowska-oleksiak, A. P. Nowak, B. Wicikowska, *RSC Adv.* **2014**, *4*, 40439.

[9] W.-S. Chang, C.-M. Park, J.-H. Kim, Y.-U. Kim, G. Jeongc, H.-J. Sohn, *Energy Environ. Sci.* **2012**, *5*, 6895.

[10] Y. Han, X. Liu, Z. Lu, *Appl. Sci.* **2018**, DOI 10.3390/app8081245.

[11] I. Kurmanbayeva, A. Mentbayeva, A. Sadykova, A. Adi, Z. Mansurov, Z. Bakenov, *Eurasian Chem. J.* **2019**, *21*, 75.

[12] Z. Favors, W. Wang, H. H. Bay, A. George, M. Ozkan, C. S. Ozkan, *Sci. Rep.* **2014**, 1.

[13] Y. Yao, J. Zhang, L. Xue, T. Huang, A. Yu, *J. Power Sources* **2011**, *196*, 10240.

[14] M. Park, X. Zhang, M. Chung, G. B. Less, A. Marie, *J. Power Sources* **2010**, *195*, 7904.

[15] M. Yoshio, R. Brodd, A. Kozawa, *Lithium-Ion Batteries*, Springer, **2009**.

[16] P. Lv, H. Zhao, J. Wang, X. Liu, T. Zhang, Q. Xia, *J. Power Sources* **2013**, *237*, 291.

[17] L. Wang, J. Xue, B. Gao, P. Gao, C. Mou, J. Li, *RSC Adv.* **2014**, *4*, 64744.

[18] Y. Liang, L. Cai, L. Chen, X. Lin, R. Fu, M. Zhang, D. Wu, *Nanoscale* **2015**, 3971.

[19] X. Cao, X. Chuan, S. Li, D. Huang, G. Cao, *Part. Part. Syst. Characterisation* **2016**, *c*, 110.

[20] C. Wang, K. Liu, W. Chen, J. Zhou, H. Lin, C. Hsu, P. Kuo, *Inorg. Chem. Front.* **2016**, *3*, 1398.

[21] C. Drummond, R. McCann, S. V. Patwardhan, *Chem. Eng. J.* **2014**, *244*, 483.

[22] S. V Patwardhan, *Chem. Commun. (Camb).* **2011**, *47*, 7567.

[23] N. R. Avery, K. J. Black, *J. Power Sources* **1997**, *68*, 191.

[24] M. N. Obrovac, L. J. Krause, *J. Electrochem. Soc.* **2007**, *154*, A103.

[25] C. C. Nguyen, B. L. Lucht, *J. Electrochem. Soc.* **2014**, *161*, 1933.

[26] S. Trask, P. Jennings, A. Mcgordon, C. Lyness, I. Bloom, **2016**, *335*, 189.

[27] G. Yuan, B. Li, X. Li, Z. Dong, W. Hu, A. Westwood, *ACS Omega* **2019**, *4*, 1095.

[28] W. Zhu, X. Meng, Y. Zhan, H. Li, J. Ma, J. Liu, C. Zhai, W. Zhang, X. Fang, T. Ding, *AIP Adv.* **2018**, *055332*, DOI 10.1063/1.5025148.

Chapter 6: Mechanistic Understanding of the Electrochemical Reduction of Silica

6.1. Introduction

In the previous chapter, the electrochemical reduction of silica via lithium in a half-cell configuration was presented. The application of PS discharging regimes and short circuiting of the half cells showed how for periods ranging from 20-400 hours' silica could be incrementally reduced and the reversible capacity of the silica electrode increased. The experiments of short circuiting the cells at 50^{o}C showed promise of achieving high reversible capacity in the shortest possible time, 500 mAh/g in 48 hours. The motivation behind reducing the total electrochemical reduction time is that this process represents an additional processing step for the use of silica as an anode material. In the current chapter, the electrochemical reduction step is studied in further detail. By building a better understanding of this electrochemical process future experiments to scale up this synthesis method can be directed more successfully.

The first cycle columbic efficiency (CE) is critical to the development of any new battery material.[1] Within a full cell configuration, a limited inventory of lithium is available as the sum of lithium in the electrolyte and cathode active material. Any irreversible reactions during the first cycle deplete lithium inventory, in the long term this leads to capacity loss in the cell. The extremely low first cycle CE of silica active materials are inherent to the reduction reaction. For the reduction of silica to silicon, lithium-ions must be consumed. Therefore, for incorporation into full-cell configuration prelithiation of silica electrodes will be required. This prelithiation step should be designed to increase electrode capacity and ensure stable cycle life according to the results presented in Chapter 5.

Figure 6.1(a), schematically shows the prelithiation of a SiO_x material performed via short circuit in a coin cell half-cell. Kim et al[2] envisage a scalable roll-to-roll process which can be applied to such electrodes, Figure 6.1(b). Prelithiation is an important facet of being able to utilise silica active material. The roll-to-roll process envisaged in Figure 6.1 will require a key understanding of the electrochemical reduction mechanism that unfolds. This will ensure that such a process will be optimised to produce high and stable capacity electrodes in the most economic and time effective way possible.

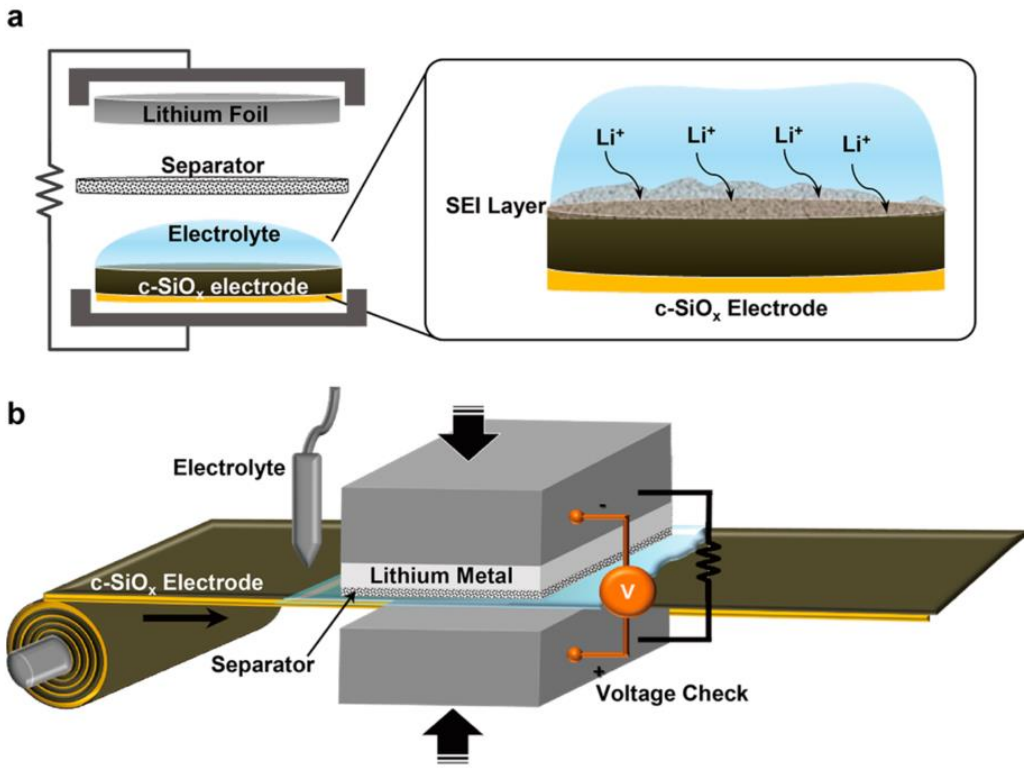

Figure 6.1. (a) graphical illustration of prelithiation process of c-SiO_x electrode and (b) a scalable roll-to-roll process scheme. Reproduced from [2].

Previous work on the electrochemical reduction of Silica may or may not report the first cycle CE. [3] [4][5][6] As discussed in Chapter 5 this value can provide little useful information about the electrochemical reduction process. Primarily this is due to there being to many unknown effects on CE including SEI formation and lithium-plating primarily in the first but also in subsequent cycles. This is additionally compounded as there is no consensus on the nature of the reduction reaction products. A detailed understanding of the electrochemical processes occurring during the initial electrochemical reduction process is crucial to further develop this technology. In this

chapter the electrochemical reduction of silica will be probed in-situ and a mechanism for the electrochemical reduction of silica will be proposed.

6.2. Experimental

Cell Preparation

Electrochemical experiments were performed using MIT2016-type coin cells with a Whatman glass fibre separator and lithium foil (from Sigma Aldrich) as the counter electrode. The electrolyte was 1M $LiPF_6$ in a 1:1 solution of ethylene carbonate (EC) and dimethyl carbonate (DMC) from Sigma Aldrich with added 5w% fluoroethylene carbonste (FEC). The composition of working electrodes was: 60w% PEHA-BIS active material, 20w% conductive additive C-65, 20w% binder carboxymethyl cellulose. The electrochemical performances were tested on a Maccor 4000M Battery and Cell test system in a 25^{o}C temperature chamber. The cut off voltage was 0.01 V versus Li/Li^{+} for discharge (lithium insertion) and 1 V versus Li/Li^{+} for charging (Li extraction). Cells where charged under a constant-current constant-voltage (CCCV) regime: galvanostically at 0.1C, unless specifically stated otherwise, and held at 0.01V until current fell below 0.05C upon discharge. The specific capacity was calculated based on active material mass. The charging rate was calculated from the fraction of active material in the electrode and based on the theoretical capacity of 680 mAh/g.

Potentiostatic discharge (PSD)

The PSD was performed on a MACCOR 4000M Battery and Cell test system. Cells were discharged galvanostatically at 0.1C to 0.01V. The cell was then subjected to 0.002 V potentiostatic discharge for 20 hours. Following this, 5 CCCV cycles were performed according to the above criteria. This procedure was looped in accordance to the desired experiment, typically 20 loops, therefore 400 hours total time at 0.002 V and 100 cycles.

Short Circuit Reduction

Short circuit reduction involved the application of a crocodile clip (RS-components) across the positive and negative electrodes of the 2016 coin cell providing a path for current flow. The short circuit was applied to freshly made cells, unless stated otherwise. The short-circuited cells were stored in a sealed glass vial and placed

within a temperature-controlled oven. The duration of short circuiting and temperature of the oven were varied as specified.

Impedance Fitting

In this chapter charge transfer processes will be studied by EIS. For an introduction to impedance and impedance spectroscopy see Chapter 2.[7] [8] Charge Transfer processes give semi-circular patterns in Nyquist plots. In a charge transfer two parallel processes are occurring, firstly the transfer of charge across a medium, secondly the build-up of the double layer capacitance. A charge transfer process can therefore be represented by a parallel electrical circuit of a resistor and capacitor. In parallel the reciprocals of impedances are additive and for these components can be simplified as equation 6.1 (See Chapter 2 for full derivation).

$$Z = \frac{R}{1+j\omega \mathrm{RC}} \qquad \text{Equation 6.1}$$

Equation (6.1) can be used to visualise the semi-circular pattern of a charge transfer: at high frequency ω tends to infinity i.e. the denominator tends to infinity and impedance to zero (circuit behaves like a capacitor). At low frequency ω tends to 0 the denominator tends to 1 so Z=R (circuit behaves like a resistor).

Electrochemical processes often do not behave as idea circuit components. Constant phase elements (CPE) are commonly used to describe capacitance as it appears in real electrochemical systems where non uniform surfaces and distribution of reaction sites effects behaviour. One physical explanation for CPE behaviour is electrode roughness caused by fractal surfaces and porosity.[8] [9] The mathematic definition is presented in equation (6.2), where p is the constant phase $(-90 \times p)^{o}$ and p is a number between 0-1, the case for p=0 is an ideal resistor and p=1 describes an ideal capacitor. The value of p can therefore be used to determine the capacitive nature of a charge transfer process.

$$Z_{CPE} = \frac{1}{Q_0(j\omega)^p} \qquad \text{Equation 6.2}$$

6.3. Results and Discussion

6.3.1 Kinetics of BIS Electrochemical Reduction

The electrochemical reduction of Silica within a lithium half-cell is a REDOX reaction: Silica is reduced to form silicon and unknown species. While lithium is oxidised to form hypothesised lithium oxides and silicate species. For lithium to be oxidised (lose an electron) said electron must pass through an external circuit to balance the charge of a redox reaction at the silica (working) electrode. This electron must pass through an external circuit due to the electronic isolation of the two electrodes by the insulating separator. Lithium ions then migrate through the separator to balance the charge of the reduction at the silica electrode. One can record the transfer of electrons from the lithium to the silica electrode by monitoring the current through the external circuit (As current is the rate of charge transfer, Equation 6.3). As the flow of electrons, the current, is caused by the reduction of silica via lithium-ions it can be used as a measure for the rate at which the reduction reaction is occurring. In other words, for one mole of lithium-ions to undergo a REDOX reaction at the silica electrode exactly one mole of electrons must pass through the external circuit. Since one mole of electrons carries a known charge and current (I) measures the flow of charge (Q) with respect to time (t) then according to Equation 6.3 the current rate is directly related to the rate of the electrochemical redox REDOX reaction.

$$I = \frac{\Delta Q}{\Delta t} \qquad \text{Equation 6.3}$$

During the PSD reduction of Silica, a constant discharge potential of 2 mV is applied to the cell in 20 h steps. In the previous chapter it was shown that performing the PSD step at 50 ^{o}C decreases the overall time needed to reach a high reversible capacity. This result is reiterated in Figure 6.2 (a), which shows the increase in capacity with just one 20 h PSD step at 50 ^{o}C compared with 25 ^{o}C. This is related to the increase in reduction reaction kinetics at higher temperature. Figure 6.2(b) presents the current profile of both cells during the first PSD step. The negative current corresponds to electrons flowing from the lithium to the silica electrode. The current response is small for the electrode at 25 ^{o}C, representing lower electron transfer to the silica electrode

and is better seen in Figure 6.2(c). Figure 6.2(c) presents the current profile for 20 PSD steps each 20 hours each. As expected the current profile for the electrode reduced at 50 ^{o}C gives a maximum in current more than an order of magnitude higher than that reduced at 25 ^{o}C, 170 µA compared with 5 µA.

The current response is small during the first 20 h PSD for the electrode at 25 ^{o}C, representing slower electron transfer to the silica electrode. As explained above the current corresponds to the rate of electrochemical reduction of the silica. Low current flow for the 25 ^{o}C electrode was why little increase in capacity during the first PSD step was observed. The current profile can be extracted from each of the 20 hour PSD step, and is presented in Figure 6.2(c). Over repeated exposure to stepwise PSD current does begin to flow into the silica electrode as shown in Figure 6.2(c). This data is extracted from the results shown in Chapter 5 (Figure 5.6). The current profile of the 50 ^{o}C electrode shows a transfer of charge during the first 20 h PSD step and as such the capacity is increased from 95-500 mAh/g.

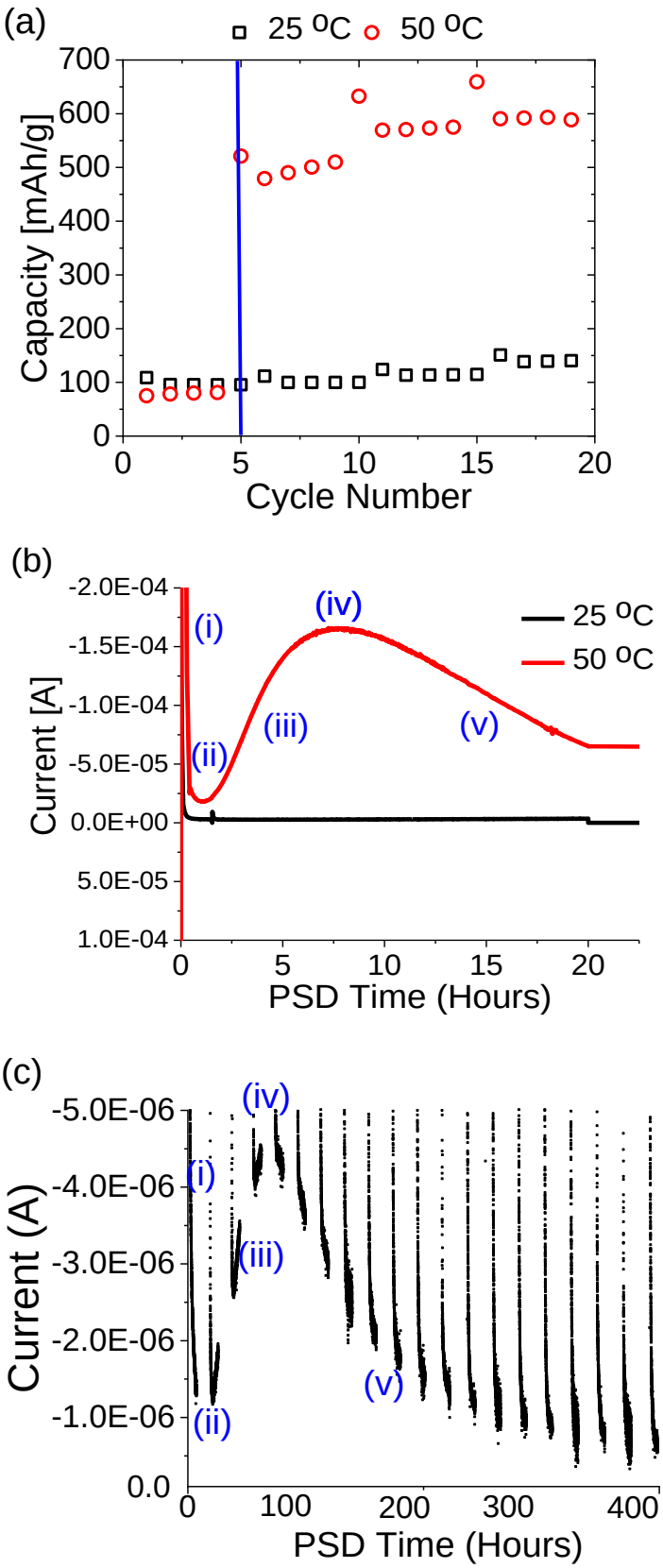

Figure 6.2. (a) Capacity vs cycle life for BIS electrodes reduced with 20-hour PSD steps (red) at 50 °C (black) at 25 °C. (b) Current responses during the first PSD step. (c) Current response of each PSD step of the 25 °C reduced electrode over 400 hours (20 PSD steps).

Although the magnitude of the current transferred between electrodes reduced at 25 ^{o}C is lower than at 50 ^{o}C when comparing the shape of the current profiles a clear pattern emerged. As the current is directly proportional to the rate of electrochemical reduction the current profile can provide insight into the mechanism behind the reaction occurring.

In Figure 6.2(b) the features of the current profile have been broken up and labelled (i-v):

(i) A spike in current as the charging regime is switched from a galvanostatic discharge at 0.1C down to 50mV to the PSD step at 2mV, during this switch the current spikes and then relaxes. (0.5h at 50 ^{o}C)

(ii) A minimum in current. A period where little current flows between the two electrodes. (0.5h to 1.5 h at 50 ^{o}C)

(iii) A period with a relatively constant increase in current up to a maximum at point (iv). (1.5 h to 7.5 h at 50 ^{o}C)

(iv) A maximum in current which corresponds to the highest rate of reduction. (7.5 h at 50 ^{o}C)

(v) A period of gradual decrease in current at a relatively constant rate. (7.5 h to 20 h at 50 ^{o}C)

Although different in magnitude the features (i-v) can be assigned to Figure 6.2(c). This is a strong indicator that the same chemical processes are occurring at both temperatures, but with faster reaction kinetics at 50 ^{o}C. A point of note is a small dissimilarity between the two current profiles during region (v). The sample reduced at 25 ^{o}C shows more asymptotic profile as the current falls. This suggests that 400 hours of PSD at 25 ^{o}C gives a more completely reduced silica. Whereas after 20 hours at 50 ^{o}C the profile did not asymptote completely suggesting the silica is not completely reduced, this is supported by Figure 6.2(a) where the increase in capacity in the following PSD steps at 50 ^{o}C leads to incremental increases in capacity.

6.3.2 Working Hypothesis for BIS reduction mechanism

With the current profiles identified above (Figure 6.2) a hypothesis was proposed to explain the features (i-v). (i) is simply due to the change in charging conditions from constant current, which ends at 50mV, to constant voltage at 2 mV. Our initial hypothesis for the electrochemical reduction is presented in Figure 6.3:

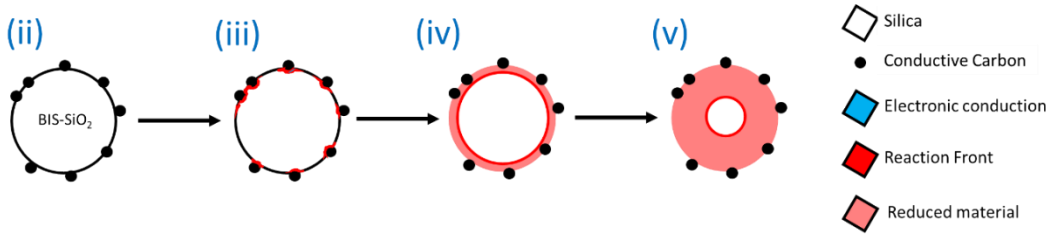

Figure 6.3. Proposed mechanism for electrochemical reduction of BIS at a particle level. Stages (ii-v) explained below.

- Stage (ii). The minimum in current indicating little to no reduction is occurring in this period. For the electrochemical reduction to occur sufficient electrical conduction pathways must be accessible at the reduction sites to balance the charge transfer of this REDOX reaction. Due to the insulating nature of silica we hypothesize that the initial reduction only occurs where the carbon conducting network is in contact with the silica material.
- Stage (iii). The period of rising current indicating an increasing rate of electrochemical reduction. We postulate that as the reaction progresses the formation of lithiated products (hypothetically, silicon, lithium silicates and lithium oxides) have increased electronic conductivity relative to pure silica.[10][11][12] Therefore as more material is gradually reduced better electronic conduction pathways to the virgin silica are formed. This increases the rate of the electrochemical reduction.
- Stage (iv). The maximum in current rate and therefore maximum rate of reduction. Here we postulate that as the surface silica is reduced the electronic conduction pathways no longer become the limiting factor for the rate of reaction. As a shell of reduced material is formed the length for lithium diffusion to reach virgin silica beneath increases. Unlike the electronic conduction process the diffusion of lithium-ions to the reaction front is a mass transfer process. At point (iv) we postulate that the reaction has electronic conduction pathways to a large amount of virgin silica sites and has penetrated the surface of the particles. However, at point (iv) further reduction

leads to increased lithium diffusion lengths and as a result this becomes the limiting factor for electrochemical reduction.

- Stage (v). The region of gradual decrease in current. As stated above we postulate that after stage (iv) the diffusion of lithium-ions to the reaction front at virgin silica becomes the limiting factor for electrochemical reduction. Therefore, as the reaction front propagates further into the particle (lithium diffusion lengths increase) and the rate of reduction decreases. In this manner it is envisaged as a variation of a shrinking core mechanism.

With the working hypothesis laid out above a number of further experiments were performed to investigate this proposed mechanism.

6.3.3 Impedance Spectroscopy of Reduced Silica Electrodes

By performing electrochemical impedance spectroscopy (EIS), the electrochemical processes occurring within this system could be studied non-invasively. Information with regards to the electrode resistance and any inductive effects related to charge transfer processes can be studied.

Figure 6.4(a) lays out the design of the impedance study at points (w-z),

EIS measurements were taken of the composite electrode in the lithiated and delithiated state.

- Point (w) (Figure 6.4 (b)) was prior to PSD treatment, at this stage a stable SEI layer has been formed. Therefore, the EIS spectra provide information about the silica electrode with an SEI layer.
- Point (x) (Figure 6.5(a)) EIS measurements were taken at 1 hour intervals during the 20 hour PSD at 50 ^{o}C. These measurements will provide information for each stage of electrochemical reduction reaction. These results are discussed further below.
- Point (y) (Figure 6.4 (c)) After one complete cycle of delithiation/lithiation EIS measurements where again taken in the lithiated and delithiated state. These spectra provide information about the reduced electrode.
- Point (z) (Figure 6.4 (d)) Having now reached a higher capacity the electrode was subject to 10 complete charge discharge cycles, and a final EIS measurement of lithiated and delithiated state was performed. These spectra will provide information on how the impedance of the electrode evolves after cycling.

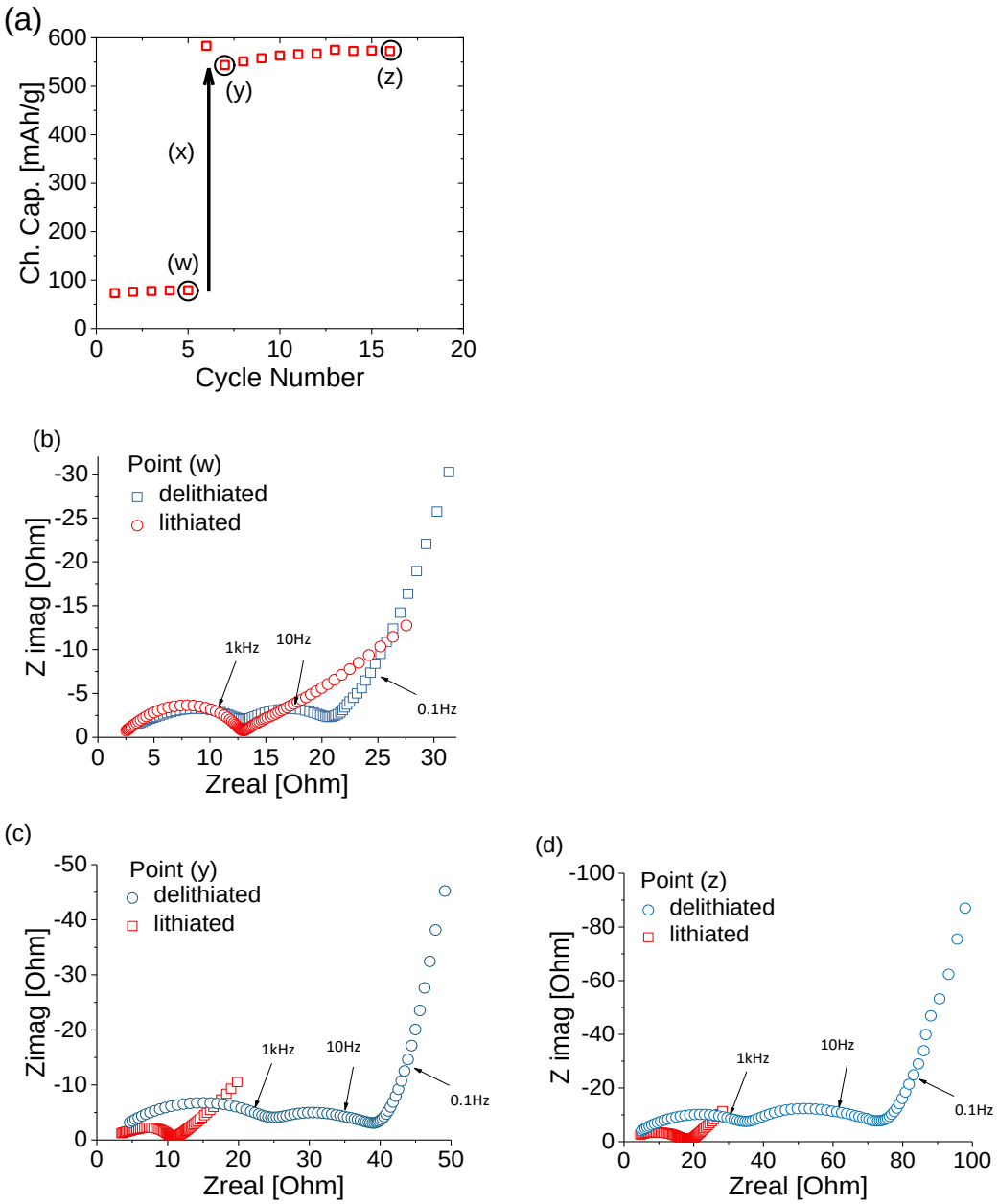

Figure 6.4. Frequencies marked on delithiated spectra. (a) Capacity vs cycle life of a PSD reduced electrode at 50 °C, points (w-z) mark were electrochemical impedance measurements were performed. (b) EIS response measured at (w). (c)) EIS response measured at (y).) EIS response measured at (z).

Figure 6.4 (b) presents the lithiated and delithiated Nyquist plots for the electrode before the PSD treatment. The delithiated spectra are similar in features to results in Chapter 5 as expected, however the EIS measurements here were performed at 50 °C. In insulating materials such as this silica electrode a negative temperature coefficient is observed with regards to resistivity, hence the overall resistances are lower at 50 °C than the previously presented results in Chapter 5, which were performed at 25 °C.

Between the lithiated and delithiated states in the electrode, the high frequency region (>1 Hz) has a similar semi-circular feature. However, at medium frequencies (1-10 Hz) an additional semi-circular feature appears in the delithiated spectrum which leads to an overall increased resistance within the delithiated electrodes. The angle of the low frequency slope is also increased in the delithiated electrode.

After the PSD for 20 hours (Figure 6.4(c)) the lithiated electrode spectra matches well with the lithiated state before PSD (Figure 6.4(b)). In the delithiated state, although the impedance spectra has the same features as before PSD, the overall resistance has increased relative to the lithiated state. In comparison, the delithiated state has increased in overall resistance after the PSD by 17 Ohms (from 21 to 38 Ohm respectively).

Figure 6.4(d) reflects the comparisons of (b and c) between the lithiated and delithiated states. However, after PSD and further 10 cycles the resistivity of both lithiated and delithiated electrode have increased, an increase of 8 Ohm in the lithiated state and 35 Ohm in the delithiated. (As a percentage this in an increase of 72% in the lithiated state resistance, and a 90% increase in the delithiated state).

The total overall resistance of the lithiated state of the electrode has consistently lower resistance and capacitance than the delithiated state as can be seen in Figure 6.4(b-d). This is true even before the PSD, Figure 6.4 (b) and therefore not completely related to the reduction products. The lithiated electrode therefore has increased electronic and lithium-ion conductivity as would be expected for lithiated silicon alloys and lithium containing species (postulated reduction products).[10][11] This finding, that the lithiated electrode materials have lower resistance, fits well with the proposed mechanism where we state that as more silica is reduced more electronic conduction pathways are established to the virgin silica.

A further hypothesis is drawn from the findings presented in Figure 6.4. After the PSD, the differences between the lithiated state and delithiated state becomes larger. Here this difference is attributed to a decrease of contacts within the material and build-up of new interphases. As after lithiation, silicon will expand +280% in volume, it was hypothesised that in the expanded (lithiated) state, there is a good contact between electrode components partly due to mechanical stresses experienced. Once the silicon species become delithiated and shrink, the electrode components experience relaxation of mechanical stresses, breaking some electrical contacts between the silicon and the host structure hence the internal resistance of the

electrode increases. This hypothesis is supported by Figure 6.4(d) which shows that after 10 cycles, a larger gap in resistance between lithiated and delithiated state has developed, as the material is subject to more cycles, more contacts are broken between the silicon species and host structure. In addition, the increase in overall resistance in the lithiated state (red) between Figure 6.4 (c) and (d) is also attributed to a build-up of new interphases within the electrode related to this volume expansion and contraction. This hypothesis is supported by the results in Chapter 5 where the stabilising of silicon capacity and definition of the differential capacity profiles eludes to an evolving silicon structure upon cycling (Figure 5.10).

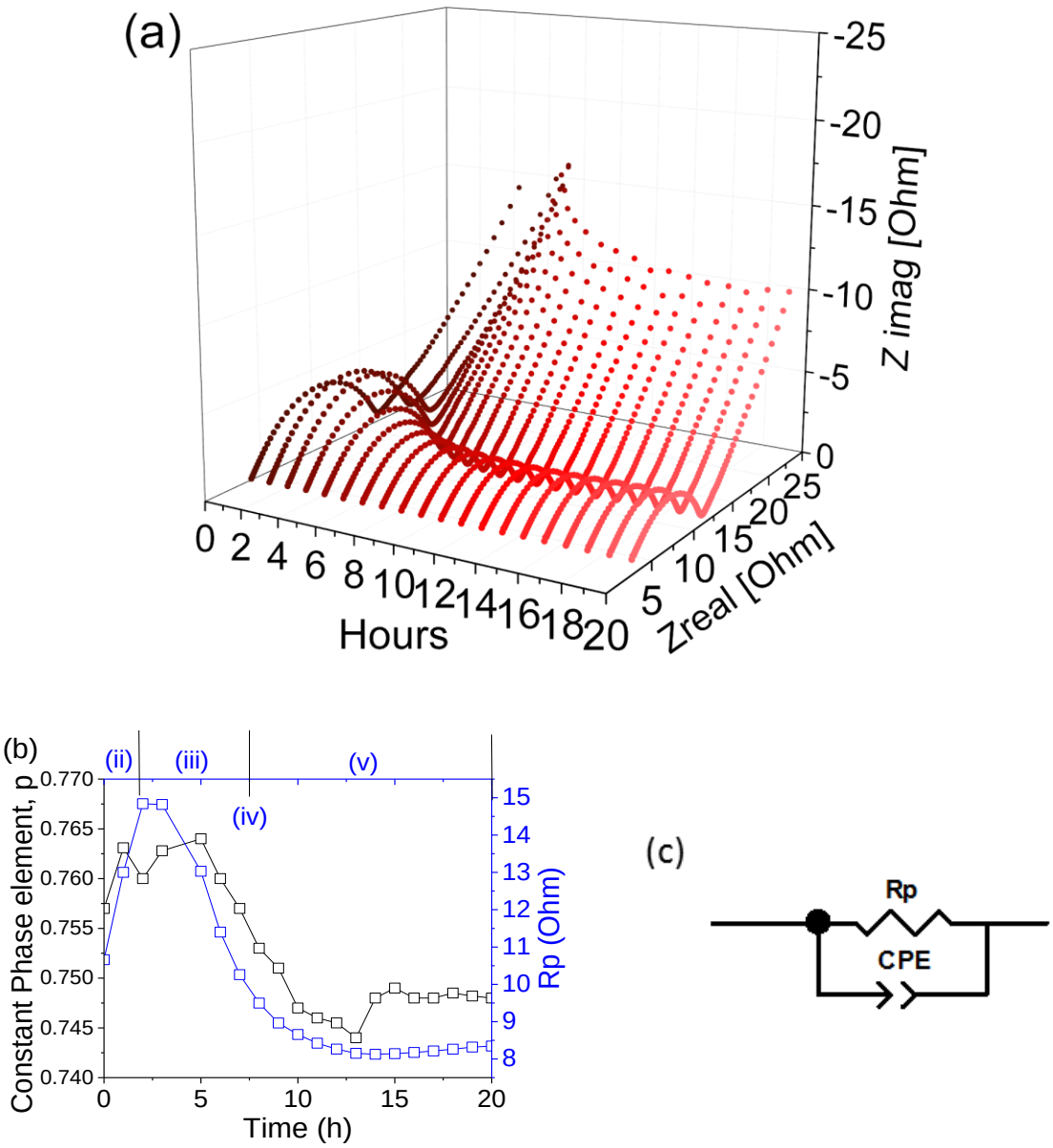

Figure 6.5. (a) three dimensional Nyquist plot of the time resolved impedance response throughout a 20 hour PSD treatment at 50 °C, (b) the resistance and CPE-P values for

the equivalent circuit (c) fitted to the high frequency semi-circular impedance response.

Figure 6.5 presents the impedance frequency response of the lithiated electrode during the 20 hour PSD treatment. These measurements were taken during stage (x) as described above and shown in Figure 6.4 (a). The features of this response were similar to the lithiated states seen throughout Figure 6.4(b-d), a single depressed semi-circle (Cole-Element) followed by a sloping impedance to lower frequencies. The cole-element can be fitted with the equivalent circuit Figure 6.5(c), a parallel resistor and constant phase element (CPE). The electrode does not behave as an ideal capacitator (as expected), therefore a CPE is used to describe the capacitive nature of this element and account for real world behaviour and the roughness of the active materials used. Fitting the time resolved impedance spectra allows for the extraction of the resistance of this element and the CPE-P factor, where p=0 is an ideal resistor and p=1 describes an ideal capacitor (As introduced above, Equation 6.2). Figure 6.5 (b) shows a profile for the CPE-P factor and the resistance of the electrode over 20 hours of PSD. A rise in the resistance and the CPE-P factor for the first 3 hours is observed. The resistance begins to decrease after 4 hours and after 6 hours for the CPE-P. Both factors decrease in magnitude and level out by 13 hours.

As described above no research exists on the processes occurring during the electrochemical reduction of silica with lithium. To the best of our knowledge this is the first EIS study to measure the progress of this electrochemical reduction reaction. The capacitive nature revealed by the EIS measurements suggests a build-up of charge on the electrode. The variance of the capacitive nature (the CPE-P factor) was used to understand the mechanism of electrochemical reduction. Likewise, the variation in total real resistance as the electrochemical reduction reaction progresses can be used to refine our previously proposed mechanism.

It is possible to correlate the capacitive and resistive nature of the electrode during the PSD (shown in Figure 6.5(b)) with the current profile features (i-v) shown in Figure 6.2(b) for this reason the time of stages (ii-v) are indicated on the top of Figure 6.5 (b):

ii. Stage (ii) is a minimum in current which begins to rise 1.5 hours into the PSD. The start of this stage corresponds with the timing of the plateau of CPE-P and resistance. During Stage (ii) the increase of capacitance (CPE-P Factor) aligns with the slowest rate of reduction. During this period charge build up at the surface of the electrode is hindering the electrochemical reduction

reaction. As we propose above during this stage reaction can only occur at sites with sufficient electron conduction pathways. The charge buildup maybe caused by lithium build up at the surface of the electrode which cannot react due to insufficient electron condition.

iii. Stage (iii) is a period with a relatively constant increase in current up to a maximum. The beginning of this rise in current corresponds with the decrease in electrode resistance (blue) starting at 4 hours. During stage (iii) we hypothesize that as silica is reduced the reduced species create new electron conduction pathways to adjacent virgin silica. Therefore, as the reaction progresses a positive feedback loop is present where the rate of the reduction reaction continues to increase. The rapid decrease in the electrode resistance during stage (iii) directly supports this proposed hypothesis.

iv. Stage (iv) is the maximum in current reached at 7.5 hours. This correlates with the decrease in the CPE-P factor, this suggests that after this maximum less charge build up occurs on the electrode surface. We postulate that the maximum in reduction rate stage (iv) occurs when the largest area of reduced material and virgin silica are in electrical contact. This maximum begins to decrease during stage (v) as the reaction front moves away from the surface of the silica particles. During which the diffusion lengths for lithium-ions to diffuse through the reduced material increase. The length required for lithium diffusion becomes the limiting factor which slowly reduces the rate of reduction. Within Figure 6.5(b) the CPE-P factor begins to fall in correspondence to stage (iv), this reduction in charge build up may indicate that the reaction front is moving away from the surface of the silica particles and into the bulk. We have established that Lithium-ion conductivity is higher within the lithiated materials than delithiated. This reduces the buildup of charge on the silica particles in line with the findings presented in Figure 6.5(b) where during stage(v) the CPE-P and the resistance decrease and begin to plateau.

The correspondence of the above features with the stages identified in the current profile can be used to strengthen our proposed hypothesis of the electrochemical reduction reaction pathway.

6.3.3 Constant Load Discharge Voltage analysis

A mechanism for the electrochemical reduction of silica was proposed above and has 5 key stages labelled (i-v). This mechanism was postulated based upon the current profile during the electrochemical reduction, this was possible because the current during the PSD is proportional to the rate of the electrochemical reduction reaction. To further investigate the mechanism during PSD an EIS study was undertaken and presented above. Based on the charge polarisation and the resistance of the silica electrode during the PSD step correlations could be drawn which support the proposed hypothesis.

From fitting the Cole-element present in the Nyquist plot the capacitive nature of the electrode during the PSD was determined Figure 6.5(b). It was shown that during stage (ii) a charge build up at the surface of the electrode occurred, this charge build-up was determined to be the cause of little electrochemical reduction occurring during stage (ii). In our hypothesized mechanism during stage (ii) electrochemical reduction reaction can only occur at sites with sufficient electron conduction pathways. This means the surface of the silica particles which have sufficient contact with the conductive carbon network. The CPE-P factor plotted in Figure 6.5(b) indicated a charge build up at this stage of the reaction. Above it has been suggested that this charge build-up may be lithium build up at the surface of the electrode sites where insufficient electronic conduction is available. In this section the voltage of silica-lithium half cells are analysed to further elude to the nature of the electrochemical reduction mechanism during stage (ii) and throughout the stages of reduction.

Chapter 5 introduced the short circuiting of silica electrode half cells to allow electrochemical reduction of silica via lithium. Short circuiting at 50 ^{o}C for 48 hours produced capacities of >500mAh/g. The use of a constant load discharge (CLD), analogous to a short circuit, was performed on a cell whilst simultaneously monitoring cell voltage and current. A CLD was chosen to be performed at 0.8 Ω, which is the equivalent resistance of a crocodile clip, to be comparable with the ‘short circuiting’ experiments described above. Figure 6.6(a) presents the capacity results showing that after 24 h CLD at 50 ^{o}C a high and stable capacity of 550 mAh/g can be reached. This is quicker than reported from 24 h of short circuiting which provided a capacity of 450 mAh/g indicating the CLD experiment was not completely analogous to the crocodile clip short circuiting.

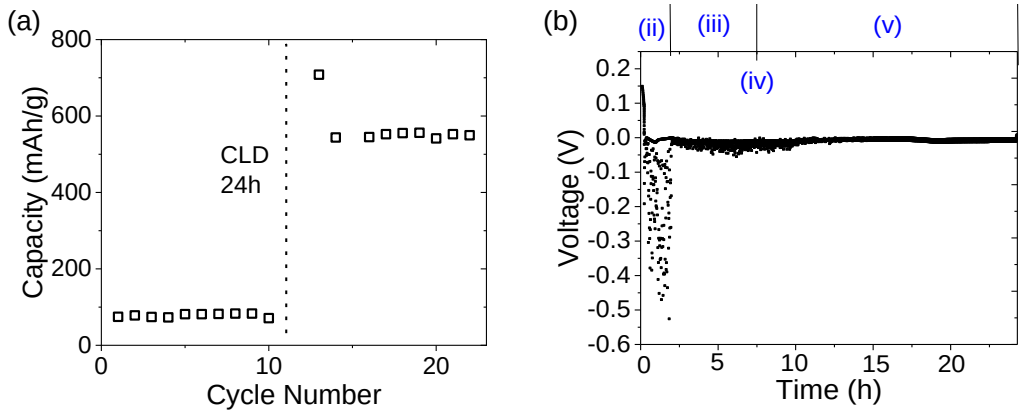

Figure 6.6.(a) capacity profile of a BIS electrode before and after 24 hours of a Constant Load Discharge((CLD) of 0.8 Ω at 50 °C. (b) voltage signal during the 24-hour CLD step.

Unlike PSD, cell voltage fluctuates and can be monitored during the constant load step (Figure 6.6(b)). The reduction of silica via lithium is spontaneous during the short circuit (constant load), however, fluctuation in the voltage during the constant load step will indicate the propensity of the reaction to occur and is an important tool in understanding the electrochemical reduction mechanism of silica.

A voltage prolife during the CLD, is of significance for the understanding of electrochemical reduction. According to the standard redox potentials of lithium and silica the reduction reaction is spontaneous, i.e. a galvanic cell (as established in Chapter 5, Equation 5.5). The relationship of cell potential and spontaneity, or Gibbs free energy, is described by the variation of the Nernst equation in Equation 6.4, where z=number of electrons transferred, F=the faraday constant (C /mol), E_{cell}=cell potential difference (V). According to Equation 6.4 for Gibbs free energy to be negative and hence a reaction to be spontaneous, the cell potential needs to be positive.[13]

$$\Delta G = -zFE_{cell} \qquad \text{Equation 6.4}$$

Therefore, in the lithium-silica half-cell, if the voltage becomes negative then this indicates lithium will no longer be transferred to the silica electrode. The lower this value becomes the more positive the Gibbs free energy of lithium transfer becomes. If the half-cell voltage is >0 V, then lithium transfer will spontaneously occur when connected via an external circuit. If the voltage across this Lithium half-cell becomes negative, then this indicates lithium will no longer be transferred to the working electrode spontaneously.

During stage (ii) of the current profile, when the current flow is at a minimum between 1-2 hours, the voltage across the half-cell fluctuates between 0 and -0.6 V throughout. As established above, during stage (ii) little to no current flows across the cell, hence no reduction of silica is occurring. However, as Figure 6.6(b) shows the potential at the electrode is changing during this time. It is possible that during this stage lithium is deposited on the surface of the silica electrode. For this lithium to reduce silica, a conduction pathway for electrons must be present. During stage (ii), lithium is deposited at the surface of the silica electrode and cannot react due to ineffective electron conduction pathways. This build-up of lithium and positive charge leads to the negative voltages in Figure 6.6(b), a build-up of charge during this period also corresponds with the increased capacitance detected during stage (ii) as measured by EIS Figure 6.5(b). As the reduction reaction progresses, initially from sites with established electronic conduction pathways, the reduced product becomes more electronically conducting, providing a positive feedback effect where the reduction reaction begins to occur at a faster rate (stage (iii)).

As the current begins to rise, stage (iii), and throughout stages (iv) and (v) the voltage fluctuates between 0 and -0.05V. After 13 hours of CLD, the voltage shows little fluctuation. The fluctuation in cell voltage observed during stages (iii), (iv) and (v) perhaps indicates that some lithium build-up on the surface still occurs in these stages but to a lower extent (as the voltage doesn't drop below -0.05V). This may suggest that the whole surface of the silica particles is still not reduced in these stages. Perhaps as electronic conduction pathways reach these sites the voltages subsequently drop as a small amount of lithium build up occurs. This may be related to the porous nature of the silica particles, pores within the particle have no way of contacting the conductive carbon network, they may however be wetted by lithium containing electrolyte. These voltage signals could be as a result of the reduction reaction front penetrating deeper into the particles and as such establishing electronic conduction pathways to these pore sites which are in contact with electrolyte. This result is more speculative than the strong negative voltage signals measured during stage (ii). However, both conclusions would support our proposed hypothesis with regards to; The reduced material providing conduction pathways to virgin silica sites, and the proposed shrinking core like mechanism of reduction within the particles.

Constant load discharge further supported our hypothesised mechanism. In addition, the voltage profile in Figure 6.6(b) indicates the majority of electrochemical reduction occurs by 13 hours. With regards to this a CLD was performed on a fresh cell to

determine capacity increase with just 13 of CLD at 50 °C (Figure 6.7(a)). A capacity of 500 mAh/g was achieved, and stable capacity of 600 mAh/g was reached after 20 cycles. The columbic efficiency is presented in Figure 6.7(b) it showed a rising CE to 95% before the CLD with CE rising to 98.6% after CLD and 30 cycles. The initial low CE is due to the formation of SEI during the first 1-4 cycles, after this the CE remains relatively low due to minor irreversible silica reduction reactions when the cell potential is low during cycling. The high and stable CE after CLD and 30 cycles indicates all irreversible reactions have completed and the cell has attained a stable cycling regime.

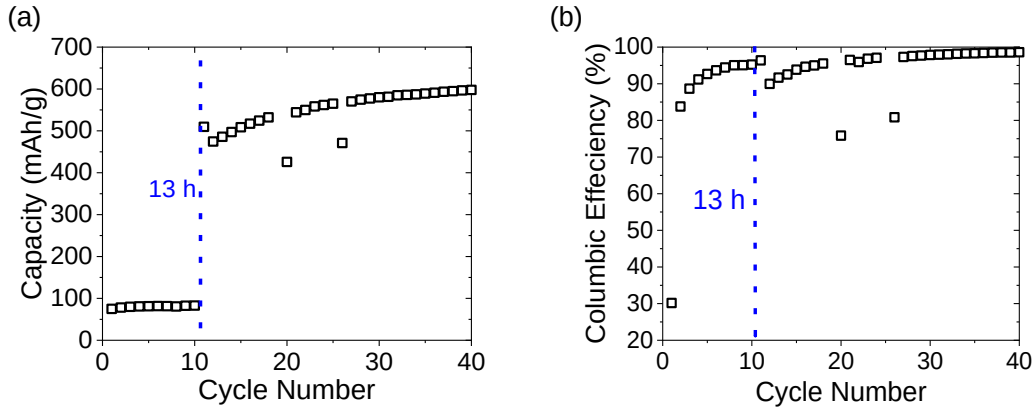

Figure 6.7. (a) Capacity profile of BIS before and after 13 hours CLD of 0.8 Ω at 50 °C. (b) Columbic efficiency of each cycle

The CLD is a novel progression of the short-circuiting reduction of silica presented in Chapter 5. In the previous chapter we highlighted that optimisation of the electrochemical reduction step will be critical for commercialisation of these materials. Throughout Chapter 5 we reduced the electrochemical reduction time to 24 hours and produced capacities of 430 mAh/g for BIS electrodes. We then compared this to the literature where 250 hours was required to reduce Stöber silica particles.[3] The use of CLD has further optimised this process where capacities of 500 mAh/g can be produced after just 13 hours of treatment.

6.3.4 Mechanism of Electrochemical reduction

In Section 6.3.2 above we proposed a working hypothesis for the electrochemical reduction mechanism underpinning BIS reduction. The current profile shown in Figure 6.2(b) has been split into distinct stages (i-v). Where stage (i) is a drop in current which is related to the change in cycling conditions from constant current to constant voltage. Figure 6.8 is presented to represent the electrochemical reduction at the level of a single BIS particle. The stages (i-v) are represented individually and are expanded on below.

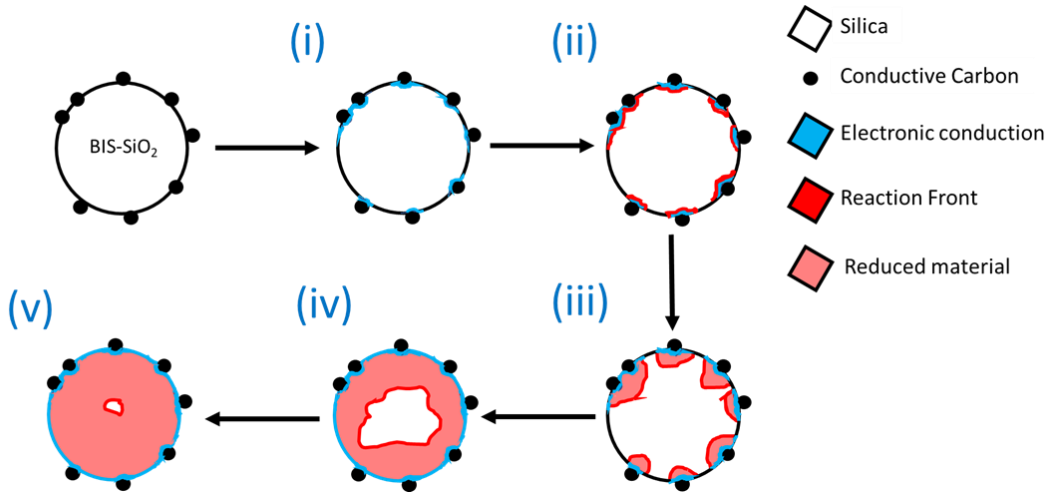

Figure 6.8. A refined graphical mechanism for the electrochemical reduction of BIS at a particle level.

During stage (ii), the minimum in current flow at 0.5-1.5 hours, it was hypothesised that lithium is depositing on the surface of the silica electrode. This hypothesis was supported by the above experiments: The increased capacitance of the electrode during this period as measured by EIS, indicated a build-up of charge. In addition, CLD was applied, negative voltages indicated the tendency of lithium to react with the electrode becomes unfavourable (positive ΔG). This means that although Li is reaching the surface of the silica, reduction of silica does not occur hence no current flow during stage (ii).

For the lithium deposited on the surface of silica to reduce, electronic conduction pathways must be accessible to balance the charge of the redox reaction. The redox reaction only occurs slowly at the limited sites with good electrical pathways to the current collector i.e. surface sites connected through the carbon conducting network. The reduced species (hypothesised Lithium silicates) have higher electronic and lithium ion conductivity than silica, as discussed above and in relation to Figure 6.4,

hence we propose a mechanism where as more silica is reduced, more pathways are available for further reduction to occur, which leads to the rise in current during the region denoted (iii). Figure 6.5(b) supports this showing that the electrical resistance of the electrode decreases during region (iii).

At the maximum current flow stage (iv), the CEP-P factor begins to decrease corresponding to a decrease in capacitive nature of the electrode. This decrease in capacitive nature suggests a lowering in the charge build up on the electrode surface. Additionally, the following region (v) displays a constant decline in current flow. During this region, the resistance and capacitance of the electrode continue to decrease. It is hypothesised that point (iv) is reached when a large electrode surface is available which has sufficient electronic conduction pathways for reduction reaction to continue/progress. It is known that electrochemical reduction of silica occurs via a shrinking core mechanism, when sufficient electronic conduction is provided.[3] During this stage, the diffusion of lithium-ions through reduced material to the reaction front at the core becomes the limiting factor.[3] It is possible that region (iv-v) represents this regime, once silica is reduced at the surface, the limiting factor becomes solid state diffusion of lithium to the reaction fronts within silica particles. This is indicated by a decrease in CPE-P factor as the reduced species better conduct lithium-ions, hence less capacitive build up on the surface of the reduced particles. Following this as the reaction fronts progress deeper into silica particles the rate of the reduction decreases, as observed in stage (v).

6.3.5 Stoichiometry from Li Transfer

It is possible to use the CE during the electrochemical reduction step to infer information about the stoichiometry of irreversible products formed (proposed $Li_xSi_yO_z/Li_vO_w$).[14] However, the accuracy of applying this technique to the methods presented above was inadequate to gain useful insight. The continual formation of SEI upset the balance of CE and perturbed measurement of the reaction stoichiometry. However, to a much greater extent, lithium plating introduced a third unknown factor which could not easily be estimated for stochiometric calculations. Therefore, no stoichiometric calculations are included in this report.

6.4. Conclusion

The mechanism of electrochemical reduction of a new silica anode material based on BIS was investigated electrochemically. In Chapter 5 the kinetics of the electrochemical reduction reaction were studied on a cycle-by-cycle basis, usually spanning >20h per cycle. In this chapter it has been shown that studying the current profile can give real time insight into the electrochemical reduction. The current profile during reduction was shown to give a typical shape which was independent of the reduction temperature. The current profile was showed 5 defined regions which were investigated in depth to develop a mechanistic knowledge of the electrochemical reduction process.

Investigating the reduction reaction at 50 ^{o}C gave vital insight for developing a mechanism of electrochemical reduction of BIS. Through impedance measurements, it was shown that the lithiated anode material has a lower electronic resistance. EIS measurements during the PSD reduction step further revealed the capacitive and resistive properties of the BIS electrode during the electrochemical reduction. In addition to the EIS measurements, voltage analysis was performed during the constant load discharge. A period of negative voltages was identified during the early stages of the electrochemical reduction which suggests lithium deposition on the BIS surface.

A mechanism for the electrochemical lithiation of silica was proposed Figure 6.8. The mechanism is based on the current profile during the PSD and supported by the EIS measurements and voltage analysis during CLD. The reaction is proposed to progress via a surface to centre mechanism. However, the initial rate of the reaction is low due to the insulating nature of the BIS. The reduction reaction therefore starts slowly at points with good electrical conductivity. As silica is reduced more electronic conduction pathways are opened in the material, due to the electronically conducting nature of the materials formed. As the reduction progresses the rate of the reaction increases until a maximum point is reached where the lithium-ion diffusion rate becomes the limiting factor. As the reduction progresses further and further from the BIS surface the rate of reaction decreases.

This mechanism is concurrent with literature findings reported in Chapter 5 where consistently silica materials with small particles and those with large conductive carbon networks reach high reversible capacity. However, no literature studies exist

with regards to studying the silica electrochemical reduction process. Therefore, this mechanism can be used a basis for further work regarding silica based active materials.

The results of detailed electrochemical measurements have been presented above. In short a surface to centre reduction mechanism is proposed which is dependent on good electrical conduction and lithium-ion diffusion pathways. From this mechanistic understanding the electrochemical reduction reaction time was reduced form over 400h to 13 h. To reduce this reduction time further, future work could focus on better electronic conduction pathways on the surface of the silica, perhaps repeating these experiments on carbon coated-BIS.

Although this work has shed new understanding on the electrochemical reduction of silica the specific scalability of this process is yet to be explored. Due to the limited lithium inventory available in a full cell the electrochemical reduction of silica will have to be performed on electrodes before cell assembly. Pre-treatment of electrodes is used in industry today as reported in Figure 6.1. It is envisioned that these processes maybe applicable to BIS electrode materials.[2] With regards to these pre-treatments the above findings of CLD and elevated temperature will be directly applicable. Future work should focus on treatment of silica electrodes and subsequent assembly into full cells, focusing on; attaining the highest stable capacity within a reasonable time, a scalable pre-treatment method, and seeking more benign electrolytes.

6.5. References

[1] J. R. Dahn, J. C. Burns, D. A. Stevens, *Electrochem. Soc. Interface* **2016**, *25*, 75.

[2] H. J. Kim, S. Choi, S. J. Lee, M. W. Seo, J. G. Lee, E. Deniz, Y. J. Lee, E. K. Kim, J. W. Choi, *Nano Lett.* **2016**, *16*, 282.

[3] F. Lepoivre, D. Larcher, J. Tarascon, *J. Electrochem. Soc.* **2016**, *163*, 2791.

[4] Z. Favors, W. Wang, H. H. Bay, A. George, M. Ozkan, C. S. Ozkan, *Sci. Rep.* **2014**, 1.

[5] B. B. Gao, S. Sinha, L. Fleming, O. Zhou, *Adv. Mater.* **2001**, 816.

[6] I. Kurmanbayeva, A. Mentbayeva, A. Sadykova, A. Adi, Z. Mansurov, Z. Bakenov, *Eurasian Chem. J.* **2019**, *21*, 75.

[7] M. Lacy, “Electrochemical Impedance spectroscopy,” can be found under http://lacey.se/science/eis/fitting-with-real-data/, **2019**.

[8] ZView, in *Oper. Man.*, Scribner Associates, Inc, **2016**.

[9] W. H. Molder, J. H. Sluyters, *J. Electroanal. Chem. Interfacial Electrochem.* **1990**, *285*, 103.

[10] W. R. H. John, *J. Solid State Chem.* **1981**, *278*, 271.

[11] I. M. Hodge, M. D. Ingram, A. R. West, *J. Am. Ceram. Soc.* **1976**, *59*, 360.

[12] K. Zhao, G. A. Tritsaris, M. Pharr, W. L. Wang, O. Okeke, Z. Suo, J. J. Vlassak, E. Kaxiras, *Nano Lett.* **2012**, *12*, 4397.

[13] A. Bard, L. Faulkner, *Electrochemical Methods: Fundamentals and Applications*, John Wiley And Sons, Inc, **1980**.

[14] T. Tan, P. K. Lee, D. . Y.W. Yu, *J. Electrochem. Soc.* **2019**, *166*, A5210.

Chapter 7: Characterisation of Electrochemical Reduction Products

7.1 Introduction

In-situ, in-operando characterisation is the pinnacle for characterising battery electrode materials. These methods provide direct analysis of materials in their working environment. However, specific equipment and cell designs are needed. Equally, in specialist cell designs, electrode material can perform differently to its performance within a cell. Ex-situ analysis can more easily be performed on post-mortem electrodes. For this study it is important to consider the sensitivity of cell reaction products to an air environment. The reduction silica electrodes within the cell occurs with negligible levels of oxygen gas and/or dissolved oxygen within electrolyte. Any analysis performed ex-situ and exposed to air may contain oxidised components along with other air contaminants.

The reaction mechanism between lithium and silica is not well understood and products of the reduction reaction are debated. This lack of clarity is a result of the reduced species being difficult to characterise. Therefore, the nature of the inactive reduced species is a key area of current research. A wealth of characterisation techniques have been utilised in an attempt to study the reduction products of silica lithium reduction: Nuclear Magnetic Resonance studies have been performed and distinct silicon environments are observed after electrochemical reduction. However, distinction between which $Li_xSi_yO_z$ species are present cannot be made.[1] X-ray photo electron spectroscopy has also been employed and although clear differences in the oxygen and silicon environments are reported, differentiation between which silicate species are formed cannot be seen.[1][2]

High Resolution Transmission Electron Spectroscopy has been able to provide some insight into the reduction products. For the first time Guo et al,[1] showed that after

the reduction reaction 'crystalline' species are present within the initial silica domains. The amorphisation of silicon after lithiation is well documented,[3] therefore any crystalline domains must be the hypothesised inactive species. Selected area electron diffraction (SAED) of these regions revealed an ordered hexagonal structure. These results also observed the same crystalline domains in the lithiated and delithiated state confirming that by-product formation is irreversible, this result of irreversible crystalline phases was also confirmed in a similar study by Chang et al.[4] The identification of a hexagonal structure strongly supports the formation of $Li_xSi_yO_z$ species. Within these studies both authors conclude that this means Li_4SiO_4 is the reduction product however this does not match with the hexagonal structure they observe.[5] This highlights the complex nature of the reduction reaction species and the difficultly of characterisation.

Some attempt to model the lithiation processes occurring during silica reduction and subsequently identify the nature of the species formed have been performed.[6–8,10] Lener et al[6] review a number reported silicates and lithium oxides from literature and show that thermodynamically all these species ($Li_4SiO_4, Li_2Si_2O_5, Li_2O$) can form spontaneously. They go on to show the dependence of the formation of these species on the cell voltage, showing that all studies reviewed lie within the spontaneous voltage regions. In a further paper their calculations show that $Li_2Si_2O_5$ has the highest enthalpy of reduction (ΔH) and the greatest probability of formation.[7] Ban et al[8] used DFT simulations to show that complete reduction and the formation of Si-Si bonds are not energetically favourable and that Li_xSiO_2 (x=2/3) species are the products of the reduction. The further study of Zhang et al[9] was with regards to silica coatings on silicon active materials. In their simulations they model the lithiation of amorphous silica with regards to the formation of Li_xSiO_2 silicates with the proposed highest lithiated state containing Li_2SiO_2. They go on to further show the enhanced electrical conductivity in the reduced species as lithium content in increased, without quantitative secondary confirmation of silicate structure these models are still to be verified.

External reduction of silica has been performed to model reactions during electrochemical lithiation. Yamamura et al[11] investigated ex-situ lithium reduction at 200 °C where crystalline Li_4SiO_4 and Li_2SiO_3 were identified. When performing electrochemical reduction of the same silica species no crystalline products were reported in diffraction patterns, this is likely due to higher temperatures being needed for product species to crystallise. Their modelling results suggested that lithium can

reduce Si-O bonds when any bond length is inequivalent, that is in amorphous structures where defects are present. They support this by showing that crystalline quartz cannot be electrochemically reduced. A similar study into prelithiation at 200 ^{o}C with lithium metal reported no crystalline $Li_xSi_yO_z$ phases identified with XRD but did identify the presence of crystalline Li_2O_2 presence. Again, this example highlights the lack of understanding of the reduction products, the difficulty in characterisation these materials, and potentially the air sensitivity of reduced electrodes.

There is a clear knowledge gap in the understanding of species formed during the electrochemical reduction of silica. The literature is unclear on the following key points: Are the products of electrochemical reduction crystalline or not? What is the stoichiometry of the silicate species formed ($Li_xSi_yO_z$)? Are the silicate species inactive or do they contribute to capacity? Is silicon responsible for the reversible capacity in these materials?

In this Chapter we present our attempt at answering these questions. Various characterisation methods are utilised to determine the structure of the bulk reduction products. For the first time the products of electrochemical reduction are characterised with XRD and XPDF to compare the crystalline and amorphous structures within the reduced electrodes. Surface-based characterisation methods are also explored and compared with similar experiments within the literature.

7.2 Experimental

This section details specific experimental procedures needed for understanding this chapter. The general experimental section concerning experiments not specified here can be read in Experimental Chapter 2.

XPDF data were collected on the I15-1 beamline at the Diamond Light Source UK, using an X-ray wavelength λ=0.161669 Å (76.69 keV). Electrode material samples were compacted into borosilicate glass capillaries of 1.17 mm (inner) diameter. Data from the samples, empty instrument, and empty capillary were collected, and integrated to 1D using DAWN.[12] Corrections for background, multiple scattering, container scattering, and attenuation were made using the GudrunX software [13].

Grazing incidence XRD was performed on a Panalytical X'Pert 3 in reflection-transmission configuration. Cu $k_{\alpha 1}$ radiation wavelength 1.5406Å was selected for diffraction measurement between 20-76.5 ^{o} with a step size of 0.1 ^{o}.

XPS measurements were performed in a front-loaded N_2 filled glovebox at 300 K. The measurement was performed on a Kratos Axis Supra instrument at < 10^{-8} Torr pressure. The area for analysis was 300 x 700 um. X-ray power was 225W with X-ray energies of 1486.7 eV. Spectra were run with 100ms dwell times and a step size of 0.1eV. Data analysis was performed in CASAXPS software.

7.3 Results and Discussion

7.3.1 Raman Spectroscopy

Raman spectroscopy was performed on electrodes after pre-treatment with PSD. Previous work of Hoyos et al. had used Raman to characterise a phase transition between Li_4SiO_4 to Li_2SiO_3 for CO_2 capture applications. These species are commonly hypothesised products of electrochemical reduction of silica and therefore it was hoped Raman spectroscopy would be able to identify these species it present. However extreme intensities were measured even for relatively low excitation energies. This phenomenon has recently been explained by Kostecki et al,[14] as fluorescence caused by fluorine-phosphorus containing species which overlap with and drown out weak Raman signals even with F-P levels <1ppm. Although all electrodes were washed in DMC prior to measurements, complete removal of F-P species was not ensured. Raman spectroscopy could not provide useful characterisation of reduced electrode products. For future reference Kostecki et al, present the use of 'Kerr gated Raman spectroscopy' for the study of post mortem electrodes;[14] this does however require central beamline facilities and was beyond the constrains of this thesis.

7.3.2 Grazing Incidence X-ray Diffraction

Grazing incidence-XRD (GI-XRD) was used to identify crystalline species within reduced silica electrodes. GI-XRD used small incident angles for the incoming x-rays, so the diffraction can be made surface sensitive. Due to the small nature of coin cell electrodes (a single electrode typically contains ~1-2mg of material), extraction of such a small amount of material is laborious and for a powder diffraction measurement many electrodes are typically needed. With the use of GI-XRD, the incidence angle and beam power can be altered such that an electrode film can be measured on its copper current collector. Figure S7.1 shows control experiments with crystalline silicon containing electrodes, which highlights this technique is sensitive to crystalline species within a composite electrode.

GI-XRD was used to characterise BIS containing electrodes Figure 7.1(a) shows the absence of crystalline species within a fresh BIS composite electrode, aside from the copper current collector. This is expected due to the amorphous nature of each constituent of the composite. Figure 7.1(b) and (c) are diffractograms of post mortem electrodes in the lithiated and delithiated state after 400h of PSD at 25 ^{o}C and 10 reversible cycles with capacities reaching more than 500 mAh/g, these sample points correspond to Figure 5.9 at 10 cycles. In order to collect these diffraction patterns the 'washed' electrodes were exposed to air. Therefore, it is possible that air contamination and oxidation was present.

Figure 7.1(b) has sharp diffraction peaks at low angles, 21.1 and 26.3 ^{o}, a curious broad feature (A) between 28.7-31.4 ^{o}, with 2 more potential broad features up to 42 ^{o} (B and C), and a final small peak at 61.8 ^{o}. Figure 7.1 (c) has one discernible but very clear diffraction peak at 26.3 ^{o} with several small potential peaks at 3/0,35,40 ^{o}. Figure 7.1 displays diffractograms collected at exposure times of 3.5 h in order to increase the intensity of diffraction peaks relative to background noise. Due to the detection of only 2 clear diffraction peaks at 21.1 and 26.3 it is difficult to identify the crystalline species present. The GI-XRD patterns were fingerprinted against all proposed and hypothetical $Li_xSi_yO_z$ containing crystalline compounds, for this analysis the small potential peaks indicated in Figure 7.1 were also screened. The compounds fingerprinted against were; Li_2SiO_3, Li_2Si_3O7, Li_5SiO_5, Li_8SiO_6, Li_4SiO_4 (see Figure S7.2). Additionally, common crystalline SEI components (Li_2O, Li_2O_2, LiF) and potential crystalline species formed during exposure to atmosphere (Li_2O, Li_2CO_3) were assessed for phase analysis. None of the species were matched via

phase analysis, although several species have their primary diffraction peak between 28-42 ^{o} the broad nature of the features and identification of only a single diffraction peak was not significant to confirm phase identification. The intense and consistent diffraction peak at 26.3^{o} did not match any of the proposed species. Of worthy note is the presence of stronger and more numerous diffraction features in the lithiated electrode. The lithiated electrode is potentially more sensitive to reaction in an air environment, and therefore stronger features are observed in Figure 7.1 (b), this may suggest these samples are subject to change in chemical composition upon exposure to air.

This experiment proved the difficulty highlighted in the literature of identifying the species formed from silica reduction. The validation of this technique on silicon containing electrodes with just 0.5 h exposure proved this technique can identify crystalline species within composite electrodes. The reduced electrodes did show at least two clear diffraction peaks at 21.1 and 26.3 ^{O} however these are not sufficient evidence to determine the presence of any of the postulated species. With this experiment it was not possible to measure diffractograms without exposure to air and therefore the few peaks identified could be due to reaction of reduced species with air.

The GI-XRD study showed the difficulty of identifying crystalline species within electrochemically reduced silica. In addition, the need for inert atmospheres for characterisation was reinforced.

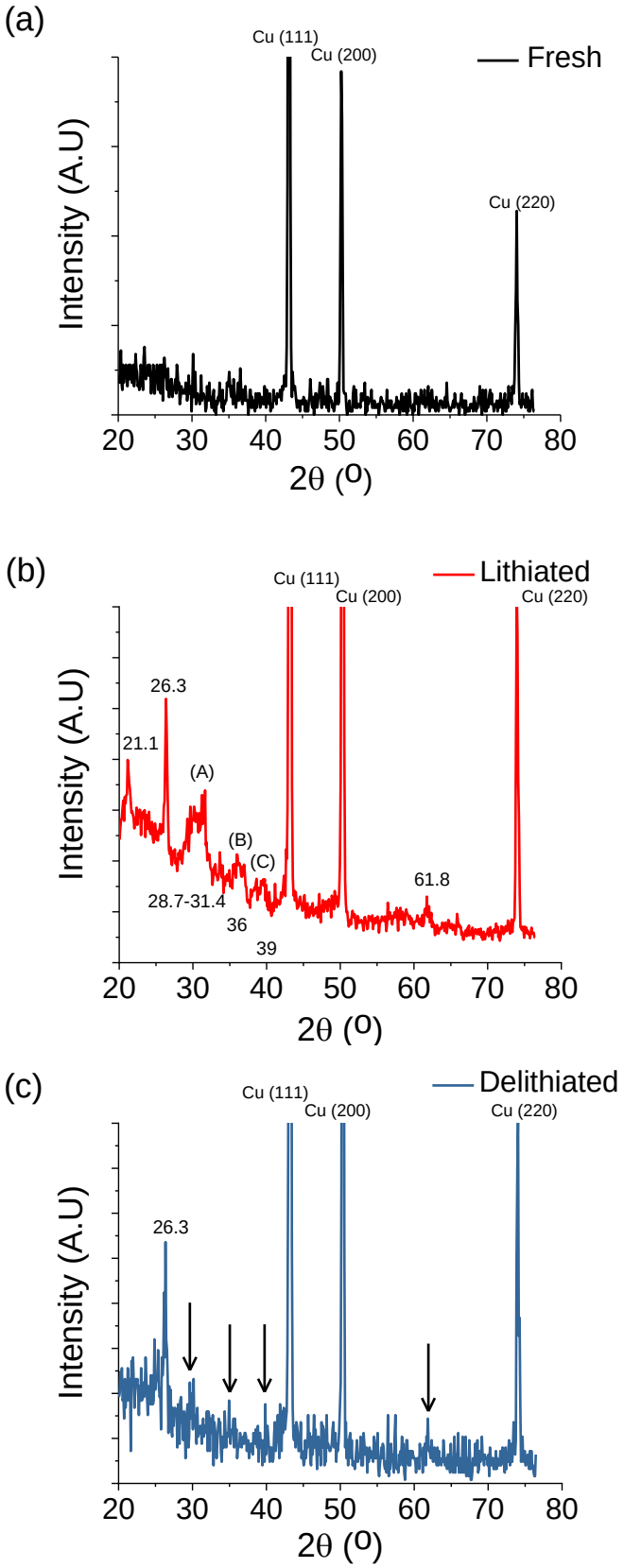

Figure 7.1. GI-XRD diffractograms of silica composite electrode corresponding to (Figure 5.9 at 10 cycles), (a) fresh electrode before cell construction. Post mortem 400h PS treated electrodes (b) lithiated state (c) delithiated state.

7.3.3 X-ray Pair Distribution Function

Following the GI-XRD experiment above, and the clear lack of consensus within the literature on the products of silica reduction, a characterisation method that may be applied to amorphous and crystalline materials is clearly needed. This section concerns the novel characterisation of the silica reduction species via total scattering pair distribution function (PDF). This technique was applied to determine the composite electrode components following the PSD reduction protocol. PDF analysis will provide both the Bragg scattering, and underlying diffuse scattering information concerning these reduction products. For the first time this allowed for the determination of long and short range order within the reduced silica species and better understanding of the chemical reduction processes occurring during electrochemical silica reduction. Although performed ex-situ, all reduction species analysed were prepared under an inert argon atmosphere post mortem in order to provide an accurate representation of the reduction products without air interference.

In this work, the silica species are the focus of the investigation, however, composite electrode compositions are required to produce a functional battery half-cell. As is common practice, carbon is included as a conductive additive to provide electronic conduction pathways and a binder is needed to enable the materials to adhere to each other and to the current collector. In this study composite electrodes identical to all previous testing were used, such that the characterisation of the reduction products would match previous characterisation and electrochemical studies. When using bulk characterisation techniques such as X-ray Pair Distribution Function (XPDF) the characteristic peaks of the passive components of the electrode will combine with the signals from the silica and the reduction products. Due to the novel nature of this work and the high sensitivity of XPDF, a detailed collection of control experiments was performed.

Control Samples

Data obtained from total scattering for a series of the initial control samples are presented in Figure 7.2, where each component of the composite electrode was characterised individually. Additionally, a crystalline silicon control sample was characterised, as silicon is hypothesised to be the major reduction product following the electrode pre-treatment reaction under investigation.

The electrode binder CMC is amorphous as is the C-65 carbon conductive additive, this was expected as neither of these species shows Bragg peaks in previous diffraction work (Figure 7.1 and Figure S7.1). The PDFs of the binder (CMC) and conductive carbon (C-65) (Figure 7.2) are almost identical; this mirrors the composition of these samples which are both primarily carbon with no crystallinity. The nearest neighbour distances of 1.42 2.46 and 2.84 Å correspond to tetragonal carbon to in a diamond lattice and match well with literature. [15,16] Longer range order starts to diminish after 5 Å consistent with an amorphous carbon structure. In addition, no peak is observed in C-65 at 3.35 Å corresponding to the spacing of carbon atom basal planes in graphite. The bond length and angles of the 1st and 2nd nearest neighbours correspond to tetragonal carbon centres with bond angles of 109.5 ^{o} (according to trigonometric calculations). The fourth (3.75 Å), fifth (4.25 Å) and beyond neighbours do not match to a diamond lattice. As this material is amorphous in nature, it is expected that the tetragonal clusters arrange in amorphous patterns with very low uniformity.

Figure 7.2 for the first time presents PDF of bioinspired PEHA silica. The predominant peak observed was the Si-O bond length 1.60 Å, with strong signals at 2.61 Å (oxygen-oxygen distance) and 3.05 Å (silicon-silicon): these are the bond lengths of the smallest repeat unit of tetragonal silica with a bond angle of 109.5 ^{o}. The intensity of peaks beyond 5 Å is much lower, suggesting a lack of and long-range order and hence reinforcing the highly amorphous nature of the PEHA-silica. Figure 7.2 also shows crystalline silicon with the bond length (2.35 Å) and nearest neighbour distances (3.83, 4.49, 5.42, 5.92, 6.66 Å …) corresponding to a diamond lattice crystal structure of silicon atoms. Figure S7.3(a) confirms the high crystallinity of this sample via diffraction, further confirmed by PDF shown in Figure S7.3(b). Figure S7.3 (b) also shows how XPDF can be used to determine long range order out to 40 Å in crystalline samples.

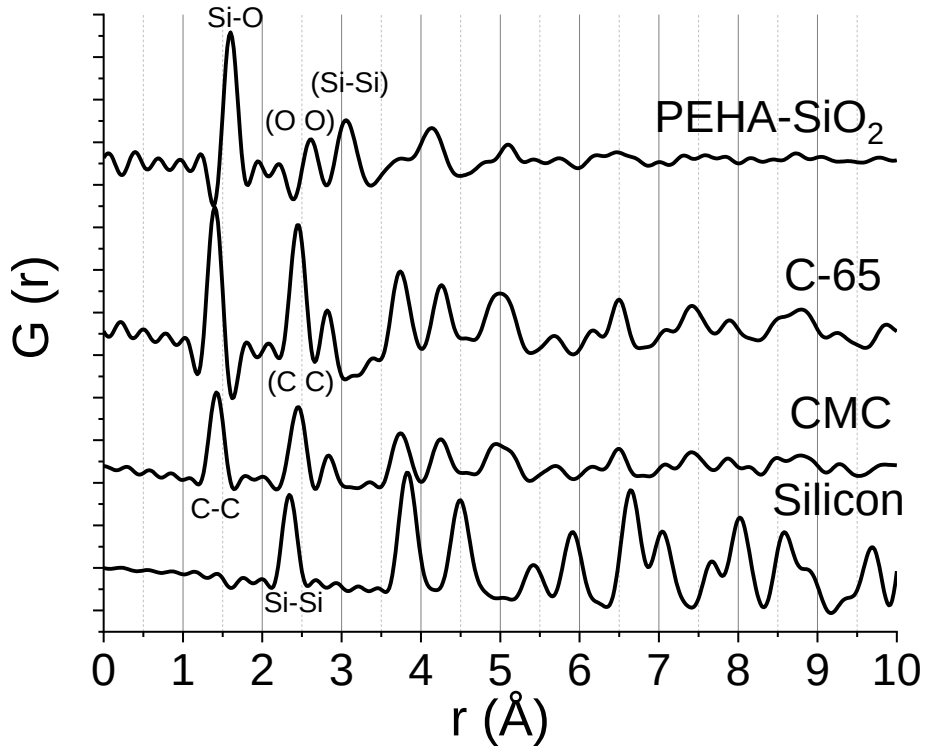

Figure 7.2. PDF of crystalline silicon -325 Mesh, CMC carboxymethyl cellulose electrode binder, C-65 carbon conductive additive, PEHA silica 'active material'(BIS).

Composite Electrode Control Samples

In order to characterise the effect of convolution between overlapping peaks, three composite electrodes were also analysed (before any electrochemical reaction, fresh electrodes). They include i) CMC binder + C-65 Carbon, ii) CMC binder + C-65 Carbon + -325 mesh Si, iii) CMC binder + C-65 Carbon + BIS silica.

A control electrode of C-65 and CMC presented in Figure 7.3 has no deviation from the pure control samples of a carbon black or binder electrode. This is expected as the control samples gave identical PDFs, and this provides support that the electrode processing step did not change the short-range order within these materials, even when combined.

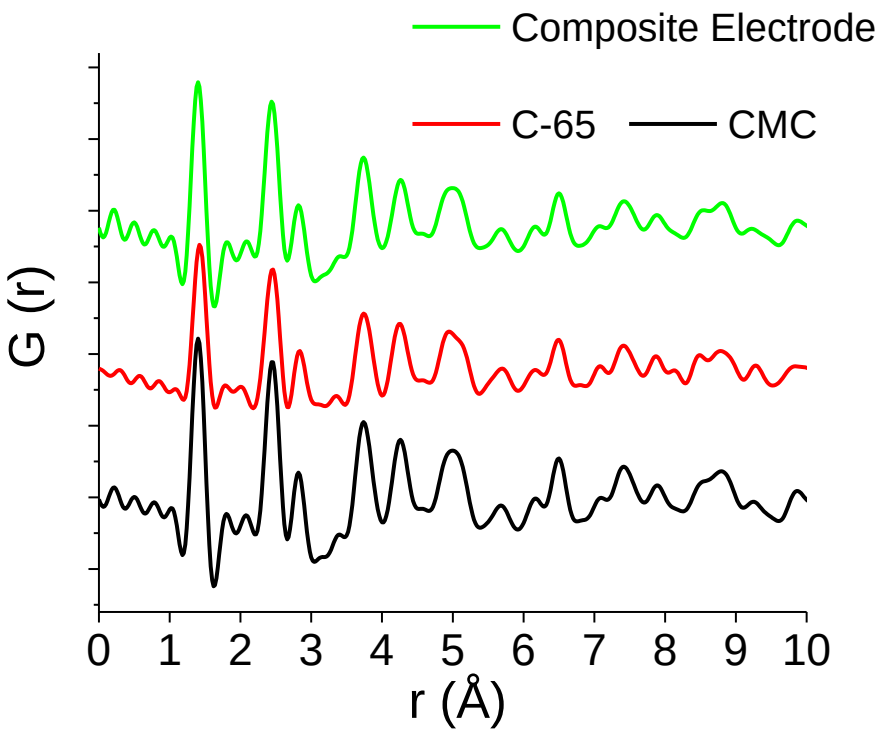

Figure 7.3. PDF of control samples combined into composite electrode of 80wt% C-65, 20wt% CMC.

Next, the PDF results for the control electrode of silicon, C-65 and CMC presented in Figure 7.4. Due to the crystalline nature of silicon and its high percentage (60 wt%) in the electrode composition, the silicon peaks dominated the PDF, while many of the carbon peaks were convoluted within the larger Si peaks. The carbon peaks at 1.42 and 2.84 Å were clearly discernible from silicon peaks and could be useful in

detecting these materials. This control PDF reassures that no changes to the short-range order occurred during the electrode manufacturing stage and that silicon peaks are still discernible in the PDF of composite electrode material.

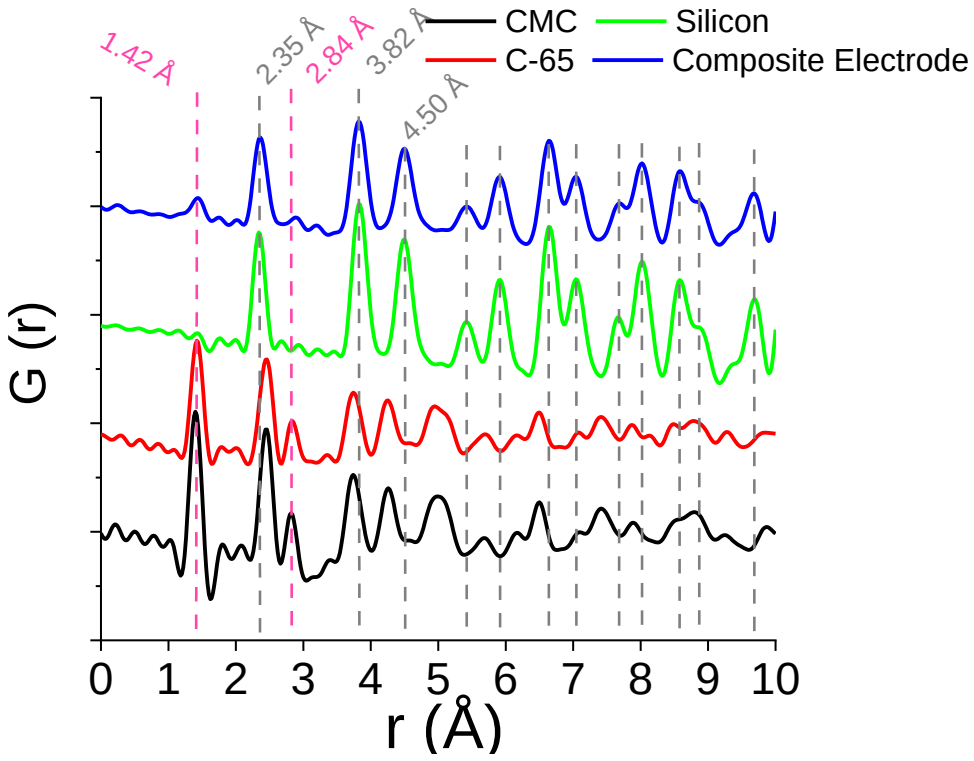

Figure 7.4 PDF of composite electrode 60wt% Si, 20wt% C-65 and 20wt% CMC. Magenta lines show the signals from C-65 and CMC. Grey lines correspond to contributions from the silicon.

Within the PEHA-SiO_2 composite electrode (Figure 7.5), the silica is the highest constituent by weight, however, due to its amorphous nature, the PDF peaks of the silica are convoluted with the carbon containing species of the electrode. Due to the amorphous nature of the PEHA-SiO_2 and lack of any long-range order beyond 5 Å, there are a limited number of signals which can be used to determine any structural changes within the electrode. The peak at 1.60 Å contains a shoulder at 1.42 Å due to carbon convolution, and this peak can be used as a strong indicator of silica structure within the electrode. The composite electrode has a more convoluted peak at 2.49 Å which is a convolution of the 2.46 Å peak (CMC+C-65) and the 2.61 Å (O O) in silica. In addition, and useful for analysis the convoluted peak in the composite material at 2.92 Å which is a convolution of the 2.84 Å peak (CMC+C-65) and the 3.06 Å (Si Si) in silica.

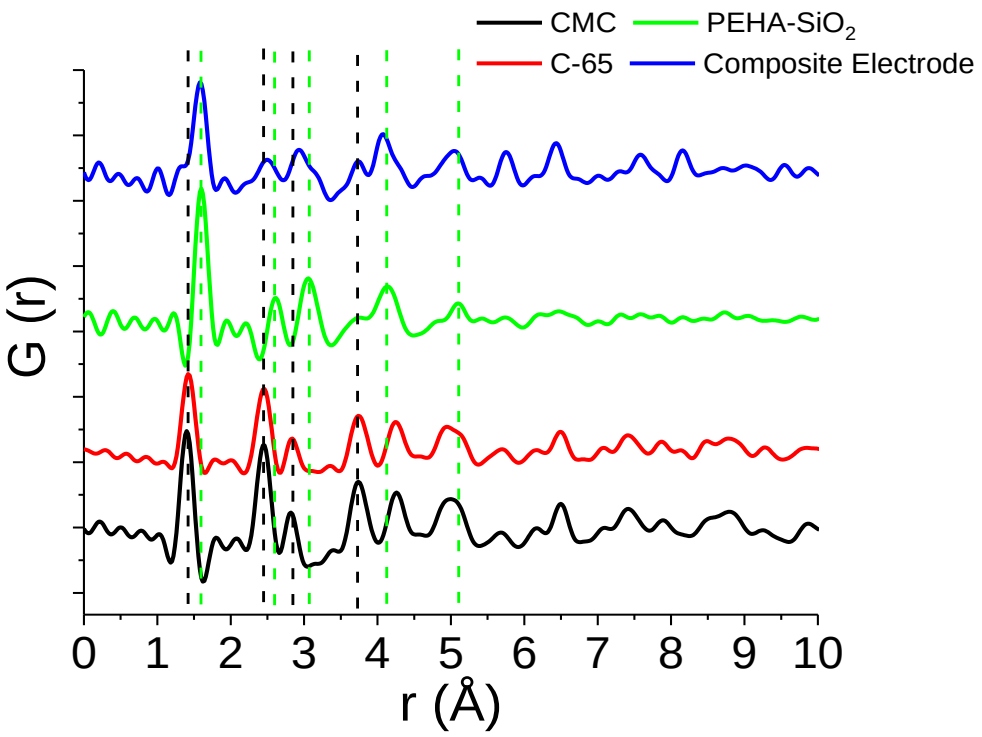

Figure 7.5. PDF of composite electrode 60wt% PEHA-SiO_2, 20wt% C-65 and 20wt% CMC. Peaks of corresponding to SiO_2 highlighted in green dashed line. Peaks corresponding to binder and conductive additive highlighted in black dashed line.

Composite electrodes post lithiation

C-65 Electrode

The effect of lithiation in amorphous carbons, such as C-65, has not previously been investigated with PDF. The capacity of 250 mAh/g achieved by C-65 arises from reversible lithium intercalation/absorption into hard carbon domains within the amorphous structure.[17] Although X-rays are less sensitive to light elements, such as lithium, any short range structural changes to the carbon host should be sensitive to PDF.

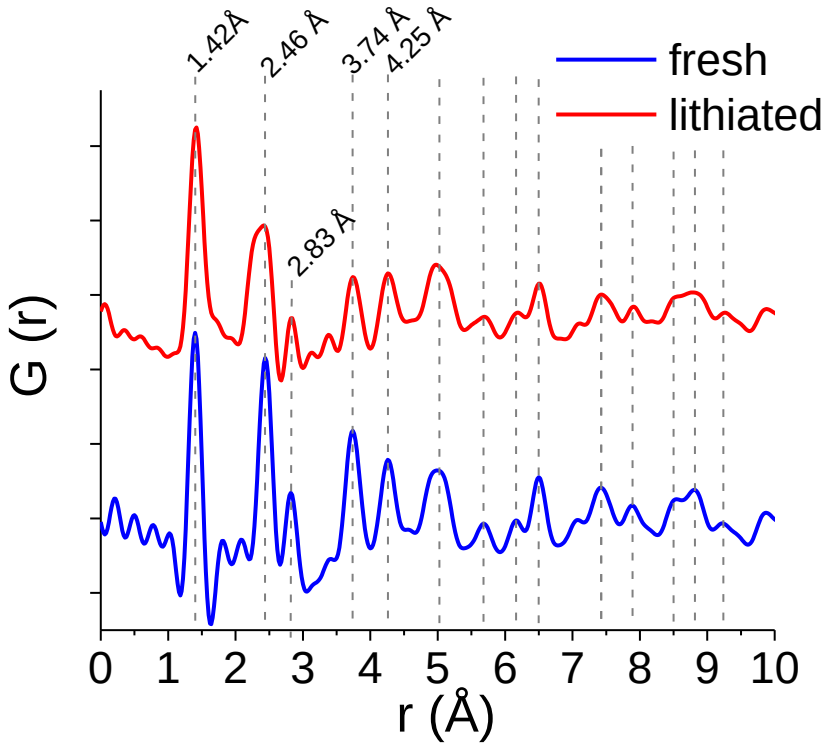

Figure 7.6. PDF of composite electrode of 80wt% C-65, 20wt% CMC before and after lithiation.

Figure 7.6 presents the lithiated and delithiated C-65 composite electrode after 5 cycles. The ratio of the 1.42 Å to the 2.46 Å peak intensity has increased in the lithiated sample. Additionally, the relative peak intensities of the peaks at 3.74 Å and 4.25 Å has reduced. A shoulder on the 2.46 Å peak at smaller radii has caused a broadening.

The lithiation of amorphous carbon does not involve the breaking or formation of any carbon-carbon bonds, however some discrepancies in the short-range structure were

clear with a broadening of the 2.46 Å peak. Beyond 5.00 Å, little change is observed in the structure between lithiated and fresh state. Distortion of the 2.46 Å peak in the lithiated state suggests changes to the carbon structure in the tetragonal lattice. It is possible that changes are occurring but only to a certain fraction of the carbon sample that is electrochemically active.

To the best of our knowledge PDF analysis of lithiation of amorphous carbon materials has not been reported previously. Lithiation in amorphous carbons is a current area of research without a definitive model.[18] Further analysis of these materials is needed to understand the mechanism of lithiation.

Silicon electrode

The effect of lithiation in crystalline silicon has been followed by ex-situ PDF measurements previously.[19] The lithiation involves an alloying process between Si and Li which requires the breaking of Si-Si bonds and leads to the complete amorphisation of any silicon species. The alloying also results in significant volume expansion, with a value of +280%. These influence the macrostructure, however there are a number of factors which can lead to only subtle changes in the local order seen in the PDF.[19]

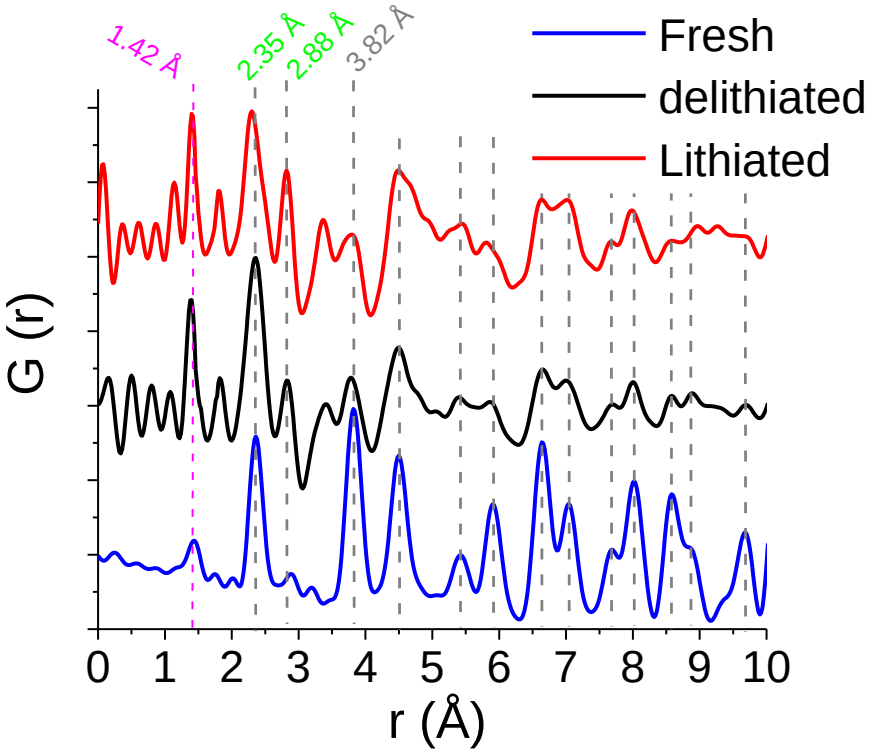

Figure 7.7. PDF of composite electrode 60wt% Silicon (-325 Mesh), 20wt% C-65, 20wt% CMC. Fresh electrode is virgin material, lithiated and delithiated have been cycled for 5 cycles and then appropriately fully delithiated or lithiated.

Figure 7.7 shows that large amounts of crystalline silicon remain in the electrode in the lithiated and delithiated state. The electrodes after cycling show much weaker signals for long range silicon order, which is due to the loss of crystallinity upon lithiation. As crystalline silicon is present in the lithiated state it is not surprising this crystalline silicon is still present in the delithiated state. Any silicon which is lithiated and subsequently delithiated will be completely amorphised and hence only Si-Si bonds (2.34 Å) will be present in the PDF and no long-range order expected. The cause of crystalline silicon remaining within the electrodes after cycling is due to the nature of the -325 Mesh (>44μm) particles used. Large particles are known to

degrade due to volume expansion during lithiation. This fracturing can leave large crystalline silicon phases electronically isolated in the electrode and unable to electrochemically participate.[20] Therefore the crystalline silicon in these PDFs is still present after cycling due to electronic isolation of some of the silicon in the electrode.

Silica electrode

As shown in Chapter 5 the PSD treatment increased the capacity of the silica containing electrode via electrochemical reduction. The reduction products are speculated but the differential capacity profiles after reduction strongly suggest elemental silicon was produced. Figure 7.8 presents the PDF of electrode samples before and after the PSD during which electrochemical reduction occurs. Firstly, a reference peak is useful to compare relative intensity changes between PDFs. The C-C (1.42 Å) is highlighted, due to the small changes that occur to the carbon species during lithiation this peak is not expected to change across this study. Note the areas and intensities of peaks are complex and are not solely related to the abundance of the relative elements. The relative ratios of peaks can be used in a qualitative manner to determine changes within the electrodes (due to the electrodes having the exact same starting compositions. Above we show the C-C peak at 1.42 Å is unaffected during lithiation/delithiation and is therefore a good reference peak.

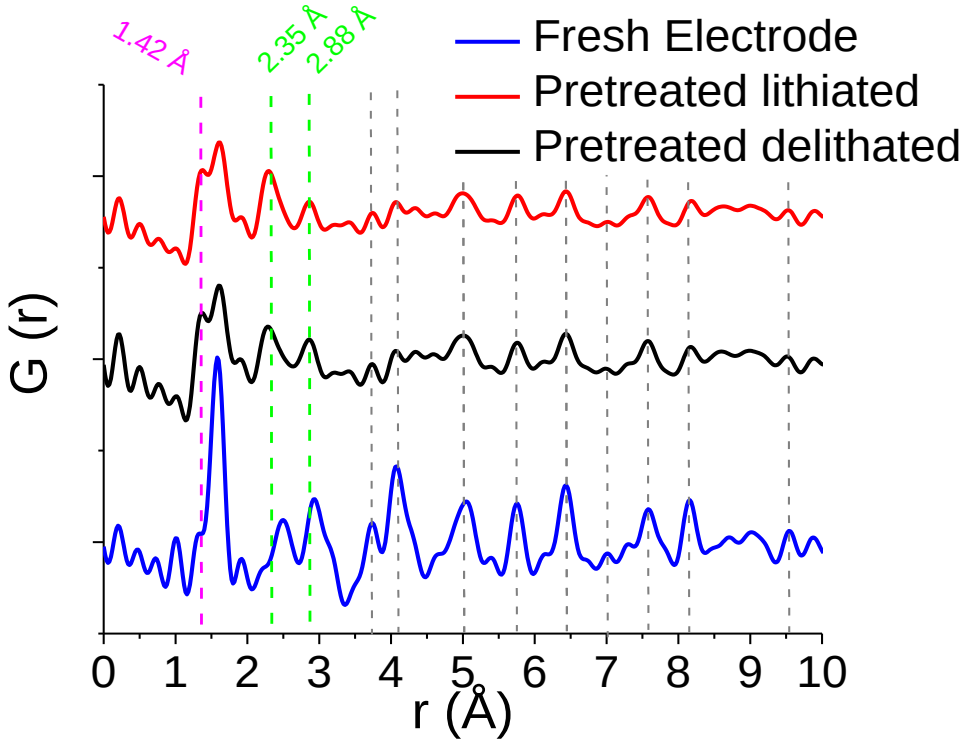

Figure 7.8. PDF of composite electrode 60wt% PEHA-SiO_2 20wt% C-65, 20wt% CMC, fresh electrode state and after PSD at 50 °C for 20 h in both lithiated and delithiated state. Magenta line highlights the C-C bon distance (unaffected during reduction). Green line highlights the main peak shifts observed during reaction.

Figure 7.8 shows that relative to the carbon peak at 1.42 Å, the peak attributed to the BIS Si-O bond at 1.60 Å reduces after the PSD. The 2.35 Å peak is introduced after the PSD and is present in the lithiated and delithiated states, more clearly seen in Figure 7.9 (b-c). The 2.35 Å peak is attributed to the presence of silicon within the electrode as hypothesised by the reduction reaction mechanism. The 2.35 Å peak matches with the control crystalline silicon samples measured in this study and with the well referenced value for a Si-Si bond length.[19] The 2.88 Å peak is shifted after pre-treatment, the original peak is shifted from its maximum at 2.93 Å, this is attributed to the loss of silica presence in the PDF and increased contributions to this peak from the carbon signal at 2.84 Å (Figure 7.9 (b-c)). Note that although this peak could potentially be lithiated silicon ($Li_{3.75}Si$) but this is unlikely as it is present in both the charged and discharged states.[19] Figure 7.9 (b-c) do not show any further peaks which match with the (blue) silicon PDF. This is attributed to a lack of long-range order within the silicon produced. This result is unsurprising due to the well-known nature of silicon becoming amorphous after lithiation (Figure 1.3).[21]

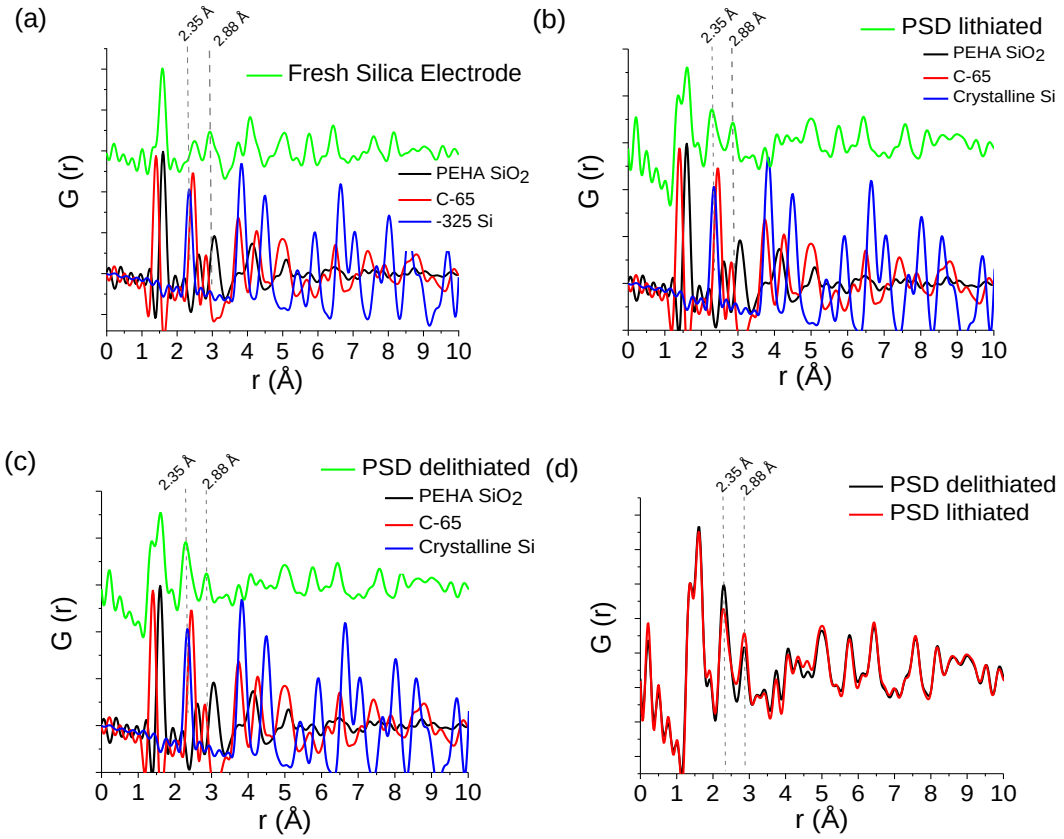

Figure 7.9. (a-c) comparison of composite electrodes with potential species present for (a)fresh PEHA silica electrode, electrodes treated with 20 h PSD at 50 oC (b)lithiated state (c) delithiated state. (d) comparison of lithiated and delithiated state relative intensities.

With the differential capacity curve as secondary evidence, we believe that the PDF identification of Si-Si single bond is accurate and is therefore the first characterisation of elemental silicon produced via lithium electrochemical reduction of silica. The addition of just the Si-Si bond in the PDF has a number of important ramifications: Firstly, silicon is present in both the lithiated and delithiated state. Secondly, no short-range order in the silicon structure is identified within the reduced electrode structure (Fingerprint Blue silicon signals with the reduced PDF, Figure 7.9). These points are discussed below.

With respect to the first above point, the presence of Si-Si bond at 2.35 Å in both the lithiated and delithiated state: It is possible that some silicon produced during the PSD is delithiated during the first delithiation and that upon subsequent lithiation not all of the reduced silicon is accessible during cycling, therefore Si-Si remains in the lithiated state. This point could be supported by the findings in the above Chapter 5, Figure 5.10, where the definition of the differential capacity curve tended to a more typical silicon profile after prolonged cycling. Previous PDF measurement of lithiation of crystalline silicon particles also observed that the 2.35 Å Si-Si remains after full lithiation.[19] In order to explain this we propose that during lithiation the highest lithiated state of silicon ($Li_{3.75}Si$) is not reached. The low electronic conductivity and relatively high current rates used for testing of these electrodes means that the highest crystalline lithiated state 'c- $Li_{3.75}Si$' will not form.[19][22][23] If all silicon is participating in lithiation during cycling then lower lithiated states, such as those proposed by C. Grey et al. (Figure 7.10 (b-c)) may form.[19] The presence of these structures in the lithiated samples would explain the presence of the Si-Si signal at 2.35 Å in the PDF of Figure 7.8 and Figure 7.9.

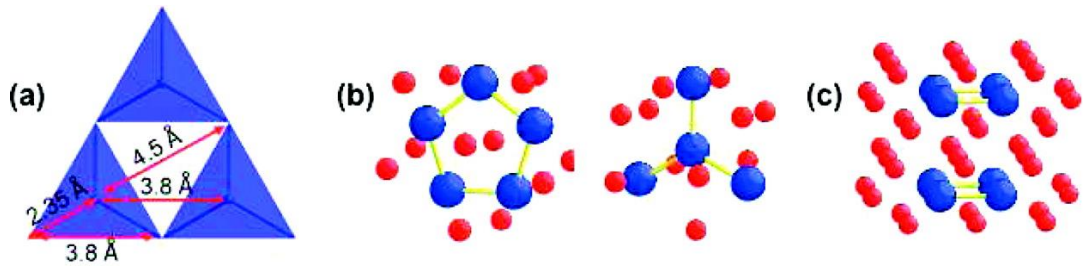

Figure 7.10. Local structures found in lithiated silicon, (a) nearest neighbour distances in Silicon diamond lattice (b) $Li_{12}Si$ rings and stars, and (c) Li_7Si dimers. Taken from[19]

With respect to the second above point of no long-range silicon order present in the PDF such as for a diamond lattice: The very low potentials and long discharge times

will lead to the lithiation of any silicon which is formed during the electrochemical reduction (PSD step). The lithiation of silicon leads to the complete amorphisation of crystalline silicon as discussed in Chapter 1 with respect to Figure 1.3. The PDFs here show the complete amorphisation of the silicon domains formed during the electrochemical reduction. It is also possible that the silicon domains formed by electrochemical reduction may be extremely small, perhaps as small as the structure presented in Figure 7.10 (b-c). This is also likely over crystalline silicon formation due to the low reaction temperature 25 ^{o}C where little energy is available for rearrangement of bonds.

7.3.4 X-ray Photo Electron Spectroscopy (XPS)

XPS analysis was performed on silica composite electrodes reduced via PSD in order to determine the presence of new lithium and silicon environments and quantify the nature of $Li_xSi_yO_z/Li_vO_w$ species formed in reduction. The analysis was performed on post mortem electrodes which had been exposed to air. However useful information can still be determined. XPS is a surface sensitive technique therefore to gain information on the bulk sample it was important that electrodes were thoroughly washed to remove SEI components. In addition, ion cluster bombardment (ICB) was performed to remove the surface layer of the electrode materials and expose the bulk. ICB was performed under vacuum immediately prior to XPS measurement.

A control sample of PEHA bioinspired silica is presented in Figure S7.4, it clearly presents the Si2p (oxide) at 107 eV and overlapping of the $Si2p_{3/2}$ and $Si2p_{1/2}$ causing asymmetry in the 101 eV peak. No carbon and no lithium were observed in the XPS of pure BIS.

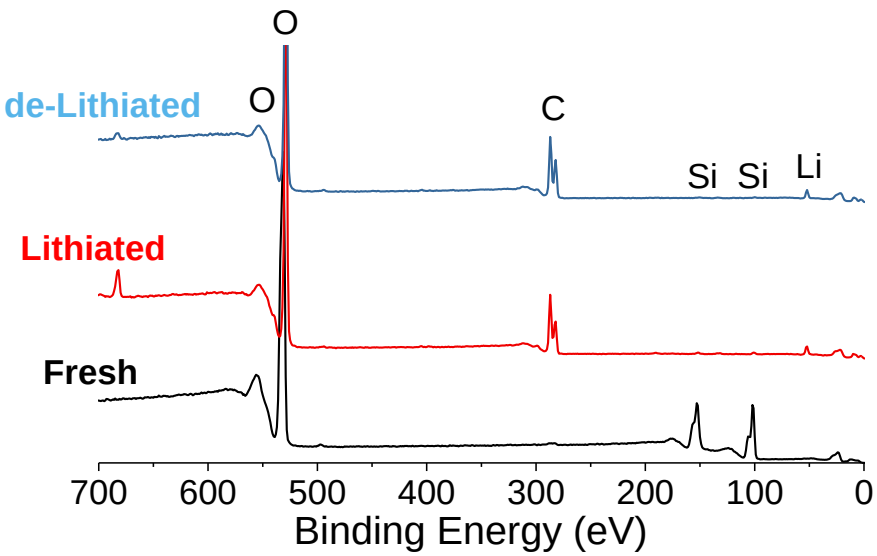

Figure 7.11. XPS spectra of composite electrodes composed of PEHA silica active material, fresh and 400h PSD treated material in lithiated and delithiated state.

While performing the XPS measurement on composite electrodes, specific surface sites on active material (silica) were designated. Figure 7.11 presents the spectra of the fresh electrode before construction into a cell; this spectrum is identical to the PEHA silica control sample as expected. The post mortem electrodes of Figure 7.11 (blue-red) have much lower signal from silicon containing species and larger

components from carbon. This suggests that the SEI removal via washing and ICB was not complete and calls into contention other studies using XPS techniques to study the reduced species.[2]

The washing and ICB steps were insufficient to remove the SEI layer of these electrodes. However, the penetration depth of the XPS measurement was deep enough to quantify the lithium and silicon containing species Figure 7.12 (a-b). Figure 7.12 (a) presents lithium 1s presence in the fresh, lithiated and delithiated electrode. As expected, no lithium was present in the fresh electrode. In the lithiated and delithiated electrode there is a slight shift in the Li 1s binding energy maximum from 52.24 - 52.50 eV respectively.

Lithium containing species are contained within anode SEI however these species, LiF and lithiated carbonates, are stable during cycling. [24],[25] Therefore, the shift in binding energy from 52.5 to 52.24 eV during lithiation could be caused by a change in lithium environment as it reacts with the reduced material. Due to unreliable reported reference values for lithium-silicon and SEI components, quantitate analysis of these spectra was not possible.

The silicon 1s spectrum presented in Figure S7.4(b) shows a slight peak shift between lithiated and delithiated state, from 100.98 to 100.14 (eV). Although the surface of active material forms an integral part of SEI the insignificant shift between the fresh and delithiated electrode suggests the silicon environment is unaffected by SEI formation. This result is somewhat unexpected as due to the electrochemical reduction reaction silica has been reduced, a larger change in the XPS spectra was therefore expected between the fresh and delithiated spectra. A shift to lower binding energies has consistently been reported for silicon in a lithiated environment (Li_xSi) (100.6 and 98.5)[2][26] and hence the shift and broadening observed in Figure 7.12 (b) (blue)) is attributed to the formation of Li_xSi.

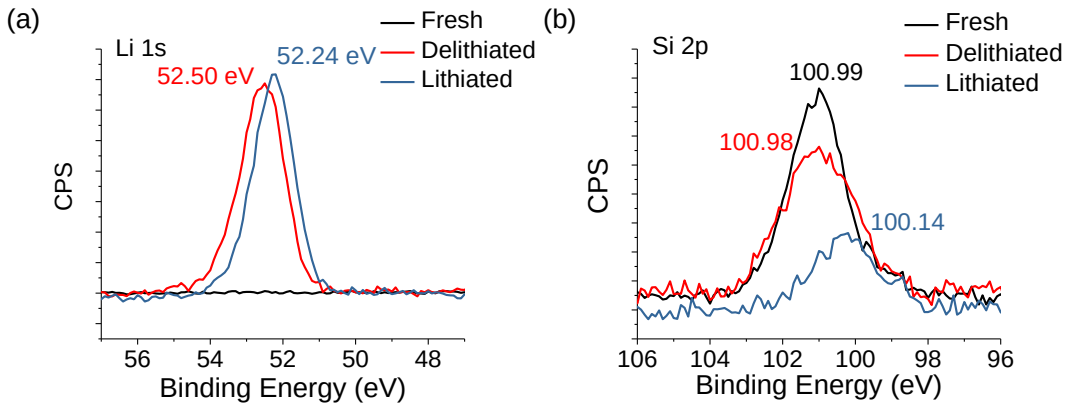

Figure 7.12. XPS of PEHA-silica electrodes in the fresh state and after PDS at 50 ºC for 20 h in both the lithiated an delithiated state. (a) lithium 1s spectra, (b) silicon 2p.

7.4 Conclusion

The products of electrochemical reduction of silica are difficult to characterise due to; the need for post-mortem or in-operando techniques, their amorphous nature and their sensitivity to atmosphere. As such there is no compelling consensus in the literature as to the exact nature of products of the electrochemical reaction. The production of silicon is the basis of using these materials as active materials and the profile of differential capacity plots has been stated as proof that silicon is formed during electrochemical reduction. However, this was an indirect characterisation method in the literature and empirical characterisation of elemental silicon was lacking.

The above work describes attempts made to characterise the silica reduction products in post mortem electrode. Raman spectroscopy was unable to provide insight due to the fluorescent interference of phosphate-ion contaminants. The formation of the SEI layer made other surface-based analysis such as XPS also unable to add understanding. The use of ICB in XPS did remove some surface SEI and was able to differentiate binding energies of silicon and lithium within the lithiated and delithiated electrodes. In future work, an XPS depth profiling experiment has been arranged, the combination of XPS and ICB can be used to profile the constituents of the electrode as a function of their distance from the surface. This depth profile may be able to determine the thickness of SEI and better identify the reduced materials. In addition, this experiment may provide insight into the proposed shrinking core mechanism for electrochemical reduction we have proposed in Chapter 6.

Bulk material characterisation routes were employed to study the reduction products. GI-XRD identified the presence of small and unorthodox diffraction peaks within the reduced electrodes. However, these peaks could not be matched with any probable crystalline species. It is most likely that these XRD peaks were caused by contamination from exposure of the electrodes with air. By determining that a bulk characterisation method was needed, and that the electrodes contained non-crystalline species, a rigorous analysis was performed with XPDF.

XPDF measurements were performed on electrode materials from post mortem cells. All measurements and preparations were under argon as to avoid air contamination. A detailed ‘fingerprint’ based PDF was built up for the composite electrode material

which contained 60 wt% BIS, 20wt% conductive carbon and 20wt% binder. The PDFs of the reduced electrode material (after PSD) showed reductions in signals from Si-O bonds in BIS. In the reduced electrode material, a clear peak was observed at 2.35 Å, this was assigned to Si-Si bonds. The characterisation of Si-Si bonds by XPDF provides direct evidence that silicon was formed in the electrochemical reduction of silica. To the best of our knowledge this is the first instance of direct characterisation of elemental silicon from the electrochemical reduction of silica. No long-range order in the silicon structures could be identified. The absence of other clear signals in the PDF meant that identification of proposed secondary reduction products ($Li_xSi_yO_z$/LiO_x species) could not be made. Now that the silicon product of reduction has been identified, future studies can focus on the characterisation of the secondary reaction products. Diffraction and scattering studies such as neutron diffraction/scattering, which are sensitive to lighter elements such as lithium, maybe able to identify these elusive species.

7.5 References

[1] B. Guo, J. Shu, Z. Wang, H. Yang, L. Shi, Y. Liu, L. Chen, *Electrochem. commun.* **2008**, *10*, 1876.

[2] A. Lisowska-oleksiak, A. P. Nowak, B. Wicikowska, *RSC Adv.* **2014**, *4*, 40439.

[3] M. T. McDowell, S. W. Lee, W. D. Nix, Y. Cui, *Adv. Mater.* **2013**, *25*, 4966.

[4] W.-S. Chang, C.-M. Park, J.-H. Kim, Y.-U. Kim, G. Jeongc, H.-J. Sohn, *Energy Environ. Sci.* **2012**, *5*, 6895.

[5] T. Tang, P. Chen, W. Luo, D. Luo, Y. Wang, *J. Nucl. Mater.* **2012**, *420*, 31.

[6] G. Lener, A. A. Garcia-blanco, O. Furlong, M. Nazzarro, K. Sapag, D. E. Barraco, E. P. M. Leiva, *Electrochim. Acta* **2018**, *279*, 289.

[7] G. Lener, M. Otero, D. E. Barraco, E. P. M. Leiva, *Electrochim. Acta* **2018**, *259*, 1053.

[8] C. Ban, B. B. Kappes, Q. Xu, C. Engtrakul, V. C. Cristian, A. C. Dillon, Z. Yufeng, *Appl. Phys. Lett.* **2013**, *100*, DOI 10.1063/1.4729743.

[9] K. Zhao, G. A. Tritsaris, M. Pharr, W. L. Wang, O. Okeke, Z. Suo, J. J. Vlassak, E. Kaxiras, *Nano Lett.* **2012**, *12*, 4397.

[10] Y. Zhang, Y. Li, Z. Wang, K. Zhao, *Nano Lett.* **2014**, *14*, 7161.

[11] H. Yamamura, K. Nobuhara, S. Nakanishi, H. Iba, S. Okada, *J. Ceram. Soc. Japan* **2011**, 855.

[12] M. W. Gerring, M. L. Hart, O. V Magdysyuk, S. Michalik, A. Smith, C. C. Tang, N. J. Terrill, M. T. Wharmby, H. Wilhelm, **2017**, 959.

[13] A. K. S. and E. R. Barney, *J. Appl. Crystallogr.* **2011**, *44*, 714.

[14] R. Kostecki, L. J. Hardwick, *Phys. Chem. Chem. Phys.* **2019**, DOI 10.1039/c9cp02430a.

[15] F. L. and J. S. Lannin, *Phys. Rev. Lett.* **1990**, *65*, 1905.

[16] H. Krzton, M. Niewiara, *Phys. Scr.* **1995**.

[17] H. Fujimoto, K. Tokumitsu, A. Mabuchi, N. Chinnasamy, T. Kasuh, *J. Power Sources* **2010**, *195*, 7452.

[18] A. Shellikeri, V. Watson, D. Adams, E. E. Kalu, J. A. Read, T. R. Jow, J. S. Zheng, J. P. Zheng, *J. Electrochem. Soc.* **2017**, *164*, A3914.

[19] B. Key, M. Morcrette, J. Tarascon, C. P. Grey, *J. Am. Chem. Soc.* **2011**, 503.

[20] D. P. Finegan, A. Vamvakeros, L. Cao, C. Tan, T. M. M. Heenan, S. R. Daemi, S. D. M. Jacques, A. M. Beale, M. Di Michiel, K. Smith, D. J. L. Brett, P. R. Shearing, C. Ban, *Nano Lett.* **2019**, *19*, 3811.

[21] J. Li, J. R. Dahn, *J. Electrochem. Soc.* **2007**, *154*, A156.

[22] K. Ogata, E. Salager, C. J. Kerr, A. E. Fraser, C. Ducati, A. J. Morris, S. Hofmann, C. P. Grey, *Nat. Commun.* **2014**, *5*, 3217.

[23] V. L. Chevrier, J. W. Zwanziger, J. R. Dahn, *J. Alloys Compd.* **2010**, *496*, 25.

[24] M. Sina, J. Alvarado, H. Shobukawa, C. Alexander, V. Manichev, L. Feldman, T. Gustafsson, K. J. Stevenson, Y. S. Meng, *Adv. Mater. Interfaces* **2016**, *3*, 1.

[25] S. Zhang, M. He, C. C. Su, Z. Zhang, *Curr. Opin. Chem. Eng.* **2016**, *13*, 24.

[26] E. Radvanyi, E. De Vito, W. Porcher, S. Larbi, **2014**, 1120.

Chapter 8:
Conclusion and Outlook

The work presented in this thesis relates to the use of silicon as an active material for LIBs. The promise of silicon for future generations of LIBs has been discussed in detail, as have the engineering challenges which need to be overcome. The root of the issues which hinder the development of high capacity and stable silicon materials is the 280% volume expansion experienced during lithiation. Although many promising materials with intricate nanostructures have been developed to overcome this challenge their commercial large-scale deployment is hindered due to intricate syntheses and expensive precursors. For these reasons we have chosen to study two promising and scalable processes which utilise inexpensive and abundant silica to produce silicon based active material for LIBs.

The work presented in this thesis represents an important advancement in two research areas of silicon active materials. Firstly, existing literature of the MgTR process was extensively reviewed and key challenges and opportunities identified. Throughout Chapters 2 and 3 contributions have been made culminating in a mechanistic understanding of MgTR process and highlighting the high capacity anodes which can be produced. Secondly the gaps within the literature understanding of silica electrochemical reduction have been identified and addressed. The primary points being: A lack in understanding of the evolution of the reduction during the first cycle, for which a detailed study and mechanistic understanding has been proposed. Secondly a lack of consensus on the nature of the reduction products, for which we present decisive support for the formation of elemental silicon as the key reduction product.

The first of these processes is the MgTR process where silica is reduced to produce porous silicon morphologies, previously it has been shown that porous morphologies are more robust to the volume changes inherent with silicon active materials. The use of MgTR is touted for its ability to maintain silica structures throughout the reduction process and therefore create porous silicon analogues from silica precursors. It was known form literature however that the MgTR did change the pore properties of the silicon analogues even if particle shapes were maintained. Within chapter 3 we

propose a reduction reaction mechanism which is responsible for the change in silicon pore properties upon MgTR.

The mechanism we proposed relates the mesopore properties of MgTR silicon analogues to the nature and interconnectivity of the silicon nanocrystallites formed. We showed that the maximum reduction temperature drives an increase of nanocrystallite sizes via sintering at higher temperature. As nanocrystallites grow larger the respective pore space between them also increases, therefore as nanocrystallite size increased the mesopore size also increased. The evolution of the nanocrystallites occurs within the silica templating structure, in this case within the secondary particle structure of BIS, this spherical structure was maintained below reduction temperatures of 850 ^{o}C.

The proposed mechanism was further verified when applying to four separate silica precursors. For each of these the trend of crystallite size dependence on reduction temperature and hence mesopore size distribution proceeded exactly according to the proposed mechanism. The reduction of non-porous quartz to produce silicon nanocrystallites and hence a mesoporous structure provided robust support to the proposed theory.

Thorough characterisation of MgTR reactants and products is often lacking within the literature. To propose this mechanism we thoroughly characterised samples, before and at different stages after MgTR. For the first time USAXS was used to characterise silicon produced via MgTR and was crucial in understanding the evolution of particle structure throughout reduction.

Within this work we have presented a parametric understanding of the MgTR parameters with a full characterisation of reactant and product properties. With this we have proposed a novel and robust mechanistic understanding of the mesoporous properties of silicon reduced by MgTR. This understanding should be used in the future when any MgTR is performed. In particular, these findings can be applied to the synthesis of tailored mesoporous silicon with hieratical control on particle structure. Based on the promising results presented in this thesis it is believe this will significantly advance the use of porous silicon as a LIB anode material.

The anode performance of porous silicon produced from BIS was found to achieve the highest capacity and most stable cycle life of all silica reduced in these works. This is attributed to the hierarchical structure of the samples. For silicon with high

purities (>50 wt%) it has been shown that a mesoporous structure is needed to achieve stable cycle life, preventing complete capacity collapse. Conversely for samples with lower purity, samples reduced at lower temperatures, lower but very stable capacities where observed with 80% capacity retention over 100 cycles. Although higher capacities can be achieved by high purity porous silicon significant work is needed to increase the cycle stability further.

The scale up of MgTR is crucial for the future development of this technique in any industrial application. The self-heating of MgTR is well known and hinders the production of silicon in large batch sizes. The use of NaCl as a thermal moderator has been employed in many literature studies. This work has shown that NaCl is crucial for scaling up the batch size during the MgTR of BIS. Preliminary investigations into the amount of NaCl needed in the reactor suggest a mass ratio of >2:1 (NaCl:reactant) is needed to prevent self-heating from modifying the silicon product. The effect of reduction temperature was also studied in conjunction with NaCl present. The same increase in crystallite size and hence pore size distribution was observed when reduction temperature is increased. A promising finding was that the introduction of NaCl increased the purity of MgTR silicon relative to when no NaCl is present. This effect is thought to be related to the enhanced mixing during reactant preparation. The increased purity caused by NaCl addition allowed for a 51 wt% silicon sample to be produced at 550 ^{o}C. The anode performance of this silicon was excellent achieving 1300 mAh/g with 19% capacity fade over 100 cycles. The stable cyclability and high capacity of this material make for a promising prospect for future investigation. If future work is to focus on the low purity but promising silicon produced at lower reduction temperatures, then this exploration would have the double benefit of lower energy input.

The second process explored within these works was the electrochemical reduction of silica by lithium. It has recently been shown that silica can react with lithium reversibly and such provide reversible capacity for a LIB. The basis behind using silica as an active material was that silica can be reduced to form silicon and some unknown species, the silicon formed can therefore reversibly react with lithium via the well understood mechanisms. A number of studies showed various silica precursors can give a range of reversible capacity and have been reviewed accordingly. Throughout the literature however almost no information exists on the first cycle irreversible processes where silica is reduced. Likewise, the chemical nature of the reduced products shows little consistency between studies and the only evidence for

silicon formation is the indirect evidence of differential capacity profiles. We therefore set out to explore the electrochemical reduction process in further detail and to characterise the reduction products.

The electrochemical reduction reaction progresses when a silica electrode was held at 2 mV in a lithium half-cell. It was previously shown by le Lepoivre et al[2] that when holding the cell at 2 mV in a potentiostatic discharge the capacity increased with longer discharge times. Developing this reduction method further we show that by applying 2 mV in a stepwise PSD and cycling the electrode in-between, it is possible to infer the extent of the electrochemical reduction reaction. By first applying this S-PSD to Stöber silica we show the new S-PSD can be used to track the extent of reduction reaction. The capacities achieved by Stöber silica electrodes are equivalent to results previously reported in the literature. We go on to explore the application of this method to two BIS samples, one pure silica the and the other with the same silica structure but with a carbon coating layer. BIS initially showed great promise as an anode material, achieving capacities of 600 mAh/g with 400 h PSD. The ability to carbon coat BIS was also shown to be advantageous by achieving higher capacity in a quicker time and having faster rate capabilities when compared with pure BIS.

The electrochemical reduction of silica represents an additional processing step required for these electrodes before they can be incorporated into full cells. We therefore highlight the need for efficient use of time for the electrochemical reduction step and explored methods for reducing reduction time.

With further investigation it was shown that the electrochemical reduction of silica will progress spontaneously in a lithium-silica half-cell. As such short circuiting such half cells should also lead to electrochemical reduction and an increase in reversible capacity of the electrodes. Initial tests were performed to study this theory and it was shown that revisable capacity was introduced into silica electrodes after short circuiting. Like the PSD method it was also shown that longer short-circuiting times lead to higher capacities. Without the need for potentiostats the short circuiting method could be performed in temperature controlled environments, as such it was shown that the reduction reaction progressed significantly faster at 50 ^{o}C.

The insight into increased reduction kinetics at 50 ^{o}C ultimately lead to the introduction of constant load discharge (CLD), which is an equivalent of short circuiting but with the use of potentiostats. With this method we show it is possible to reduce silica electrodes with just 13 hours of CLD and achieve capacities of 500

mAh/g. This example represents a significant decrease in reaction time compared with previously reported studies where hundreds of hours are required for the electrochemical reduction.[2] This result highlights the novel contributions of these findings in the ability to track, measure and control the extent of reduction reaction and ultimately to reduce the time needed for this additional processing step.

The ability to directly carbonise BIS post synthesis has been highlighted, and the associated decrease in reduction times to achieve high capacity and the improved rate capabilities have been shown. We developed this further by impregnating BIS with other carbon precursors of glucose and mesophase pitch. We successfully increased the carbon loading in BIS to 9.7 wt% and as hypothesised this decreased the reduction time required to reach high capacity. Impregnation and carbonisation with that method provides another tool for reducing the electrochemical reduction time of silica anodes.

To better understand the electrochemical reduction a number of investigations were performed to track the extent of the reduction between battery cycles and to quantify the extent of reduction in real time. This was achieved by monitoring the current flow between the silica and lithium electrodes. This current profile displayed identical profiles regardless of the temperature at which reduction was performed indicating the mechanism of reduction was independent of temperature. The features of the current profile were broken down into five distinct regions denoted (i-v). With these five regions we postulate a shrinking core like mechanism; where the electrochemical reduction proceeds initially at surface sites with good electrical conduction pathways and as more material is reduced an increasing network of electrical conduction forms increasing the rate of reduction, beyond this as the reaction front moves away from the surface of these silica particles the rate of reduction decreases as the mass transport of lithium-ions to the reaction front becomes a limiting factor. The new mechanistic understanding was further supported by EIS measurements and an analysis of voltage experienced across the cell during a CLD. This robust mechanism may be applied in future work to tailor silica materials specifically to reduce reduction time. This could be achieved by more uniform carbon coating networks on the silica materials so good electronic conduction pathways are present at the start of the reduction.

In the final chapter we attempted to characterise the reduction species produced form electrochemical reduction of silica with lithium. As we highlight with our literature review there is little consensus on the chemical nature of reduced species and exists

some conflicting reports. We raise the nature of characterising LIB materials via post mortem methods and the requirement of specialist testing equipment and importance of minimising air contamination. In our initial XRD post mortem studies we were not able to decisively discern any crystalline species present after reduction, however the exposure of these samples to air did leave this experiment inconclusive. This inconclusive experiment highlighted the difficulty in characterising the electrochemical reduction products of silica. We therefore set out on an expansive study using XPDF using equipment where air contamination could be eliminated, this study was aimed to provide information on both the crystalline and amorphous nature of the reduction products. In Chapter 7 we show how the electrochemical reduction significantly changed the presence of short range order within the reduced material. We conclude that the quantity of Si-O bonds (from silica) is reduced during reduction. In addition, we show the presence of Si-Si bonds within the reduced electrode, to the best of our knowledge this is the first characterisation of elemental silicon within reduced silica electrodes. The identification of Si-Si bonds conclusively proves that silicon is a product of the electrochemical reduction and responsible for the reversible capacity in these electrodes. Unfortunately, we were unable to characterise any of the postulated lithium silicates or lithium oxides within the reduced structure. However due to the low scattering experienced between X-rays and light elements such as lithium this result is not unsurprising. We propose a future experiment using neutron total scattering to further probe the PDF's of these samples and hopefully identify the other by-products of the reduction.

The work presented in this thesis provides a significant advancement to the literature in the understanding of two reduction processes used to create high capacity silicon anodes. In both cases a detailed parametric study has been performed to expand the knowledge of how key reaction parameters effect the reduction product. This detailed study has lead, in both cases, to a high level, mechanistic understanding of these relevant and promising chemical processes. Both of which have showed great promise in providing high capacity stable silicon electrodes. With the understanding of these processes future work can be purposefully directed to the optimisation of these reactions.

We envisage future work on these two processes should focus on scale-up. For MgTR we have shown how NaCl can be successfully used to scale up the reduction process. Further work required larger furnaces, however, we recommend the exploration of lower temperature reduction (550 ^{o}C) not only does this reduce the

energy input of the synthesis route but these lower purity samples have shown promising capacities and cyclability. For the electrochemical reduction of silica, we have reduced the electrochemical reduction time to 13 hours. By applying the findings from our mechanism and increasing the initial electrical conductivity of the silica, potentially by better carbon coating or the use of conductive binders. Additionally, reducing the size of the BIS silica particles should reduce the lithium diffusion lengths for total particle reduction. The work on the electrochemical reduction used typical electrolytes from LIB's ($LiPF_6$ in carbonates), if cheaper water-based electrolytes can be employed the commercial viability and the environmental footprint of this method would be significantly more promising.

The hope for this work is that a foundation has been provided for continued exploration of MgTR and electrochemical reduction of silica, as there are many applications and opportunities awaiting investigation.

Supporting Information

1.1 Chapter 1

Table S1. Key data abstracted from literature sources to quantify: 1 silica properties, 2 Magnesiothermic reduction conditions, 3 Silicon production properties, 4 Anode Performance properties and testing criteria, 5 key electrode parameters.

Phyto derived silica (excluding diatoms)

1.Source Silica Surface area m^2/g Porosity Pore volume	2.Reduction Methods Molar ratio Mg:SiO_2 Temperature Duration Ramp rate		3.Product Silicon BET Surface Area Porosity Pore volume		4.Performance Initial Stable Capacity Charging Rate Number of cycles %capacity retn	5.Testing Variables % active material mass in electrode Electrolyte additives Binder
Rice Husks [1] 289 m^2/g Mesoporous 0.45 cm^3/g	(a) 2.5:1 650°C 2hours 5°C/min	(b) 2.5:1 650°C 2hours 40°C/min	(a) 245 m^2/g Mesoporosity 0.74 cm^3/g	(b) 54 m^2/g Few Mesop 0.11 cm^3/g	(a) 1750 mAh/g[a] 2.1 A/g 300 cycles 86%	65% active mass 1%VC PVDF
Rice Husks[2] 221 m^2/g 0.49 cm^3/g	(a) 2.5:1 650°C 7 hours 1°C/min	(b) 2.5:1 650°C 7 hours 5°C/min	(a) 267 m^2/g Mesoporosity 1.1 cm^3/g [b]	(b) 7.5 m^2/g 0.11 cm^3/g	(a) 2294 mAh/g[c] 0.2 A/g 100 57%	60% active mass 2%VC additive Alginate
Rice Husks [3] 213 m^2/g Mesoporous 2-10nm Mesoporous 0.29 cm^3/g	2.5:1 650°C 7 hours		150 m^2/g Mesoporous Mesoporous vol 0.60 cm^3/g		≈1600 mAh/g 1.0 A/g 100 cycles 76%	60% active mass 'Contained' VC Alginate

Rice Husks [4] [d] 234 m^2/g Mesoporous 1.4-4.3nm 0.425 cm^3/g	2.5:1 500°C 7 hours 5°C/min	42 m^2/g Meso-Macroporous 0.31cm^3/g	1400 mAh/g 0.08 A/g 50 cycles 65%	60% active material 1.5% VC Alginate
Rice Husks [5] 286 m^2/g Mesopores 5nm	2:1 850°C 3 hours	47 m^2/g 10-50nm pores	1600mAh/g 0.2A/g 100%*	60% active material 5w%FEC PAA binder *Testing with Carbon Coating only Very low mass loading reported 72% cap retention for 100 cycles with more conventkional loading.
Reed[6] 101 m^2/g Mesoporous 0.22 cm^3/g	2.5:1 650°C 6hours 5°C/min	224 m^2/g Mesoporous 0.70cm^3/g	2435 mAh/g 2.1 A/g 200 cycles 45%	70%active mass Carbon coating PVDF
Reed Horsetail[7] 233 m^2/g 0.35 cm^3/g 6nm APD	2:1 600°C 1 hour 1:1 w-ratio reactants:NaCl	117 m^2/g 0.24 cm^3/g 9nm APD	N/a	N/a
Bamboo Silk[7] 0.47 m^2/g 0.35 cm^3/g 19nm APD	2:1 600°C 1 hour 1:1 w-ratio reactants:NaCl	356m^2/g 0.56 cm^3/g 8nm APD	N/a	N/a

[a]5°C/min sample [b]typo present in paper 1.1 m^3/g unlikely [c]1°C/min silicon APD =Average Pore Diameter [d] leached and unleached comparison

Micro and mesoporous silicon

Source Silica Surface area m^2/g Porosity Pore volume	Reduction Methods Molar ratio Mg:SiO_2 Temperature Duration Ramp rate		Product Silicon BET Surface Area Porosity Pore volume	Performance Initial Stable Capacity Charging Rate Number of cycles %capacity retn	Testing Variables % active material mass in electrode Electrolyte additives Binder
Silicon Particles[8] <74um nonporous	Step 1 2.1:1 500°C 10 hour	Step 2 Air atm 650°C 10hours	86.6 m^2/g Mesoporous 4nm pores	3200 mAh/g 0.36 A/g 85cycles 64%	60% active mass Alginate SiO_2 passivated layer
Aerogel [9]	5:1 500°C 10 hour	Air atm 650°C 5 hours	239 m^2/g Mesoporous 4nm pores	1782 mAh/g 0.36 A/g 100 cycles 82%	60% active material 5% FEC Alginate SiO_2 passivated layer
Sand [9]	5:1 500°C 10 hour	Air atm 650°C 5 hours	23.9 m^2/g Mesoporous ≈30nm APD	≈1782 mAh/g 0.36 A/g 100 cycles 82%	60% active material 5% FEC Alginate SiO_2 passivated layer
Diatom[9]	5:1 500°C 10 hour	Air atm 650°C 5 hours	74 m^2/g Mesoporous ≈30 APD	≈1400 mAh/g 0.36 A/g 100 cycles 71%	60% active material 5% FEC Alginate SiO_2 passivated layer

SBA-15[9]	5:1 500°C 10 hour	Air atm 650°C 5 hours	103 m^2/g Mesoporous Majority 4-16nm	≈1300 mAh/g 0.36 A/g 100 cycles 77%	60% active material 5% FEC Alginate SiO_2 passivated layer
SBA-15[10]	2.5:1 650 °C 7 hours 5°C/min		74 m^2/g Mesoporous 28nm APD 0.56cm^3/g	2727 mAh/g 4.2 A/g 100 53%	60% active material 1:1 CMC:SBR 2w%VC
SBA-15[10]	2.5:1 650°C 7 hours 5°C/min		74 m^2/g Mesoporous 28nm ave 0.56 cm^3/g	1500 mAh/g 4.2 A/g 100 cycles 94.4%	60% active material 1:1 CMC:SBR 2w%VC CVD carbon coating
SBA-15[11]	3.5:1 500°C[e]		162 m^2/g Mesoporous 2-10nm	2918 mAh/g 0.05A/g 50 cycles 34%	40% active material PVDF Ni foam cc
Nanorods [12] 666 m^2/g 3.4nm diam pores 1.49 cm^3/g	2:1 650°C 5 hours 10°C/min		128 m^2/g Mesoporous nanoparticles 3.5nm diam pores + distribution around 42nm 0.66 cm^3/g	≈2600 mAh/g 0.4 A/g 80 cycles 40%	80% active material Polyimide binder
Nanorods[13]	2.5:1 670°C 5 hours		255 m^2/g Mesoporous Nanorods (~50nm dia) 12nm ave diam 0.64 cm3/g	1400 mAh/g 0.2A/g 170 cycles 74%	70%active material Alginate

Nanowires[14]	3.125:1 600°C 5 hours	157 m^2/g Mesoporous cross-linked Nanowires 40-65nm diam 0.33cm^3/g	1300 mAh/g 2.5 A/g 1000 cycles 49%	80% active mass CMC
Nanowires [15] 10-20nm diameter Length several ~20µm	2:1 500°C 6 hours 10°C/min	3-5nm particles accumulated alone original nanowire shape	1200 mAh/g 0.045 A/g 55 cycles 54%	80% active mass PVDF
Microspheres[16]	2.5:1 650°C 2 hours	200 m^2/g Mesoporous <6nm 0.25cm^3/g	≈3000 mAh/g 0.1 A/g 100 cycles ≈100%	70%active material PVDF
Purified Sand [17] Nonporous >5um-50nm particles	2.25:1 700°C 6 hours 5°C/min 5:1 w-ratio reactants:NaCl	323 m^2/g Mesoporous	≈1700mAh 1.8 A/g 1000 cycles 70%	70% Active material PAA Carbon coating 2% VC
Stöber Spheres [18] 400nm diameter	3:1 800°C 12 hours	Porous Silicon Spheres composed submicron nanoparticles	2300 mAh/g 0.1A/g 50 cycles 10%	60%active material PVDF Carbon coating improved performance

Stöber Spheres [19] 200nm 12 m^2/g	1:2.25 700°C 5°C/min 6hours 1:10w SiO_2:NaCl		215 m^2/g Meso and microporous	≈1700mAh/g 1.8 A/g 500 cycles >80%	70% active material Alginate
Diatomite[20]	Step 1 Al powder 900°C 3 hour	Step 2 Mg reduction 700°C 3 hours 5°C/min	Mesoporous	1750 mAh/g 1.8A/g 100 cycles 86%	70% active material (70w%Si 30w%Al) PAA+CMC 10w% FEC
Diatomaceous Earth [21] 6 m^2/g Mainly Microporous	2.5:1 650°C 6 hours 5°C/min		96 m^2/g Mainly Mesoporous	1300mAh/g 0.2mA/cm^2 30 cycles 29%	75% active material Alginate 2% VC
Diatomite [22]	1:1 NaCl 5:1 850°C 14 hours.		Silicon nanoparticles ~100nm	2500 100 mA/g 24 cycles 60%	5v% FEC

Glass bottles [23] **Macroporous silicon**	1:2.10 1:2.25 700°C 5°C/min 6hours	-	1420 mAh/g 1.8A/g 400 cycles 72%	70% active material PAA 1:1, v/v FEC:DMC
Source Silica Surface area m^2/g	Reduction Methods Molar ratio $Mg:SiO_2$	Product Silicon BET Surface Area	Performance Initial Stable Capacity	Testing Variables % active material mass in electrode
Porosity Pore volume	Temperature Duration Ramp rate	Porosity Pore volume	Charging Rate Number of cycles %capacity retn	Electrolyte additives Binder
Mesoporous Powder [24] 10nm APD	2.5:1 650°C 6 hours 5°C/min	Macroporous Particles Ave 200nm	≈2400 mAh/g 0.72 A/g 100 cycles 69%	80% active material 2% VC PVDF
Silica spheres 200nm average diameter [25]	1.9:1 700°C 5 hours 5°C/min	Macroporous ~200nm	1162 mAh/g 2.0 A/g 800 cycles 91%	70% active material (of which 13.5%=Carbon coating via CVD) CMC 3%VC

≈denotes numerical data not stated, approximated from graphical data inferred from report

Notable non-electrochemistry papers

Source Silica Surface area m^2/g Porosity Pore volume	Reduction Methods Molar ratio Mg:SiO_2 Temperature Duration Ramp rate		Product Silicon BET Surface Area Porosity Pore volume	
Diatom frustules[26] 1.65 m^2/g	2.5:1 650°C 2.5hour 3 °C/min		541 m^2/g 0.7 cm^3/g Significant micropores	
Diatomaceous earth[27]	(a) 2.25:1 650°C 2.5 hour	(b)2.25:1 650°C 2.5 hour 1:10 wt-ratio reactants:NaCl	(a) 5.2 m^2/g 0.01 cm^3/g	(b) 295 m^2/g 1.2 cm^3/g 22nm APD
SBA-15[28] 542 m^2/g 1.13cm^3/g 8.34nm APD	1.5:1 670°C 1.5hour 3 °C/min		Shape Retained 605m^2/g 1.54cm^3/g 10.17nm APD	
SBA-16[28] 679 m^2/g 0.65cm^3/g 5.63nm APD	1.5:1 670°C 1.5hour 3 °C/min		Ordered porosity destroyed 230m^2/g 0.63cm^3/g 8.25nm APD	

1.2 Chapter 2

Scherrer Equation Derivation

Braggs law is given as:

$$\lambda = 2dsin\theta$$

For Scherrer analysis if both sides are multiplied by the integer (n) such that (nd= t) where (t) is the thickness of the crystal the following equation is formed.

$$n\lambda = 2ndsin\theta = 2tsin\theta$$

This form can be considered as the nth order reflection from a set of planes with interplanar distances of (t). nλ can therefore be considered a constant for the size of the crystal. Differentiating both sides of the equation leads to:

$$0 = 2\Delta tsin\theta + 2tcos\Delta\theta$$

The value of $\Delta\theta$ can be positive or negative, but it is the absolute value that must be taken.

$$t = \frac{\Delta tsin\theta}{cos\Delta\theta}$$

The smallest increment in t which is possible is d (the space between a two crystal planes). Using $\Delta t = d$ and substituting $\frac{\lambda}{2} = dsin\theta$ from Braggs law gives:

$$t = \frac{\lambda}{2cos\Delta\theta}$$

This absolute value represents the half-width at half maximum (FWHM/2). So to determine a measurable peak broadening $2\Delta\theta$ is used as it is obtainable from the full width at half maximum (FWHM) and is denoted B:

$$t = \frac{\lambda}{Bcos\theta}$$

This is the final form of the Scherrer equation. A shape factor can be added for more sophisticated analysis. In this work shape factor of 0.9 is used as shown in Equation 2.2. Instrument broadening must be considered as discussed.

Range of relevance Scherrer analysis

To explain the range of relevance of the Scherrer analysis it is best to consider a crystal with thickness (t) measured in a direction perpendicular to the set of reflecting planes (Figure S2.1 (top)). With regards to the Bragg angle θ as a variable, θ_B is the exact angle which satisfies Braggs law. The rays depicted, A, D …. M make exactly this angle. Ray D' is reflected off the first plane below the surface and is therefore exactly one wavelength out of phase with A'. The M' scattered ray is reflected by the mth plane below the surface and is m wavelengths out of phase with A'. The diffracted beam of maximum intensity is therefore a combination of A',D' …M' when the diffraction angle is $2\theta_B$.

If we consider incident rays that make Bragg angles only slightly different from θ_B, the destructive interference is not complete. The incident rays B and C are examples of this Figure S2.1 (top). Ray B makes a slightly larger angle $\theta_1$such that ray L' in the mth plane (m+1) wavelengths is out of phase with B'. This means that midway in the crystal there is a plane scattering a ray which is one-half wavelength out of phase with B'. These rays destructively interfere with each other and so do the other rays from similar pairs of planes throughout the crystal. This has a net effect that rays scattered by the top half of the crystal annul those scattered by the bottom half. The intensity of the beam diffracted at angle $2\theta_1$ is therefore zero. This same maxim applies to the angle θ_2 and the incident rays C and N.

It follows that the diffracted intensity at angles near $2\theta_B$ but not greater than $2\theta_1$or less than $2\theta_2$ will not be zero. The curve of diffracted intensity vs 2θ will have the shape in Figure S2.1(bottom a) in contrast to the ideal diffracted curve Figure S2.1(bottom b).

The width of the diffraction curve increases as the thickness of the crystal decreases. For a crystal with 1 mm diameter the breadth B then B ~2×10^{-7} radian and be to small to be observed. Such a crystal would contain 10^7 lattice planes which would satisfy Braggs law. However, for a crystal only 50 nm it would typically contain 500 planes and the diffraction curve would be relatively broad (4×10^{-3} radian). The accuracy of measuring Broadening (B) of this manner is the limiting factor for determining crystallite size via Scherrer analysis. With more precise detectors the natural broadening (peak broadening minus any instrumental broadening) caused by small crystallites can be more accurately determined.

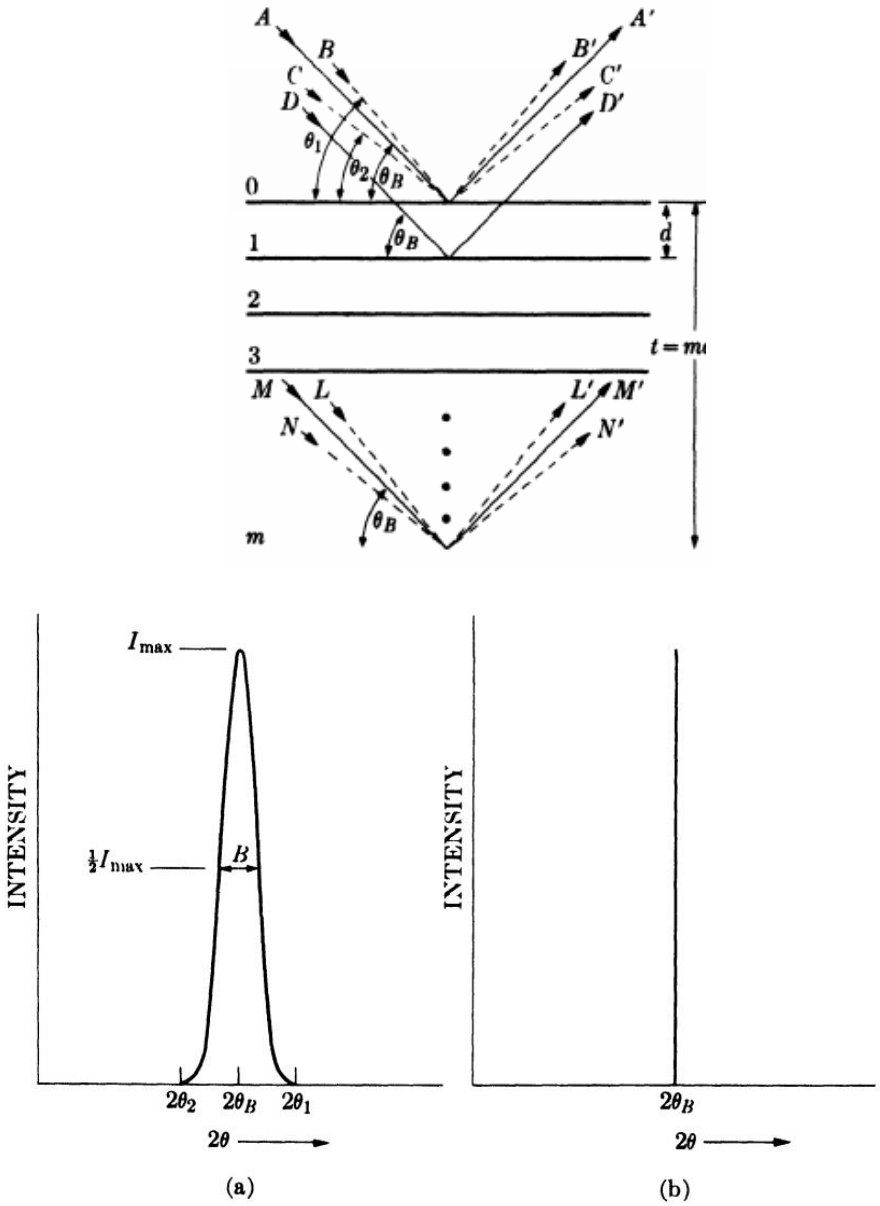

Figure S2.1. Effect of crystallite size on diffraction curves. Taken from[29]

1.3 Chapter 3

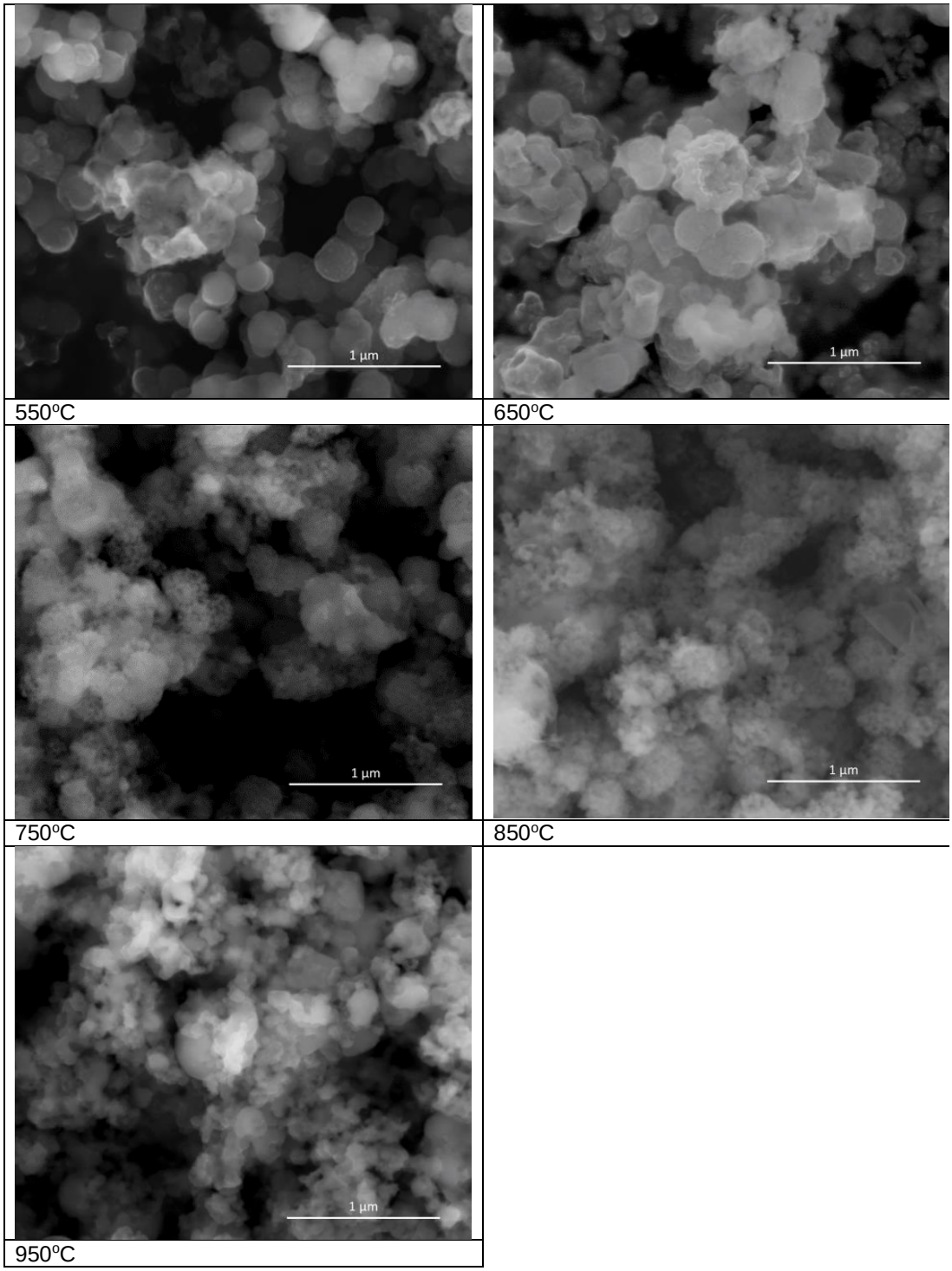

Figure S.3.1. SEM images of BIS reduced at temperatures 550 – 950 ºC.

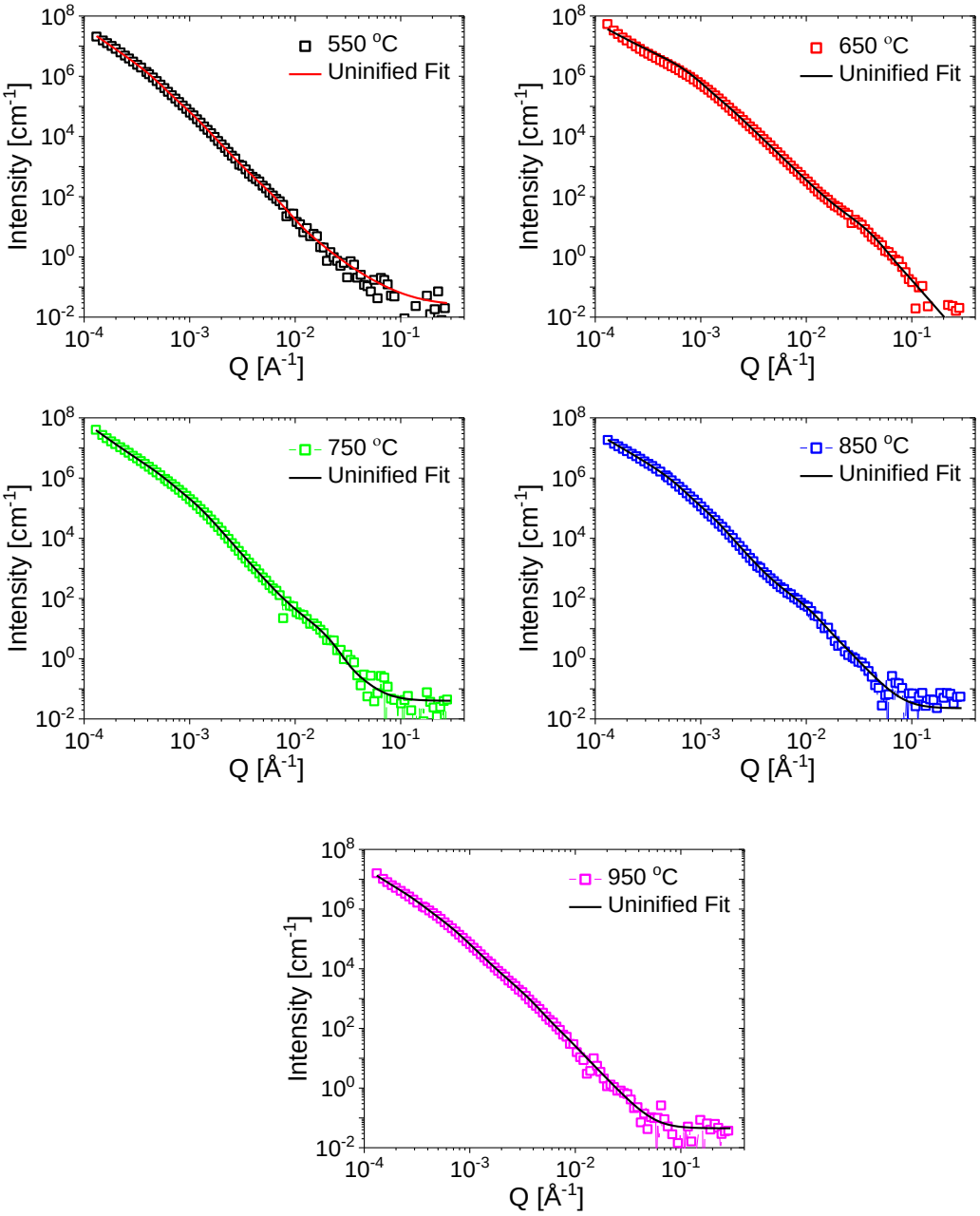

Figure S.3.2. USAXS data of porous silicon reduced at temperatures between 550-950 ºC. Not all data points shown for clarity.

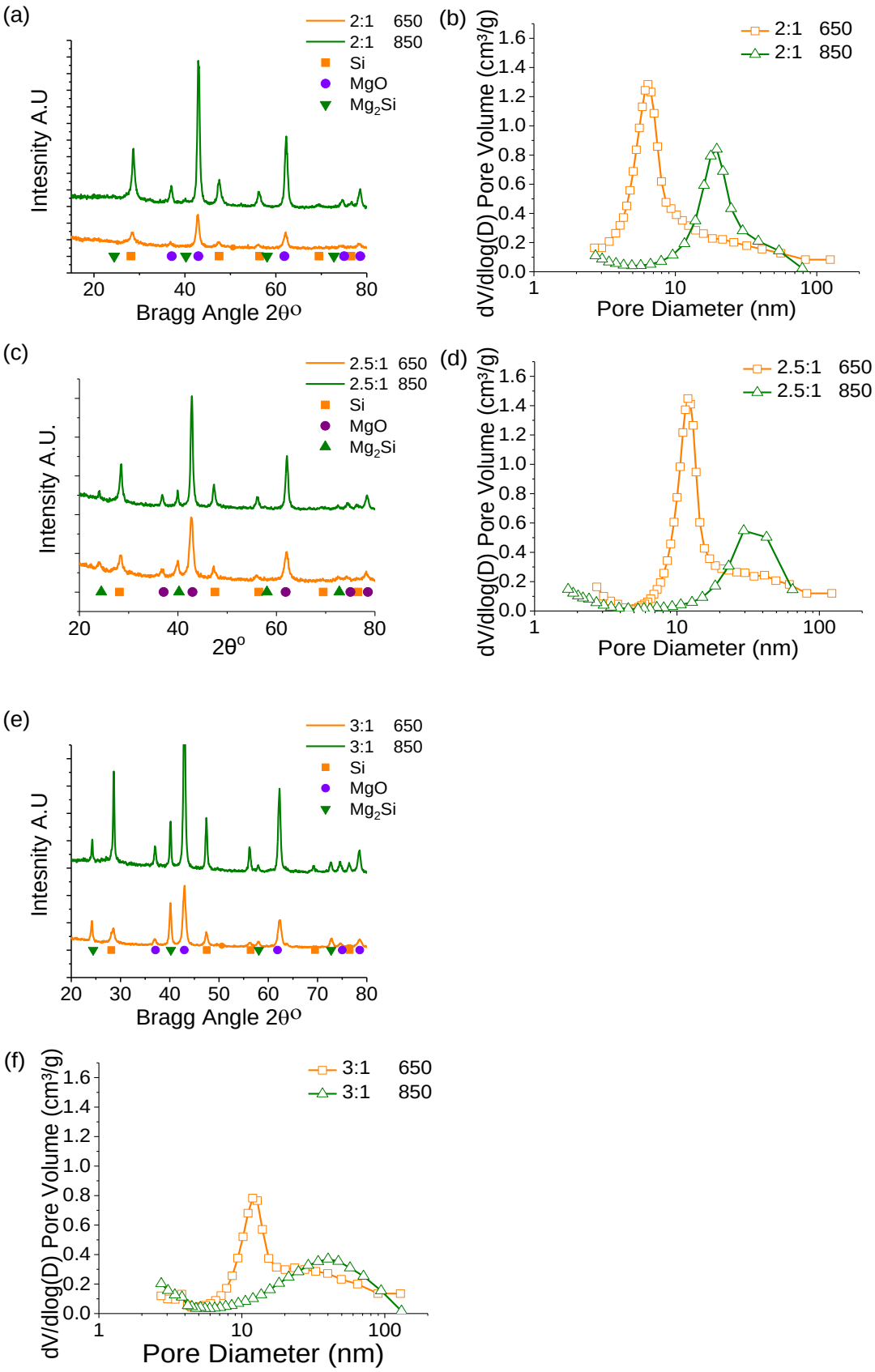

Figure S.3.3 Silicon/silica composites reduced at 650 and 850 ºC with 2:1, 2.5:1 and 3:1 stoichiometric ratios of Mg:SiO_2. (a,c,e) Diffraction patterns of after acid washing. (b,d,f) BJH pore size distributions.

1.4 Chapter 4

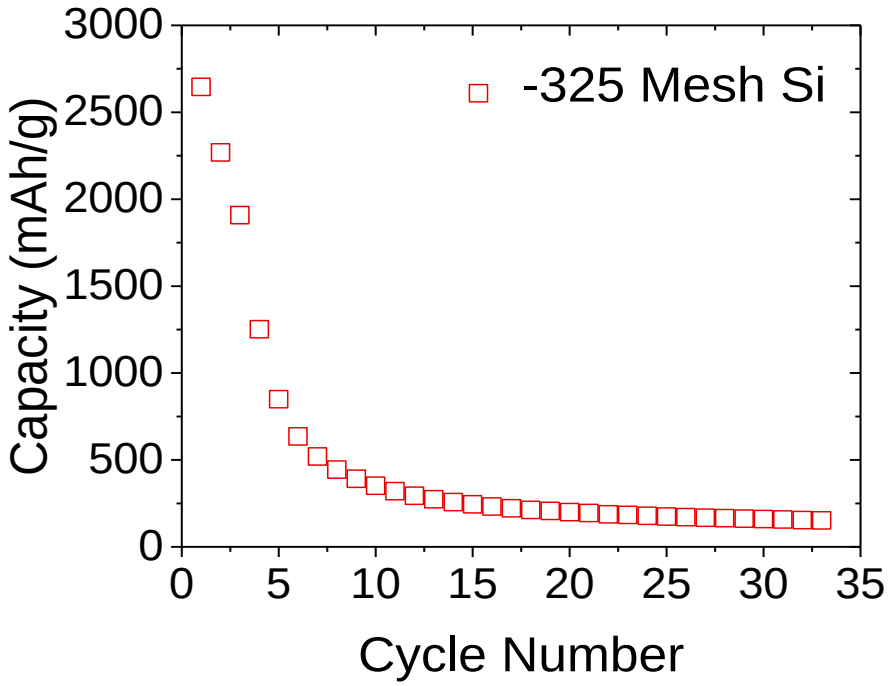

Figure S4.1. Capacity vs cycle life of micron sized silicon particles (-325 mesh)

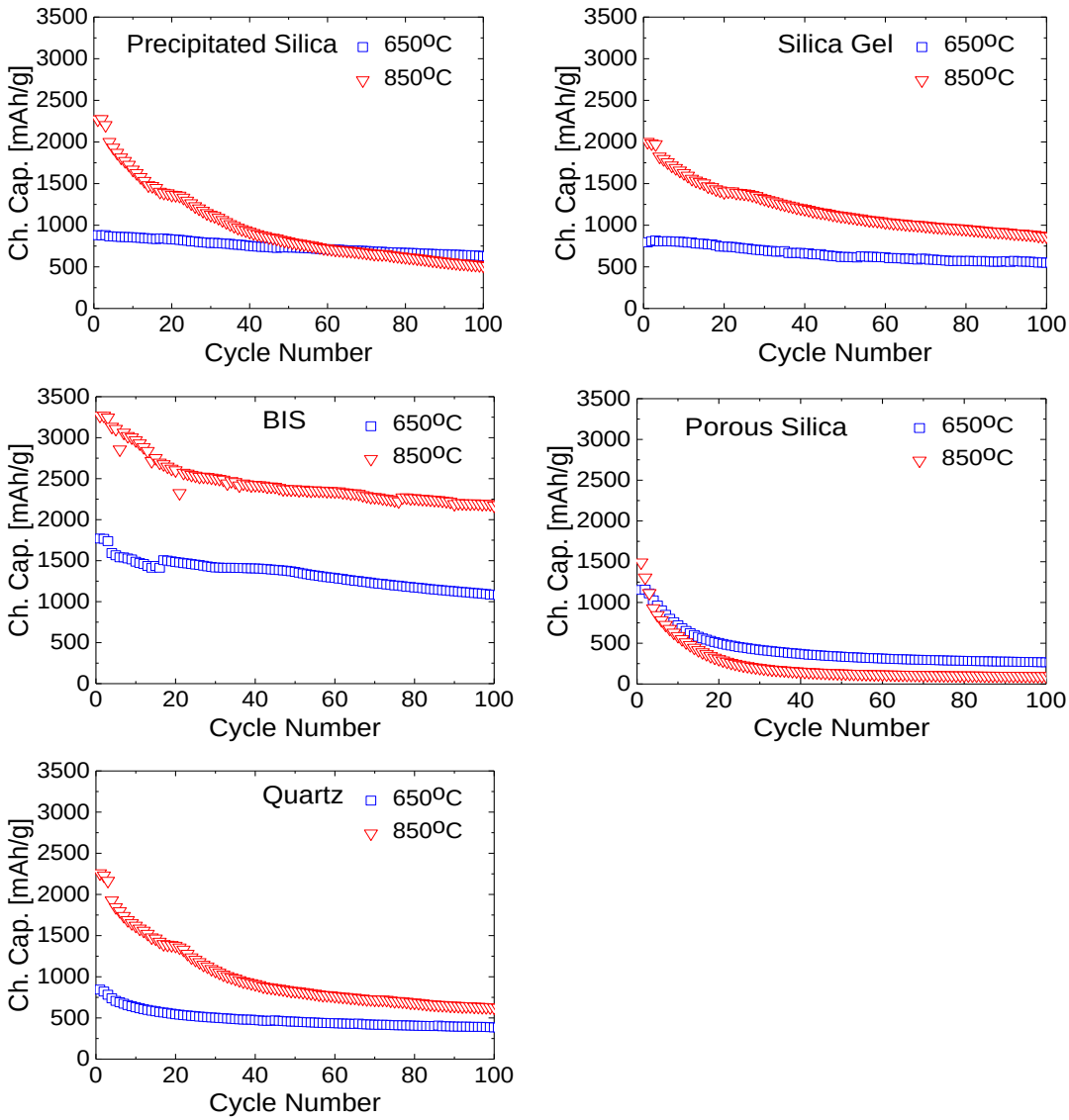

Figure S4.2. Discharge capacity of porous silicon/silica composites reduced at 650 and 850 ºC

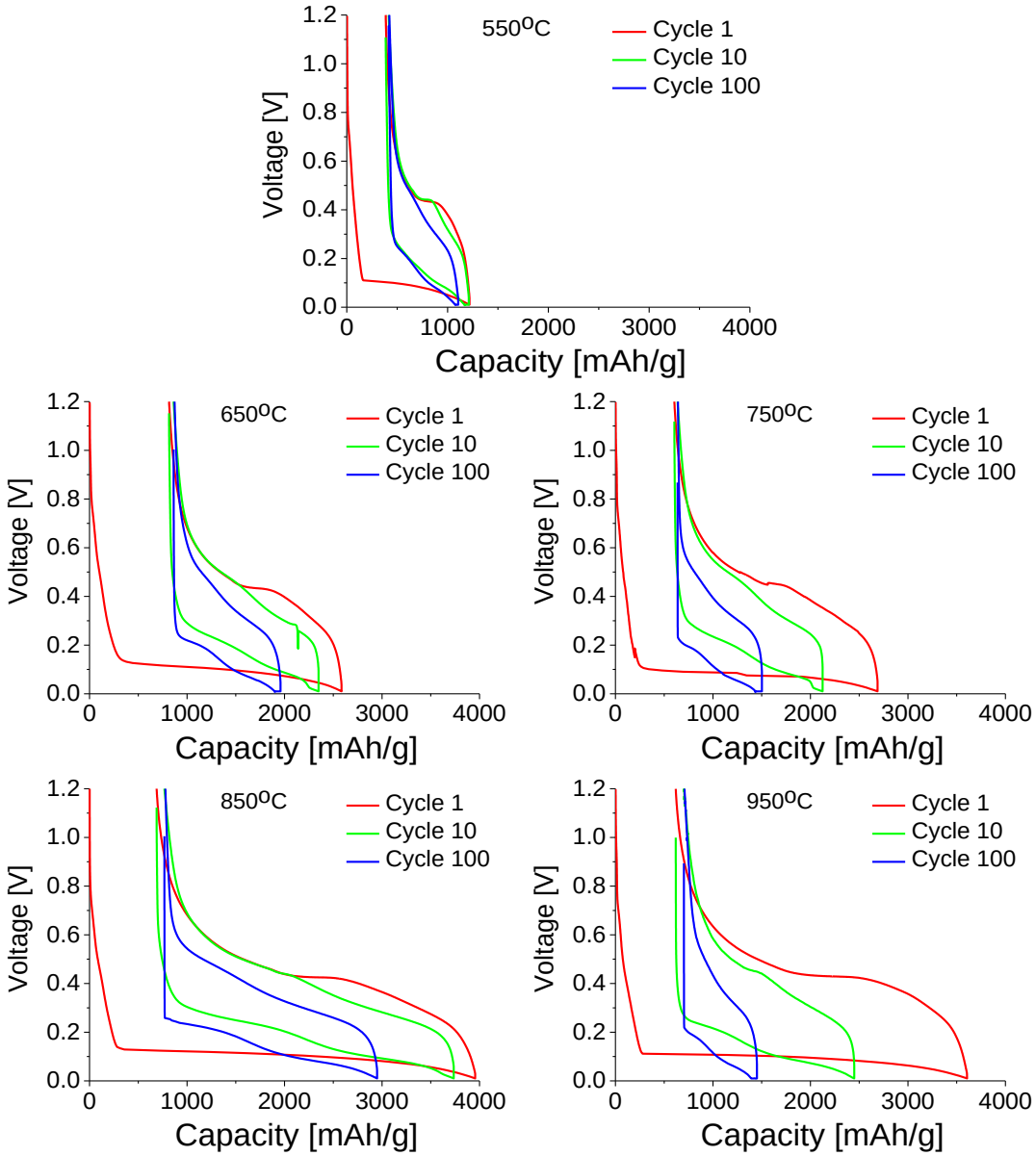

Figure S4.3. Voltage capacity profiles of the 1st, 10th and 100th cycles for silicon reduced from 550-950 ºC

1.5 Chapter 5

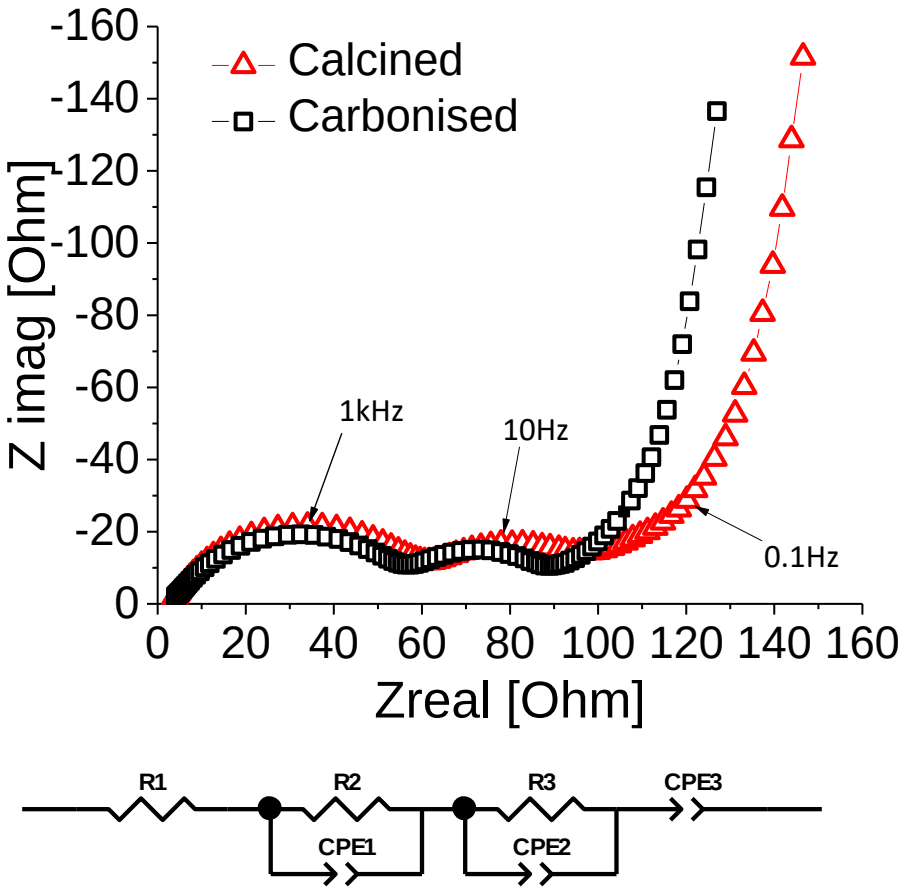

	R_s (Ω)	R_c (Ω)	R_{ct} (Ω)	wt% Carbon
SiO_2-Charged	3	59	50	0
C-SiO_2-Charged	3	54	42	5wt%

Figure S5.1. EIS Nyquist plots and equivalent circuit used for fitting. Table presents results for solution resistance, charge transfer resistance

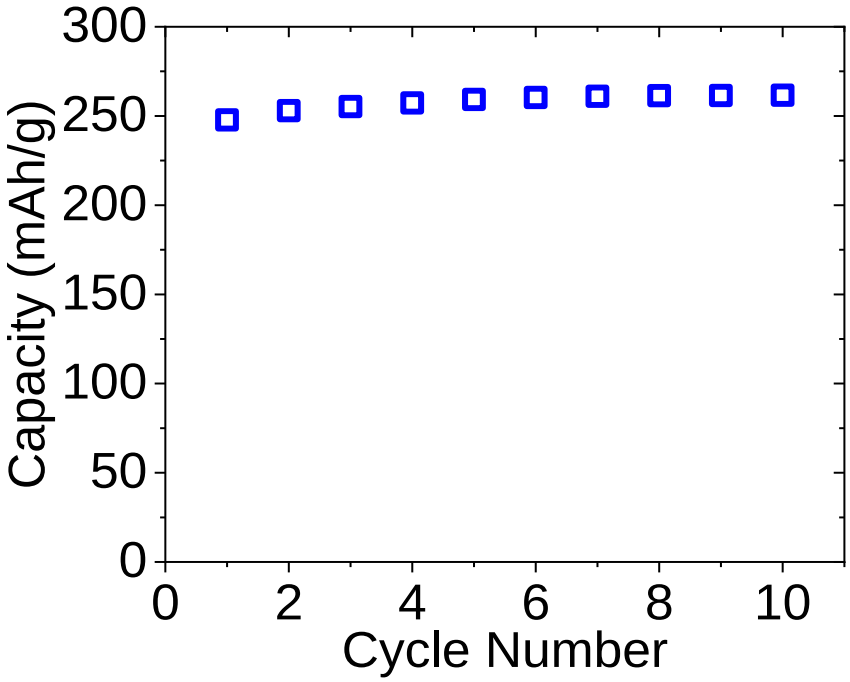

Figure S5.2. Capacity of C-65 used as conductive additive

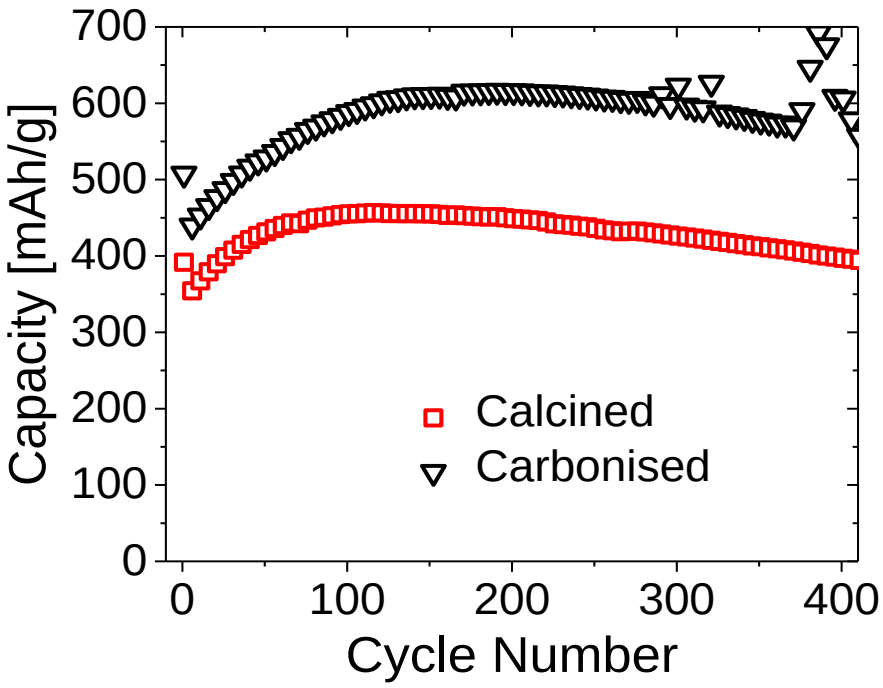

Figure S5.3. Capacity of BIS electrodes over 400 cycles at C/2.

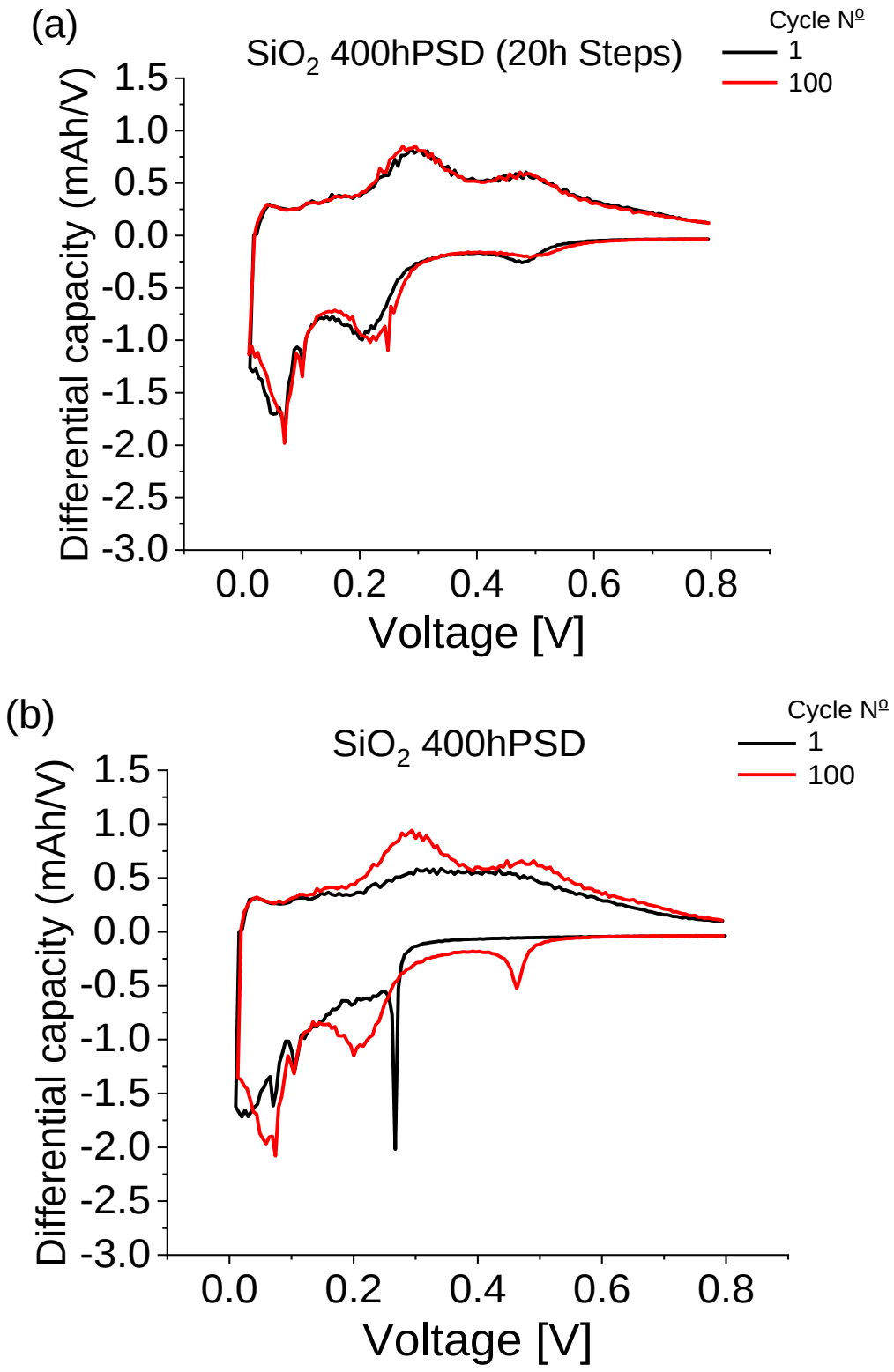

Figure S5.4. Differential capacity plots Calcined BIS, comparison of (a) 400 hour S-PSD (5 galvanostatic cycles every 20 hours) and (b) 400 hours C-PSD.

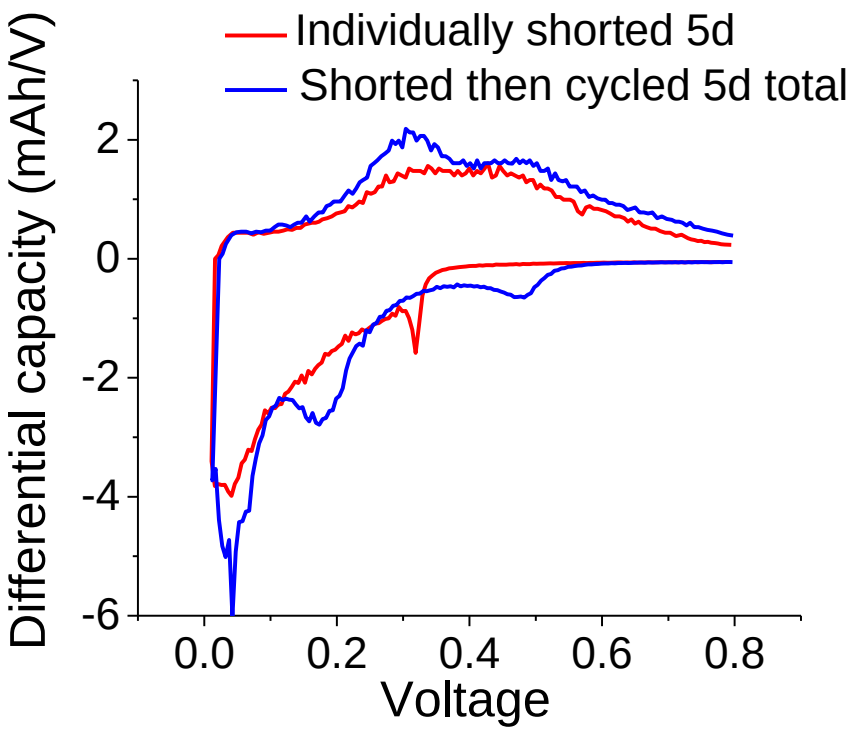

Figure S5.5. Differential capacity plot of cells short circuited at 50 °C, (red) shorted for 5 days then cycled. (blue) shorted 1 day at a time and cycled for 10 cycles at a time.

1.6 Chapter 7

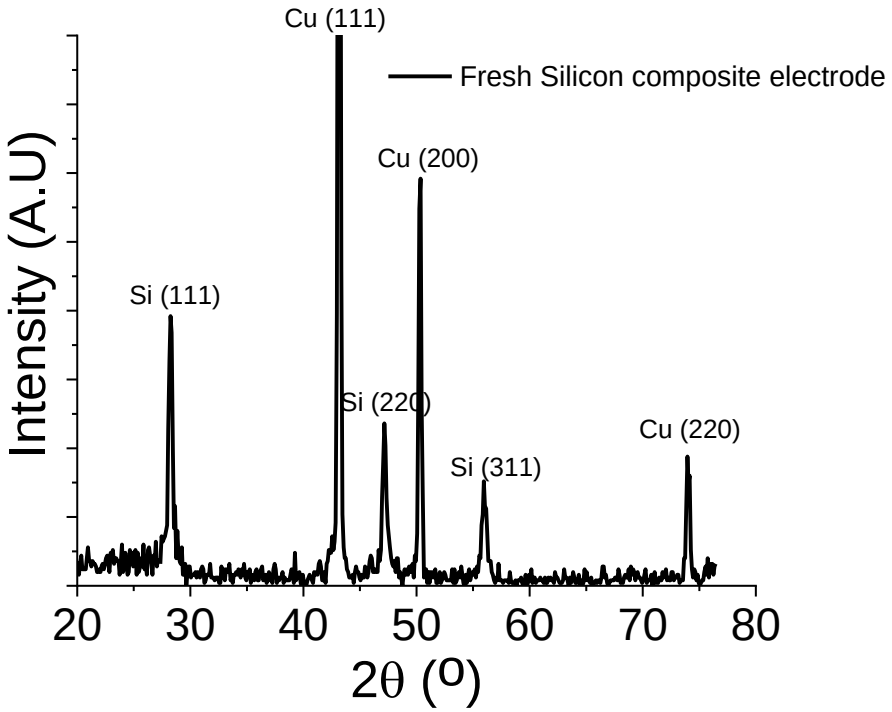

Figure S7.1. Gi-XRD of a crystalline silicon containing electrode pre-cycling.

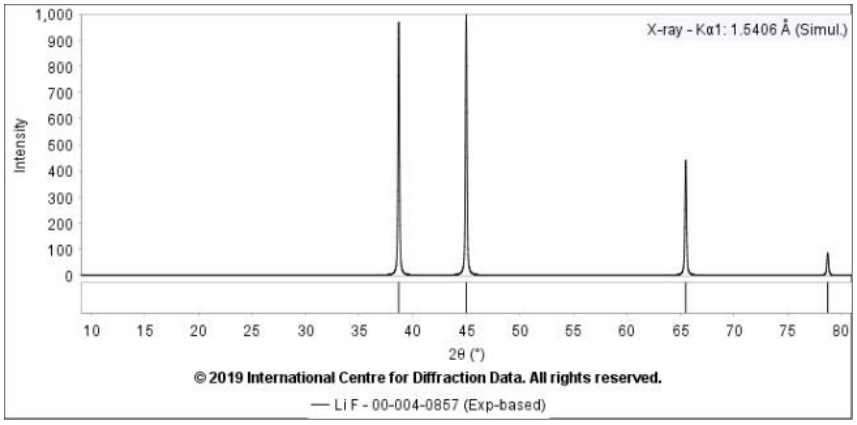
X-ray - Kα1: 1.5406 Å (Simul.)
Intensity
2θ (°)
© 2019 International Centre for Diffraction Data. All rights reserved.
— Li F - 00-004-0857 (Exp-based)

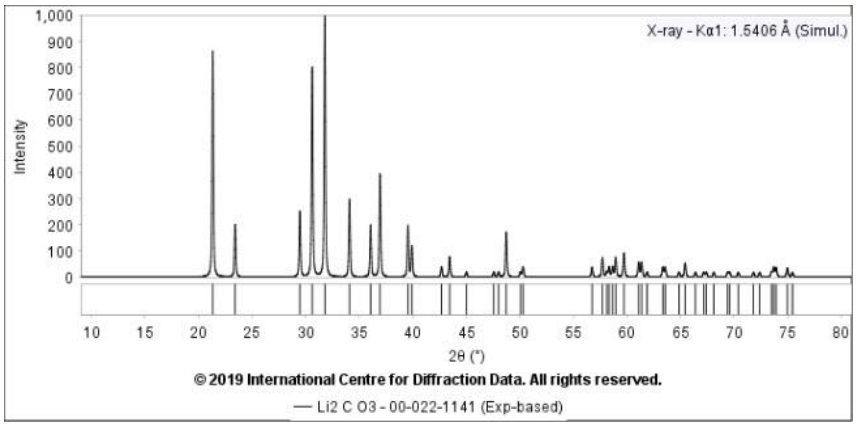
X-ray - Kα1: 1.5406 Å (Simul.)
Intensity
2θ (°)
© 2019 International Centre for Diffraction Data. All rights reserved.
— Li2 C O3 - 00-022-1141 (Exp-based)

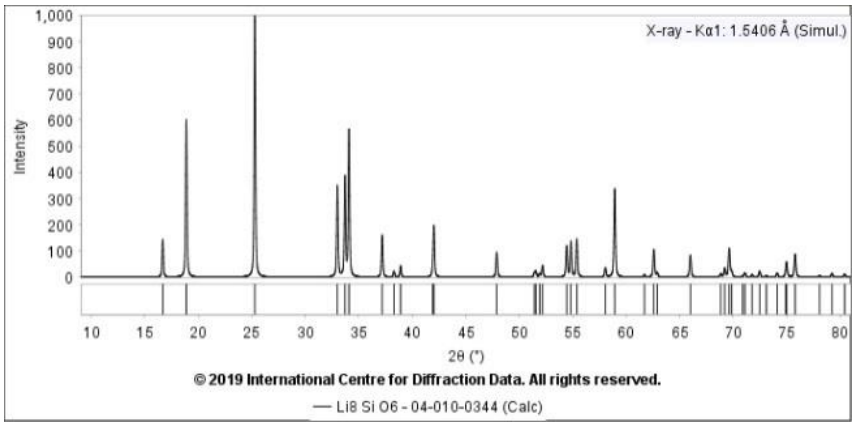
X-ray - Kα1: 1.5406 Å (Simul.)
Intensity
2θ (°)
© 2019 International Centre for Diffraction Data. All rights reserved.
— Li8 Si O6 - 04-010-0344 (Calc)

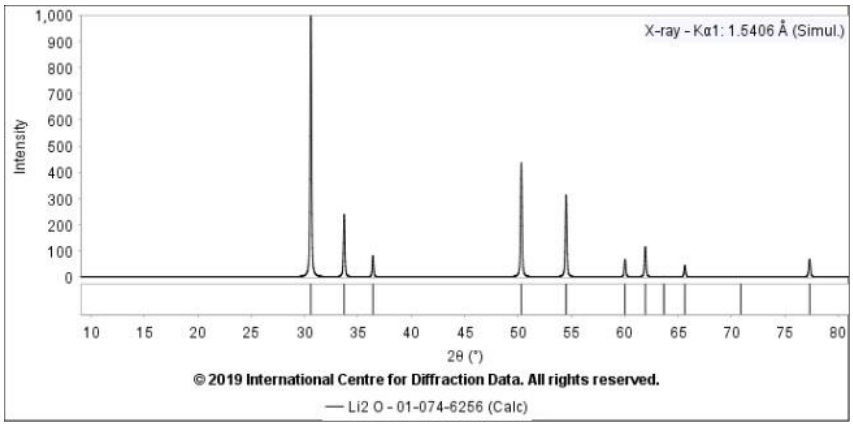
X-ray - Kα1: 1.5406 Å (Simul.)
Intensity
2θ (°)
© 2019 International Centre for Diffraction Data. All rights reserved.
— Li2 O - 01-074-6256 (Calc)

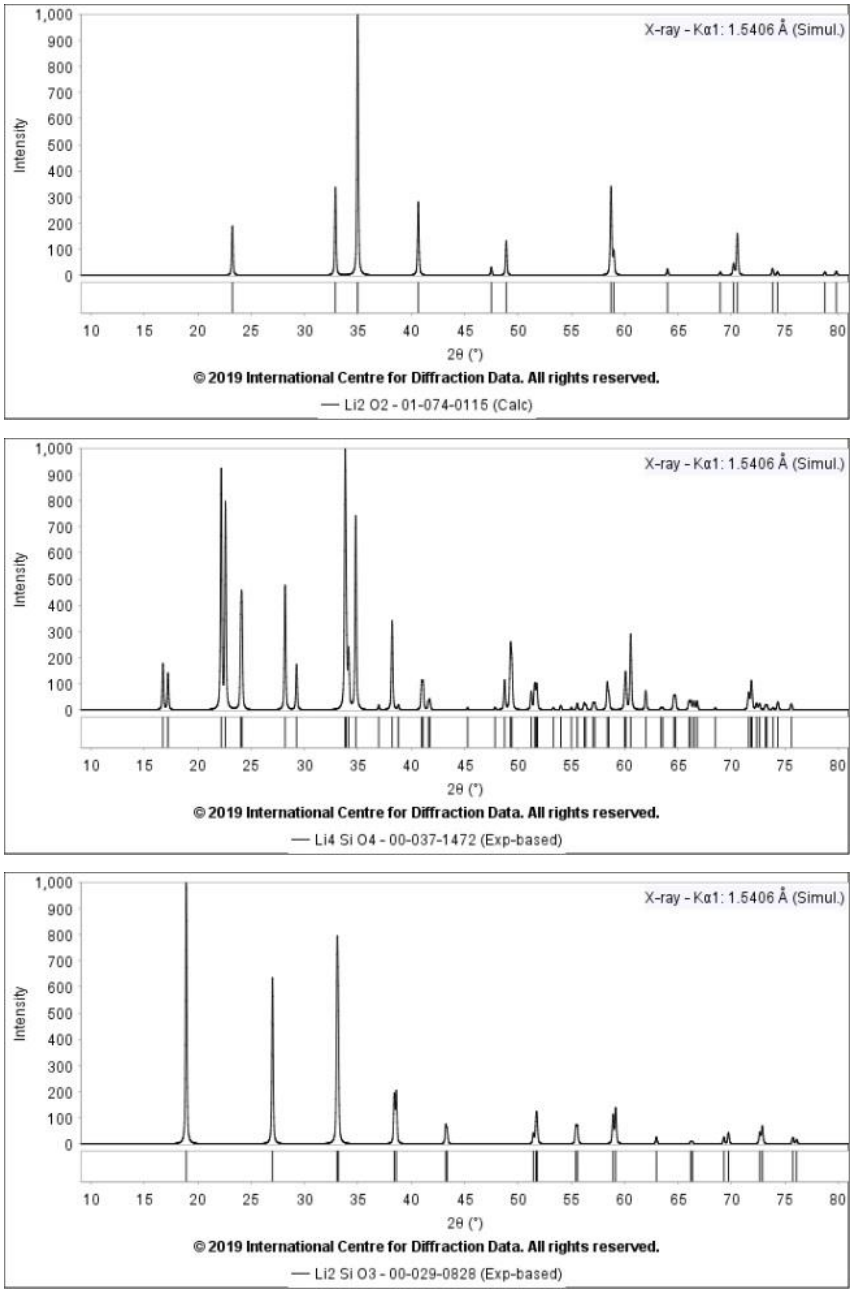

Figure S7. 2. ICDD PDF cards of $Li_xSi_yO_z/LiO_x$ species cross reference in the GI-XRD study.

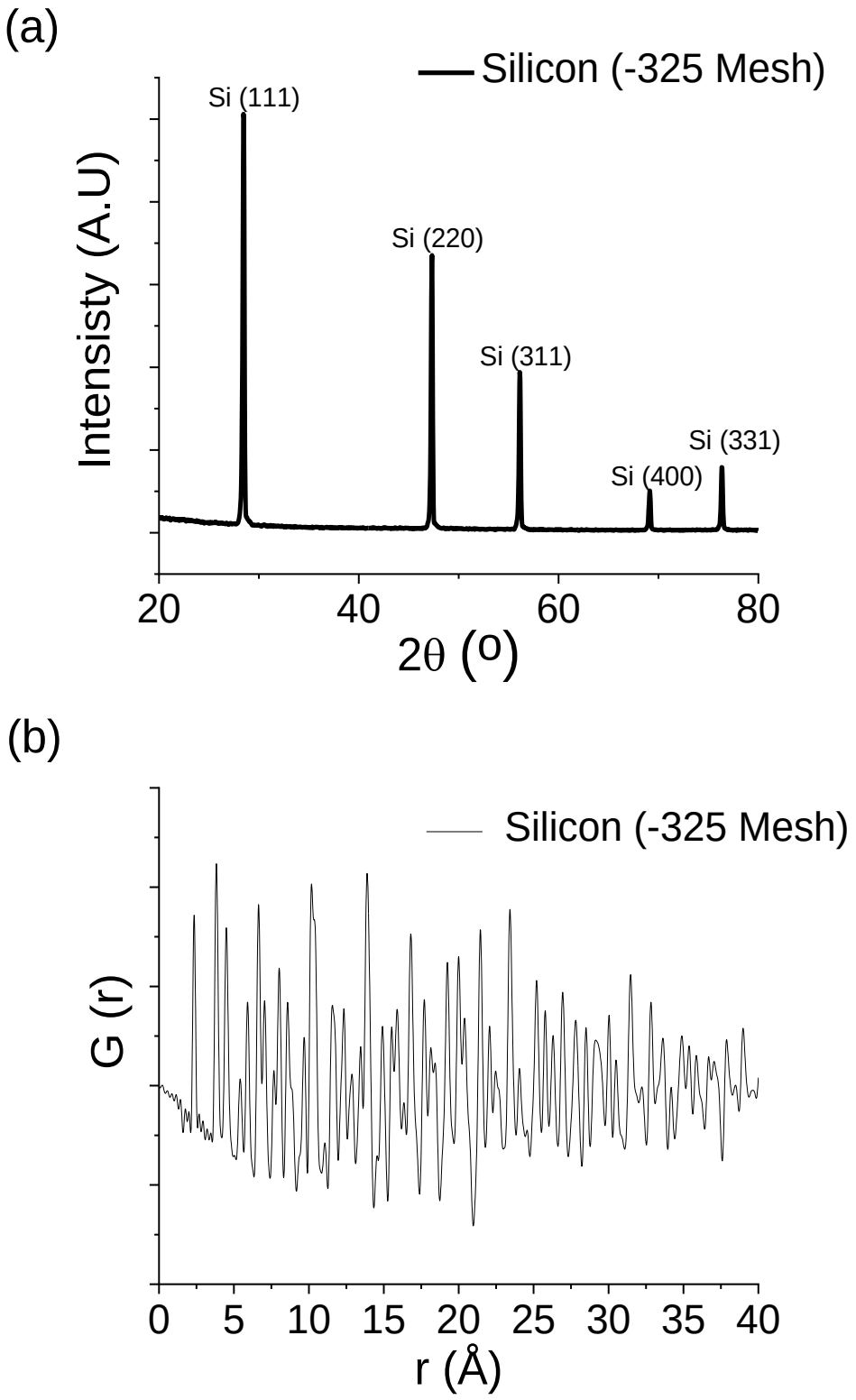

Figure S7. 3. (a) XRD and (b)XPDF of crystalline silicon -325 Mesh.

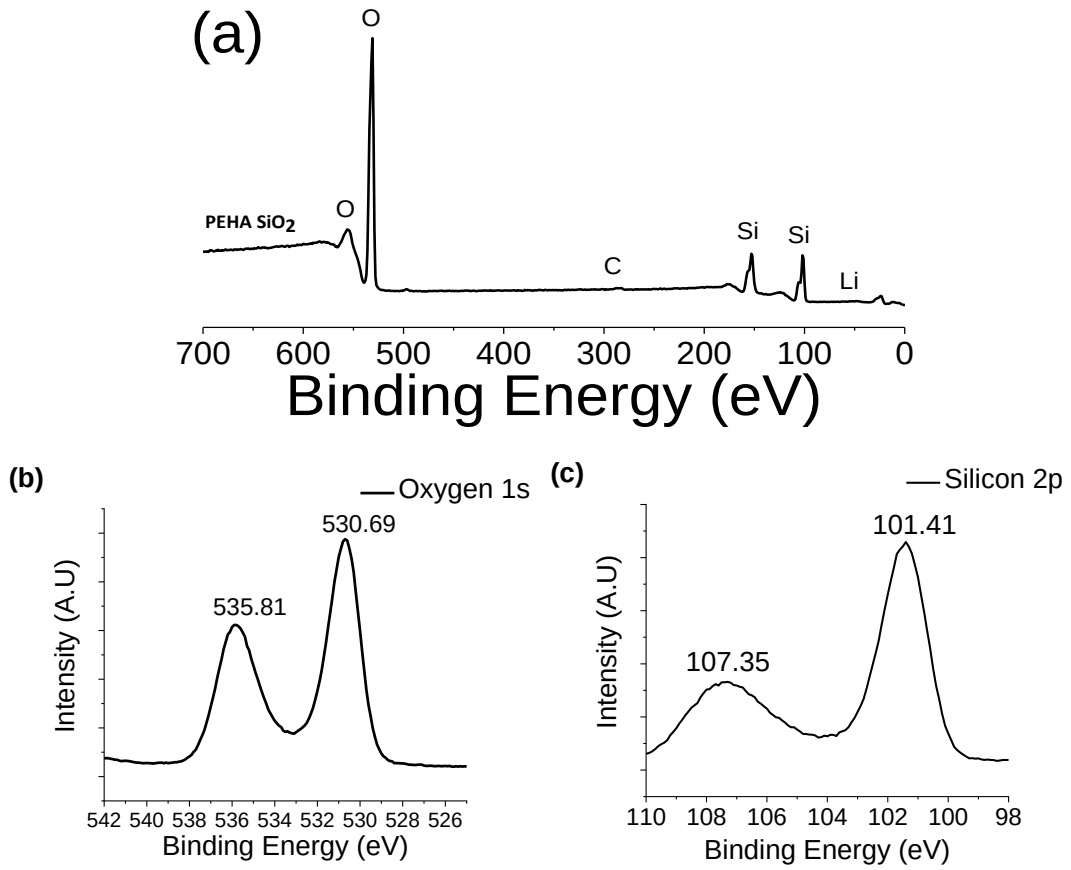

Figure S7.4. XPS data of BIS. (a) full spectrum of Binding Energies, (b) Oxygen 1s spectra, (c) Silicon 2p spectra.

1.7 References

[1] N. Liu, K. Huo, M. T. McDowell, J. Zhao, Y. Cui, *Sci. Rep.* **2013**, *3*, 1.

[2] L. Shi, W. Wang, A. Wang, K. Yuan, Y. Yang, *J. Alloys Compd.* **2016**, *661*, 27.

[3] A. Xing, S. Tian, H. Tang, D. Losic, Z. Bao, *RSC Adv.* **2013**, *3*, 10145.

[4] S. Liu, B. Liu, Y. Yao, P. Dong, S. Zhao, *J. Wuhan Univ. Technol. Sci. Ed.* **2016**, *31*, 965.

[5] D. Soo, M. Ryou, Y. Joo, S. Bin, J. Wook, **2013**, *110*, 12229.

[6] J. Liu, P. Kopold, P. A. vanAken, J. Maier, Y. Yu, *Angew. Chemie - Int. Ed.* **2015**, *54*, 9632.

[7] L. Batchelor, A. Loni, L. T. Canham, M. Hasan, J. L. Coffer, *Silicon* **2012**, *4*, 259.

[8] J. Liang, X. Li, Z. Hou, C. Guo, Y. Zhu, Y. Qian, *Chem. Commun.* **2015**, *51*, 7230.

[9] J. Liang, X. Li, Z. Hou, W. Zhang, Y. Zhu, Y. Qian, *ACS Nano* **2016**, *10*, 2295.

[10] H. Jia, P. Gao, J. Yang, J. Wang, Y. Nuli, Z. Yang, *Adv. Energy Mater.* **2011**, *1*, 1036.

[11] W. Chen, Z. L. Fan, A. Dhanabalan, C. H. Chen, C. L. Wang, *J. Electrochem. Soc.* **2011**, *158*, A1055.

[12] C. Wang, J. Ren, H. Chen, Y. Zhang, K. Ostrikov, W. Zhang, Y. Li, *Mater. Chem. Phys.* **2015**, *173*, 89.

[13] Y. Zhou, X. Jiang, L. Chen, J. Yue, H. Xu, J. Yang, Y. Qian, *Electrochim. Acta* **2014**, *127*, 252.

[14] J. Chen, L. Yang, S. Rousidan, S. Fang, Z. Zhang, S. Hirano, *Nanoscale* **2013**, *5*, 10623.

[15] X. Liu, Y. Gao, R. Jin, H. Luo, P. Peng, Y. Liu, *Nano Energy* **2014**, *4*, 31.

[16] D. Qiu, G. Bu, B. Zhao, Z. Lin, *J. Solid State Electrochem.* **2015**, *19*, 935.

[17] Z. Favors, W. Wang, H. H. Bay, Z. Mutlu, K. Ahmed, C. Liu, M. Ozkan, C. S. Ozkan, *Sci. Rep.* **2014**, *4*, 5623.

[18] J. Xie, G. Wang, Y. Huo, S. Zhang, G. Cao, X. Zhao, *Electrochim. Acta* **2014**, *135*, 94.

[19] W. Wang, Z. Favors, R. Ionescu, R. Ye, H. H. Bay, M. Ozkan, C. S. Ozkan, *Sci. Rep.* **2015**, *2*, 2.

[20] S. Choi, T. Bok, J. Ryu, J. I. Lee, J. Cho, S. Park, *Nano Energy* **2015**, *12*, 161.

[21] L. Shen, X. Guo, X. Fang, Z. Wang, L. Chen, *J. Power Sources* **2012**, *213*, 229.

[22] L. fen Guo, S. yun Zhang, J. Xie, D. Zhen, Y. Jin, K. yan Wan, D. gao Zhuang, W. quan Zheng, X. bing Zhao, *Int. J. Miner. Metall. Mater.* **2020**, *27*, 515.

[23] C. Li, C. Liu, W. Wang, Z. Mutlu, J. Bell, K. Ahmed, R. Ye, M. Ozkan, C. S. Ozkan, *Sci. Rep.* **2017**, 1.

[24] Y. Yu, L. Gu, C. B. Zhu, S. Tsukimoto, P. A. van Aken, J. Maier, *Adv. Mater.* **2010**, *22*, 2247.

[25] H. Wu, N. Du, X. Shi, D. Yang, *J. Power Sources* **2016**, *331*, 76.

[26] Z. Bao, M. R. Weatherspoon, S. Shian, Y. Cai, P. D. Graham, S. M. Allan, G. Ahmad, M. B. Dickerson, B. C. Church, Z. Kang, H. W. Abernathy, C. J. Summers, M. Liu, K. H. Sandhage, *Nature* **2007**, *446*, 172.

[27] W. Luo, X. Wang, C. Meyers, N. Wannenmacher, W. Sirisaksoontorn, M. M. Lerner, X. Ji, *Sci. Rep.* **2013**, *3*, 2222.

[28] M. Guo, X. Zou, H. Ren, F. Muhammad, C. Huang, S. Qiu, G. Zhu, *Microporous Mesoporous Mater.* **2011**, *142*, 194.

[29] B. D. Cullity, *Elements of X-Ray Diffraction*, Adison-Wesley Publision Company, Inc, **1978**.

End